



ScuDo
Scuola di Dottorato ~ Doctoral School
WHAT YOU ARE, TAKES YOU FAR



Doctoral Dissertation
Doctoral Program in Energy Engineering (34th cycle)

Heat and mass transfer in porous materials for passive energy-conversion devices

Towards the water and energy nexus

Matteo Alberghini

* * * * *


Supervisors

Prof. Pietro Asinari
Prof. Alberto Tiraferri
Prof. Eliodoro Chiavazzo

Politecnico di Torino
June 19, 2022

This thesis is licensed under a Creative Commons License, Attribution - Noncommercial-NoDerivative Works 4.0 International: see www.creativecommons.org. The text may be reproduced for non-commercial purposes, provided that credit is given to the original author.

I hereby declare that the contents and organisation of this dissertation constitute my own original work and does not compromise in any way the rights of third parties, including those relating to the security of personal data.


.....
Matteo Alberghini
Turin, June 19, 2022

Acknowledgements

This dissertation is the result and synthesis of the main research projects conducted during my PhD activity, which took place between the Energy Department of the Politecnico di Torino (PoliTo) and the Mechanical Engineering Department of the Massachusetts Institute of Technology (MIT). Several people and organizations contributed to this achievement and deserve to be acknowledged.

First of all, I want to recognize the fundamental contribution of my supervisors, who guided me by identifying the most innovative and visionary topics to work on. In particular, I thank Pietro Asinari for believing and investing in my potential and giving me the opportunity to test myself in international and cutting-edge environments. A special thanks also goes to Matteo Fasano, for being a supportive mentor, for inspiring me to find my own way, and for demonstrating what qualities must be cultivated to become a successful leader and researcher.

During these years at PoliTo my path has crossed with that of several colleagues and friends. In particular, among them I would like to thank Matteo Morciano, who patiently shared with me all his knowledge, with whom I shared most of my research activity and uncountable hours inside and outside the laboratory. Surely without him this thesis would not be as it is today. During my stay at MIT I was kindly hosted by Prof. Gang Chen and Dr. Svetlana Boriskina; I would particularly like to thank Svetlana for making me feel to all intents a member of her team and for trusting me to lead in full autonomy part of her research activity; moreover, a special acknowledgement goes to Marcelo and Volodymir, whose experience and contribution were fundamental to perform some of the experiments reported in Chapter 3 (operating the integrating sphere, FTIR, SEM and micro-CT).

I also had the privilege of collaborating with other institutions and organizations. In particular, some of the preliminary experimental work for the project reported in Chapter 4 was performed at the Istituto Nazionale di Ricerca Metrologica (INRiM) under the supervision of Vito Fericola and Fabio Bertiglia, whom I thank for their support. Finally, I would like to thank Paolo Sirianni and Alessio Testa of Microla, and Matteo Giardino of DISAT for the fabrication, SEM imaging, and coating of the samples reported in Chapter 5. Finally, I would like to acknowledge the financial support received from the Clean Water Center and the MITOR initiative, which made my doctoral journey possible.

Abstract

In the contemporary transition scenario, optimizing the water-energy nexus is crucial to reducing the environmental impact of several essential energy-intensive applications. For example, state-of-the-art desalination plants require up to 750 MWh/day to operate, while traditional cooling and heating systems account for 10.5% of total energy used in the US. In addition, large-scale plants require significant investment and maintenance, which may not be affordable or feasible in some areas of the world. In stark contrast, passive devices based on water wicking and evaporation offer a sustainable alternative to several traditional technologies, ranging from cooling to water treatment. Taking advantage of material-driven transport mechanisms, they do not require high-grade energy inputs and their working principle does not rely on mechanical moving parts. These features make passive devices particularly cost-effective, robust, and optimal for off-grid installation.

In this context, this dissertation focuses on the design, analysis, and application of porous media in passive technologies, with the aim of demonstrating the feasibility of high-performance devices with a new and more sustainable approach. Starting from the development of a comprehensive theoretical framework to analyze their heat and mass transfer performance, the discussion advances to their experimental characterization and, finally, to their perspective application in laboratory-scale prototypes, developed from a proof-of-concept perspective. Following this line, this thesis focuses on three different applications.

First, a novel polyethylene fabric with engineered transport properties is proposed for personal thermal management. Theoretical models, solved both analytically and numerically, were used to relate the micro-structure and chemistry of the fabric surface to the resulting performance. Experimentally, the created fabric reported better thermoregulation capabilities than conventional commercial textiles, such as polyester and cotton, which were used as a reference throughout the characterization process. Thus, the use of the proposed material for garments promises to reduce the internal cooling demand during hot seasons and, at the same time, the properties of polyethylene allows reducing the environmental footprint of its production, use and disposal phases.

Successively, the issue of thermal management was addressed shifting from a single user application (namely, engineered textiles for personal thermal management) to a system-level approach (e.g., a cooling system for buildings); that is, by proposing a modular multistage device capable of generating a net cooling capacity driven solely by the salinity difference between two solutions. The concept was investigated both theoretically and experimentally: a 4-stage laboratory-scale device was fabricated and characterized; the results were used to validate a theoretical 0-D model, which was subsequently employed to optimize the device performance. The

tested device, despite being far from optimality, has demonstrated considerably better performance than other passive cooling approaches, proving the potential of this technology.

Both discussed applications exploit capillary transport to achieve the desired performance: comfortable fabrics are required to effectively wick and evaporate sweat, while the cooling device must self-supply distilled water to be considered entirely passive. Therefore, the final application proposed focuses on the structure itself of porous media, envisioning a novel class of textured, ultra-thin and rigid materials. The concept was tested on aluminum sheets, which were machined by femtosecond laser to obtain V-shaped grooves and, subsequently, covered with silica. The obtained material was able to exhibit stable capillary properties even when exposed to saline solutions for more than 250 hours. Therefore, it was envisaged for use in a passive device for solar desalination: an analytical model was used to investigate the productivity and optimal size of the device depending on the properties of the used capillary materials. By providing general guidelines for the design of passive device based on wicking and evaporation, this section aims to demonstrate the potential of using structured materials to improve the scalability and performance of passive technologies.

Concluding, by proposing novel materials, functioning principles and design layouts, this thesis seeks to create a bridge between fundamental research on heat and mass transfer phenomena and applied engineering challenges.

Publications

Part of the work contained in this dissertation was also previously published in the following articles:

1 – Alberghini, M., Morciano, M., Fasano, M., Bertiglia, F., Fernicola, V., Asinari, P., & Chiavazzo, E. (2020). Multistage and passive cooling process driven by salinity difference. *Science advances*, 6(11), eaax5015.

2 – Alberghini, M., Hong, S., Lozano, L. M., Korolovych, V., Huang, Y., Signorato, F., Zandavi, S. H., Fucetola, C., Uluturk, I., Tolstorukov, M. Y., Chen, G., Asinari, P., Osgood, R. M., Fasano, M., & Boriskina, S. V. (2021). Sustainable polyethylene fabrics with engineered moisture transport for passive cooling. *Nature Sustainability*, 4(8), 715-724.

3 – Alberghini, M., Boriskina, S. V., Asinari, P., & Fasano, M. (2022). Characterisation and modelling of water wicking and evaporation in capillary porous media for passive and energy-efficient applications. *Applied Thermal Engineering*, 208, 118159.

4 – Alberghini, M., Morciano, M., Giardino, M., Perrucci, F., Scaltrito, L., Janner, D., Chiavazzo, E., Fasano, M., & Asinari, P. (2022). Textured and rigid capillary materials for passive energy-conversion devices. *Advanced Materials Interfaces*, 2200057.

The following articles were published as part of the Ph.D. activity but were not included in this dissertation:

1 – Bergamasco, L., Alberghini, M., Fasano, M., Cardellini, A., Chiavazzo, E., & Asinari, P. (2018). Mesoscopic moment equations for heat conduction: characteristic features and slow-fast mode decomposition. *Entropy*, 20(2), 126.

2 – Alberghini, M., Morciano, M., Bergamasco, L., Fasano, M., Lavagna, L., Humbert, G., ... & Asinari, P. (2019). Coffee-based colloids for direct solar absorption. *Scientific reports*, 9(1), 1-11.

3 – Cardellini, A., Alberghini, M., Rajan, A. G., Misra, R. P., Blankschtein, D., & Asinari, P. (2019). Multi-scale approach for modeling stability, aggregation, and network formation of nanoparticles suspended in aqueous solutions. *Nanoscale*, 11(9), 3979-3992.

- 4 – Bergamasco, L., Alberghini, M., & Fasano, M. (2019). Nano-metering of solvated biomolecules or nanoparticles from water self-diffusivity in bio-inspired nanopores. *Nanoscale research letters*, 14(1), 1-11.
- 5 – Antonetto, G., Morciano, M., Alberghini, M., Malgaroli, G., Ciocia, A., Bergamasco, L., ... & Fasano, M. (2021). Synergistic freshwater and electricity production using passive membrane distillation and waste heat recovered from camouflaged photovoltaic modules. *Journal of Cleaner Production*, 318, 128464.
- 6 – Mancardi, G., Alberghini, M., Aguilera-Porta, N., Calatayud, M., Asinari, P., & Chiavazzo, E. (2022). Multi-Scale Modelling of Aggregation of TiO₂ Nanoparticle Suspensions in Water. *Nanomaterials*, 12(2), 217.

Contents

1	Introduction	1
1.1	Objective and structure of the dissertation	2
1.2	Applications-specific context	5
1.2.1	Personal thermal management	5
1.2.2	Sustainable passive cooling	12
1.2.3	Capillary materials for energy-conversion devices	13
2	Mass transfer in micro-porous media: theoretical framework	15
2.1	Analytical evaluation of the contact angle	18
2.1.1	Shape parameters of a sessile droplet on cylindrical fibers	18
2.1.2	Shape parameters of a sessile droplet on a flat surface	20
2.2	Capillary pressure in an ideal yarn	21
2.2.1	Capillarity in a multi-fiber infinite and dense yarn	23
2.2.2	Capillarity in a multi-fiber infinite and sparse yarn	24
2.2.3	Maximum porosity of a finite-size ideal yarn	26
2.3	Capillary pressure in V-shaped open grooves	27
2.3.1	Neglecting gravity – maximum grooves width	28
2.3.2	Capillary pressure in micro-sized grooves	30
2.4	Dynamic wicking model	32
2.4.1	Wicking in an infinite multi-filament dense yarn	32
2.4.2	Wicking in V-shaped grooves	34
2.4.3	Transition to volume-averaged parameters	34
2.4.4	Permeability in fibrous media	36
2.4.5	High evaporative fluxes	36
2.5	Differential formulation of wicking	40
2.6	Mass transfer through a hydrophobic membrane	44
3	Sustainable polyethylene fabrics with engineered water transport properties	49
3.1	Experimental investigation	51
3.1.1	Fabrication and characterization of the fibers and yarn structure	51
3.1.2	Evaluation of the water-fiber contact angle	53

3.1.3	Oxygen-plasma treatment and infrared spectroscopy	56
3.1.4	Wicking performance	58
3.1.5	Evaporation performance	62
3.1.6	Optical properties and radiative heat transfer	66
3.1.7	Setup characterisation and parameters estimation	69
3.2	Analytical prediction of the textile performance	71
3.2.1	Numerical evaluation of the surface free energy of cylindrical fibers	71
3.2.2	Theoretical wicking performance	75
3.2.3	Model fitting and structure optimization	80
3.3	Finite elements analysis of the textile performance	82
3.3.1	Wicking	83
3.3.2	Evaporation	83
3.3.3	Radiative heat transfer	89
3.3.4	Performance assessment	94
3.4	Conclusions	99
4	Multistage and passive cooling process driven by salinity difference	103
4.1	Functioning principle	104
4.2	Device characterization	107
4.2.1	Experimental setup	107
4.2.2	Experimental protocol	108
4.3	Measurement of the membrane resistance coefficient	110
4.4	Lumped-parameters heat transfer model	112
4.5	Cooling performance: experimental investigation	116
4.6	Different operating conditions	120
4.6.1	Influence of salt type and concentration	120
4.6.2	Influence of device stratigraphy	121
4.6.3	Maximum cooling capacity	124
4.6.4	Preliminary considerations on three-components mixtures	126
4.6.5	Performance comparison with radiative cooling technologies	129
4.7	Passive solar cooling	130
4.8	Considerations on the environmental and life-cycle issues	134
4.9	Cost analysis of the lab-scale prototype	135
4.10	Conclusions	136
5	Textured and rigid capillary materials for passive energy-conversion devices	139
5.1	Crafting and characterization of the rigid capillary material	140
5.2	Wetting and wicking performance	143
5.3	Durability and surface functionalization	146

5.4	Modelling and experimental evaluation of the capillary properties	152
5.5	Application in solar desalination	157
5.6	Conclusions	165
6	Conclusions and perspectives	167
A	Temperature-dependent physical properties of water and air	173
B	Evaluation of the uncertainty of measurements	175
B.1	Yarn porosity	175
B.2	Position of the water front	176
B.3	Contact angle	176
B.4	Evaporation tests	177
B.5	Absolute permeability	178
B.6	Temperature	178
B.7	Distillate flow rate	180
B.8	Specific thermal power	181
B.9	Thermal conductance	182
B.10	Membrane resistance coefficient	182
B.11	Activity coefficient	183
C	Lumped-parameters representation of a passive desalination de-	
	vice	185
C.1	Thermal network	185
C.2	Lateral losses	188
C.3	Performance	189
	Nomenclature	193
	Bibliography	197

Chapter 1

Introduction

Climate change threatens to alter ecological and social balances, causing water and food shortages, extreme weather events, increased incidence of diseases and severe economic losses [1]. Despite a persistently animated public debate, the scientific community agrees in ratifying its existence [2] and in attributing to human activities a key role in the acceleration of this phenomenon [3]. To reduce the impact of climate change, world's nations have committed to keeping global temperatures well below 2 °C compared to pre-industrial levels by signing the Paris Agreement [4]. To achieve this goal, in the next few years the global greenhouse gas emissions must be greatly reduced, reaching the net-zero by 2050 to limit the temperature increase to 1.5 °C [5]. This objective will require a dramatic short-term transition toward carbon-neutral technologies, an effort that must be shared by the entire scientific community, both academic and private.

In this scenario, the water-energy nexus is a key aspect in reducing the environmental impact of human activities. Water and energy are two closely related fields: a wide range of applications require huge volumes of water to generate or operate energy assets and, on the other hand, the supply or management of water resources is often largely energy intensive [6]. Examples of applications in the 'water for energy' field include the production of oil (0.43 m³ of water/m³ of oil for traditional extraction, which increases to 7 m³/m³ for in-situ tar sands mining [7]) and bio-fuels (3.6 m³ of water/m³ for corn-based ethanol, which increases to 11.6 m³/m³ for sugarcane-based ethanol [8]), power generation (270 TL used in the United States in the year 2000, accounting for 47.8% of the total water used [9]), irrigation (31% of the total water used in the US in the year 2005 [10]), cooling and heating. At the same time, energy is crucial for wastewater treatment (approximately 0.5 kWh/m³ [11]), desalination (ranging from 3.7 kWh/m³ to 6 kWh/m³ for reverse osmosis systems [12], more than 40% of the total cost of operation [13]), pumping and water distribution. Clearly, the applications in which water and energy are interconnected are numerous and each requires a specific technical treatment, both from a theoretical and engineering perspective. With the aim of mitigating

climate change, the best strategy would be to develop novel devices that require the least amount of high-quality energy to operate (e.g., electricity). Therefore, the environmental footprint of these devices would reside solely in their manufacturing and disposal stages, which would be a significant paradigm shift compared to the devices commonly used to address most of the aforementioned applications.

Following this concept, the recent interest in water wicking and evaporation from porous materials has exponentially increased due to their use in passive technologies addressing the water-energy nexus, most of which rely on hydrophilic porous media. Water wicking and evaporation are crucial phenomena in a broad variety of industrial applications, ranging from food processing [14] to paper-based diagnostic [15], from water desalination [16–18] to soil science [19]. As an example, Wu and co-workers, inspired by a traditional siphon, developed a self-pumping device for the collection of crude oil spills, whose working principle is based on capillarity and a tailored oleophilic hierarchical surface [20]. In the field of thermal management, Dai and co-workers developed a copper-based mesh able to increase the evaporative cooling of fluids thanks to the effect of capillary transport and thin film evaporation [21]. These phenomena are also crucial in the field of humidity harvesting from the atmosphere, where metal organic frameworks [22] and hydrogels [23] were successfully used in proof-of-concept implementations. Capillary transport and evaporation are even used to harvest electrical energy exploiting the streaming potential of water flowing in charged micro-channels [24, 25]. Such devices do not require high-quality energy inputs (e.g., electricity) and, thanks to the absence of mechanical moving parts (e.g., pumps and compressors), need low maintenance and are usually cheap. Furthermore, they are optimal for off-grid installations and, in general, promote the sustainable transition towards the water-energy nexus. As the performance of these passive systems are strictly determined by the efficiency of the heat and mass transfer mechanisms involved, their comprehension is crucial to correctly design novel porous materials with optimised performance. Although their working principle is apparently simple, it is based on the synergistic coupling between the geometric and chemical-physical properties of the surface of the materials used, which are often engineered at the micro- and nano-scale. Therefore, each of their implementations has a high technological content and should be accompanied by an accurate theoretical understanding of the fundamental phenomena involved. In this way, their model-based design can be envisioned, optimizing their performance and reducing the gap with their active counterparts, thus contributing to the transition of the energy sector towards sustainability.

1.1 Objective and structure of the dissertation

The goal of this dissertation is to demonstrate the possibility of exploiting passive heat and mass transfer mechanisms to design and engineer high-performance

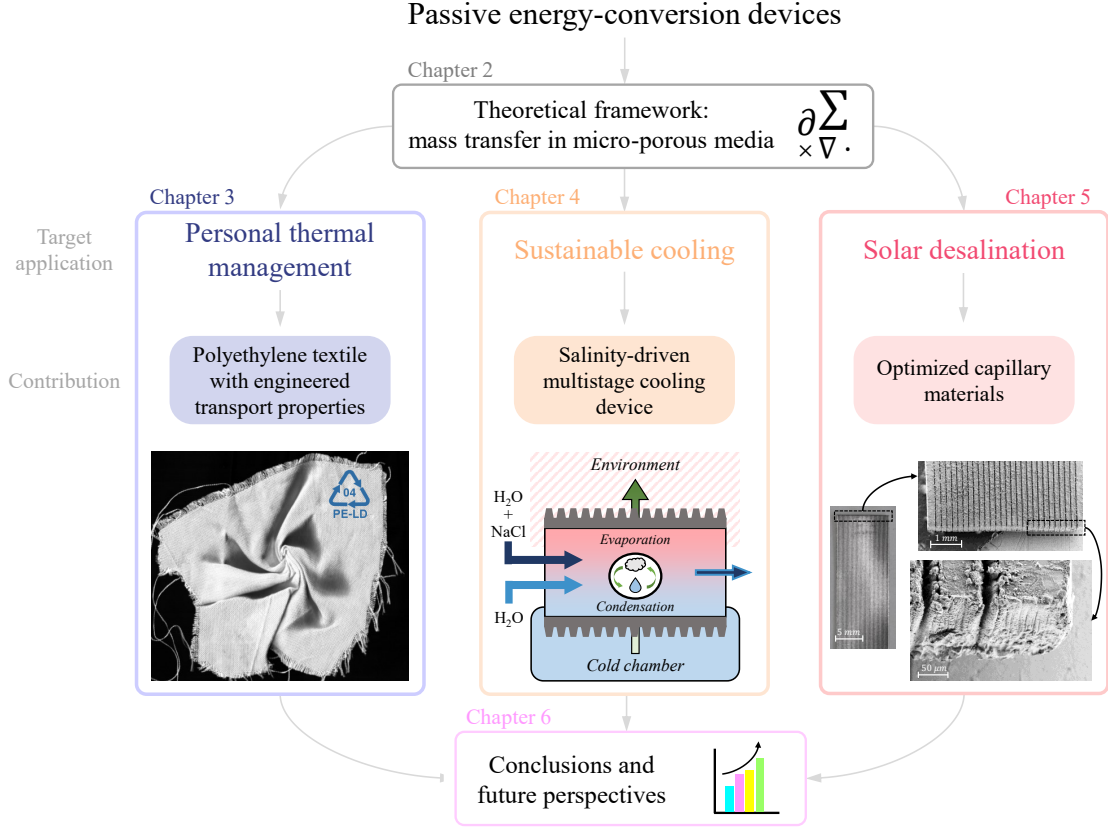


Figure 1.1: **Structure of the dissertation.** Flowchart representing the organization of this work, highlighting the applications addressed and the main contributions developed throughout the thesis.

devices for the water-energy nexus. The focus was set on three applications where passive devices could provide a marked changeover compared to traditional solutions: personal thermal management, cooling, and desalination, all envisioned in a passive fashion. Each of these applications was addressed in a dedicated chapter of this dissertation, where a new device concept is envisioned, implemented and tested. Each proposed technology was investigated both theoretically and experimentally: starting from modelling their underlying physical phenomena, the obtained theoretical results were used to predict and optimize their performance. Finally, laboratory-scale prototypes were created to demonstrate the validity of the concept. For the sake of clarity, the structure of the dissertation was schematized in Fig. 1.1.

First, Chapter 2 introduces the theoretical framework common to all the applications discussed in this work, namely capillary transport in porous media. Starting from the integration of Laplace equation, the fundamental relations needed to describe the capillary force in structured porous media were derived for given channel

geometries and material properties, focusing on fibrous media and grooved substrates. The results obtained were used to derive 1-dimensional analytical models describing the dynamic wicking transient when the porous surface is subject to evaporation. Finally, relying on water retention curves, the theoretical framework was extended deriving a differential formulation of capillary transport, permitting comparison with unstructured porous media (e.g., paper and non-woven fabrics), while also allowing to describe imbibition in complex 2-D and 3-D geometries, as those most recently presented in the literature [26–29]. The theoretical results obtained in this chapter were used throughout the dissertation with a twofold intent: to interpret the experimental results; to optimize the performance of the crafted devices.

Chapter 3 demonstrates that polyethylene (PE) fibers can be functionalized and woven to create a breathable fabric for personal thermal management. Importantly, the textile fabrication was performed without any chemical treatment (e.g., polydopamine) and without blending the PE fibers with other materials (e.g., cotton), as previously reported in the literature [30, 31], which would have compromised the fabric recyclability. First, the chapter focuses on the experimental characterization of its micro-structure and thermal properties, where the latter, for simplicity, were assessed by the individual investigation of three phenomena: wicking, evaporation, and radiation. Then, the obtained results were used to validate the models derived in Chapter 2, which, finally, were employed to analyze the relationship between the fabric micro-structure, surface chemistry, and environmental conditions on determining the overall fabric thermal performance. Summarizing the achieved results, this dissertation reports a novel all-polyethylene hydrophilic fabric with enhanced capillary and drying performances, which were compared with those of commercial fabrics (among the others, cotton and polyester), assumed as reference competitors. As a result, the proposed textile presented the lowest wet-to-dry time (17% and 59% faster than polyester and cotton, respectively) and the best wicking capabilities (comparable with cotton, 35% better than polyester) in standard tests.

Chapter 4 develops an alternative approach to passive evaporative cooling by proposing a membrane-based multistage device able to generate a net cooling capacity by exploiting the salinity difference between two feed solutions instead of relying on the humidity content of ambient air. The modular device does not need external energy to operate, as it relies on capillarity and on vapour pressure difference; therefore, its working principle can be considered as entirely passive. The concept was deployed to implement a 4-stage prototype, whose performance was characterized under different working conditions and used to validate a dedicated theoretical model. Despite being in its early stages and being developed just as a proof-of-concept lab-scale prototype, the proposed technologies overcomes the performance and limits of both traditional evaporative and radiative cooling solutions: the best performing configuration tested achieved a maximum specific cooling capacity of approximately 170 W m^{-2} and a minimum temperature $4 \text{ }^\circ\text{C}$ lower than

the surrounding environment.

Finally, Chapter 5 introduces a new research avenue in the design of passive devices by replacing traditional porous materials with rigid capillary layers engraved with optimized V-shaped grooves. The use of thin components able to preserve their planarity can increase the scalability of multistage layouts, such as the one proposed in Chapter 4: more stages can be stacked before incurring in dry-out and, furthermore, it would allow to remove expensive and fragile components without compromising its functionality. The concept was tested using aluminum sheets: the foils were machined by femtosecond laser and coated by silica, which was essential to achieve the observed long-term stability of the capillary properties, even when exposed to salt solutions. As a case study, the novel material was envisaged for use in a passive multistage solar desalination device, originally proposed in Ref. [17]. The achievable productivity and maximum size of the device were estimated by a coupled heat and mass transfer model, which was also employed to explore the impact of different thermal and capillary properties on the key performance indexes of the device.

In conclusion, this dissertation presents three entirely passive technologies as alternatives to the various existing and widely developed solutions, mostly with high environmental impact (see the in-depth discussions reported in section 1.2). However, since the various devices proposed were investigated exclusively in a proof-of-concept perspective, this work also serves to highlight their major limitations and the aspects on which future research should focus in view of their scale-up.

1.2 Applications-specific context

This section focuses on introducing the context of the applications discussed, highlighting why the proposed solutions can help reduce their environmental impact.

1.2.1 Personal thermal management

Personal thermal management (PTM) can simply be translated into people’s fundamental need for thermal comfort – to stay warm in colder seasons and to cool down in warmer climates. Although it may seem like a marginal and straightforward task, thermoregulation plays a crucial role in determining large-scale energy consumptions. For this reason, the installation of heating, ventilation, and air conditioning (HVAC) systems is common practice in most buildings, both public and private. However, these systems have an excessive energy consumption [32]: according to the U.S. Department of Energy, the energy used in residential buildings for space heating and cooling purposes amounts to approximately to 10.5% of the total national energy consumption and to about 55% of total energy consumed in

households [33]. In addition, HVAC systems are only effective in closed environments and operate on a suboptimal strategy, namely by conditioning the entire ambient rather than focusing on the comfort of each occupant. In this scenario, smart and engineered textiles represent a passive, extremely customizable and flexible technology, optimal to reduce energy consumption related to PTM [34]. In fact, changing the temperature set points by 4 °C of HVAC systems for both cooling and heating can lead to a reduction in their energy consumption by up to 45% and 35% for hot and cold seasons, respectively [35].

However, the traditional textile industry is far from being sustainable: consumerism, the ‘fast fashion’ phenomenon, and an extraordinary reduction in the clothing prices have caused the manufacturing of clothes to almost double in the last 15 years, while their average life span has been shortened by almost 40% in the same period [36]. As a consequence, clothing are disposed before the technical end of their life-cycle [37]. The best strategy to reduce their environmental footprint is to increase the recycle and reuse of old garments, which is far from being optimal: considering Europe as an example, only 15 - 20% of the textiles disposed are recycled ($\sim 50\%$) or reused ($\sim 50\%$, sent towards developing countries), while the remainder ends up in landfills or is incinerated [38]. This being the case, most of the textiles currently produced are created using raw materials and, considering current production trends, it has been estimated that by 2050 the impact per garment use must be reduced by more than 30% to remain within the 2 °C temperature increase target [39].

In 2018, fiber production totaled more than 100 gigatonnes and is expected to reach 150 gigatonnes by 2030 [40]. Production volumes are dominated by synthetic fibers, with polyester being the most widely used material (polyethylene terephthalate, PET, over 50% of total production), followed by cotton ($\sim 25\%$, see Fig. 1.2). However, in this context the equation ‘natural = sustainable’ can lose its validity: the use of natural fibers such as cotton, linen, or silk, commonly perceived as eco-sustainable, hides a high environmental impact, understandable only by analyzing the entire life cycle of the fabric. Comparing the life cycle assessment (LCA) parameters of the two most widely produced materials, namely cotton and PET, it is clear that the cradle-to-gate cycle of natural fibers requires more water, fertilizer, chemicals and land-use, and is therefore linked to much higher ecotoxicity than synthetic fibers (see their LCA in the table 1.1). Specifically, the entire cotton production process requires more than 5700 m³ of water per ton of material produced, while PET requires only about 130 m³, which is in stark contrast to the goal of reducing water depletion. At the same time, however, even newly produced petroleum-based materials such as PET cannot be considered eco-friendly, as they require a significantly higher consumption of non-renewable energy to be produced (95 GJ/t vs. 36 GJ/t for cotton), even considering the possibility of energy recovery from their incineration at the end of their life cycle (81 GJ/t vs. 26 GJ/t for PET and cotton, respectively), and are linked to almost twice the production of GHGs

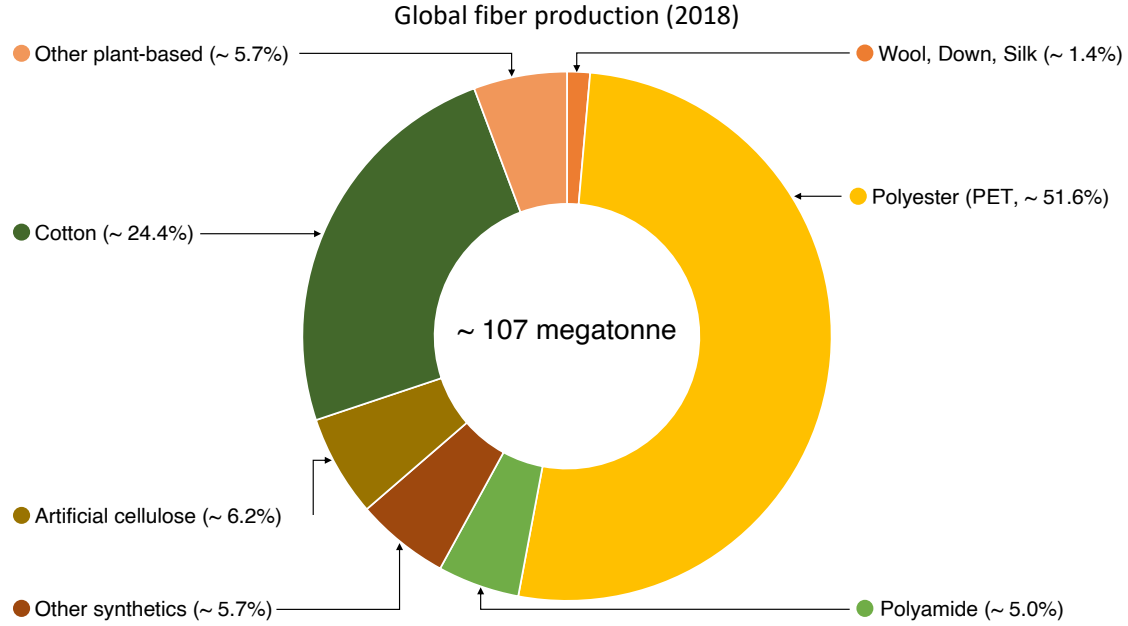


Figure 1.2: **Global fiber production in 2018.** Split of the global production of textile fibers in 2018, for a total amount of 107 megatonne. More than 60% of the total produced amount is due to synthetic fibers. Data retrieved from Ref. [40]

compared to cotton (4.1 tonnes CO₂ eq./t for PET) [41].

	Cotton	PET
Ozone layer depletion ($\times 10^{-4}$ kg CFC11 eq./t)	2.0	0.7
Human toxicity (kg 1,4DB eq./t)	1700	4393
Freshwater aquatic ecotoxicity (kg 1,4DB eq./t)	17310	58
Terrestrial ecotoxicity (kg 1,4DB eq./t)	1568	12
Acidification (kg SO ₂ eq./t)	41	21
Eutrophication (kg PO ₄ ³⁻ eq./t)	22	1.2

Table 1.1: **Life-cycle assessment of cotton and polyester (PET).** The data, retrieved from Ref. [41], are expressed in equivalent kilograms of chemical compounds considered as most harmful for each category.

Recent advances in materials science and engineering have produced several new technologies aiming to address the problem of personal thermal management without relying on the aforementioned fashion industry materials. Conventional approaches to PTM rely on air blowing fans, liquid cooling, or phase change materials directly integrated into clothing for warm seasons [42, 43] or electric heaters

for cold ones [44]. On the other hand, advanced strategies utilize self-tuning microstructures, aiming to optimize all heat transfer mechanisms, including radiation, which is often overlooked despite nearly 50% of the heat produced by the human body is dissipated through this mechanism [45]. In this direction, several advanced materials have been proposed in the literature. For example, Cui and co-workers [46] have used silver nanowires to provide traditional fabric with reflection properties in the IR spectrum: since human thermal radiation has its emission peak at the $9 \mu\text{m}$ wavelength (see section 3.1.6), a metal mesh woven significantly finer than that size would present a high reflection coefficient, while remaining permeable to air and moisture. Following this approach, it was calculated a possible energy saving of more than 350 W per person in case of heating, which, considering public buildings, would translate into substantial costs reduction. Differently, Zhang and collaborators [47] proposed in a recent seminal work an environment-responding fabric capable of adapting its micro-structure by absorbing or releasing moisture, thus being able to passively tune its optical properties. The core element of fibers were made of a blend of cellulose and triacetate, which were subsequently coated by multi-walled carbon nanotubes. As a result, the dry and tightly packed fibers are IR-reflective, thus preventing the dispersion of body heat; by absorbing body moisture, the yarns swell and loosen their meshes, increasing their IR transparency by over 35%.

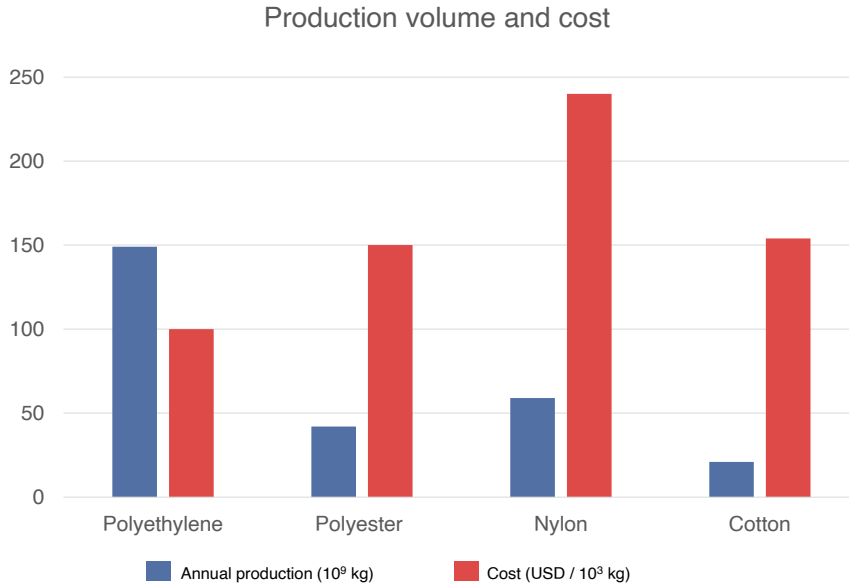


Figure 1.3: **Global production volume of different materials.** Data retrieved from Ref. [48].

Among the different materials proposed, polyethylene (PE) has emerged as a

particularly promising material for multipurpose textiles. PE can be a promising material for wearable textile production owing to its high transparency for long-wavelength infrared radiation emitted by the human body, which is provided by its particular molecular structure [49, 50]. Infrared transparency of polyethylene garments may allow the body heat to escape radiatively, providing a passive cooling mechanism not available when using conventional materials, which all exhibit high infrared absorptance. Visible opacity of polyethylene fabrics can be simultaneously achieved by engineering either the fiber or the pore sizes to scatter the short-wavelength visible light efficiently. The concept was proposed by Tong and co-workers in their pioneering work [51], where they predicted by an accurate theoretical model the possibility to obtain an infrared transparent fabric by weaving 1 μm fibers into 30 μm yarns, achieving 97% IR transparency and adequate visible opacity. Subsequently, the research group led by Cui and Fan [30, 31] demonstrated the concept by producing a fabric based on nano-porous PE, achieving an excellent infrared transparency of 77%. Furthermore, follow-up experiments on nano-porous polyethylene films and fiber-based knitted textiles confirmed their passive cooling performance [31, 52, 53]. However, a fabric has to be hydrophilic, breathable, soft and vapor permeable to be comfortable to wear. For this reason, the nano-PE was treated by micropunching, coated with polydopamine and supported by a cotton mesh. Although promising, this technique requires several steps, including chemical treatments and the combination with cotton. From the point of view of environmental impact, this multi-material, although performing well, would be significantly more difficult to recycle and would contain both natural and synthetic materials, combining their respective toxicity problems aforementioned. However, these issues could be avoided if the same properties of wearability and comfort could be achieved directly through a mono-material polyethylene fabric, without the addition of other chemicals or materials. Such a fabric could combine excellent thermal performance, thus addressing PTM and reducing the energy consumption of HVAC systems, as well as a reduced environmental impact compared to the alternatives proposed so far.

In fact, PE is one of the most-produced materials in the world: reaching annual production levels above 100 million tons, it outclasses all the other traditional textile materials ever produced and, at the same time, has the lowest price per tonne (see Fig. 1.3). Upholding circular economy principles in textile industry requires the use of new raw materials with lower environmental impact, upcycling existing plastic waste, as well as enhancing fabrics longevity and multi-functionality to promote re-use over recycling [55]. The Higg Materials Sustainability Index (MSI) database [56] can be used to prove that the fabrication process of woven fabrics made of melt-spun PE yarn exhibit the lowest environmental footprint among all common woven textiles, including cotton, linen (flax), wool, silk, nylon, and polyester. The data shown in Fig. 1.4 reveal that PE fabrics are expected to outperform conventional textiles by all indicators, including climate change, ozone depletion, human and

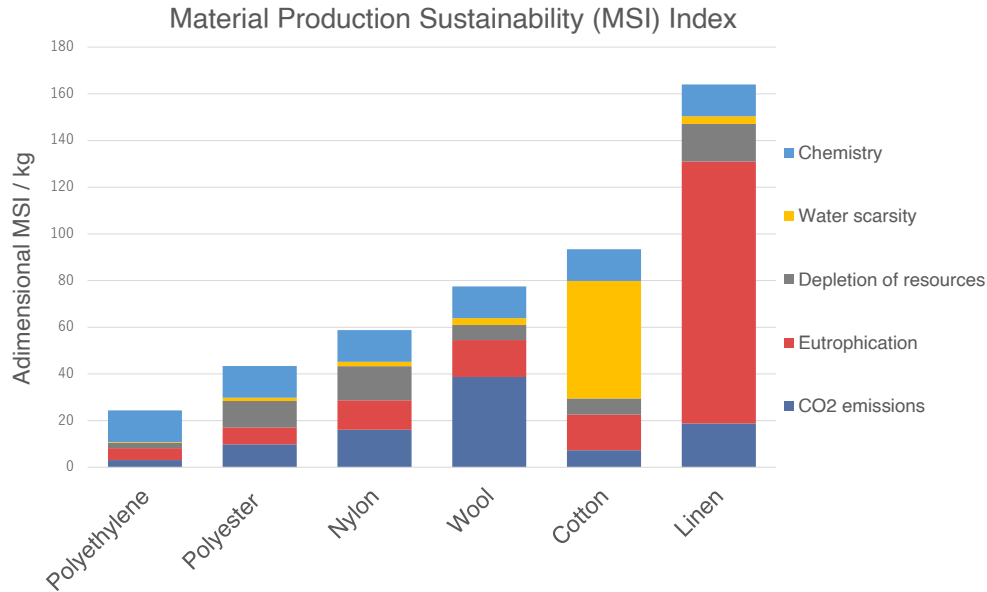


Figure 1.4: **MSI index of common materials used in the fashion industry.** Data retrieved from Ref. [54].

ecosystem toxicity, particulate matter release, terrestrial acidification, freshwater and marine eutrophication, as well as fossil and water resource depletion, further elevating the sustainability profile of polyethylene-based textiles. Furthermore, the MSI Higg index only accounts for the environmental footprint incurred during the production and end-of-lifecycle phases. Studies show that textiles and garments may leave even larger environmental footprints in the course of their usage phase, by consuming energy, water, and chemicals during washing and tumble-drying processes [57, 58].

The reuse of polyethylene waste would be particularly useful to decongest landfills. In fact, in 2003 Western Europe had a production of more than 98 kg of plastic per capita, for a total of almost 49 million tons, and more than 78% of this is made of thermoplastics (thus including PE) [59]. Considering that 80% of post-consumer plastic ends up in landfills, while only 8% is incinerated and 7% recycled, the current waste stocking levels poses serious health and environmental problems due to the production of greenhouse gases [60]. In this sense, PE boasts multiple simple and proven processes of industrial separation and recycling [61, 62]: being sorted on the basis of its mid-infrared footprint [63], PE waste can be either mechanically separated and reprocessed via melt-extrusion, chemically processed and depolymerized into its monomers, incinerated, or converted into a new fuel source at the end of its lifespan [64]. The possibility of easily recycling PE (either mechanically or chemically) allows for additional reduction in the environmental footprint

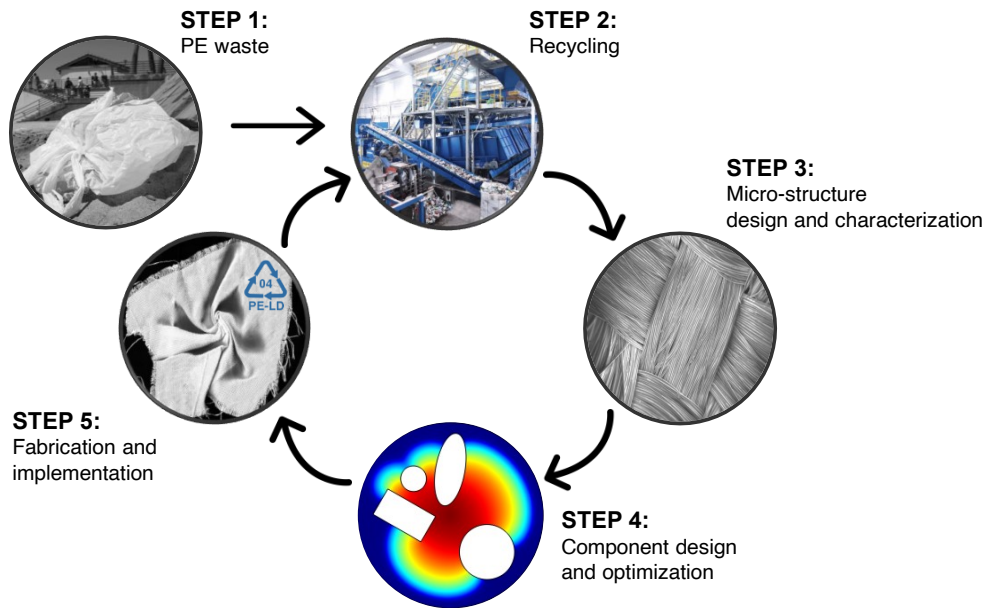


Figure 1.5: **Circular process envisioned for the production of high-performance PE fabric from plastic waste.** Starting by upcycling polyethylene waste, functionalized single-material PE fibers can be created. By model-based optimization of the desired textile properties, the final product can be manufactured by standard industrial equipment and, once it has reached the end of its life cycle, can be easily recycled into a new product.

of single-material polyethylene textiles [65]. Nonetheless, the textile industry has long neglected the large-scale use of PE in clothing, due to the poor breathability and wettability of the fibers, which may result in an uncomfortable final product. However, PE would make it possible to create new, high-performance garments also from recycled material, with great potential for the circular economy and, at the same time, reducing the energy consumption needed for indoor air conditioning during hot seasons. This allows to imagine a completely new process for the production of plastic-based fabrics, exclusively mono-material and entirely recyclable, starting from currently unused waste (see Fig. 1.5).

In this regard, by combining good wearability, thermoregulation capabilities, recyclability and quick-drying, the proposed all-polyethylene textile aims to address the issue of personal thermal management while representing a sustainable alternative to traditional materials.

1.2.2 Sustainable passive cooling

Personal thermal management (PTM) technologies, such as the engineered textiles discussed in section 1.2.1, could be crucial to reduce the energy demand and environmental impact of HVAC systems. However, it is difficult to imagine the total removal of HVAC in favor of single-user cooling or heating strategies: several construction standards require different volumes of air changes per hour (e.g., ASHRAE 170 [66]), whether it is a small commercial unit or a large hospital, in order to ensure healthy environments. In fact, poor ventilation poses health hazards such as intoxication from high amounts of CO₂ or increased transmission rates of infectious diseases [66, 67]. Furthermore, recent studies suggest a rapidly increasing growth of the cooling demand due to climate change [68, 69]. However, recirculating filtered air or supplying fresh air leads to increased energy use. Therefore, in addition to efficient and sustainable PTM strategies, it is also crucial to imagine new and eco-friendly solutions to reduce the energy consumption of conventional HVAC techniques.

Nowadays, vapour compression technologies are utilized for fulfilling most of the cooling demand, despite they can cause seasonal peaks in electricity consumption. In addition, vapour compression technologies typically involve refrigerants with high global warming potential, such as chlorofluorocarbons [70]. In recent years, several air-mediated evaporative cooling technologies have been developed, representing a viable alternative to traditional conditioning systems. As an example, these advanced technologies comprise desiccants to reduce the vapour content of the inlet air, thus increasing its evaporative cooling potential. Such strategies might be based on liquid or dry desiccants, such as lithium chloride solutions or zeolites, which require to be regenerated at low temperatures, respectively in the range of 50-70 °C and 80-100 °C [71]. Despite promising a reduction of peak energy demand of 80%, fluid desiccants force frequent maintenance of the equipment due to their high corrosivity [72], while zeolites have a short life-time due to their inability to entirely desorb all bound vapour molecules upon regeneration [73]. Alternatively, the Maisotsenko-cycle [74] allows to cool the inlet air from ambient conditions to dew point temperature, showing efficiencies from 1.5 to 4 times higher with respect to traditional cooling systems based on vapour compression [75]. However, the cooling potential of evaporative solutions strongly depends on the inlet conditions of ambient air, thus presenting substantial limitations when employed in humid climates.

Low-cost, environmentally friendly and scalable approaches that provide a net cooling capacity without resorting to electricity may be therefore highly beneficial to alleviate the environmental impact of current cooling technologies. In this respect, daytime radiative cooling has shown an impressive development, as evidenced by the several recently published works [51, 76–81]. Radiative cooling can

be considered as a passive cooling approach able to self-operate, since all the involved processes occur without mechanical moving parts or auxiliaries. The general concept of radiative cooling is a rather old one [82, 83] and, in fact, modest cooling effects (i.e. in the order of 50 W m^{-2}) can be achieved by directional approaches (namely, a solar-tracking reflecting surface) relying on commonly available materials [84]. Only the recent advances in material science have allowed substantial cooling capacity from daytime radiative cooling. Since the pioneering work of Fan and collaborators in 2014 [77], many attempts have been made and impressive daytime radiative cooling performances were reported in the literature, including highly scalable optical metamaterials with noontime radiative cooling power exceeding 90 W m^{-2} at vanishing temperature difference [78, 79]. Besides the intrinsic thermodynamic limitations of such systems (approximately 160 W m^{-2} [80]), passive radiative cooling of buildings can only be regarded as a partial success from the engineering perspective. In fact, the typical high humidity of tropical regions – where cooling is mostly requested – significantly hinders the possibility of radiating infrared radiation into the outer space through the infrared atmospheric window, namely by exploiting the transparency of the atmosphere between $8\text{-}13 \mu\text{m}$ wavelengths. Therefore, alternative passive cooling techniques possibly effective also in the presence of high humidity or dusty conditions are highly desirable.

In this context, the novel cooling device proposed in this thesis allows to achieve cooling capacities above the thermodynamic limit of radiative cooling and its performance is not affected by the ambient humidity or the concentration of particulate in the air. Moreover, its modular design and the possibility to operate with salt solutions at different concentrations allows to adjust the specific cooling capacity achievable, the maximum obtainable temperature difference (with respect to the surrounding environment) and its consumption.

1.2.3 Capillary materials for energy-conversion devices

As discussed earlier in this chapter, energy-consuming applications might be addressed by relying on passive devices. In this field, capillarity plays a crucial role as it allows to move working fluids without the need of mechanical moving parts (e.g., pumps) to overcome viscous losses or small hydraulic heads. In fact, both applications discussed in sections 1.2.1 and 1.2.2 rely on capillarity: capillary smart textiles allow to efficiently wick and spread the sweat away from the skin, which is essential to grant comfort and wearability, and to allow faster drying rates; the briefly introduced passive cooler relies on capillarity to feed a component with the freshwater needed for its functioning. Therefore, capillary materials are crucial in passive applications to reduce the need of external energy sources, offering a simple and frugal approach to fluid transport, and simplifying the whole assembly of the device. Obviously, the amount of fluid transportable through capillary flow is small compared to traditional active systems, so, in a broad engineering sense,

their use might seem limited. However, several new technologies proposed in the literature aiming to address the water-energy nexus consistently rely on capillarity alone to function, demonstrating the importance of investigating diverse and novel application possibilities.

Natural porous media can be characterized by stochastic (e.g. soil, sponges) or ordered (e.g. wood, lungs) structures. Their man-made counterparts are numerous and widely adopted in most industries, for instance filters, textiles (woven and nonwoven), absorbents, ceramics or tissue scaffolds [85]. Engineering the capillary properties of porous materials has been pursued to achieve improved thermal [86], mechanical [87], electrical [88], optical [89] and biomedical [90] performance. In addition to intrinsically porous materials (e.g. MOF [91]), the recent research has focused on manufacturing processes that can control finely either material addition (e.g. 3D printing [92, 93]) or removal (e.g. laser etching [89, 94]) from bulk materials to design a precise pores architecture. Applications have been proposed for steam generation [95], desalination [96, 97], salt precipitation [98], water sanitation [99], solar thermal energy harvesting [89], and cooling [54], among others. Clearly, optimizing the capillary properties of the porous materials is crucial to enhance their overall performance: poor capillarity may lead to dry-out during continuous evaporative processes, and would significantly limit the maximum achievable device size [17]. Thus, sub-optimal capillary properties would significantly hinder the productivity and scalability of the system overall.

The aforementioned applications typically rely on non-structured capillary materials, such as paper or commercial textiles, which, however, offer limited degrees of optimisation given their non-ordered structure. Some pioneering works have proved the potential of structured capillary structures in several areas of heat and mass transfer [100] and microfluidics [101]. Importantly, on one hand the capillary nature of traditional materials is critical for endowing energy-conversion devices with their intrinsic passive nature; on the other hand, the very low thermal conductivity of those materials introduces unavoidable thermal resistances that may detrimentally affect the overall device performance. The availability of metal-based capillary materials with controllable structure may offer new opportunities to effectively attack the above issue, while allowing to design engineered (and stable) pores architectures with microscopic precision and scalability.

In this regard, the proposed laser-etched, silica-coated aluminum substrate offers a promising starting point for developing durable and optimized capillary substrates with the goal of increasing the performance and scalability of passive devices, especially multistage layouts.

Chapter 2

Mass transfer in micro-porous media: theoretical framework¹

Wetting phenomena and capillary flow in porous media are omnipresent in several natural and technological applications at the intersection of chemistry, physics, and engineering. Their application ranges from industrial-scale processes (e.g., oil recovery [103] and enhanced heat transfer [104]) to water treatment [105, 106], from micro-fluidics [107–109] to life-sciences and advanced materials [110–113]. Thus, optimizing water transport in micro-porous media would pave the way for new classes of passive and energy-efficient materials capable of redefining the standard of a wide range of applications.

Capillary flow is governed by the interplay of the physicochemical properties of the three phases present in the system: the solid porous matrix; a first fluid, generally gaseous (i.e. air); a second fluid, generally a liquid (i.e. water). The balance of forces at the three-phases contact line produce a curvature of the fluid-fluid interface, which generates a pressure difference ΔP across the interface itself according to the Laplace's equation [114]:

$$\Delta P = \gamma_{lv} \left(\frac{1}{R_1} + \frac{1}{R_2} \right), \quad (2.1)$$

where γ_{lv} is the fluid-fluid surface tension, R_1 and R_2 are the main radii of curvature of the fluid-fluid interface. The shape of the interface, thus its curvature, determines which fluid wets the porous matrix, filling its pores. For the sake of simplicity, as the two fluids considered in this chapter are air and water, the subscript lv was dropped and the water-air surface tension was simply referred to as γ . The surface chemistry and micro-structure of a porous matrix are crucial in determining its wetting behavior. Therefore, modelling its capillary pressure requires a precise

¹Part of the work included in this chapter was also previously published by Alberghini et al. in Refs. [54, 87, 102].

knowledge of the shape of the liquid-air interface and chemical composition of the three phases considered. However, despite the simplicity of Eq. 2.1, the prediction of fluid transport in non-ordered or complex ordered structures often demand to resort to numerical simulations [93, 115, 116]. Under particular assumptions, complex systems can be reduced to simpler geometries, and the capillary pressure can be estimated via analytical relations by formulating the free energy balance of the system. This approach allows for a reasonable adherence to the system under investigation while allowing for a deep understanding of the effect of the geometric parameters on capillarity and, at the same time, its optimization.

A simple and straightforward way to determine the wetting behaviour of a surface with respect to a specific fluid requires to evaluate their equilibrium contact angle by the sessile droplet method. The procedure consists of a simple imaging technique requiring to place a fluid droplet on the surface of interest and directly measure the contact angle. As described above, wetting is determined by the interaction of three phases, thus a specific combination of solid substrate, wetting and surrounding fluids, and test conditions (namely, temperature and ambient humidity) determine a univocal equilibrium condition. However, non-homogeneous surface roughness or chemistry (e.g., obtained by coating or plasma treatment), curvatures, or steep variations in the droplet profile could lead to large uncertainties in the evaluation of the average contact angle. Section 2.1 introduces the theoretical framework needed to evaluate the contact angle on cylindrical and planar surfaces. The method described allows to evaluate the contact angle by measuring the size of a droplet (namely, its height and length), thus avoiding the use of a digital goniometer.

Then, section 2.2 introduces the theoretical framework required to estimate the capillary forces in a multi-filament yarn. Yarns are complex systems where the fibers shape, arrangement and surface chemistry determine their passive transport properties. Textiles are usually woven or knitted into complex patterns; as the fibers get disordered, bent and twisted, assessing the exact shape of the water meniscus as it proceeds by capillary rise is extremely difficult. However, by simplifying the the problem geometry, assimilating the yarn structure to an array of cylindrical fibers arranged in a regular lattice, it is possible to estimate and optimize the capillary transport in textiles.

Similarly, section 2.3 investigates capillary transport in laser-etched open channels by reducing their complex and irregular geometry to ideal V-shaped grooves. The work was framed in the context of structured capillary materials for energy-conversion devices and aims to design a novel class of passive components with engineered micro-structure and surface chemistry to overcome the limits of non-structured materials. The engraving process allowed to promote wicking on an otherwise flat surface: the resulting substrate combines the mechanical, thermal and chemical properties of rigid materials (e.g., metals or polymers) with the capillary properties obtained by the etching process. The model-based design and

optimization of these components aimed to enhance the performance and scalability of passive devices.

The modeling results obtained for multi-filament yarns and V-shaped grooves were used in section 2.4 to derive a time-dependent analytical model for the wicking transient, relating the capillary performance to the micro-structure and hydrophilicity of the material. The classic Lucas-Wahsburn approach [117], commonly used for this purpose, has limited use as it does not include the effect of gravity. However, modelling gravitational effects might be crucial when designing the maximum useful size of large capillary components or optimizing their performance. Therefore, a time-explicit equation for capillary rise was derived for both the systems under consideration, starting from their geometrical description. Then, the proposed model was compared with a one-dimensional formulation derived from Darcy's law, which describes motion in porous media via a volume-averaging approach. The analytical equations obtained were used to obtain the capillary parameters for the systems under consideration, allowing to compare the performance of the two systems under consideration with that of other non-structured porous media. Most applications concerning capillary media in passive devices require to evaporate the wicked liquid as it flows through the porous matrix. Therefore, the classic approach based on Darcy's law was extended, implemented and validated against previous analytical solutions. The model ascribed to the specific evaporation rate \dot{m}_e , which was considered constant over the sample surface, an extra pressure drop to the water flowing in the grooves. The explicit time discretization scheme used is particularly suited to investigate configurations at the limit of dry-out, making it adequate to explore the limits of passive components for water transport.

The dynamic wicking model introduced in section 2.4, despite being effective and sufficient in several case-studies, only allows to investigate 1-dimensional (1-D) processes. As several recent studies proposed 2-D and 3-D passive components exploiting capillary suction [26, 27, 29, 96, 118], the modelling framework was shifted to a differential description based on mass conservation, enabling a finite element implementation of imbibition, which is more suitable to investigate the capillary transport in complex geometries. In section 2.5, the classical Darcy law was extended via the Maulem-van Genuchten approach, which relates the capillary pressure to the water content in the porous structure, namely its saturation. Unlike the method proposed in the previous sections, this approach does not require a detailed geometric representation of the micro-structure of the porous matrix, which is instead described by means of volume-averaged parameters. The proposed formulation favors a numerical rather than analytical description of the imbibition process, which allows the analysis to be extended from 1-D to 3-D systems.

Finally, section 2.6 discusses a different aspect of mass transfer in a micro-porous system: vapor transport across a hydrophobic membrane. In the context of water desalination, the working principle requires salt water and fresh water to flow on either side of the membrane; the physicochemical and geometrical features of the

membrane, namely its hydrophobicity and pores size, avoid contamination between the two fluid flows. The temperature and activity gradients between the two feeds generates a net flow of water vapor across the membrane, thus allowing separation of the solvent from the dissolved non-volatile components. Although based on different physical phenomena, this application is closely related to capillary transport since several passive devices (e.g., devices for solar desalination [17, 54, 96, 119–121]) rely on both to operate.

2.1 Analytical evaluation of the contact angle

2.1.1 Shape parameters of a sessile droplet on cylindrical fibers

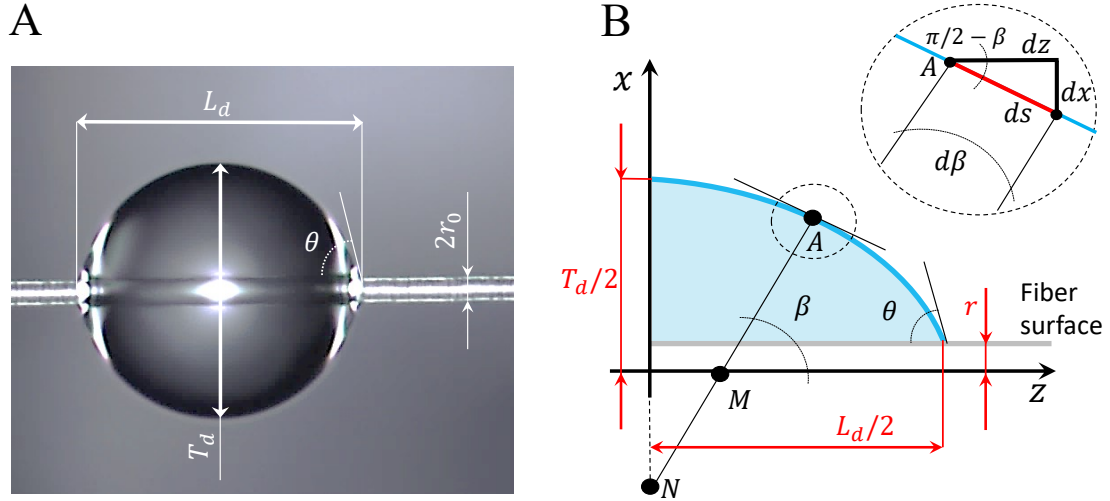


Figure 2.1: **Equilibrium contact angle of a drop on a fiber.** (A) The fiber radius, the droplet thickness and length were evaluated from microscope images to compute the water-fiber contact angle from Eqs. 2.7 to 2.9. (B) Schematics of a droplet on a fiber. If the droplet is sufficiently small to neglect the effect of gravity, its two planes of symmetry can be used to simplify the derivation of the differential equation describing its profile.

Neglecting the effect of gravity, the equilibrium condition of a droplet on the surface of a fiber requires a constant Laplace's over-pressure ΔP over its entire extension [114, 122]. Thus, for this purpose, Laplace's equation (see Eq. 2.1) was re-arranged as:

$$\frac{\Delta P}{\gamma} = c_1 = \frac{1}{R_1} + \frac{1}{R_2}, \quad (2.2)$$

where γ is the water-air surface tension, R_1 and R_2 are the principal radii of curvature of the droplet surface at a given position, and c_1 is a generic constant. The assumption a symmetric droplet with respect to the fiber, as the one displayed in Fig. 2.1A, allows to simplify the mathematical formulation of the problem. Referring to Fig. 2.1B, the two principal radii of curvature are identified by the segments AN, in the plane of the figure, and AM, in the plane containing the segment and perpendicular to the figure. Thus:

$$\begin{aligned} AN = R_1 &= \frac{x}{\sin \beta}, \\ AM = R_2 &= \frac{ds}{d\beta}. \end{aligned} \quad (2.3)$$

See Fig. 2.1B for definitions of parameters x , β , and s . Substituting Eq. 2.3 in 2.2, the latter was rewritten as:

$$c_1 = \frac{\sin(\beta)}{x} + \cos(\beta) \frac{d\beta}{dx} = \frac{1}{x} \frac{d}{dx} (x \sin(\beta)). \quad (2.4)$$

Eq. 2.4 was integrated as:

$$\frac{c_1 x^2}{2} + c_2 = x \sin(\beta), \quad (2.5)$$

where the constants c_1 and c_2 were computed considering the boundary conditions:

$$\begin{aligned} x|_{z=0} &= T_d/2, \\ \beta|_{z=0} &= \pi/2, \\ x|_{z=L_d/2} &= r, \\ \beta|_{z=L_d/2} &= \pi/2 - \theta, \end{aligned} \quad (2.6)$$

obtaining the final form:

$$\sin(\beta) = \left(\frac{r \cos(\theta) - T_1}{r^2 - T_1^2} \right) x + \frac{1}{x} T_1 r \left(\frac{r - T_1 \cos(\theta)}{r^2 - T_1^2} \right), \quad (2.7)$$

where $T_1 = T_d/2$. See Fig. 2.1A for the definitions of parameters T_d , L_d , and r . Referring to Fig. 2.1B, the derivative of the droplet profile can be expressed as:

$$\frac{dx}{dz} = -\frac{1}{\tan(\beta)} = -\frac{\sqrt{1 - \sin^2(\beta)}}{\sin(\beta)}. \quad (2.8)$$

Eq. 2.7 was used to express $\sin(\beta)$; Eq. 2.8 is the differential equation describing the droplet profile. Thus, the length of the droplet was computed as:

$$L_d = 2 \int_0^{L_d/2} dz = 2 \int_r^{T_d/2} \frac{\sin(\beta)}{\sqrt{1 - \sin^2(\beta)}} dx. \quad (2.9)$$

Eqs. 2.7 to 2.9 were used in an iterative procedure to compute the contact angle of a symmetric water drop on a fiber given its shape parameters, namely the fiber radius r , the droplet thickness T_d and length L_d (see section 3.1.2). The external surface of the water droplet was computed as:

$$A_d = 2\pi \int_{-\frac{L_d}{2}}^{\frac{L_d}{2}} \frac{x}{\sin(\beta)} dz = 4\pi \int_{\frac{T_d}{2}}^r -\frac{x}{\cos(\beta)} dx, \quad (2.10)$$

which was numerically integrated recalling that $\cos \beta = (1 + \tan^2(\beta))^{-0.5}$ and considering Eqs. 2.7 and 2.8 to express $\tan(\beta)$ as a function of the droplet profile x . Similarly, the volume of the droplet was computed as:

$$V_d = \pi \int_{-L_d/2}^{L_d/2} x^2 dz - V_{df} = 2\pi \int_{\frac{T_d}{2}}^r -x^2 \tan^2 \beta dx - V_{df}, \quad (2.11)$$

where $V_{df} = \pi r^2 L$ is the volume of the fiber surrounded by the droplet.

2.1.2 Shape parameters of a sessile droplet on a flat surface

Also in this case, the contact angle can be evaluated by measuring the height T_d and half-width L_d of the droplets (see Fig. 2.2), under the assumption of negligible effect of gravity, namely $L_d \ll \sqrt{\gamma/(\rho g)}$ [114].

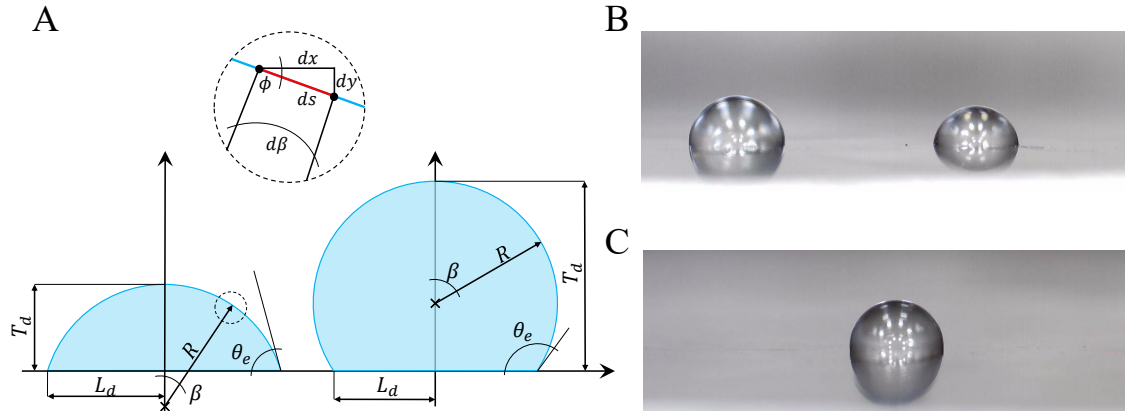


Figure 2.2: **Experimental evaluation of the contact angle on flat surfaces.** (A) Schematics of two water droplets under the assumption of negligible effect of gravity on a hydrophilic (left) and hydrophobic (right) surfaces. (B-C) Millimetre-sized water droplets on a flat aluminum plate. As it can be observed, the assumption of approximately spherical shape holds both for contact angles lower (B) and greater (C) than $\pi/2$.

Considering the surface of a spherical droplet and referring to the nomenclature reported in Fig. 2.2A, it holds:

$$ds = \frac{dx}{\cos(\beta)} = R d\beta, \quad (2.12)$$

where R is the radius of the spherical droplet. Thus, L_d was evaluated by integrating Eq. 2.12:

$$L_d = \int_0^{L_d} dx = \int_0^\theta R \cos(\beta) d\beta = R \sin(\theta), \quad (2.13)$$

where θ is the contact angle. The radius of the droplet was evaluated relying on simple geometrical arguments:

$$R = \frac{L_d^2 + T_d^2}{2T_d}. \quad (2.14)$$

Substituting Eq. 2.14 in Eq. 2.13, θ was evaluated as:

$$\theta = \begin{cases} \arcsin(2L_d T_d / (L_d^2 + T_d^2)) & \text{if } R > T_d \\ \pi - \arcsin(2L_d T_d / (L_d^2 + T_d^2)) & \text{if } R < T_d, \end{cases} \quad (2.15)$$

where the cases $R > T_d$ and $R < T_d$ refer to hydrophilic (see Fig. 2.2B) and hydrophobic (see Fig. 2.2C) interactions, respectively.

2.2 Capillary pressure in an ideal yarn

To understand, predict, and engineer the mechanisms of the moisture transport through yarns and textiles, a model of the liquid transport through capillaries in a multi-filament yarn was developed. The internal structure of the yarn was approximated as an infinite assembly of identical parallel fibers with circular cross sections, tightly packed into a periodic structure with identical distances between neighboring filaments. The yarn was assumed as composed of non-ideally wetting fibers (i.e., with contact angles ranging from zero to 90 degrees) arranged in either a hexagonal (Fig. 2.3A) or a square (Fig. 2.3B) periodic lattice. The along-the-yarn wicking process was considered dominant, as the ratio between the thickness of the fabric (perpendicular to fiber axis) and the length of the yarn (parallel to fiber axis) is on the order of 10^{-2} . The input parameters of the model are the fiber radius r , the yarn porosity ϕ and the water-fiber contact angle θ .

The porosity of the periodic hexagonal-lattice and the square-lattice yarns, namely the ratio between the void and the total area within a representative volume element, are related to the fiber radius and the inter-fiber separation by geometrical

considerations as:

$$\begin{aligned}\phi_H &= 1 - \frac{\pi}{2\sqrt{3}\left(1 + \frac{d}{r}\right)^2}, \\ \phi_S &= 1 - \frac{\pi}{4\left(1 + \frac{d}{r}\right)^2}.\end{aligned}\tag{2.16}$$

Here, r is the fiber radius, $2d$ is the surface-to-surface distance between adjacent fibers (see Fig. 2.4B), and the subscripts H and S refer to the hexagonal and square lattices, respectively. Eq. 2.16 was used to evaluate the minimum porosity of both types of the fiber arrangements, which corresponds to the situation when the adjacent fibers are in direct contact, namely $d = 0$, leading to $\phi_{H,min} = 9.3\%$ and $\phi_{S,min} = 21.5\%$. In this work, the capillary pressure in a multi-filament system

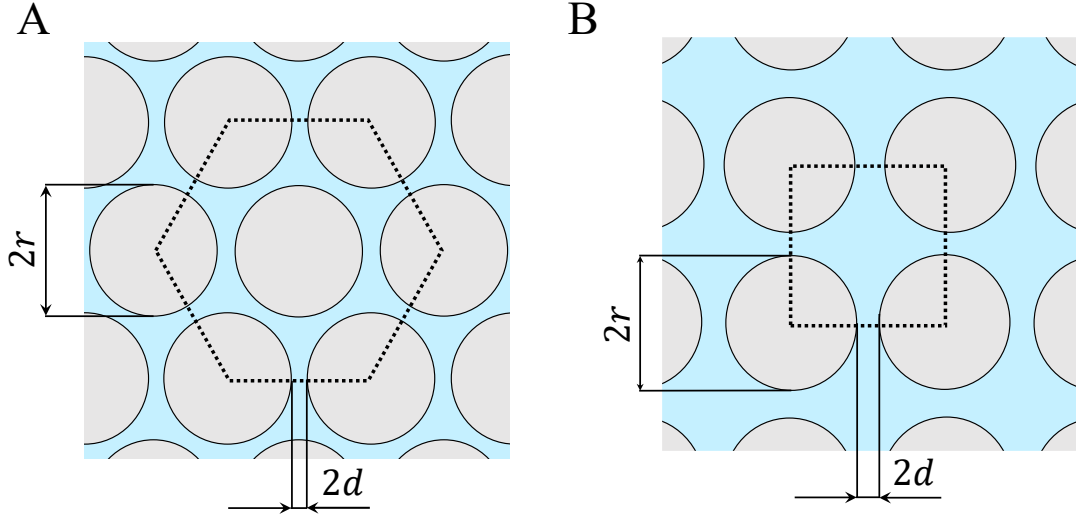


Figure 2.3: **Schematics of possible fibers arrangements in an ideal yarn.** (A-B) Schematics of the elementary computational cells of a cross-section of an ideal yarn with a periodic hexagonal (A) or square (B) fiber arrangement. The grey circles represent the fibers composing the yarn. The water transport was modeled in the direction parallel to the fibers axes.

was evaluated as a function of the maximum capillary rise H_m , which was computed according to the model proposed by Princen [123, 124]. Thus, $P_c = \rho g H_m$, where ρ is the density of the wicked fluid and g is the gravitational acceleration. H_m is a function of the yarn porosity, the fiber radius and the water-fiber contact angle, and the correct theoretical tools needed for its evaluation depend on the yarn porosity. At $\phi = \phi_{min}$, the contact between adjacent fibers leads to an asymptotically infinite capillary rise. For $\phi > \phi_{min}$, two types of menisci form in the system: a higher water column between each pair of adjacent fibers, and a lower one in the channel

formed by each triplet or quadruplet of fibers in the unit cell of a periodic lattice (see Fig. 2.4A-B). The equations required to compute the height of the two menisci are described in section 2.2.1. With the increase of the yarn porosity, the higher water column is reduced more than the lower one, until they join at the critical value of porosity ϕ_{cr} (see section 2.2.2). Finally, ϕ_m is the maximum value of the porosity for which the capillary rise still takes place, which depends on the fiber-water contact angle θ , the number of fibers in the yarn, and their arrangement. The method used to evaluate ϕ_m was reported in section 2.2.3.

2.2.1 Capillarity in a multi-fiber infinite and dense yarn

Considering the case of a dense yarn, where the term ‘dense’ defines a porosity in the range $\phi_{min} < \phi < \phi_{cr}$, the water-fiber interaction leads to the formation of two types of menisci, as sketched in Fig. 2.4A-B. The higher one forms between each pair of adjacent fibers (light blue dashed area), the lower one forms in the channel created by each triplet of fibers (dark blue dashed area). The heights of the two menisci, respectively $H_{m,1}$ and $H_{m,2}$, can be computed considering the corresponding force balance between the vertical component of the surface tension and the weight of the water column subtended to each meniscus:

$$F_i = H_{m,i} \rho g A_i, \quad (2.17)$$

where A_i is the cross-section of the water column sustained by the capillary force F_i . In the current section, the subscripts “1” and “2” were used to refer the height-dependent parameters to $H_{m,1}$ and $H_{m,2}$, respectively.

The cross section of the water column subtended each higher meniscus (the light blue shaded areas of Fig. 2.4B) can be computed as:

$$A_1 = 2r^2 \left[\frac{2R_1}{r} \sin(\alpha_1) \cos(\theta + \alpha_1) - \alpha_1 + \sin(\alpha_1) \cos(\alpha_1) - \left(\frac{R_1}{r} \right)^2 \left(\frac{\pi}{2} - \theta - \alpha_1 - \sin(\theta + \alpha_1) \cos(\theta + \alpha_1) \right) \right], \quad (2.18)$$

where R is the external radius of curvature of the water column, r is the fiber radius, and α is the angle between the line connecting the centers of two adjacent fibers C-C and the radius connecting the center of a fiber to the triple-contact line of the water meniscus. The curvature radius R can be geometrically computed as:

$$\frac{R_i}{r} = \frac{1 + \frac{d}{r} - \cos(\alpha_i)}{\cos(\theta + \alpha_i)}. \quad (2.19)$$

The capillary force consists of two contributions: a component directed upwards due to the water-fiber interaction $F_{1,up}$, and a component directed downwards due to

the water-air interaction $F_{1,dw}$. The two components can be respectively expressed as:

$$\begin{aligned} F_{1,up} &= 4\gamma r \alpha_1 \cos(\theta), \\ F_{1,dw} &= -4\gamma \left(\frac{\pi}{2} - \theta - \alpha_1 \right) R_1. \end{aligned} \quad (2.20)$$

Substituting Eq. 2.20 on the left-hand side of Eq. 2.17, and Eqs. 2.18–2.19 on the right-hand side of Eq. 2.17, a quadratic equation was obtained, which was iteratively solved for a given fiber separation d to obtain the corresponding maximum height of the higher meniscus from the equilibrium between the Laplace's and the hydrostatic pressure:

$$H_m = \frac{\gamma}{\rho g R}. \quad (2.21)$$

The height of the lower meniscus can be calculated similarly to the previous case, by balancing the water-fiber capillary force, only directed upwards, and the weight of the water column subtended to the meniscus (dark blue shaded area in Fig. 2.4B). The cross-section of the water column at the height $H_{m,2}$ can be computed as [123]:

$$\begin{aligned} A_2 &= 3r^2 \left\{ \left(\frac{R_2}{r} \right)^2 \left[\frac{\cos^2(\theta + \alpha_2)}{\sqrt{3}} + \frac{\pi}{2} - \theta - \alpha_2 - \sin(\theta + \alpha_2) \cos(\theta + \alpha_2) \right] \right. \\ &\quad + \frac{R_2}{r} \left[\frac{2\cos(\theta + \alpha_2) \cos(\alpha_2)}{\sqrt{3}} - 2\sin(\alpha_2) \cos(\theta + \alpha_2) \right] \\ &\quad \left. + \frac{\cos^2(\alpha_2)}{\sqrt{3}} + \alpha_2 - \frac{\pi}{6} - \sin(\alpha_2) \cos(\alpha_2) \right\}, \end{aligned} \quad (2.22)$$

while the upward capillary force can be computed as:

$$F_{1,up} = 3\gamma r \left[2 \left(\frac{\pi}{2} - \alpha_2 - \theta \right) \frac{R_2}{r} + \left(\frac{\pi}{3} - 2\alpha_3 \right) \cos \theta \right]. \quad (2.23)$$

Eqs. 2.22–2.23 were substituted in Eq. 2.17 to obtain another quadratic form, which was iteratively solved for a given value of d to evaluate the corresponding maximum height $H_{m,2}$ from Eq. 2.21. The maximum heights of the two menisci for different values of the relative fibers distance $2dr^{-1}$ are plotted in Fig. 2.4C for a bundle of fibers with $r = 50 \mu\text{m}$ and $\theta = 50^\circ$, arranged in a hexagonal structure.

2.2.2 Capillarity in a multi-fiber infinite and sparse yarn

Considering the case of a sparse yarn, where the term ‘sparse’ defines a porosity in the range $\phi_{cr} \leq \phi < \phi_m$, the maximum capillary height H_m was evaluated by considering the yarn as composed by an infinite number of fibers [124] (see Fig.

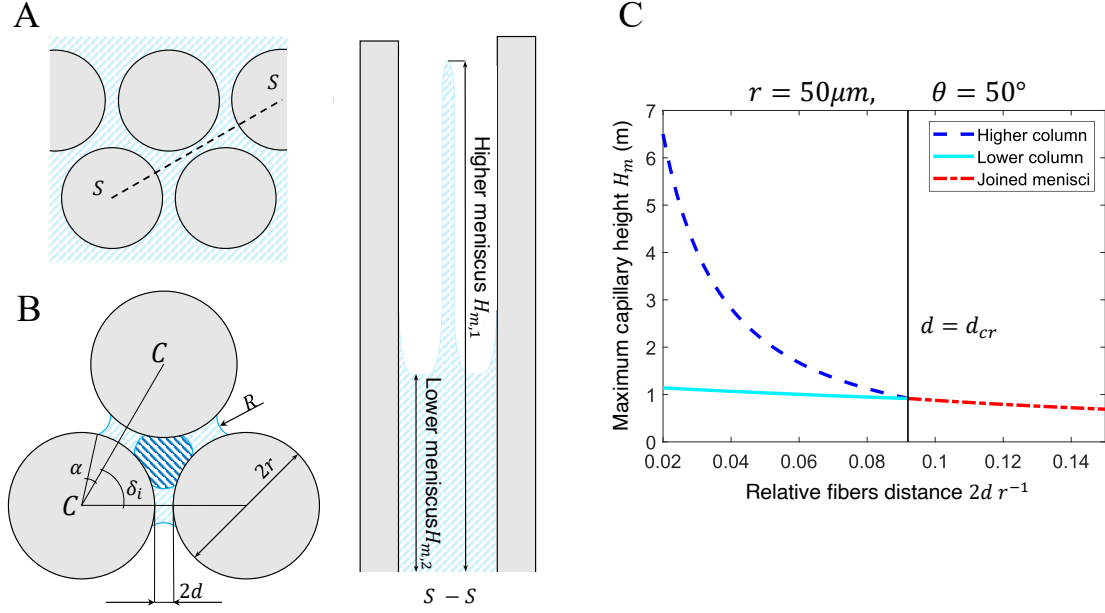


Figure 2.4: **Theoretical modelling of the capillary suction in a periodic infinite array of parallel fibers with a hexagonal symmetry.** (A) Sketch representing the two menisci formed in the system when the yarn porosity is $\phi < \phi_{cr}$. (B) Schematics of the water columns formed in a three-fiber system. The higher meniscus forms between each pair of adjacent fibers (light-blue shaded area), while the lower meniscus forms in the channel created by each triplet of fibers (dark-blue shaded area). (C) Dependence of the maximum height of the water columns on the relative fibers separation $2d r^{-1}$. The height of the higher meniscus decreases faster than the other one, until they merge at $d = d_{cr}$. The depicted results were obtained for $r = 50 \mu\text{m}$ and $\theta = 50^\circ$.

2.3). When this assumption holds, the water menisci at the boundary between each computational cell and its neighbors were considered flat in the plane perpendicular to the fiber axis, and the downward force acting on the water column at the boundary of the yarn can be neglected. Thus, at the equilibrium, H_m was computed considering the force balance between the vertical component of the surface tension at the water-fiber interface and the weight of the water column [123, 124]. The force balance was expressed as:

$$F_c = H_m \rho g A, \quad (2.24)$$

where A is the lattice-dependent cross-section of the liquid column, ρ is the water density, g is the gravitational acceleration, and F_c is the capillary force, expressed as:

$$F_c = \gamma p \cos \theta. \quad (2.25)$$

Here, p is the wetted perimeter, and θ is the liquid-fiber contact angle. Considering the hexagonal and square fiber arrangements, it holds:

$$\begin{aligned} p_H &= 6\pi r, \\ p_S &= 2\pi r, \\ A_H &= r^2 \left(6\sqrt{3} (1 + d/r)^2 - 3\pi \right), \\ A_S &= r^2 \left(4 (1 + d/r)^2 - \pi \right). \end{aligned} \tag{2.26}$$

Thus, the above equations was re-arranged to obtain the maximum capillary height for both lattice symmetries:

$$H_m = \frac{2 \cos(\theta) (1 - \phi)}{r l_c^2 \phi}, \tag{2.27}$$

where $l_c^2 = \rho g / \gamma$. As it can be seen, H_m only depends on the fiber radius r , contact angle θ and yarn porosity ϕ , justifying their choice as the design parameters. Clearly, lower values of fiber radius, fabric porosity and contact angle (i.e., more hydrophilic fibers), lead to higher capillary pressure. However, the interplay of these parameters in determining the optimal wicking performance of a fabric is made complex by their influence on the fabric permeability (see section 2.4.4), i.e. the inverse of the resistance that the porous matrix opposes to the fluid flow. In fact, by maximizing geometrically the capillary pressure (very small and highly packed fibers), the permeability is minimized (high viscous resistance), thus hindering capillary spreading. The relationship between these parameters is discussed in more detail in section 3.2.2.

2.2.3 Maximum porosity of a finite-size ideal yarn

The maximum porosity ϕ_m , namely the maximum porosity for which the capillary rise still takes place, was computed from the force balance between the upward capillary force acting on the perimeter of the wet fibers, and the downward component of the air-water surface tension acting on the water column at the outer boundary of the yarn. The vertical liquid column presents a single, height-dependent curvature radius R , which determines the maximum capillary height from Eq. 2.21.

Defining α as the angle between the line connecting the centers of two adjacent fibers and the radius connecting the center of a fiber to the triple-contact line of the water meniscus (see Fig. 2.4B), when $\alpha + \theta = \pi/2$, the curvature radius $R \rightarrow \infty$ and no capillary rise can take place. Therefore, the force does not depend on the weight of the water meniscus, and the following condition holds:

$$p_{sl} \gamma \cos \theta - p_{lv} \gamma = 0, \tag{2.28}$$

where p_{sl} is the wet perimeter of the fibers and p_{lv} is the perimeter of the air-water contact line in the plane perpendicular to the fiber axes. At the limit of null capillary suction $\alpha + \theta = \pi/2$ and $R \rightarrow \infty$, Eq. 2.28 was rewritten as:

$$\begin{aligned} & \left(\sum_{i=1}^{n_{fB}} R \left(\delta_i + 2 \left(\frac{\pi}{2} - \theta \right) \right) + 2\pi R n_{fD} \right) \cos \theta \\ & - n_{fB} 2R \left(1 - \sin \theta + \left(\frac{d}{R} \right)_m \right) = 0 \end{aligned} \quad (2.29)$$

where n_{fB} is the number of fibers on the boundary of the yarn, n_{fD} is the number of fibers completely surrounded by water, and δ_i the angle between the lines connecting the center of the i -th fiber at the yarn boundary with the center of its neighboring boundary fibers (see Fig. 2.4A,B). For the hexagonal arrangement, four values of δ_i are possible: $\pi/3$, $2\pi/3$, π and $4\pi/3$; while for the square arrangement the possible configurations of δ_i are: $\pi/2$, π and $3\pi/2$.

Under the assumption of $n_f \rightarrow \infty$, the ratio $n_{fD}/n_{fB} \rightarrow 0$, and Eqs. 2.16 and 2.29 lead to $\phi_m \rightarrow 1$, meaning that even infinitely distant fibers produce a relevant capillary suction, which is clearly non-physical. To overcome this limit and provide a more reliable estimation of the maximum fibers distance allowed to promote capillary suction, a growth model of an ideal yarn was developed, which automatically computes n_{fD} , n_{fB} and δ_i for a given n_f and fiber arrangement. The resulting ideal, finite-size yarn was supposed to be composed of concentric layers of fibers, starting from a central core unit, and added one by one to maintain at best the circular shape of its border. A MATLAB routine was implemented to perform the computation for $n_{tot} = n_{fB} + n_{fD} > 13$ and $n_{tot} > 4$ for the hexagonal and square arrangement, respectively.

2.3 Capillary pressure in V-shaped open grooves

Capillarity in V-shaped grooves is determined by the shape of the water meniscus formed within the groove, which is a function of the groove geometry and the contact angle. Generally, due to the influence of gravity and the complex shape of the contact line, the radii of curvature of the meniscus are not constant and must be described by second order differential equations. This makes the evaluation of the Laplace's over-pressure, and therefore of the capillary properties of the groove, rather complex. Gravity might be neglected in straight and small grooves and the water-air interface can be described by a single and constant radius of curvature, while the meniscus can be considered as a cylinder-shaped [125]. The range of validity of these assumptions are investigated in section 2.3.1 considering a tilted hydrophilic plate immersed in water. Then, the obtained results were used in 2.3.2 to derive an analytical expression of the capillary force in sub-millimeter

V-grooves based on their geometrical parameters and surface chemistry (via the contact angle).

2.3.1 Neglecting gravity – maximum grooves width

Due to capillarity, the flat water surface bends to form a meniscus which, at the equilibrium, rises up to y_m and extends to x_m , before merging with the unperturbed horizontal surface (see Fig. 2.5A). The shape of the meniscus in the V-shaped grooves is not affected by gravity if the width of the groove w is small compared to $2x_m$ [126]. Given the tilt angle α and the equilibrium water-plate contact angle θ , Eq. 2.1 was integrated to evaluate x_m .

For a flat plate, the radii of curvature are expressed in Cartesian coordinates as:

$$\begin{aligned} R_1 &= -\frac{(1 + \dot{y}^2)^{3/2}}{\ddot{y}}, \\ R_2 &\rightarrow \infty, \end{aligned} \quad (2.30)$$

where $y = y(x)$ is the vertical coordinate and the negative sign is due to the concavity of the water meniscus. Considering vertical capillary rise, Laplace's under-pressure is continuously balanced by gravity, therefore Eqs. 2.1 and 2.30 were combined as:

$$\gamma \ddot{y} (1 + \dot{y}^2)^{-3/2} = \rho g y, \quad (2.31)$$

where ρ is the water density and g is the gravitational acceleration. The former equation was simplified considering:

$$\frac{d}{dx} \left((1 + \dot{y}^2)^{-1/2} \right) = -\dot{y} (1 + \dot{y}^2)^{-3/2} \ddot{y} = -\frac{1}{l_c^2} y \dot{y}, \quad (2.32)$$

where $l_c = \sqrt{\gamma/(\rho g)}$ is the capillary length [114]. Eq. 2.32 was easily integrated by parts, yielding:

$$(1 + \dot{y}^2)^{-1/2} = \sin(\beta) = -\frac{1}{2l_c^2} y^2 + c_1, \quad (2.33)$$

where β is the slope of s with respect to the vertical reference. The first equality in Eq. 2.33 holds on simple geometrical arguments (see the inset in Fig. 2.5A). Considering $\dot{y} = y|_{x \rightarrow \infty} = 0$ as boundary condition, the integration constant was evaluated as $c_1 = 1$. Referring to the symbols of Fig. 2.5A, Eq. 2.33 was used to derive the the maximum height reached by the meniscus y_m :

$$\begin{aligned} \beta|_{y_m} &= \pi/2 - \alpha + \theta, \\ y_m &= l_c \sqrt{2(1 - \cos(\alpha - \theta))}. \end{aligned} \quad (2.34)$$

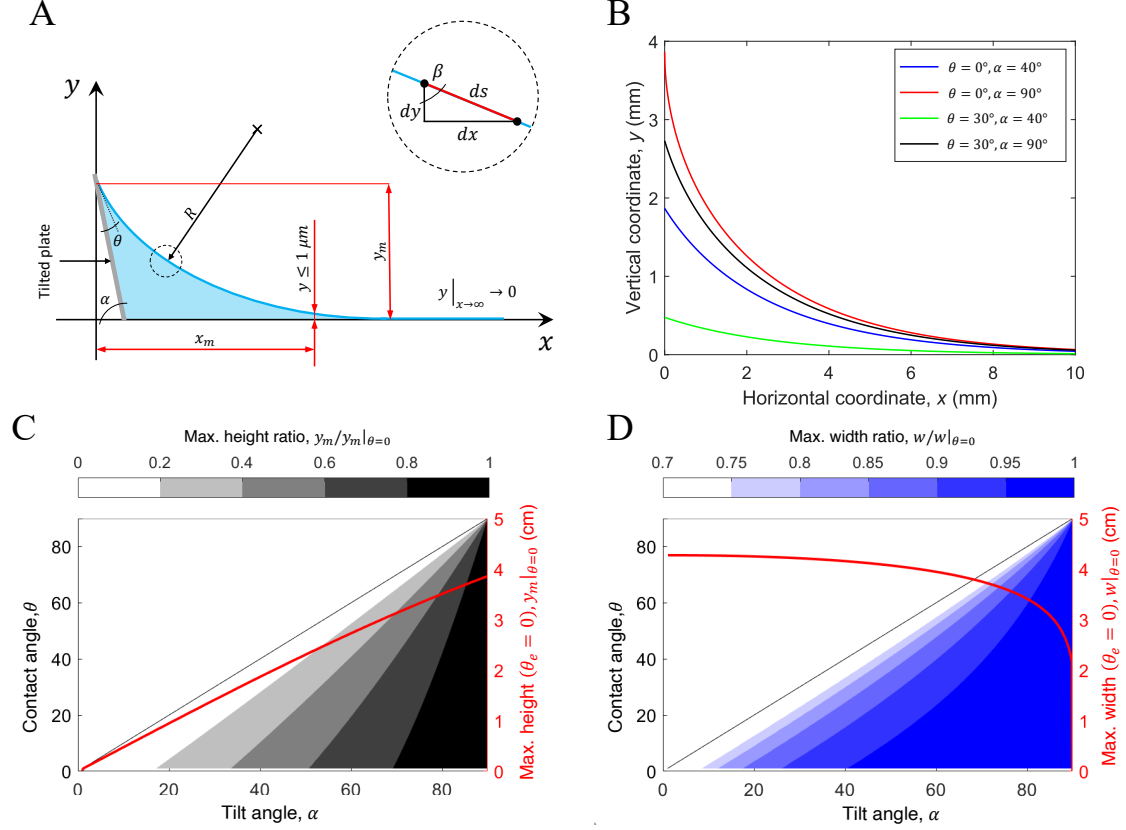


Figure 2.5: **Modelling the effects of gravity on the shape of the meniscus.** (A) Schematics of the shape of a meniscus facing an attractive plate tilted by an angle α . The system was supposed to be at the equilibrium after the plate was immersed in a large reservoir. The maximum extension of the meniscus from the wall x_m was arbitrarily located where the meniscus height is smaller than $1 \mu\text{m}$. (B) Effects of the equilibrium contact angle θ and the plate tilt angle α on the meniscus shape. Lower values of θ and higher values of α result in higher capillary rises. (C) Map showing the maximum capillary rise y_m on a tilted flat plate as a function of the tilt angle α and θ . (D) Map showing the maximum width of the V-shaped groove $w = 2x_m$ as a function of the tilt angle α and θ . The solid black lines in panels (C) and (D) represent the theoretical limit of the model $\theta = \alpha$, which relates to a flat meniscus and, thus, no capillary pressure.

Eq. 2.33 was integrated again considering Eq. 2.34 as boundary condition to obtain the implicit equation of the height of the meniscus y for a given distance x from the wall [114, 127]:

$$x = l_c \left(\operatorname{acosh} \left(\frac{2l_c}{y} \right) - \operatorname{acosh} \left(\frac{2l_c}{y_m} \right) - \sqrt{4 - \frac{y^2}{l_c^2}} + \sqrt{4 - \frac{y_m^2}{l_c^2}} \right). \quad (2.35)$$

Eq. 2.34 predicts $y \rightarrow 0$ for $x \rightarrow \infty$, thus x_m was arbitrarily evaluated as the minimum distance to obtain $y \leq 1 \mu\text{m}$.

The water-plate contact angle θ and the plate tilt angle α significantly affect the shape of the water meniscus (see Fig. 2.5B), which has a steeper profile for higher values of α and lower values of θ . Fig. 2.5C shows the maximum height reached by the water meniscus (grey-scale map), on the order of centimeters, scaled on the maximum height reached by the meniscus considering similar α and $\theta = 0$ (solid red line). This result was used to evaluate the maximum groove width $w = 2x_m$ (see Fig. 2.5D, blue-scale map), which is almost constant for the whole range of α and rapidly decreases to zero as $\alpha \rightarrow \theta$. Note that $\theta < \alpha$ is the necessary condition for the meniscus formation, which leads to a net ΔP and, therefore, to capillary rise (see Eq. 2.34). The obtained values of the groove maximum width w are in the order of centimetre, which justifies the assumption of a constant and circular meniscus shape in micro-sized grooves.

2.3.2 Capillary pressure in micro-sized grooves

Justified by the results presented in section 2.3.1, the effect of gravity on the meniscus shape in sub-millimeter grooves was neglected and, thus, the radius of curvature R was considered constant. As a consequence, Eq. 2.1 was rewritten as:

$$\Delta P = -\gamma \frac{1}{R} = \gamma \frac{d\beta}{ds} = \gamma \sin(\beta) \frac{d\beta}{dx}, \quad (2.36)$$

where s is the planar curve describing the cylindrical water meniscus (see the inset in Fig. 2.6 A). Being the radius of curvature R a constant (where the subscript 1 was dropped), Eq. 2.1 implies constant ΔP . Therefore, Eq. 2.36 was integrated by separation of variables, leading to:

$$\Delta P = -\frac{2\gamma}{w} \cos(\beta) \Big|_{\pi/2-\alpha+\theta}^{\pi/2}, \quad (2.37)$$

where the second boundary condition was formulated considering symmetric grooves, namely $\beta|_{x=w/2} = \pi/2$. Eq. 2.37 was formulated neglecting the pinning of the water meniscus at the edges of the groove [125]. Being the height of the groove $h_g = w \tan(\alpha)/2$, Eq. 2.37 leads to the following expression of the radius of curvature:

$$R = \frac{h_g}{\tan(\alpha) \sin(\alpha - \theta)}. \quad (2.38)$$

Eq. 2.38 was written assuming the groove to be entirely filled by water in the y direction, justified by the results presented in section 2.3.1 (see Fig. 2.5C). However, considering a system where gravity is actually negligible (e.g., in horizontal grooves), this assumption can be proved valid by evaluating the derivative of the

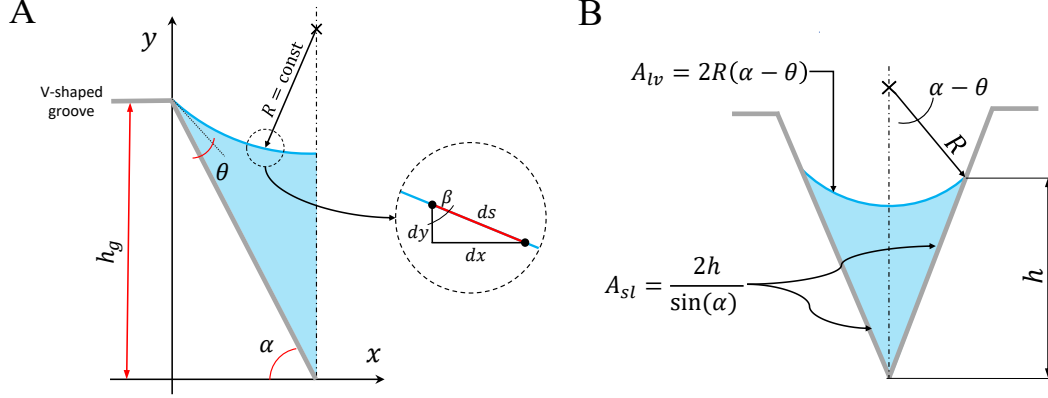


Figure 2.6: **Schematics of the capillary model in V-shaped grooves.** (A-B) Schematics of a sub-millimetre V-shaped groove filled by water highlighting the main parameters in the proposed theoretical model: the groove tilt angle α , the water-groove equilibrium contact angle θ and the height of the groove h_g . The model neglects the effect of gravity and the pinning of the meniscus at the edges of the groove.

free energy E given with respect to the meniscus height h , namely dE/dh (see Fig. 2.6B). The free energy per unit length of a V-shaped groove immersed in air and partially wetted by water was evaluated as:

$$\begin{aligned} E &= (\gamma_{sl} - \gamma_{sv})A_{sl} + \gamma A_{lv} = \\ &= \gamma(A_{lv} - A_{sl} \cos(\theta)), \end{aligned} \quad (2.39)$$

where γ_{sl} and γ_{sv} are the solid-liquid and solid-gas surface tensions, respectively, A_{sl} and A_{lv} are the solid-liquid and liquid-gas contact areas, respectively. The second equality considers the Young-Dupré equation [114, 126], expressing the equilibrium at the three-phases contact line:

$$\gamma_{sl} + \gamma \cos \theta = \gamma_{sv}. \quad (2.40)$$

The contact areas per unit length in the z direction can be evaluated by geometrical arguments as (see Fig. 2.6B):

$$\begin{aligned} A_{sl} &= \frac{2h}{\sin(\alpha)}, \\ A_{lv} &= 2R(\alpha - \theta) = \frac{2h(\alpha - \theta)}{\tan(\alpha) \sin(\alpha - \theta)}, \end{aligned} \quad (2.41)$$

where, neglecting the effect of gravity, the radius of the water meniscus was expressed according to Eq. 2.38 for a generic height h . Thus, dE/dh was rewritten

as:

$$\frac{dE}{dh} = \gamma \left(\frac{2(\alpha - \theta)}{\tan(\alpha) \sin(\alpha - \theta)} - \frac{2 \cos(\theta)}{\sin(\alpha)} \right). \quad (2.42)$$

Being $\theta < \alpha$ the condition to have non-zero ΔP , it can be numerically verified that Eq. 2.42 is negative for any tilt angle in the range $0 < \alpha < 90$, where the extremes of the boundary were willingly omitted.

Finally, the capillary force promoting transport of fluid along the groove (namely, in the z direction of Fig. 2.6A-B) was evaluated as the z -derivative of the free energy E [123, 128, 129]. Thus, substituting Eq. 2.41 in 2.39, the capillary force F_c in V-shape grooves was written as:

$$F_c = -\frac{dE}{dz} = 2h_g\gamma \left(\frac{\cos(\theta)}{\sin(\alpha)} - \frac{\alpha - \theta}{\tan(\alpha) \sin(\alpha - \theta)} \right). \quad (2.43)$$

2.4 Dynamic wicking model

The classic approach to model analytically the time-dependent position of the water front H_t during wicking is the Lucas-Washburn model [125, 130], which predicts the capillary rise by imposing the equilibrium between the capillary and the viscous forces, respectively F_c and F_μ . However, this approach overlooks the gravitational force F_g , which becomes predominant in components designed to overcome small hydraulic heads and to deliver the fluid without relying on circulation pumps [117, 131].

The one-dimensional force balance along the z direction determining capillary rise can be expressed as:

$$F_c = F_\mu + F_g, \quad (2.44)$$

where F_c is the capillary force, F_μ is the viscous force and F_g is the gravitational force. To solve Eq. 2.44, some common simplifying assumptions were considered: as a first approximation, evaporation was neglected; the gas-liquid surface has a constant shape during imbibition and the height of water meniscus is negligible with respect to the height the water front along the z axis, namely H_t [123]; the flow conditions in the grooves are coherent with a Poiseuille flow, and the viscous losses are determined by the channel cross-section rather than by the shape of the liquid surface [125, 132]; the capillary channels are small enough to neglect the effect of gravity on the shape of the meniscus. If these assumptions hold, Eq. 2.44 can be solved to derive a dynamic wicking model for a multi-filament yarn (see section 2.4.1) and for V-shaped grooves (see section 2.4.2).

2.4.1 Wicking in an infinite multi-filament dense yarn

The capillary force in an infinite multi-filament yarn was evaluated by the model reported in section 2.2.2 as $F_c = H_m \rho g$, where the maximum height achievable by

vertical imbibition H_m was evaluated from Eq. 2.27. A similar result could have been obtained by analyzing the free energy E of a yarn wet up to a generic height H_t :

$$E = (\gamma_{sl} - \gamma_{sv})p_{H,S}H_t + \gamma_{lv}A_{lv}, \quad (2.45)$$

where $p_{H,S}$ is the wet perimeter of the fibers arranged in hexagonal or square arrangement, A_{lv} is the liquid-air contact area, and γ_{sl} , γ_{sv} and γ_{lv} are the solid-liquid, solid-air and liquid-air surface tensions. Note that assuming the yarn as composed by an infinite array of fibers leads to $A_{lv} = o(p_{H,S})$, which can then be neglected in Eq. 2.45. Considering the Young's equation [133], Eq. 2.45 was rewritten as:

$$E = -\gamma_{lv} \cos(\theta)z p_{H,S}. \quad (2.46)$$

The capillary force F_c was evaluated as the derivative of the free energy E with respect to the capillary rise z [123, 128, 129]. Similarly, a water column of height z supported only by capillary forces is subject to a gravitational force F_g proportional to the cross section capillary cross section, while the viscous force F_μ was expressed by considering a Poiseuille flow. Thus:

$$\begin{aligned} F_c &= -\frac{dE}{dz} = \gamma p_{H,S} \cos(\theta), \\ F_\mu &= 8\pi\mu z \frac{dz}{dt}, \\ F_g &= z\rho g A_{H,S}. \end{aligned} \quad (2.47)$$

where the subscript lv is dropped, and $p_{H,S}$ and $A_{H,S}$ were evaluated from Eq. 2.26. Substituting Eq.2.45 in Eq. 2.44, the position of the water front is described by a first order differential equation:

$$\gamma p_{H,S} \cos(\theta) = 8\pi\mu z \frac{dz}{dt} + A_{H,S}\rho g z, \quad (2.48)$$

which was re-arranged and integrated by separation of variables:

$$\int_0^t \frac{1}{8\pi\mu} dt = \int_0^{H_t} \frac{z}{C_1 - C_2 z} dz = \int_0^{H_t} \left(-\frac{C_1}{C_2(C_2 z - C_1)} - \frac{1}{C_2} \right) dz, \quad (2.49)$$

where $C_1 = \gamma p_{H,S} \cos(\theta)$ and $C_2 = A_{H,S}\rho g$. The extremes of integration on the right-hand side are evaluated assuming $z|_{t=0} = 0$ as initial condition, while the front height evaluated at the time t was referred to as $z|_t = H_t$. Solving Eq. 2.49 it holds:

$$\frac{t}{8\pi\mu} = -\frac{C_1}{C_2^2} \ln(C_2 H_t - C_1) - \frac{H_t}{C_2} + C_1 \ln(-C_1)/C_2^2, \quad (2.50)$$

which is implicit with respect to H_t . Eq. 2.50 was made explicit with respect to H_t by using the definition of the main branch of the Lambert W function, namely W_0 ,

which can be used to solve the family of equations $ye^y = x$ in the form $y = W_0(x)$, being $x \geq 0$ and y real numbers. Thus, Eq. 2.50 was rearranged as:

$$-\exp\left(-1 - \frac{C_2^2}{8\pi\mu C_1}t\right) = \frac{C_2 H_t - C_1}{C_1} \exp\left(\frac{C_2 H_t - C_1}{C_1}\right), \quad (2.51)$$

which, given the definition of W_0 , was used to derive the explicit equation of H_t as a function of the wicking time t , namely:

$$H_t = \frac{C_1}{C_2} \left[1 + W_0\left(-\exp\left(-1 - \frac{C_2^2}{8\pi\mu C_1}t\right)\right) \right]. \quad (2.52)$$

2.4.2 Wicking in V-shaped grooves

The capillary force F_c can be derived from the surface free energy per unit length, which is a function of the solid-liquid and liquid-gas contact areas, A_{sl} and A_{lw} respectively (see section 2.3.2). Similarly to the results presented in section 2.4.1, it can be written:

$$\begin{aligned} F_c &= -\frac{dE}{dz} = h_g \gamma 2 \left(\frac{\cos(\theta)}{\sin(\alpha)} - \frac{\alpha - \theta}{\tan(\alpha) \sin(\alpha - \theta)} \right) = h_g \gamma p^*, \\ F_\mu &= 8\pi\mu z \frac{dz}{dt}, \\ F_g &= \rho g z h_g^2 \left(\frac{1}{\tan^2(\alpha)} \left(\tan(\alpha) + \frac{\cos(\alpha - \theta)}{\sin(\alpha - \theta)} - \frac{\alpha - \theta}{\sin^2(\alpha - \theta)} \right) \right) = \rho g z h_g^2 A^*, \end{aligned} \quad (2.53)$$

where μ is the dynamic viscosity of the wetting fluid. The free energy can be evaluated from Eq. 2.39, and the cross-sectional area of the channel, namely $h_g^2 A^*$, can be evaluated by geometrical arguments from the schematics shown in Fig. 2.6A.

Substituting Eq.2.53 in Eq. 2.44, the position of the water front is described by a first order differential equation:

$$h_g \gamma p^* = 8\pi\mu z \frac{dz}{dt} + h_g^2 A^* \rho g z. \quad (2.54)$$

by the definition of $C_1 = h_g p^* \gamma$ and $C_2 = h_g^2 A^* \rho g$, Eq. 2.54 was solved following the same procedure presented in section 2.4.1 leading to Eq. 2.52.

2.4.3 Transition to volume-averaged parameters

The dynamic imbibition of a single-phase fluid in a saturated, rigid porous matrix under isothermal conditions can be modelled by combining Darcy's law and the continuity equation [87, 131]:

$$\nabla \cdot \left(-\frac{K}{\phi\mu} (\nabla \langle P \rangle - \rho \mathbf{g}) \right) = 0, \quad (2.55)$$

where ϕ and K are respectively the effective porosity and absolute permeability of the porous matrix, $\langle P \rangle$ is the pore-averaged pressure of the fluid. Considering a wicking transient along the grooves axes (in the z direction for vertical wicking), K was considered as a constant and Eq. 2.55 was used to derive a one-dimensional equation for the front position H_t as a function of time. Considering the boundary conditions [87]:

$$\begin{aligned} P \Big|_{z=0} &= P_{atm}, \\ p \Big|_{z=H_t} &= P_{atm} - P_c + \rho g H_t, \end{aligned} \quad (2.56)$$

where P_{atm} is the atmospheric pressure, $P_c \sim \Delta P$ is the capillary pressure and the averaging parentheses were dropped for the sake of simplicity. Integration of Eq. 2.55 in one dimension, subject to Eq. 2.56, leads to:

$$P_c \ln \left| \frac{P_c}{P_c - \rho g H_t} \right| - \rho g H_t = \frac{\rho^2 g^2 K}{\phi \mu} t, \quad (2.57)$$

which is indeed equivalent to Eq. 2.50. Therefore, the wicking parameters were evaluated by similarity arguments comparing Eq. 2.57 with those obtained in sections 2.4.1 and 2.4.2. Concerning the ideal multi-filament yarn, it can be written:

$$\begin{aligned} K &= \frac{\phi_{H,S} A_{H,S}}{8\pi}, \\ P_c &= \frac{p_{H,S} \gamma}{A_{H,S}} \cos(\theta), \\ A_H &= 3\pi r^2 \left(\frac{1}{1 - \phi_H} - 1 \right), \\ A_S &= \pi r^2 \left(\frac{1}{1 - \phi_S} - 1 \right), \end{aligned} \quad (2.58)$$

where $\phi_{H,S}$ was evaluated from Eq. 2.16 or by an appropriate experimental characterization, and $p_{H,S}$ was evaluated from Eq. 2.26. Similarly, the following definitions hold for V-shaped grooves:

$$\begin{aligned} \phi &= \frac{h_g}{d \tan(\alpha)}, \\ K &= \frac{\phi h_g^2 A^*}{8\pi}, \\ P_c &= \frac{\gamma P^*}{h_g A^*}, \end{aligned} \quad (2.59)$$

where the absolute porosity ϕ is defined as the ratio between the void and the total volume of material containing the grooves (see Fig. 2.7A), and d is the center-to-center distance between two adjacent grooves. Eqs. 2.58 and 2.59 link K and

P_c to the geometry of the grooves, to the liquid-air surface tension γ and liquid-solid equilibrium contact angle θ , and can be used to compare the performances of different, common unstructured capillary materials (e.g. woven or non-woven textiles, foams and hydrogels) to those of the proposed micro-structured materials.

2.4.4 Permeability in fibrous media

Alternatively, the microscopic permeability K of unidirectional fibrous media (namely, the multi-filament yarn) in the direction of the fibers axis can be evaluated as [134, 135]:

$$K = r^2 \exp \frac{(B + C(1 - \phi))}{(1 - \phi)^m}, \quad (2.60)$$

where the parameters

$$\begin{aligned} B &= 5.43 - 18.5(1 - \phi_{min}) + 10.7(1 - \phi_{min})^2, \\ C &= -4.27 + 6.16(1 - \phi_{min}) - 7.1(1 - \phi_{min})^2, \\ m &= -1.74 + 7.46(1 - \phi_{min}) - 3.72(1 - \phi_{min})^2, \end{aligned} \quad (2.61)$$

depend on the minimum porosity ϕ_{min} that can be achieved considering a specific lattice arrangement under the densest packing scenario. Eqs. 2.60 and 2.60 express K as a function of the fiber radius, the yarn porosity, and the lattice structure, coherently with its physical meaning, and has been previously validated against finite element simulations in the porosity range 0.1÷0.9 [134, 135]. The minimum porosity of both types of the fiber arrangements corresponds to the situation when the adjacent fibers are in direct contact, namely $d = 0$, and was computed by Eq. 2.16, leading to $\phi_{H,min} = 9.3\%$ and $\phi_{S,min} = 21.5\%$.

2.4.5 High evaporative fluxes

Water tends to evaporate whenever in direct contact with a mixture of gasses non-saturated by its own vapour. Considering a porous medium partially immersed in a wetting fluid and exposed to air, the evaporation rate from the porous surface is driven by the temperature of the two fluids (e.g. water and air) and the content of the fluid vapour in the air. Consequently, evaporation affects the wicking transient and determines the maximum height reached by the water front, which is related the maximum size of components relying on wicking and evaporation for their operation. Hence, it is essential to model the effect of evaporation on the wicking transient to correctly design passive devices.

The total mass flow rate in the grooves $\dot{M}(z, t)$ (expressed in kg s^{-1}) includes the mass flow rate needed for the advancement of the water front at given time $\dot{M}_{H_t}(t)$, and the mass flow rate needed to balance the fluid evaporating from the

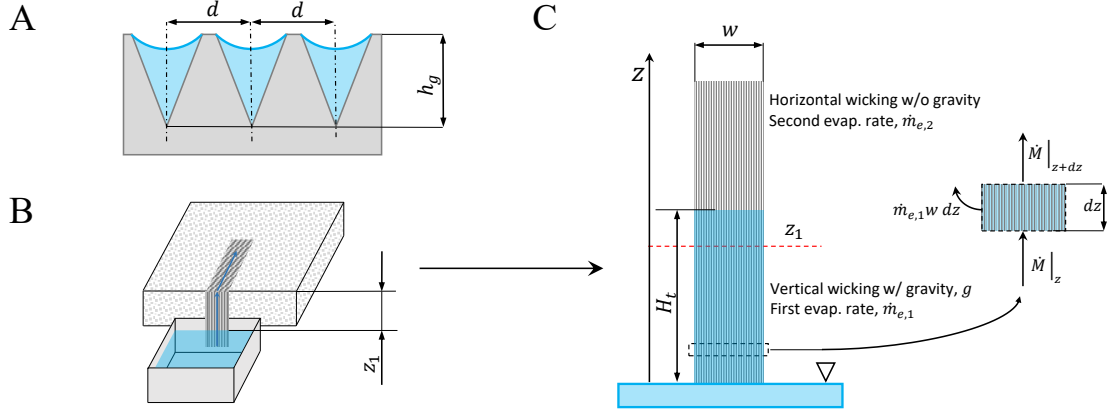


Figure 2.7: **Including high evaporative fluxes in the wicking model.** (A) Cross sectional view of the V-shaped grooves highlighting the main geometrical features used to compute the flow parameters of an equivalent porous medium (see section 2.4.3). (B-C) Schematics of the vertical-horizontal imbibition setup including two different evaporation rates. The setup mimics the typical layout of multistage passive desalination devices reported in Refs. [17, 96, 119], where vertical sections (usually exposed to the ambient or partially insulated) feed sea water to the horizontal stack by capillary. The model developed neglects the effect of the bend at z_1 on the capillary pressure.

wet surface $\dot{M}_e(z, t)$ [136]. Therefore, it holds:

$$\dot{M}(z, t) = \dot{M}_{H_t}(t) + \dot{M}_e(z, t). \quad (2.62)$$

$\dot{M}_e(z, t)$ might be caused by one or more specific evaporation rates $\dot{m}_{e,i}^{tot} \geq 0$, which were assumed as constant over a portion of the sample surface. As an example, consider the simplified schematics reported in Fig. 2.7B-C or Refs. [17, 54]: $\dot{m}_{e,1}^{tot}$ might be zero if the sample is insulated from the surrounding environment, while $\dot{m}_{e,2}^{tot}$ might be governed by membrane transport properties (e.g. see section 2.6) or by specific ambient conditions (e.g., temperature, humidity, wind speed and solar irradiation). Being constants, each specific flux $\dot{m}_{e,i}^{tot}$ assumes the temperature of the evaporating surface to be locally homogeneous and to neglect the progressive build up of vapour above the evaporating surface. The present work accounts for $i = \{1,2\}$ different fluxes; the generalisation to $i \geq 3$ is beyond the scopes of this work, as the applications considered are limited to two evaporating zones.

Note that in case of structured porous media, the effective evaporative surface could be lower than the total area exposed to the environment. Thus, a normalization coefficient should be considered in case the evaporative flux $\dot{m}_{e,i}^{tot}$ acts on a wet surface with non-unitary porosity. This is the case of V-shaped grooves: referring the symbols reported in Fig. 2.7C, the wet grooved aluminum sample is subject to

two specific evaporative fluxes:

$$\dot{m}_e(z) = \begin{cases} \dot{m}_{e_1} = 2\dot{m}_{e_1}^{tot}h_g/(d \tan(\alpha)) & \text{if } z \leq z_1 \\ \dot{m}_{e_2} = 2\dot{m}_{e_2}^{tot}h_g/(d \tan(\alpha)) & \text{if } z > z_1, \end{cases} \quad (2.63)$$

where the coefficient $2h_g/(d \tan(\alpha))$ is included to consider that, with respect to the sample surface, only the planar projection of the grooves is wet and contributes to evaporation (see Fig. 2.7A). Clearly, if $d = 2h_g/\tan(\alpha)$, namely in the limit of touching grooves, $\dot{m}_e = \dot{m}_e^{tot}$. For the sake of simplicity, the superscript *tot* was dropped for the rest of this section.

Considering the height reached by the water front at a given time t , namely H_t , two possible cases must be considered: when $H_t \leq z_1$, the wet portion of the sample is only subject to $\dot{m}_{e,1}$; when $H_t > z_1$, the evaporative flux, thus the fluid flowing within the grooves, depends on both $\dot{m}_{e,1}$ and $\dot{m}_{e,2}$. For the sake of simplicity, the following equations omit the explicit dependence of the various quantities on the considered time t .

Case 1: $H_t \leq z_1$ The balance of the mass fluxes across an elementary sample volume is (see Fig. 2.7C):

$$\dot{M} \Big|_z = \dot{M} \Big|_{z+dz} + \dot{m}_{e,1}w dz, \quad (2.64)$$

where w is the width of the sample. At the inlet, namely at $z = 0$, the total mass flux includes the flux needed for advance of the water front \dot{M}_{H_t} , and for the flux needed to compensate the evaporation from the whole wet surface $\dot{M}_e = \dot{m}_{e,1}wH_t$ [136]. Integrating Eq. 2.64 from the inlet to a generic height z , it holds:

$$\int_{\dot{M}_{H_t} + \dot{M}_e}^{\dot{M}_z} d\dot{M} = - \int_0^z \dot{m}_{e,1}w dz, \quad (2.65)$$

which was solved to evaluate the mass flux at a given height $z < H_t$, namely:

$$\dot{M}_z = \dot{M}_{H_t} + \dot{m}_{e,1}wH_t \left(1 - \frac{z}{H_t}\right). \quad (2.66)$$

Consequently, \dot{M}_z is linear and has its maximum value at the inlet and decreases as z increases. The mass flow rate can be defined in terms of the flow velocity as $\dot{M} = v\phi h_g w \rho$, where the thickness of the equivalent porous medium was assumed to be equal to the height of the grooves h_g (see section 2.4.3 and Fig. 2.7A). The former relation was used to define the speed of the evaporating mass flux, namely:

$$v_e \Big|_{H_t \leq z_1} = \frac{\dot{m}_{e,1}H_t}{\phi h_g \rho} \left(1 - \frac{z}{H_t}\right). \quad (2.67)$$

Eq. 2.64 was reformulated in terms of the fluid velocity:

$$\phi h_g \rho w \left(v_{H_t} \Big|_z + v_e \Big|_z \right) = \phi h_g \rho w \left(v_{H_t} \Big|_{z+dz} + v_e \Big|_{z+dz} \right) + \dot{m}_{e,1} w dz, \quad (2.68)$$

which, considering the definition of v_e given in Eq. 2.67, was rearranged as:

$$\phi h_g \rho w \frac{v_{H_t} \Big|_{z+dz} - v_{H_t} \Big|_z}{dz} = 0. \quad (2.69)$$

Eq. 2.69 is analogous to the continuity of \dot{M}_{H_t} , namely:

$$\nabla \cdot (v_{H_t}) = 0 \quad (2.70)$$

Case 2: $H_t > z_1$ Following the same procedure, substituting Eq. 2.63 in Eq. 2.64 and integrating from the inlet to a generic height z , Eq. 2.66 becomes:

$$\dot{M}_z = \begin{cases} \dot{M}_{H_t} + w \left(\dot{m}_{e,2}(H_t - h_1) + \dot{m}_{e,1} h_1 \left(1 - \frac{z}{z_1} \right) \right) & \text{if } z \leq z_1 \\ \dot{M}_{H_t} + \dot{m}_{e,2} w H_t \left(1 - \frac{z}{H_t} \right) & \text{if } z > z_1. \end{cases} \quad (2.71)$$

Recalling the definition of mass flux, Eq. 2.71 was used to derive the velocity of the fluid flux needed to balance the effect of evaporation:

$$v_e \Big|_{H_t > z_1} = \begin{cases} \left(\dot{m}_{e,2}(H_t - h_1) + \dot{m}_{e,1} h_1 \left(1 - \frac{z}{z_1} \right) \right) / (\phi h_g \rho) & \text{if } z \leq z_1 \\ \dot{m}_{e,2} H_t \left(1 - \frac{z}{H_t} \right) / (\phi h_g \rho) & \text{if } z > z_1. \end{cases} \quad (2.72)$$

Similarly to the previous case, it can be easily shown that substituting Eq. 2.72 in 2.68 leads to Eqs. 2.69 and 2.70.

Time-discretization Consider the case where the water front has reached the height H_t at time t . Therefore, Eqs. 2.67, 2.70 and 2.72 were used to determine the velocity v_{H_t} of the advancing water front, which was used to evaluate $H_{t+dt} = H_t + v_{H_t} dt$ at time $t + dt$. The procedure was iterated to evaluate the curve (H, t) for different grooves shapes and evaporation rates. For this purpose, Darcy's law can be combined with Eq. 2.70 to evaluate the pressure field of the mass flux \dot{M}_{H_t} at the time t :

$$\nabla^2 P_t = 0, \quad (2.73)$$

where the permeability and porosity of the material were assumed as constants. Eq. 2.73 was solved with a finite differences scheme for each time t by applying proper boundary conditions: in addition to those reported in Eq. 2.56, an extra pressure drop due to \dot{M}_e was included [136]. Considering the velocity of the evaporating flux v_e , Darcy's law can be used to evaluate the related pressure drop ΔP_e for $H_t \leq z_1$:

$$\Delta P_e \Big|_{H_t \leq z_1} = \frac{\mu \phi}{K} \int_0^{H_t} v_e dz = \frac{\mu}{2K h_g \rho} \dot{m}_{e,1} H_t^2, \quad (2.74)$$

while Eq. 2.72 was used for the case $H_t > z_1$:

$$\begin{aligned} \Delta P_e \Big|_{H_t > z_1} &= \frac{\mu \phi}{K} \left(\int_0^{z_1} v_e \Big|_{z \leq z_1} + \int_{z_1}^{H_t} v_e \Big|_{z > z_1} \right) = \\ &= \frac{\mu}{K h_g \rho} \left(z_1 \left(\dot{m}_{e,2}(H_t - z_1) + \frac{1}{2} \dot{m}_{e,1} z_1 \right) + \frac{1}{2} \dot{m}_{e,2} (H_t - z_1)^2 \right). \end{aligned} \quad (2.75)$$

Eqs. 2.74 and 2.75 were used to reformulate appropriately Eq. 2.56 to account for evaporation:

$$\begin{aligned} P \Big|_{z=0} &= P_{atm}, \\ P \Big|_{z=H_t} &= \begin{cases} P_{atm} - P_c + \rho g H_t + \Delta P_e \Big|_{H_t \leq z_1} & \text{if } H_t \leq z_1 \\ P_{atm} - P_c + \rho g z_1 + \Delta P_e \Big|_{H_t > z_1} & \text{if } H_t > z_1. \end{cases} \end{aligned} \quad (2.76)$$

Eq. 2.76 was formulated assuming a vertical capillary rise for $z \leq z_1$ and horizontal for $z > z_1$ (see Fig. 2.7C), coherently with the application investigated in this work. Once the new pressure field at time $t + dt$ is evaluated, the advancing front velocity can be computed as:

$$v_{H_t} = \frac{K}{\phi \mu} \frac{P_{H_t} - P_0}{H_t}. \quad (2.77)$$

The scheme was iterated until the target simulation time is reached. Being iterative, the procedure requires an initial non-zero height of the water front, as the initial condition $H_t \Big|_{t=0} = 0$ would not be coherent with the model assumptions expressed in section 2.4 and would result in an infinite pressure gradient. Thus, being the time-step considered equal to $dt = 0.1$ s, the initial height of the water front $H_t \Big|_{t=dt}$ was evaluated as:

$$H_t \Big|_{t=dt} = \sqrt{\frac{2K P_c}{\phi \mu} dt}, \quad (2.78)$$

where the effects of gravity and of evaporation was neglected [131]. The proposed scheme was validated against the analytical relation proposed by Fries *et al.* [136] for vertical capillary rise with a single specific evaporation flux, obtaining excellent agreement.

2.5 Differential formulation of wicking

The dynamic imbibition of a single-phase fluid in a rigid porous material under isothermal condition can be modelled by combining Darcy's law:

$$\mathbf{v}_D = -\frac{K k_{r,l}}{\mu} (\nabla P_l + \rho_w \mathbf{g}), \quad (2.79)$$

and the mass conservation of the wetting fluid [137]:

$$\frac{\partial \rho}{\partial t} + \nabla \cdot (\rho \mathbf{v}) = -f, \quad (2.80)$$

where \mathbf{v}_D is Darcy's velocity, P_l is the pressure field of the wetting fluid and $k_{r,l}$ the relative permeability for the wetting fluid.

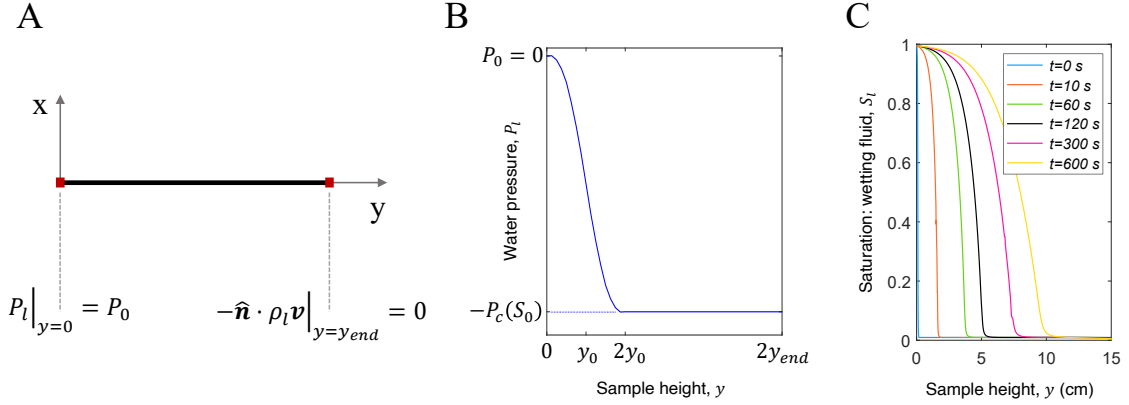


Figure 2.8: **Numerical modelling of water wicking.** (A) Schematic of the finite elements 1-dimensional model used to estimate the Van Genuchten parameters. The picture reports the boundary conditions used in the simulations at the beginning ($y = 0$) and at the end ($y = y_{end}$) of the simulation domain. (B) Qualitative representation of the assigned initial values of the pressure fields in the domain, with $P_0 = 0$ Pa the relative ambient pressure and $S_0 = 0.01$ the initial saturation of the fabric, necessary to improve the numerical stability. A transition zone around $y_0 = 1$ mm is required to grant numerical stability and an initialisation coherent with the left boundary conditions. (C) Profile of the wetting fluid saturation S_l at different instants obtained from the 1-dimensional finite elements simulation. The results represent the motion of water within the porous domain during the wicking transient (*i.e.* the height of the water front H_t and the front thickness).

Furthermore, ρ and μ are respectively the density and dynamic viscosity of the liquid phase within the porous medium, \mathbf{v} is the velocity field, and $-f$ is the sink term representing the evaporation rate of the wetting fluid. Eqs. 2.79 and 2.80 were combined considering that:

$$\begin{aligned} \rho &= \rho_l S_l \phi, \\ \mathbf{v} &= \frac{\mathbf{v}_D}{S_l \phi}, \end{aligned} \quad (2.81)$$

where ϕ is the porosity of the matrix, S_l is defined as the saturation of the wetting fluid. S_l is defined as the ratio between the volume occupied by the wetting fluid

and the total volume of the pores, thus it ranges from 0 to 1. Considering the saturation of the wetting fluid S_l (*i.e.* water) and of the non-wetting fluid S_{nw} (*i.e.* air), it holds:

$$S_l + S_{nw} = 1. \quad (2.82)$$

S_l is generally normalised considering its irreducible fraction $S_{r,l}$, namely the minimum amount of wetting fluid always present in the porous matrix, and the residual fraction of the non-wetting fluid $S_{r,nw}$ [138, 139]:

$$\Theta_l = \frac{S_l - S_{r,l}}{1 - S_{r,nw} - S_{r,l}}, \quad (2.83)$$

which bounds the saturation of the wetting fluids in the range $S_{r,l} \leq S_l \leq 1 - S_{r,nw}$. However, this works assumed that the porous structure is entirely connected and accessible to water, and that the water can completely evaporate from the fabric, namely, $S_{r,nw} = 0$ and $S_{r,l} = 0$, which lead to $\Theta_l = S_l$.

In the limit of incompressible fluids and of a rigid porous matrix, Eqs. 2.79, 2.80 and 2.81 were combined as:

$$\rho_l \phi \frac{\partial S_l}{\partial t} + \nabla \cdot \left[-\rho_l \frac{K k_{r,l}}{\mu} (\nabla P_l + \rho_l \mathbf{g}) \right] = -f. \quad (2.84)$$

Eq. 2.84 can be solved if a relationship between P_l and S_l is provided, which requires the introduction of capillary pressure and a retention model. The capillary pressure P_c is defined as the difference between the pressure of the non-wetting and wetting fluids at their interface, namely:

$$P_c = P_{nw} - P_l. \quad (2.85)$$

A retention model, instead, explicitly formalizes the dependency of the capillary pressure with the saturation of the pores, thus $\Theta_l = \Theta_l(P_c)$. One of the most widely used retention functions was proposed by van Genuchten [140]:

$$\Theta_l = \left(\frac{1}{1 + \left| \beta \frac{P_c}{\rho_l g} \right|^n} \right)^m, \quad (2.86)$$

where β and n are material-dependent parameters, and $m = 1 - 1/n$. Similarly, the relative permeability was correlated to S_l according to the combined model proposed by Mualem-van Genuchten [138–140]:

$$k_{r,l} = \Theta_l^L \left[1 - \left(1 - \sqrt[m]{\Theta_l} \right)^{m\gamma} \right]^2, \quad (2.87)$$

where L is a material-dependent parameter [139]. Here, as the porous matrix was supposed to be rigid during the absorption transient, the water retention curve

described by Eq. 2.86 was assumed as the same for both imbibition and draining. In case of swelling media (e.g. soil science), instead, the model should account for possible hysteresis, thus different values of β , L and n should be considered for the imbibition and draining.

As commonly assumed in wicking phenomena [131], the air pressure was considered constant within the porous matrix. Thus, referring to Eq. 2.85 and recalling that $\Theta_l = S_l$ was assumed here, it can be written:

$$\frac{\partial S_l}{\partial t} = \frac{\partial S_l}{\partial P_c} \frac{\partial P_c}{\partial t} = - \frac{\partial S_l}{\partial P_c} \frac{\partial P_l}{\partial t}. \quad (2.88)$$

Eq. 2.88 was then substituted in Eq. 2.84, which becomes:

$$- \rho_l \phi \frac{\partial S_l}{\partial P_c} \frac{\partial P_l}{\partial t} + \nabla \cdot \left[-\rho_l \frac{K k_{r,l}(S_l)}{\mu} (\nabla P_l + \rho_l g) \right] = -f. \quad (2.89)$$

The model proposed in Eqs. 2.86, 2.87 and 2.89 can be used to describe the capillary suction in a hydrophilic porous media once its absolute permeability to the wetting fluid K and the material-dependent parameters β , L and n are known. For the sake of clarity, Fig. 2.8A shows a schematic of a 1-dimensional configuration, including the applied boundary conditions, performing vertical capillary suction. The pressure field P_l was computed by solving Eq. 2.89, and was then used to evaluate the time and space evolution of S_l by Eqs. 2.85 and 2.86. The position of the water front H_t at the time t can be evaluated by analysing the saturation curve. At the water inlet, a fixed-pressure boundary condition $P_l = P_0$ was used, where $P_0 = 0$ Pa is the relative ambient pressure; no-flow condition was applied at the outlet (see Fig. 2.8A). Coherently with the boundary conditions, the initial values of the pressure field were evaluated using a step function:

$$P_l(y) = \begin{cases} P_0 & \text{if } y \leq y_0 \\ P_0 - P_c(S_0) & \text{if } y > y_0, \end{cases} \quad (2.90)$$

where y is the vertical coordinate, $y_0 = 1$ mm the assumed initial height of the water front, $S_0 = 0.01$ the assumed initial saturation of water in the textile (necessary to improve the numerical stability [141]), and the relation $P_c = P_c(S_0)$ was obtained from Eq. 2.86 as a function of the material dependent parameters n and β . Eq. 2.90 was smoothed considering a transition zone $y_0 \pm 1$ mm and continuous second order derivative. A qualitative representation of the initial values used in the 1-D simulations is reported in Fig. 2.8B. A few numerical assumptions were considered to ease the convergence of the solver: the relative permeability of the wetting fluid $k_{r,l}$ constrained in the range $10^{-3} \leq k_{r,l} \leq (1 - 10^{-3})$; the saturation of the wetting fluid limited to $S_l \leq 0.99$ [141]; a ramp function r with a transition zone equal to 0.8 and continuous second derivative added to the denominator of Eq. 2.86, namely

[142]:

$$\Theta_l = \left(\frac{1}{1 + \left| \beta \cdot r \left(\frac{P_c}{\rho_l g} \right)^n \right|} \right)^m. \quad (2.91)$$

At this stage, the effect of evaporation on the time dependent position of the water front can be neglected, and the wetting fluid properties were considered as constants. For the sake of clarity, the representative and simplified case study of a 1-dimensional porous medium (see Fig. 2.8A) implemented and solved (see Fig. 2.8C). The wetting process is expressed in terms of the saturation profile S_l at different time frames. At the beginning of the simulation ($t = 0$ s, solid blue line) the porous material is dry, namely $S_l = 0$, while its bottom end is put in contact with the reservoir, *i.e.* $S_l|_{y=0} = 0.99$. As the simulation proceeds, the water front advances, modifying the saturation profile within the textile according to the wicking parameters. The position of the water front at a given time-step was evaluated as the first position with respect to the imbibition point, referenced as $y = 0$, reaching a saturation $S_w < 0.05$.

2.6 Mass transfer through a hydrophobic membrane

The specific flow rate of water vapour through a micro-porous hydrophobic membrane is a complex phenomenon, affected by the vapour chemical potential, the molecular interactions with the other gaseous species (namely, the components of air) and with the porous matrix. The mass transfer of the i -th specie of a mixture through a micro-porous membrane can be expressed by the combined Maxwell-Stefan and dusty-gas models [143]:

$$-\frac{\chi_i}{R_g T} \frac{d\zeta_i}{dy} - \frac{\chi_i K_{me} \tau_{me}}{\mu \phi_{me} D_{i,K}} \frac{dP}{dy} = \sum_{j=1, j \neq i}^n \left(\tau \frac{\chi_j N_i - \chi_i N_j}{c_t D_{ij} \phi_{me}} \right) + \frac{N_i \tau}{c_t \phi_{me} D_{i,K}}, \quad (2.92)$$

where χ_i and ζ_i are the molar fraction and chemical potential of species i , R_g is the ideal gas constant, T is the average temperature of the system, c_t is the total molar concentration, N_i is the molar flux of species i , n is the total number of components in the mixture, P is the bulk fluid pressure. K_{me} , τ_{me} and ϕ_{me} are respectively the absolute permeability, tortuosity and effective porosity of the membrane, which were considered as constant. D_{ij} is the diffusion coefficient of species i in species j and $D_{i,K}$ is the Knudsen diffusion coefficient. Eq. 2.92 was written considering one-dimensional mass transfer, justified by the large aspect ratio of the membrane. Eq. 2.92 can be simplified and solved analytically by relying on some common approximations: the non-condensable components of air were considered as a single gas, reducing the system to only two components, namely

water vapour and air; both components were considered as ideal gasses [17, 54, 96], thus allowing to rewrite the chemical potential as: $\zeta_i = \zeta_{i,0} + R_g T \ln(\chi_i)$, where $\zeta_{i,0}$ is the chemical potential of pure species i ; the temperature and pressure gradients can be neglected when evaluating of the chemical potential; it can be shown by scaling arguments that the contribute of the viscous flow can be neglected [144]; the air in the membrane can be considered as still, thus its molar flux was set to zero [17, 54, 96, 144]. Thus, Eq. 2.92 was rewritten for the water vapour as:

$$-\frac{d\chi_w}{dy} = \frac{\tau_{me} N_w}{\phi_{me} c_t D_{wa}} \left(1 - \chi_w + \frac{D_{wa}}{D_{w,K}} \right), \quad (2.93)$$

where the subscripts w and a refer to water vapour and air, respectively. Eq. 2.93 was integrated by separation of variables across the thickness of the membrane d_{me} :

$$\int_{\chi_{w,e}}^{\chi_{w,c}} -\frac{d\chi_w}{1 + \omega_D - \chi_w} = \int_0^{d_{me}} \frac{\tau_{me} N_w}{\phi_{me} c_t D_{wa}} dy, \quad (2.94)$$

where $\omega_D = D_{wa}/D_{w,K}$. In Eq. 2.94, the molar fraction at the evaporator and at the condenser were respectively evaluated by their partial pressure, namely:

$$\begin{aligned} \chi_w |_{y=0} &= \chi_{w,e} = P_w^e(T_e) a_e / P \\ \chi_w |_{y=d_{me}} &= \chi_{w,c} = P_w^e(T_c) a_c / P, \end{aligned} \quad (2.95)$$

where $P_w^e(T_e)$ and $P_w^e(T_c)$ are respectively the temperature-dependent effective vapour pressure at the evaporator and at the condenser, a_e and a_c are the activity coefficients of the solutions at each end of the membrane [54], which account for the presence of salt on the evaporator side.

Considering a flat liquid surface in equilibrium with the surrounding environment, the vapour pressure P_w , expressed in Pa, can be evaluated by the Antoine's equation [145]:

$$P_w = \frac{101325}{760} 10^{A_a - B_a / (C_a + T)}, \quad (2.96)$$

where $A_a = 8.07$, $B_a = 1730.63$ and $C_a = 233.42$ are component-specific constants and T is the reference temperature, expressed in degrees Celsius. Since the output of the Antoine's equation is expressed in mmHg, a conversion coefficient was introduced to express p_{sat} in Pa. To consider the effect of the meniscus curvature at the water-air interface, the vapour pressure was corrected according to the Kelvin's equation to the effective value P_w^e :

$$P_w^e = P_w \exp \left(\frac{P_w^e - P_w - \gamma / R}{\rho R_g T} \right), \quad (2.97)$$

where P_w is the equilibrium vapour pressure evaluated by Eq. 2.96, R is the meniscus curvature, γ is the liquid-air surface tension and T is the reference temperature,

expressed in Kelvin. Clearly, if the liquid-air interface is flat (namely $R \rightarrow \infty$) Eq. 2.97 leads to $P_w^e \rightarrow P_w$. Eq. 2.97 is implicit, and was iteratively solved to evaluate the effective vapor pressure P_w^e above the evaporating meniscus and was used in Eq. 2.95 to evaluate the extremes of integration of Eq. 2.94. The activity coefficient of water-salt solutions were estimated by the Raoult law for ideal mixtures, which is valid in the limit of low concentrations:

$$a \approx \frac{1}{1 + mM_wN_i}, \quad (2.98)$$

where m is the molality of the solution, M_w is the molar mass of water and N_i is the number of ions composing the salt, assuming complete dissociation. Clearly, $a = 1$ for distilled water, while the activity coefficient decreases at higher concentrations. Thus, the specific mass flow rate of water vapour J_w was evaluated as:

$$J_w = N_w M_w = \frac{\phi_{me} c_t D_{wa} M_w}{\tau_{me} d_{me}} \ln \left(\frac{1 - \frac{P_w^e(T_c) a_c}{P(1+\omega_D)}}{1 - \frac{P_w^e(T_e) a_e}{P(1+\omega_D)}} \right), \quad (2.99)$$

where D_{wa} and c_t are assumed as constant in the interval of integration. However, the dependence of D_{wa} on temperature could be taken in consideration considering the following polynomial expression [146]:

$$D_{wa} = -2.755 \cdot 10^{-6} + 4.479 \cdot 10^{-8} T + 1.656 \cdot 10^{-10} T^2, \quad (2.100)$$

being T the average membrane temperature.

A possible configuration for membrane distillation devices include a porous spacer in series to the microporous hydrophobic membrane [17, 54]. Considering a plastic support with thickness d_s , porosity ϕ_s and unitary tortuosity (i.e., straight cylindrical pores), the molar fraction of the water vapour at the evaporator side, at the interface between the membrane and the support, and at the condenser side were respectively evaluated as:

$$\begin{aligned} \chi_w |_{y=0} &= \chi_{w,e} = P_w^e(T_e) a_e / P \\ \chi_w |_{y=d_{me}} &= \chi_{w,s} = P_w(T_s) a_s / P \\ \chi_w |_{y=d_s+d_{me}} &= \chi_{w,c} = P_w^e(T_c) a_c / P, \end{aligned} \quad (2.101)$$

where the activity coefficient at both ends of the spacer are unitary, as, thanks to the hydrophobic membrane, for $y > d_{me}$ the water vapour only faces distilled water. Thus, the specific mass flux of water vapour J_w flowing through the spacer was obtained by integrating Eq. 2.93 considering the boundary conditions expressed in Eq. 2.101, obtaining:

$$J_w = \frac{\phi_s c_t D_{wa} M_w}{d_s} \ln \left(\frac{1 - \frac{P_w^e(T_c)}{P}}{1 - \frac{P_w^e(T_s)}{P}} \right), \quad (2.102)$$

where the large and straight pores of the spacer allow to assume $\omega_D \approx 0$ and $\tau_s \approx 1$, thus neglecting Knudsen diffusion in the spacer.

If $\chi_w \ll 1$, Eqs. 2.102 and 2.95 can be linearised by a first-order Taylor expansion, leading to:

$$\begin{aligned} J_w \Big|_{y=0}^{y=d_{me}} &= \frac{\phi_{me} D_{wa} M_w}{\tau_{me} d_{me} R_g \bar{T}_{me}} \frac{1}{(1 + \omega_D)} (P_w(T_s) - a_e P_w^e(T_e)) = C_3 \Delta P_{me} \\ J_w \Big|_{y=d_{me}}^{y=d_{me}+d_s} &= \frac{\phi_s D_{wa} M_w}{d_s R_g \bar{T}_s} (P_w^e(T_c) - P_w(T_s)) = C_4 \Delta P_s, \end{aligned} \quad (2.103)$$

where the activity coefficients at $y = d_{me}$ and $y = d_{me} + d_s$ were assumed as unitary, ΔP_{me} and ΔP_s are respectively the pressure drops across the membrane and the spacer, \bar{T}_{me} and \bar{T}_s are respectively the average temperature within the membrane and the spacer. Eq. 2.103 allows to interpret the fluxes of water vapour with an electrical analogy, thus as driven by a pressure difference ΔP_i through a porous layer with resistance $B_i = 1/C_i$. Therefore, relying on continuity:

$$\begin{aligned} J_w \Big|_{y=0}^{y=d_{me}+d_s} &= B (a_c P_w^e(T_c) - a_e P_w^e(T_e)) = \\ J_w \Big|_{y=d_{me}}^{y=d_{me}+d_s} &= C_4 (a_c P_w^e(T_c) - P_w(T_s)), \end{aligned} \quad (2.104)$$

where $B = 1/C_3 + 1/C_4$ is the total resistance opposed to the mass transport by the membrane and the spacer, expressed as a series of resistances, namely:

$$\frac{1}{B} = \frac{d_{me} \tau_{me} R_g \bar{T}_{me}}{\phi_{me} D_{wa} M_w} + \frac{d_{me} \tau_{me} R_g \bar{T}_{me}}{\phi_{me} D_{w,K} M_w} + \frac{d_a R_g \bar{T}_a}{\phi_a D_{wa} M_w}. \quad (2.105)$$

Finally, Eqs. 2.104 and 2.105, obtained from the linearisation of the specific mass fluxes performed in Eq. 2.103, were used in the non-linearised equation of the specific water vapour flux thorough the membrane to express $P_w(T_s)$, obtaining a less crude approximation of J_w , namely:

$$J_w = \frac{\phi_{me} D_{wa} M_w P}{\tau_{me} d_{me} R_g \bar{T}_{me}} \ln \left(\frac{1 - (a_c P_w^e(T_c) - \frac{B}{C_4} (a_c P_w^e(T_c) - a_e P_w^e(T_e))) / P (1 + \omega_D)}{1 - a_e P_w^e(T_e) / (P (1 + \omega_D))} \right). \quad (2.106)$$

The Knudsen diffusion coefficient for water vapour at a reference temperature is defined as [143]:

$$D_{w,K} = \frac{d_p}{3} \sqrt{\frac{8 R_g \bar{T}}{\pi M_w}}, \quad (2.107)$$

where d_p is the average size of pores diameter, and the membrane tortuosity τ_{me} is correlated to the membrane porosity through [147]:

$$\tau_{me} = \frac{(2 - \phi_{me})^2}{\phi_{me}}. \quad (2.108)$$

Chapter 3

Sustainable polyethylene fabrics with engineered water transport properties¹

As described in the introduction, textiles for passive personal thermal management could help to reduce the energy demand of traditional air conditioning technologies and, thus, their environmental impact. However, to embrace a fully sustainable approach to the problem, the entire life cycle of textiles has to be considered: summarizing the discussion developed in section 1.2.1, the manufacturing phase of both natural fibers (such as cotton and linen) and petroleum-based synthetic materials (e.g., polyester) has an extremely high environmental impact. On the other hand, the most advanced fabrics recently proposed for passive thermoregulation are often fabricated as layered multi-materials, which drastically reduces their recyclability. In this context, the use of polyethylene (PE) appears as a promising strategy to produce high-performance fabrics from all-recycled raw material. A garment must be breathable to be considered as comfortable, thus rapidly driving sweat away from the skin and promoting its evaporation. This can be easily achieved by hydrophilic fibers; however, PE is a weakly hydrophobic material. Therefore, providing capillary properties to PE yarns is crucial to promote their usage for personal thermal management purposes.

This Chapter proposes for the first time high-performing all-polyethylene fabrics manufactured with standard industrial equipment and processes, providing a competitive and sustainable alternative to traditional fabrics for personal thermal management during hot seasons. Here is demonstrated that properly engineered woven PE textiles composed of multi-filament yarns can comprise excellent optical

¹Part of the work included in this chapter was also previously published by Alberghini et al. in Refs. [87, 102]. The Supplementary Videos mentioned in this chapter are included among the multimedia resources attached to the thesis.

properties, efficient moisture wicking and fast-drying performance. By the synergistic optimization of their micro-structure, surface chemistry and their heat and mass transfer properties, the aim was to create a new class of eco-friendly materials for personal thermal management. The Chapter covers the procedure used to characterize, both experimentally and theoretically, a proof-of-concept plain woven sample fabricated using industrial-scale equipment, by applying and extending the framework proposed in Chapter 2.

First, section 3.1 deals with the characterization of the surface chemistry, the multi-scale geometrical features and thermal properties of the textile. In particular, section 3.1.1 covers the experimental procedure used to evaluate the average yarn porosity, thickness and surface roughness of the woven PE fabric. Successively, the hydrophilicity and average surface free energy of the fibers were investigated in sections 3.1.2 and 3.2.1. Then, as the heat and mass transfer mechanisms involved are inherently coupled, the problem was divided into three different sub-problems, which were individually investigated by dedicated experiments: wicking, evaporation and radiative heat transfer (see sections 3.1.4, 3.1.5 and 3.1.6, respectively).

Second, the data obtained were interpreted by the 1-D analytical model, introduced in section 2.2, which relates the micro-structure of the fabric to its capillary performance (see section 3.2.2). The model, calibrated on experimental data, was then used to extrapolate the optimal micro-structure of a plain-woven textile and to assess its thermal performance in different working conditions, providing general guidelines for the fabrication of polymeric textiles for high-performance clothing (see section 3.2.3).

Afterwards, the differential description of mass transport in porous media, introduced in section 2.5, was used to fit material-dependent Mualem-van Genuchten parameters by means of a finite element model (see section 3.3.1). This approach allows to evaluate the imbibition performance of 2- and 3-dimensional geometries and to compare the micro-structural properties of the proposed woven fabric with those of more complex materials, both structured and unstructured. Consistently, models for evaporative and radiative heat transfer (see sections 3.3.2 and 3.3.3, respectively) were also formalized and validated on the results presented in section 3.1, thus introducing a comprehensive theoretical framework of passive thermoregulation phenomena. Finally, the different phenomena were coupled and employed to evaluate how different environmental conditions affect the thermal performance of PE fabric in the context of passive thermal management applications (see section 3.3.4).

3.1 Experimental investigation

3.1.1 Fabrication and characterization of the fibers and yarn structure

The polyethylene fibers and yarns have been fabricated by standard fiber melt spinning process from the linear low-density polyethylene (LLDPE) and high-density polyethylene (HDPE) granules and pellets (Alfa Aesar). The multi-filament LLDPE yarns have been fabricated by the MiniFibers Inc. (Johnson City, TN) on an industrial-scale melt-spin extruder. The yarns are composed of 247 individual filaments with 2 dpf (denier per filament). The polyethylene fabric (see Fig. 3.1A) has been woven on an industrial loom from a multi-filament yarn composed of 247 fibers each. The woven textile is neither mechanically reinforced by blending it with other fibers nor chemically treated to add a hydrophilic coating to the fiber surfaces. The multi-filament yarns have been woven into a plain-weave textile on an industrial-scale loom at the Shingora Textile Ltd. (Ludhiana, Punjab, India). The fiber thickness and the dense woven pattern (plain - or tabby - weave) of the PE textile shown in were chosen to optimize the efficient moisture transport and fast-drying performance of the material, and thus to promote higher comfort feeling and efficient passive cooling via evaporative process.

The cross-sectional view of the woven PE fabric was obtained with a high-resolution micro-CT scanner (Zeiss Xradia 620 Versa, 0.4x objective), with a resolution of $2 \mu\text{m px}^{-1}$ over 360° rotation and a total scan time of 5 hours. The top-view (Fig. 3.1D) and the cross-sectional images (section S-S) were reconstructed by using the Dragonfly software and are shown in Fig. 3.1D. The morphology and structural characterization of the tested fabrics was performed by a high-resolution scanning electron microscope (HR-SEM, Zeiss, model Merlin) operated at 1 kV with a secondary electron detector. For SEM imaging, the samples were coated with a 50 nm-thick layer of carbon. The average fiber diameter was obtained from over 100 measurements performed on the SEM images with the help of the ImageJ software (see Fig. 3.1E). The average diameter of the PE fibers in the yarn is $(18.5 \pm 6.2) \mu\text{m}$ (see Fig. 3.1B).

The average yarn porosity was measured from multiple cross-sectional images obtained via micro-CT measurements. Each slice contains the cross section of four full yarns (see Fig. 3.1D, section S-S). The central parts of each of the four yarns were extracted from the images, paying attention to exclude the fibers on the border of the yarn. The procedure was repeated for 12 slices, with a pace of $100 \mu\text{m slice}^{-1}$, for a total of 48 different cross sections. The images were processed with the MATLAB Image Processing Toolbox to obtain binary images. In particular, the function “imbinarize” has been used, which processes the grey-scale input assigning to each pixel a black-and-white value given an imposed sensitivity level S_0 , included in the range from 0 to 1, with higher values of S_0 allowing darker pixels to be

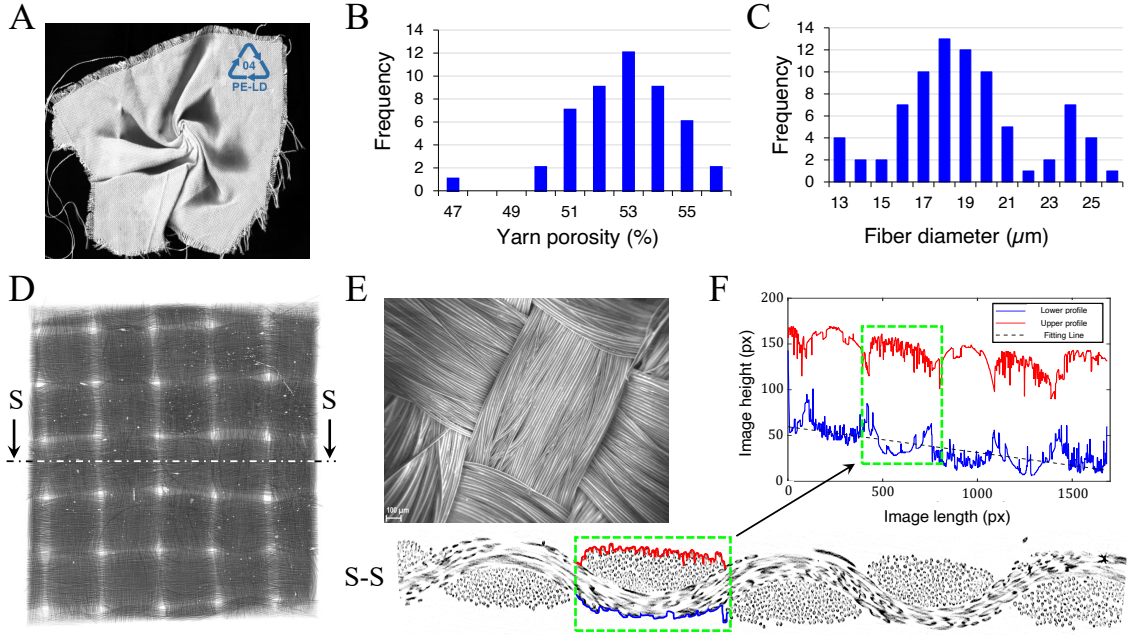


Figure 3.1: **Characterization of the textile micro-structure.** (A) Optical image of the polyethylene textile. Frequency distribution of the (B) yarn porosity and (C) fiber diameters, respectively obtained from the (D) 3-dimensional reconstruction from Micro-CT (evaluated from the digital assembly of 541 sections S-S) and from (E) SEM. (F) The images of 23 different sections were post processed to evaluate the average thickness of the air gap g_a between the horizontal fabrics (considered at rest) and its support. The processed images were used to evaluate the lower (blue line) and upper (red line) boundary of the fabric. g_a was evaluated as twice the average distance of the lower profile from its fitting line (dashed black line).

recognized as white. Then, the yarn porosity ϕ was computed as the ratio between the number of the white pixels and the total number of the pixels in the image. Consequently, ϕ depends on the set sensitivity level S_0 . In the present work, the yarn porosity was computed for each image with a sensitivity level varying in the range from 0.4 to 0.6, with a pace of 10^{-3} . For each value of sensitivity in that range, the yarn porosity was computed and averaged over the results obtained for 48 different images, and the uncertainty of the result was evaluated as the standard deviation of the sample. The results were fitted via the least square method with a first order polynomial in the form: $\phi = a_1 S_0 + a_0$. The reported yarn porosity is evaluated from the fitted curve for $S_0 = 0.5$. As a result, the fibers are arranged in a closely packed yarn with an average porosity of $(53.0 \pm 4.8) \%$ (see Fig. 3.1C). The fiber thickness and the dense woven pattern (plain - or tabby - weave) of the PE textile shown in Fig. 3.1A were chosen to optimize the efficient moisture transport

and fast-drying performance of the material, and thus to promote higher comfort feeling and efficient passive cooling via evaporative process.

The heat transfer between a fabric and its supporting substrate is affected by the average thickness of the air gap between the two surfaces, which hinders their thermal contact. The air gap g_a was estimated by a MATLAB image processing routine applied on the sections obtained via the micro-CT, where the textile sample was horizontally placed (at rest) on a smooth stage within the equipment. g_a was evaluated as the average distance between the first layers of fibers and the supporting plane. Thus, 23 images, each containing the cross section of 5 yarns, had a resolution of $2.732 \cdot 10^{-6}$ m px⁻¹ and were converted to binary images and analysed. The surface roughness observable from the micro-CT images (see Fig. 3.1D, section S-S) was used to evaluate the average distance between the sample surface and a given rigid support plane (see Fig. 3.1F, blue curve). As it can be observed in Fig. 3.1F, the images were not planar, thus the profile was fitted with a first grade polynomial $y'_p = c_1 x_p + c_2$, where x_p is the horizontal position of the textile boundary in px. The average distance of the textile from the plane g_a , expressed in meters, was evaluated as twice the average distance of each point of the profile from the fitting line:

$$g_a = 2.732 \cdot 10^{-6} \cdot \frac{2(y_p - y'_p)}{\sqrt{1 + c_1^2}}, \quad (3.1)$$

where y_p is the measured position of the textile boundary at a given x_p . The procedure was repeated for the upper profile (see Fig. 3.1F, solid red line) and the results averaged. The micro-CT images were also used to evaluate the air gap between the fabric and an horizontal supporting surface resulting in $g_a = (7.1 \pm 3.4) \cdot 10^{-5}$ m. The reported expanded uncertainty was evaluated as the standard deviation of the 46 measurements considered, with a coverage factor $k_u = 2$ [148].

3.1.2 Evaluation of the water-fiber contact angle

The water-fiber contact angle θ was computed by measuring the ratio between the maximum length and the thickness of droplets deposited on a PE fiber and the fiber radius [122, 149] (see Fig. 3.2). The fibers were extracted from randomly picked yarns in woven PE fabric samples. The extremities of each fiber were fixed with tape on two glass slides. Water was sprayed above the setup to allow the deposition of water droplets on the surface of the fiber. A confocal microscope coupled to a Raman spectrometer (Horiba, LabRAM HR Evolution) was used to observe and photograph the droplets deposited on the fibers. The effect of evaporation was reduced by limiting the air speed in the proximity of the microscope objective. Then, the contact angle of each droplet was measured a second time, by taking the second photograph 20 seconds after the first one. Conservatively, the

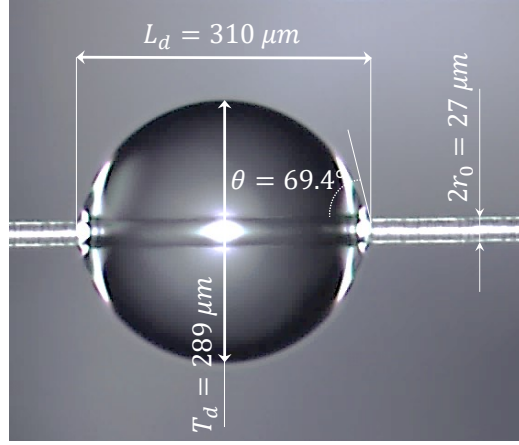


Figure 3.2: **Optical image of a droplet on a circular fiber.** Optical images can be used to evaluate the geometrical parameters of the droplets and used to evaluate the contact angle θ by employing the theoretical model described in section 2.1.1. To maintain pertinence with the case of study, the fiber radius r and the droplet volume V_d used to compute the theoretical equilibrium contact angle between a water droplet and a nylon fiber (see section 3.2.1), were evaluated from the shape parameters shown in this picture.

maximum value between the two measurements was accepted if the variation (due to evaporation) was lower than 5%. A maximum of two droplets per each fiber were photographed before replacing the sample. The contact angle reported was obtained by averaging the measures from more than 16 droplets per each tested material.

The water-fiber contact angle was computed by measuring the height and length of each photographed droplet deposited on a fiber (see Fig. 3.2). Then Eqs. 2.7 to 2.9 were applied to retrieve the theoretical value of θ . Considering as initial guess values $\theta_{g_1} = 1^\circ$ and $\theta_{g_2} = 90^\circ$, a MATLAB code was used to solve iteratively Eqs. 2.7 to 2.9 until the predicted drop length is equal to the value of L_d experimentally evaluated, given a threshold tolerance of 10^{-4} . The resulting value of θ_e was compared with the results obtained through the method proposed by Carrol [122] and Kralchevsky *et al.* [149], finding a discrepancy within 0.1%. The theoretical contact angle of pristine PE is approximately 94° , which would not allow the fiber surface wetting or a capillary suction in the yarn (see section 2.2). However, our data show that the surface of the melt-spun PE fibers is weakly hydrophilic, resulting in a reduced average water-fiber contact angle of $\theta = (71.3 \pm 3.3)^\circ$, sufficient to promote wicking in the woven fabric. The observed fiber surface hydrophilicity is likely a result of the fiber surface oxidation during the PE thermoforming by the melt-spin

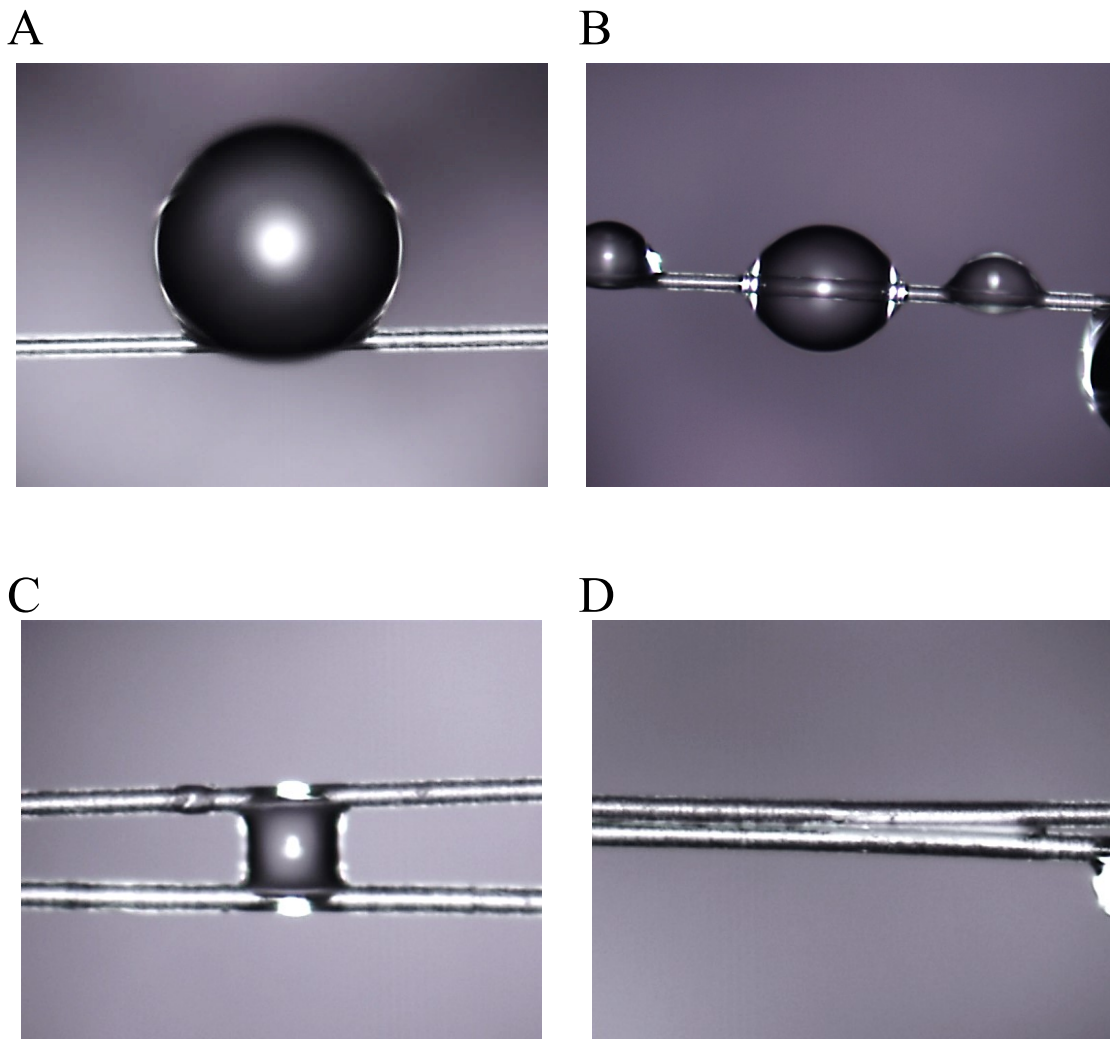


Figure 3.3: **Wettability properties of the PE fibers.** Despite presenting an overall weak hydrophilicity, the same fiber may present zones of both strong hydrophobicity (A) and good hydrophilicity (B-C), demonstrating uneven surface properties. (D) If the separation of two hydrophilic fibers is small enough, the droplet would spread over their surface. By increasing the number of fibers, the maximum distance achievable while still observing spreading decreases (see section 2.2.3).

fabrication process in air, and is in line with prior observations of the water contact angles on ultra-high molecular weight polyethylene (UHMWPE) fibers [150]. Polymer thermoforming is known to not only oxidize the surface of the material but also to form initiation sites for future oxidation in the presence of oxygen even

at ambient temperatures [151]. Accordingly, the PE fiber surface oxidation can be further increased in magnitude and duration by additional fiber treatment, such as oxygen-plasma or UV-ozone, during or after the fabrication [152]. Furthermore, in section 3.2.1 is shown that the water-fiber contact angle is not related to the fiber shape but is uniquely determined by the balance of the surface free energy at the three-phases contact line. Thus, the observed θ and the hydrophilicity of the PE fabric are due to a fabrication-process-induced increase of the surface free energy, by approximately 25% with respect to pure PE, which remains stable for 3-4 testing cycles (see section 3.2.1 and Fig. 3.4).

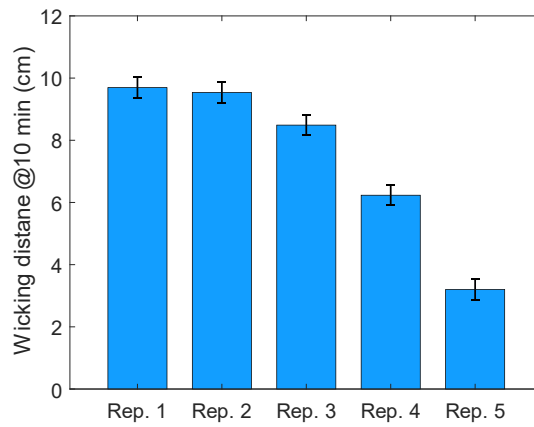


Figure 3.4: **Durability of the hydrophilicity of the PE fabric.** Vertical wicking (see section 3.1.4) tests are repeated five times on the same sample to evaluate the durability of the surface functionalization provided by the fabrication process. The progressive decrease of the height reached by the water front can be ascribed to the progressive reduction of the fibers surface tension when put in contact with water. The performances remain stable for 3-4 cycles before degrading.

3.1.3 Oxygen-plasma treatment and infrared spectroscopy

The homogeneity of the PE fiber surface and its hydrophilicity (see Fig. 3.3) can be improved by functionalizing their surface. Thus, as an example, the water-fiber contact angle on our PE fibers was measured after treating the fibers with oxygen plasma for 1, 3 and 10 minutes. The woven PE fabric samples were treated with a plasma cleaner from Harrick Plasma (model PDC-32G) with a maximum Radio Frequency (RF) power of 18W, in an oxygen environment and three different durations of treatment, namely 1, 3 and 10 minutes. The chamber of the plasma cleaner was initially purged two times with oxygen. After the purge, the woven

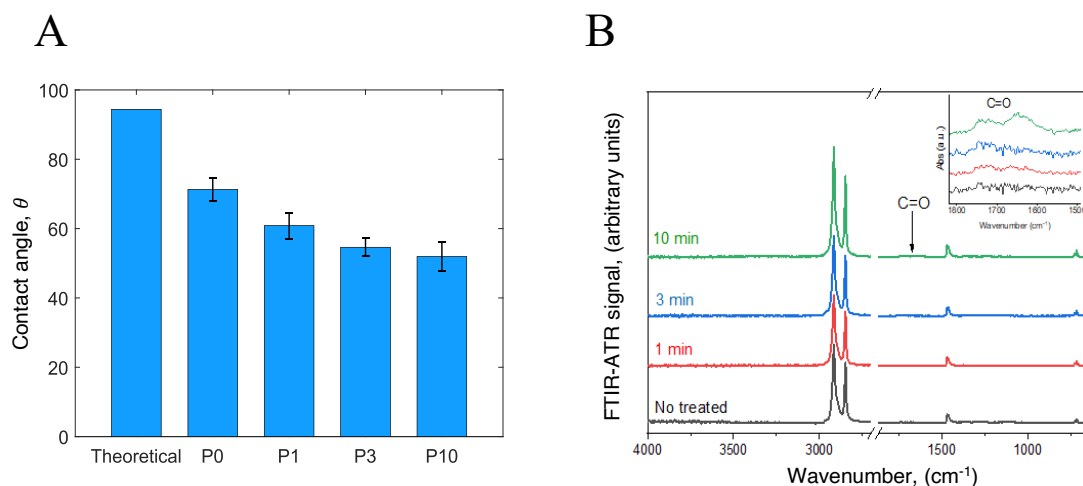


Figure 3.5: **Surface properties of the PE fibers.** (A) The experimentally measured contact angle between water and plasma-treated PE fibers compared to a reference value for a pristine material, obtained from the theoretical model reported in 3.2.1. Gradual increase of the PE fiber hydrophilicity via low-power plasma treatment can be achieved (P0-P10 labels correspond to 0, 1, 3 and 10 minutes of exposure to plasma treatment, respectively). (B) Oxidation of the fiber surface is verified by the attenuated total reflection (ATR) FTIR spectroscopy, showing a minor modification of the functional groups on the surface. The inset highlights the wavelength band between 1500 cm^{-1} and 1800 cm^{-1} , corresponding to the C=O stretching bond, where the treated fibers show an enhanced absorption, proving the effectiveness of the treatment.

PE sample was placed inside the reaction chamber under an oxygen flow suitable to set the pressure inside the chamber in the range of 800 – 1000 mTorr, which was around 0.85 SCFH. Afterward, the RF radiation was turned on at the maximum power during each treatment time (i.e., 1, 3 or 10 minutes). The 10-minute treatment was done in two steps, 5 minutes each, to avoid the overheating of the instrument. After the time has elapsed, the RF was turned off, the oxygen flow was closed, and the chamber was vented with Nitrogen. The results are plotted in Fig. 3.5A for three different exposure times, 1 minute (P1), 3 minutes (P3) and 10 minutes (P10). The resulting contact angles are $(60.8 \pm 3.8)^\circ$, $(54.6 \pm 2.6)^\circ$ and $(51.9 \pm 4.3)^\circ$, respectively corresponding to a reduction of θ by 14%, 23% and 27%. The corresponding data for the pristine PE films and the untreated as-spun woven PE yarns (P0) are also shown for comparison. The results show that a short treatment with a low-power source allows obtaining homogenous surface hydrophilicity, while longer exposure times do not yield further significantly-significant decrease of the contact angle, in agreement with prior studies [153, 154].

Finally, to eliminate the possibility of PE contamination by another material that would reduce the fiber surface energy, we investigated the purity of the chemical composition of the PE fibers by the Fourier Transform Infrared Spectroscopy measurements, aided by the Attenuated Total Reflectance technique (FTIR-ATR). The surface chemistry of fibers comprising the woven PE fabrics was probed via the Fourier Transform Infrared (FTIR) spectroscopy, using the Attenuated Total Reflectance (ATR) mode. For this, a Nicolet 6700 spectrometer equipped with a Nicolet Continuum Microscope with an ATR objective with Germanium crystal was used. After visually selecting the desired area for analysis, the Germanium ATR crystal was moved into place and the sample stage was raised so that the contact was made with the fabric surface. The contact pressure was controlled by a pressure monitoring device to ensure reproducibility of the results. ATR-FTIR spectra were collected in the range $4000\text{-}650\text{ cm}^{-1}$ at resolution of 4 cm^{-1} and were averaged over 32 scans. On the other hand, the FTIR-ATR spectra of the plasma-treated fibers accordingly show a slight increase in the infrared absorptance in the frequency range $1600\text{ cm}^{-1}\text{-}1700\text{ cm}^{-1}$, corresponding to the spectral signature of the C=O stretching bond, and indicating the presence of the oxygen functional groups on the fiber surface (see section 3.5).

3.1.4 Wicking performance

The wicking performance of the woven textile were investigated by horizontal and vertical wicking tests. The analysed samples were approximately 20 cm high and 2.5 cm wide. The bottom end of the fabric samples were dipped approximately 2 mm deep into a box filled with distilled water. An infrared camera (FLIR ETS230) was used to measure the time-dependent position of the water front H_t for 45 seconds, in case of horizontal imbibition, and for 10 minutes, in case of vertical tests. The experiments were performed at controlled ambient conditions. The obtained images were post-processed via the MATLAB Image Processing toolbox. A schematic of the characterisation procedure is represented in Fig. 3.6A-C. The setup was also used to measure the maximum height reached in a vertical wicking test H_m , which tends to a plateau value as capillary pressure is balanced by the pressure exerted by the fluid column, namely $H_m = H_t|_{t \rightarrow \infty}$. An extensive description of the experimental procedure employed to measure the vertical wicking performance and h_m is reported in Ref. [87].

To assess the horizontal wicking performance, the sample was placed on a polytetrafluoroethylene (PTFE) surface and dipped approximately 1 mm deep into the distilled water reservoir. The PTFE surface was chosen for its hydrophobicity, thus avoiding to interfere with the dynamic imbibition process. The absolute permeability K of the plain woven PE was evaluated from the time-dependent position of the water front H_t obtained from the horizontal wicking test. As the effect of

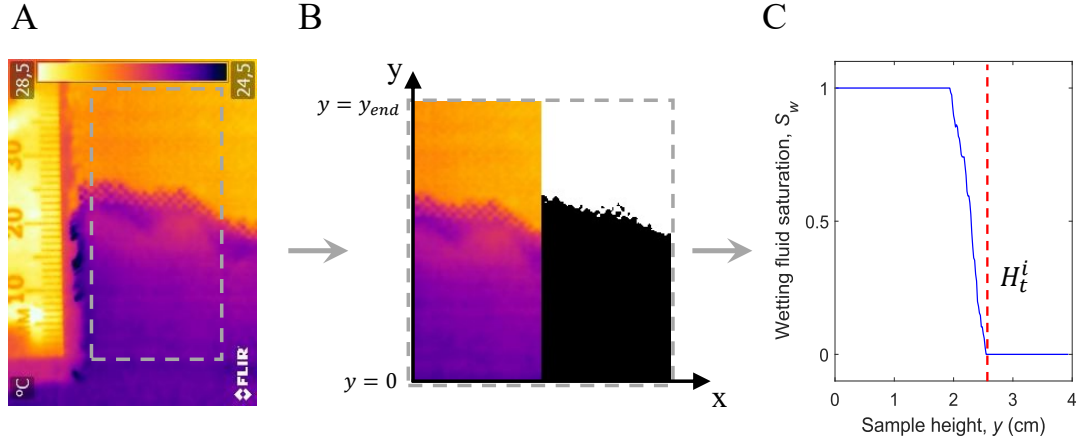


Figure 3.6: **Experimental investigation of the wicking performance.** (A) A frame extracted from the video recorded with the IR camera during the vertical wicking of the PE fabric by water. The aluminum ruler was used to estimate the conversion scale from px to mm. The difference between the optical properties of the wet (purple) and dry (orange) zones of the textile allows their simple distinction. (B) The central part of the textile sample was converted to binary black/white image and used to estimate the position and thickness of the water front. The homogeneity of the front allows to reduce the complexity of the system from 2-D to 1-D. (C) The saturation was averaged along the width of the sample to obtain an equivalent 1-dimensional saturation curve along the y axis. The height of the water front during the i -th measurement H_t^i was evaluated as the first point with average saturation S_w lower than 5%.

gravity can be neglected, H_t can be computed as [131]:

$$H_t = \sqrt{\frac{2KP_c}{\phi\mu_w}t}, \quad (3.2)$$

where P_c is the capillary pressure, ϕ the fabric porosity and μ_w is the dynamic viscosity of the wetting fluid. Considering the textile as an isotropic and rigid porous medium (no fabric deformation or swelling was observed during experiments, since textile samples were tested on rigid supports), Eq. 3.2 can be written in the form: $H_t = C_5\sqrt{t}$, where C_5 is a constant which can be evaluated from the experimental observations of H_t by least squares fitting. Thus, the absolute permeability K results to be:

$$K = \frac{C_5^2\phi\mu_w}{2P_c}. \quad (3.3)$$

The maximum height H_m reached by the water front in the vertical imbibition test is directly related to the capillary pressure P_c , which is the macro-scale counterpart of the micro-scale structure, namely the arrangement of the fibers in the

yarn [123, 124]. At the equilibrium, P_c balances the height of the water column wicked within the porous medium, thus the capillary pressure can be evaluated as $P_c = \rho_w |\mathbf{g}| H_m$, being ρ_w the density of the wetting fluid and \mathbf{g} the gravitational acceleration. Averaging the results of three repetitions, the maximum height was evaluated as $H_m = (13.8 \pm 0.8)$ cm.

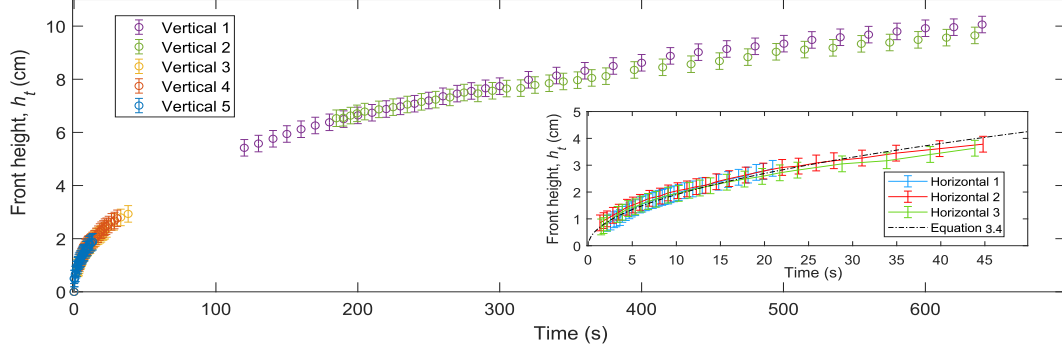


Figure 3.7: Results of the vertical (main plot) and horizontal (inset) wicking tests. The data obtained from the horizontal test, the porosity ϕ and the capillary pressure P_c are used to retrieve the permeability through Eq. 3.4.

Fig. 3.7 reports the results of the vertical (main figure) and horizontal (inset) wicking experiments. The time dependent position of the water front H_t can be described under the sharp front approximation [131] (see Fig. 3.6A-C), thus Eq. 3.2 can be used to fit the data (inset of Fig. 3.7, black dashed line). The data obtained from the horizontal setup were used to evaluate the absolute permeability of the textile K to water from Eq. 3.3, which was evaluated as $K = (7.1 \pm 1.8) \cdot 10^{-12} \text{ m}^2$. The obtained permeability was coherent with the theoretical values of K evaluated by applying Eqs. 2.60 – 2.61, which resulted in $K_s = (4.6 \pm 3.6) \cdot 10^{-12} \text{ m}^2$ and $K_h = (3.5 \pm 2.8) \cdot 10^{-12} \text{ m}^2$ for ideal square and hexagonal arrangements, respectively. Note that the expanded uncertainties reported were evaluated considering the experimental uncertainties of the fibers radius and porosity.

Since the measured value of H_m might be affected by the evaporation of water, the evaporation rate during the vertical wicking tests was measured to assess its effect on H_m . A high-precision balance (ML204, Mettler Toledo) was used to measure the mass of the textile sample, which increased with time as the water front advanced; H_m was evaluated when the mass of the sample reached the steady state. At this stage, the volume of water evaporating from the sample surface is constantly refilled by the capillary action. As the dipped end of the sample was removed from the water basin, the weight measured by the balance started to decrease linearly with slope \bar{M}_{ev} (measured in kg s^{-1}) due to evaporation. Thus,

the specific experimental evaporation rate \bar{m}_{ev}^{exp} (measured in $\text{kg m}^{-2} \text{s}^{-1}$) could be evaluated as:

$$\bar{m}_{ev}^{exp} = \frac{1}{N} \sum_i^N \frac{\bar{M}_{ev,i}}{2h_{m,i} \cdot w_i}, \quad (3.4)$$

where w_i is the width of the i -th sample and $N = 3$ is the number of tests averaged, which resulted in an average specific evaporation rate of $\bar{m}_{ev}^{exp} = (3.31 \pm 0.11) \text{ kg m}^{-2} \text{ s}^{-1}$. Note that the lateral thickness of the samples, approximately 1% with respect to the frontal surface, was assumed having a negligible effect on the evaporation losses. \bar{m}_{ev}^{exp} was used to model the theoretical effect of evaporation on the wicking performances of the textile. Then, the capillary model presented in section 2.2 was used to evaluate the capillary pressure P_c and absolute permeability K for an ideal yarn with the same micro-scale parameters as the textile used (namely, number of fibers per yarn, fibers diameter and yarn porosity). The parameters obtained were plugged into the dynamic wicking model discussed in section 2.4.5 which, with respect to Eq. 3.2, includes the effects of evaporation rate and gravity. The model was used to estimate the possible discrepancy between the height reached by the water front whether an evaporation rate of $\bar{m}_{ev}^{exp} = (3.31 \pm 0.11) \text{ kg m}^{-2} \text{ s}^{-1}$ was considered or neglected. The two configurations can be compared considering the instant t when the height of the water front of the evaporating configuration is equal to H_m , namely $H_t^{ev} = H_m = 13.8 \text{ cm}$. At the same instant, the height of the water front of the configuration neglecting evaporation is $H_t^{no-ev} = 14.3 \text{ cm}$. As this discrepancy is within the uncertainty of the measured value of H_m , the effect of water evaporation was safely neglected.

The water wicking capability of the woven PE fabric was compared with those of several types of conventional fabrics according to the AATCC 1977 standard, by partially submerging fabric samples into a water bath and measuring the height of the wet area forming in each sample 10 minutes after its exposure to water. A common reservation to the use of polyethylene for wearable textiles stems from the inherent PE hydrophobicity, which is expected to prevent perspiration wicking. The results reported in Fig. 3.8E, demonstrated that this problem can be overcome by the proper textile engineering on the nano-, micro- and macro-scales: the comparison revealed that the water wicking properties of the woven PE fabrics exceed those of natural (cotton and linen) and synthetic (polyester) commercial woven textiles with the same plain-weave pattern (see Fig. 3.8A-D). This result seems counter-intuitive because polyethylene is known to be inherently hydrophobic, and PE films (including conventional low-density PE films and non-woven Tyvek[®] PE material used in the experiment) are often used as waterproof covers and tarps. As expected, the Tyvek[®] sample did not exhibit any vertical water wicking in the AATCC 1977 test. The observed moisture wicking performance of the woven PE fabric is a result of a combination of the surface properties of individual fibers, the average fiber diameter, and the yarn composition, as extensively discussed in sections 3.1.2 and 3.1.3.

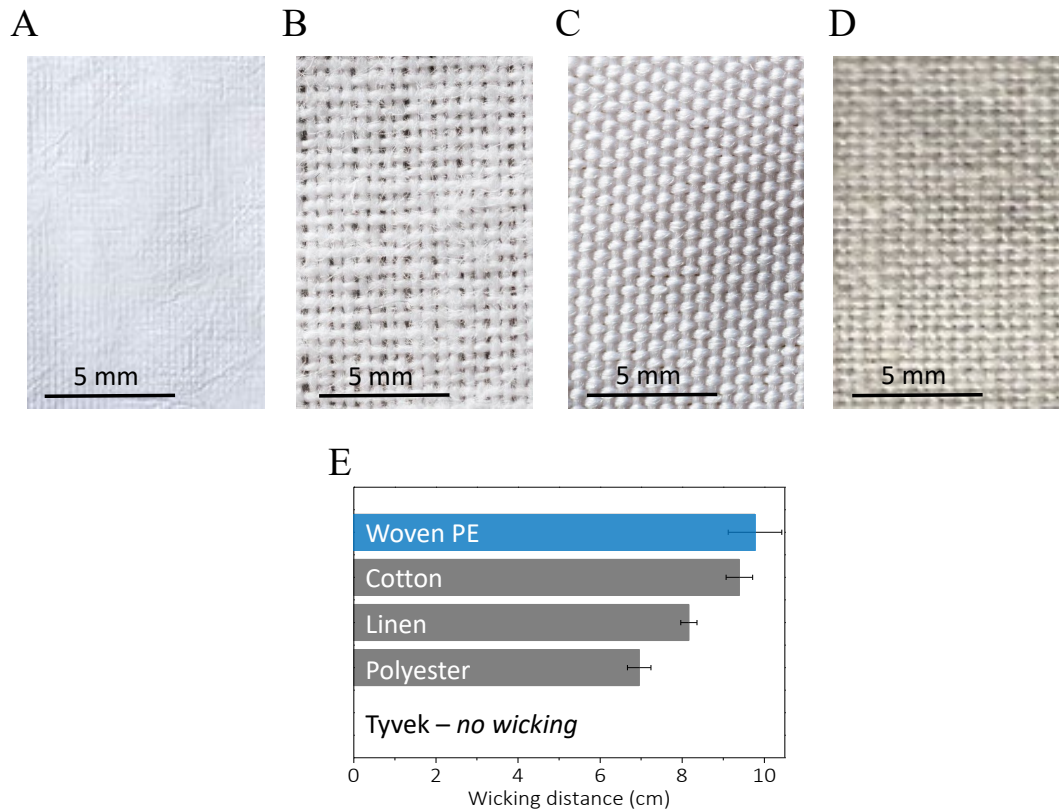


Figure 3.8: **Comparison of the wetting properties of the PE fabric with commercial textiles (A-D)** High-resolution photographs of the commercial textiles chosen as references in the vertical wicking test: (A) non-woven Tyvek[®] PE, (B) woven cotton, (C) woven polyester, and (D) woven linen textiles. (E) Vertical wicking distances in the woven PE fabric (blue bar) and in commercial woven textiles (gray bars) ten minutes after their contact with water. The corresponding data taken for the commercial non-woven PE material Tyvek[®] revealed no wicking action.

3.1.5 Evaporation performance

The drying properties of the fabrics were measured via the ISO 17617 standard (method B) with modifications. The setup and experimental protocol used to investigate the effect of evaporative cooling on the textile temperature is schematised in Fig. 3.9A-B. The circular fabric test specimens (50 ± 2) mm in diameter were kept at the room temperature and relative humidity $RH = (40 \pm 5)\%$, measured with a hygrometer (RH820, OMEGA Engineering), for one day. The ambient temperature was monitored with a thermistor (model 4033, OMEGA Engineering) and maintained at (23.6 ± 0.3) °C. Each sample was laid in a Petri dish placed on a

precision balance (Mettler Toledo, NewClassic ML), weighed and removed. Then, (0.25 ± 0.02) mL of distilled water was applied using a micropipette to the center of the base of a Petri dish and covered by the test fabric specimen. The whole setup was exposed to the environment, whose temperature and humidity are measured during the experiment. The weight loss caused by the water evaporation was measured for 2 minutes. With these data, the drying time and drying rate (% per minute) were calculated using the least squares fitting method.

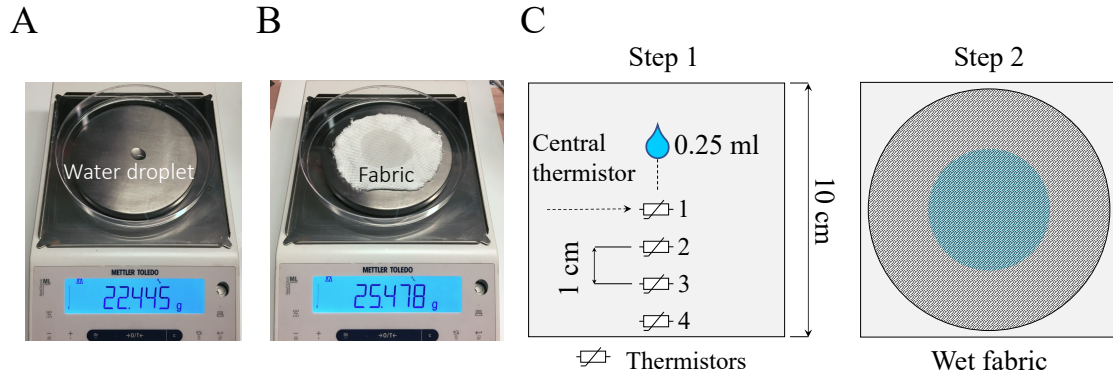


Figure 3.9: **Experimental setups and procedure for the evaluation of water evaporation performance.** (A-B) Photographs of the experimental setup used to measure the drying rate of textiles according to the ISO 17617 standard with modifications. (C) Schematic of the experimental setup for assessing the evaporation of wetting fluid from the textile. *Step 1*: four thermistors were used to evaluate the temperature distribution during the test. A (0.25 ± 0.2) mL droplet was poured with a micro-syringe on the central thermistor. *Step 2*: the dry fabric sample was placed on the setup, the water droplet was absorbed and spread within the textile, and evaporation started. The effect of evaporative cooling on the substrate temperature, assumed to be approximately equal to the textile temperature, was assessed by four thermistors.

To evaluate the effect of the evaporation on the spatial temperature distribution, the evaporation tests were repeated by substituting the Petri dish with a polystyrene plate (2 cm thick, 10 cm \times 10 cm wide). A thermistor (model 4033, OMEGA Engineering) was placed at the center of the specimen surface. Three other thermistors were positioned in radial direction from the central one with an equal spacing of 1 cm (Fig. 3.9C) and covered with a water-resistant tape, to prevent the direct contact between the distilled water and the sensing elements. The distilled water basin was kept on a heated magnetic stirrer to maintain the temperature difference between the reservoir, measured with a properly insulated thermistor, and the average temperature of the plate surface within 0.2 °C. The micropipette was kept immersed in the reservoir to achieve thermal equilibrium

with water. All the data from the thermistors were acquired with a digital data logger (OM-CP-OCTPRO, OMEGA Engineering) using a sampling frequency of 1 sample s^{-1} .

While the woven PE fabric is wicking moisture efficiently, water does not penetrate inside the PE fibers (see [Supplementary Video 1](#)), allowing it to evaporate efficiently from the fiber surface. In contrast, it is known that performance of natural fibers such as cotton and linen is hindered by the water absorbed and subsequently trapped within the fiber volume, which typically reduces the fabric drying rate [155]. The fist evaporation test described allowed to evaluate the performance of different fabrics under a testing condition similar to perspiration wicking and evaporation from the fabric-covered skin surface. In this situation, moisture transport both across and along the fabric contributes to the droplet spread and evaporation. Note that due to the structure of the woven fabric (see Fig. 3.3C-D), efficient moisture wicking in the direction along the yarn not only helps to spread the droplet laterally but also promotes vertical moisture transport across the fabric to its top surface.

Comparison of the data for the vertical test wicking distance (see Fig. 3.8E) and the horizontal test drying rate (see Fig. 3.10A-B) show that while woven PE fabrics outperform other tested textiles on both measures, the materials that exhibit good wicking performance may underperform significantly in the combined wicking-drying test. This situation is observed for textiles made of natural fibers such as cotton and linen due to their moisture-trapping properties [155]. In contrast, the very slow drying rate measured for the non-woven Tyvek[®] PE film is predominantly influenced by the material hydrophobicity, which inhibits water wicking, traps water under the textile, and ultimately slows down the evaporation process. This combination of the observed fast wicking and the subsequent fast evaporation exhibited by the woven PE fabric is generally advantageous for applications in wearables and bedding, promoting both personal comfort feeling and the evaporative cooling functionality. It also offers an opportunity to reduce both the temperature and the duration of the tumble-drying cycle, resulting in energy savings and lowered environmental impact. Fabrics that promote efficient moisture transport and evaporation offer a passive way of cooling the human body (or any surface they cover) via the process of evaporative cooling.

To measure and compare the evaporative cooling performance of different fabrics, it is convenient to analyze the temperature distribution underneath different types of drying fabrics over time: Fig. 3.10C-D report the temperature distribution of the woven PE and cotton, respectively. The radial temperature distribution on the simulated skin was evaluated by recording the input from all the four thermistors, exploiting the axial symmetry of the water front propagation. Efficient moisture transport along the woven PE textile followed by the efficient evaporation process yielded fast droplet spreading, maximizing the evaporation surface and

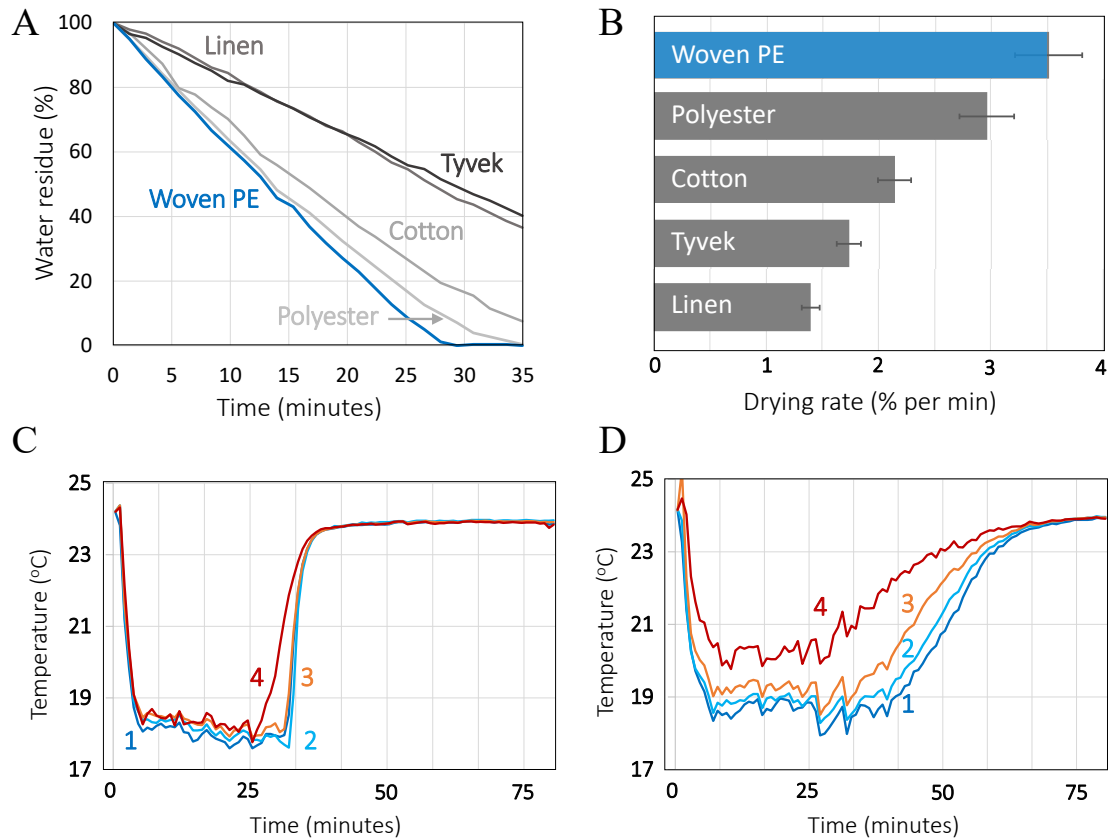


Figure 3.10: **Experimental water evaporation performance.** (A-B) Drying rate of the woven PE fabric and conventional textiles. The drying rate of the commercial non-woven PE material Tyvek[®] is also shown for comparison. (C-D) Temperature measurements underneath woven PE (C) and cotton (D) fabrics covering a drop of water deposited on top of thermistor 1. The numbers reported refer to the different thermistors placed beneath the sample surface (see Fig. 3.9C).

providing a uniform temperature distribution on the skin under the wet area. As a result, the drying rate of the sessile droplet on the simulated skin covered by the woven PE fabric has been measured to be 3.2 times higher than on a bare skin surface (namely, the setup was not covered by any fabric). As shown in Fig. 3.10C, all the four thermistors registered sharp initial temperature drop, followed by even sharper reverse transition as the temperature returned to its initial value upon complete evaporation of water. The steep slope of the initial temperature drop is the result of the fast water front propagation and simultaneous fast evaporation, while the steep slope of the temperature recovery process is due to the PE hydrophobicity, which prevents water capture inside the PE fiber volume and thus thermal inertia. In stark contrast, cotton (see Fig. 3.10D) and linen exhibited slower initial temperature drops and much longer temperature recovery times, with

the areas further away from the fabrics center cooling down less than the center. The observed performance is once again governed by the water absorption inside the volume of natural fibers, which hinders initial propagation of the water front, reduces the evaporation surface, and slows down the evaporation process. This property increases the drying time of natural textiles, reduces comfort, and leads to longer times and higher temperatures of tumble-dry processes, thus increasing energy consumption. The polyester fabric exhibited evaporative cooling performance intermediate between those of the woven PE and natural textiles, while the effectiveness of evaporative cooling of Tyvek[®] and bare skin surfaces was severely hindered by the lack of moisture wicking and spreading via capillary transport, leading to a reduced evaporation rate and uneven temperature distribution on the sample surface.

3.1.6 Optical properties and radiative heat transfer

The optical transmittance and reflectance of the fabric and the reflectance of the painted surface of the heater in the ultraviolet (UV), visible (VIS) and near-infrared (NIR) ranges were evaluated via a UV-VIS spectrometer (Agilent Cary 5000) equipped with an integrating sphere. The infrared (IR) transmittance and reflectance of the fabric were evaluated with an infrared-diffuse-gold-coated integrating sphere (PIKE technologies) with a FTIR spectrometer (Thermo Nicolet 5700). The optical coefficients were obtained by averaging three measurements, each referenced to a blank test. The characterization results can be seen in Fig. 3.11. In addition, the spectra obtained in the IR and UV-VIS-NIR bands are compared with the blackbody radiation at 37 °C (typical human body temperature) and the AM0 spectrum, respectively. These data were used in section 3.3.3 to evaluate spectrum-averaged coefficients, useful to describe both theoretically and numerically the thermal performance of textiles.

The effect of the optical properties of the textile on its thermal comfort performance was experimentally investigated both indoor and outdoor. A schematic of the experimental setup is represented in Fig. 3.12A. Two silicone heaters (SRFRA-4/5-P, OMEGA Engineering) were used to provide a constant heat flux to the fabric during the experiments. Two thermistors (model 4033, OMEGA Engineering) were applied with a high thermal conductivity paste at the center and at 1 cm from the boundary of the top surface of each heater. A digital data logger (OM-CP-OCTPRO, OMEGA Engineering) was used to measure the temperature of the thermistors with a sampling frequency of 1 Hz. The lower surface of the heater was attached to two identical polystyrene boxes (8 cm thickness, 20 cm x 13 cm width) to minimise the heat losses downwards. The heaters were connected in parallel to a power supplier, which provided a current of 0.143 A and a voltage of 15.7 V to the circuit. Thus, each heater was constantly supplied with $P_{in} = 1.12$ W

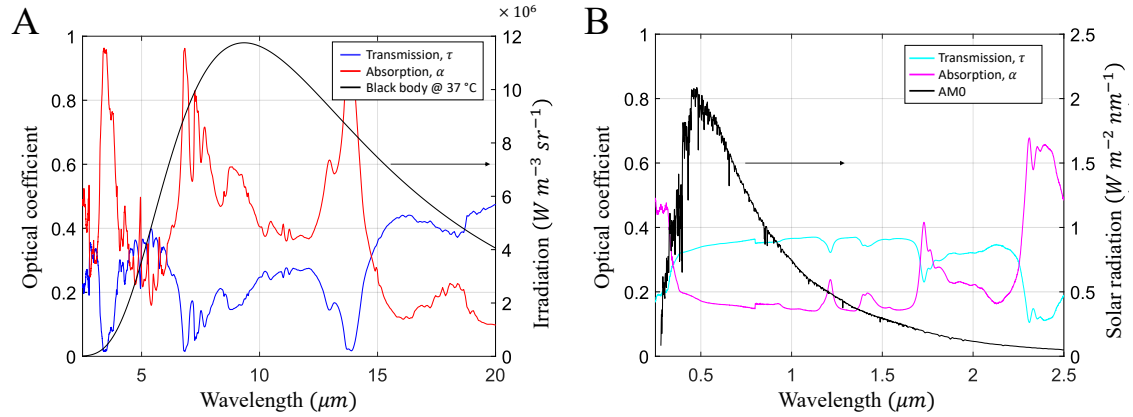


Figure 3.11: **Optical properties of the proposed woven PE fabric** The transmittance, absorption and reflection properties of the proposed woven PE fabric were experimentally evaluated in the infrared (A) and visible (B) portion of the spectrum.

(namely, 140 W m^{-2}) for the duration of the experimental campaign. During outdoor experiments, a pyranometer (LP PYRA 08, Delta Ohm) was used to measure the incoming solar radiation. At the beginning of indoor tests, the power supplied was switched on and the two heaters were left uncovered until the steady state was reached (*i.e.* when the temperature readings were statistically comparable). Afterwards, a dry circular textile sample (with radius 5 cm) was placed above one silicone heater. The steady state was considered reached when the standard deviation of at least 1000 temperature acquisitions was lower than 0.1°C . Then, the equilibrium temperature was measured for approximately 4000 s and the average value and its standard deviation evaluated.

The experimental setup described in Fig. 3.12A was used to evaluate the radiative heat transfer properties of the textile by measuring the temperature difference between the covered and uncovered setups, both indoor and outdoor. Note that the two setups used are identical. The results of indoor test are shown in Fig. 3.12B. Before placing the fabric on one of the setups (dashed black line), the temperature difference between the two central thermistors (blue and green data) is negligible, as also the temperature difference between two boundary thermistors (red and magenta data). Then, after a transient of approximately 25 minutes, the steady state was reached, and the temperature difference ΔT between the covered and the uncovered setup was $\Delta T = (3.5 \pm 0.5)^\circ\text{C}$ or $\Delta T = (2.9 \pm 0.5)^\circ\text{C}$, considering respectively the center or the boundary. However, the surface temperature of the heaters was not homogeneous: the measured temperature difference between the two thermistors placed at the center and on the boundary of the heaters were $\Delta T_{cov} = (2.3 \pm 0.5)^\circ\text{C}$ and $\Delta T_{unc} = (2.9 \pm 0.5)^\circ\text{C}$, respectively for the covered and uncovered setups. The discrepancy between the two values is coherent with their

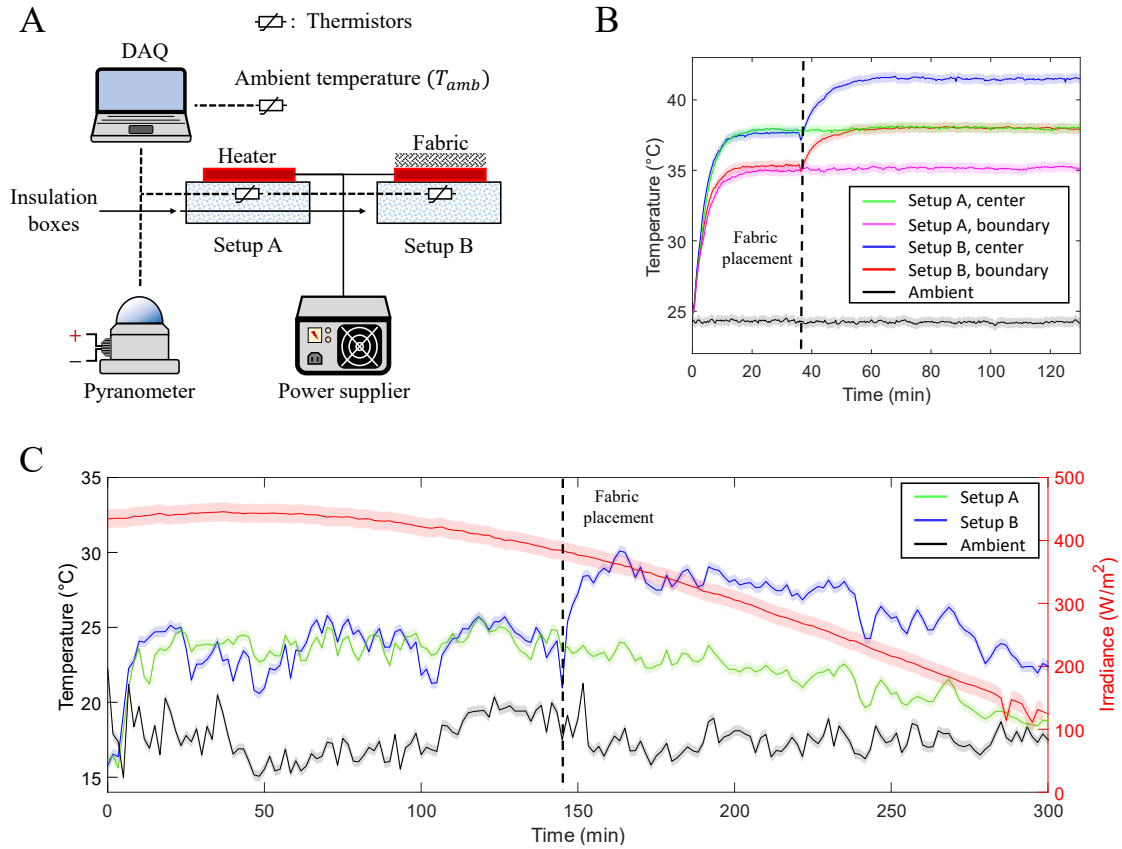


Figure 3.12: **Experimental investigation of the radiative heat transfer performance.** (A) Schematic of the experimental setup to assess the thermal performance of the fabric either indoor or outdoor. Two heaters were connected in parallel to a power supplier. The surface temperature of the two heaters was monitored with two thermistors each, while the solar radiation and the ambient temperature were measured with a pyranometer and a thermistor, respectively. (B) Results of the indoor test. The temperature difference measured by the thermistors at the center (solid blue and green curves) and at the boundary (solid red and magenta curves) of the heaters is due to the non-homogeneous distribution of the input heat. The solid lines represent the average values and their shaded contour their uncertainty, which is the same for both configurations. (C) Results of the outdoor test. The plot reports only the temperatures measured by the thermistor placed at the center of the specimens. The solid lines represent the average values and their shaded contour their uncertainty.

uncertainty and, therefore, statistically comparable. The results of outdoor test are presented in Fig. 3.12C, where only the temperature transients of the central thermistors were reported. The test was performed supplying $P_{in} = 1.12 \text{ W}$, as during the indoor test, while the noise affecting the temperature readings is due

to the wind. First, the two setups were both left uncovered for approximately 150 mins. At this stage, the average temperature difference between the two heaters was negligible. As soon as one of the heaters was covered (approximately at minute 150, solid blue line), the measured temperature increased. The effect of the sun is blatant: as the solar radiation progressively decreased from 450 W m^{-2} to 100 W m^{-2} , so did the temperature difference ΔT , ranging from approximately 6.5°C to approximately 4°C , both higher with respect to the indoor setup. This result highlights the importance of tailoring the UV-VIS-NIR properties to achieve the desired outdoor performance (e.g. heating or cooling).

3.1.7 Setup characterisation and parameters estimation

The experimental results reported in sections 3.1.5 and 3.1.6 were also used to evaluate some characteristic parameters of the experimental setups used, which were successively used to compare the experimental and theoretical thermal performance of the textile. In particular, finite element models were used to evaluate the heat transfer coefficients of the two different polystyrene insulating boxes used ($U_{b,1}$ and $U_{b,2}$ in sections 3.1.5 and 3.1.6, respectively), the non-homogeneous heating characteristic of the silicone heaters described in section 3.1.6, the optical absorption coefficient $\bar{\alpha}_h$ of the white paint covering the heaters, and the averaged outdoor convection coefficients during the in-field tests reported in section 3.1.6.

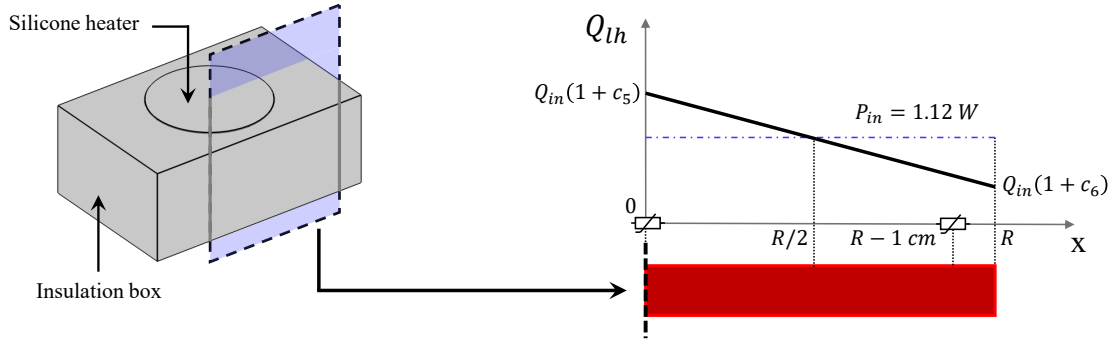


Figure 3.13: **Schematic of the 2-dimensional simulation setup used to evaluate the thermal properties of the heaters.** To account for the non-homogeneity of the experimental heat flux supplied P_{in} , the simulated input heat flux Q_{ih} was modelled as a linear function P_{in} (dashed blue line), symmetric with respect to $R/2$ and higher at the center of the heater, considering $c_5 = -c_6$, as expressed in Eq. 3.6. The schematics also reports the positions of the two thermistors placed on the heaters surfaces.

Evaluation of the heat transfer coefficients of the insulating boxes

The polystyrene insulation used to assess the evaporative cooling potential of the proposed woven PE fabric (see section 3.1.5) was represented as a 2 cm thick parallelepiped with a 10 cm \times 10 cm upper surface. The thermal conductivity of the polystyrene was taken as $k = 0.0325 \text{ W m}^{-1} \text{ K}^{-1}$. The heat transfer coefficient of the insulating box U_b was evaluated by imposing an inward heat flux (P_{in} , expressed in W) through the circular surface occupied by the textile, supposed isothermal, and measuring the total flux dissipated towards the environment as:

$$U_b = \frac{P_{in}}{A_b (T - T_{amb})}, \quad (3.5)$$

where T_{amb} is the ambient temperature, T is the temperature of the isothermal surface providing the inward heat flux, A_b is the total surface of the box exchanging heat with the environment. An adiabatic condition was applied on the lower surface of the domain, which was placed on a plastic support, while the remaining surfaces were assumed to dissipate heat by natural convection. The resulting heat transfer coefficient of the considered setup was evaluated numerically (by finite elements model) as $U_{b,1} = 0.987 \text{ W m}^{-2} \text{ K}^{-1}$, which was used to estimate the out-of-plane heat flux as $\hat{\mathbf{n}} \cdot \mathbf{q} = q_b = U_{b,1}(T - T_{amb})$ in section 3.3.2.

Similarly, the insulation properties of the 3-dimensional polystyrene box (8 cm thick, 20 cm \times 13 cm upper surface) used in section 3.1.6 to assess the radiative heat transfer properties of the textile were simulated following the same procedure described above. The thermal conductivity of the polystyrene was set to $k = 0.0325 \text{ W m}^{-1} \text{ K}^{-1}$; an adiabatic condition was considered on the bottom boundary; natural convection was imposed on the the lateral and the top surfaces; the circular heater was represented as a isothermal and adiabatic surface. Thus, the heat transfer coefficient was evaluated from Eq. 3.5 by imposing a given heat flux P_{in} (in W) to the circular surface occupied by the heater, and it resulted to be $U_{b,2} = 0.227 \text{ W m}^{-2} \text{ K}^{-1}$, which was used to estimate the out-of-plane heat flux as $\hat{\mathbf{n}} \cdot \mathbf{q} = q_b = U_{b,2}(T - T_{amb})$ in section 3.3.3.

Modelling of the non-homogeneous input heat flux

As it can be observed in Fig. 3.12B, the surface temperature of the heaters was not homogeneous, thus the experimental temperature curves of the uncovered configuration (solid green and magenta lines) were used to calibrate the constants c_5 and c_6 in Eq. 3.6 and also to evaluate the average IR emissivity of the surface $\bar{\alpha}_h$. The measured surface temperature of the uncovered setup was used to evaluate the non-homogeneous heating characteristic proper of the silicone heaters, modelled as a linear function of the heater radius R , and the optical absorption coefficient of the white paint $\bar{\alpha}_h$. A schematic of the simulation setup to evaluate the thermal properties of the silicone heaters is reported in Fig. 3.13. The thermal flux provided

by the heater Q_{lh} (expressed in W m^{-3}) was described as a linear function of the radial coordinate with an equal imbalance percentage at the center c_5 and at the border c_6 of the heater, namely:

$$Q_{lh} = (kx + p)/(d_z \pi R^2),$$

$$\begin{cases} k = P_{in} R^{-1} (-c_5 + c_6) \\ p = c_5 P_{in} \\ c_5 + c_6 = 0 \end{cases} \quad (3.6)$$

where x is the radial coordinate with $x = 0$ at the center of the heater, $R = 5.08$ cm is the radius of the heater and $P_{in} = 1.12$ W is the heat flux experimentally provided to the heater by the power supplier. Convective heat transfer was modelled on the bottom surface of the heater, with $U_{b,2} = 0.227$ $\text{W m}^{-2} \text{K}^{-1}$; the top surface of the setup was supposed to be subject to natural convection. The upper part of the heater was considered as a diffuse surface with constant emissivity $\bar{\alpha}_h$. The simulation iteratively adapted the values of c_5 and $\bar{\alpha}_h$ to minimise the difference between the measured temperature of the surface and the numerical results, which led to $\bar{\alpha}_h = 0.866$ and $c_5 = -c_6 = 0.169$.

Estimation of the outdoor convection coefficient

Due to the presence of variable wind speed, the convection coefficient h was evaluated by an iterative least-squares fitting procedure, which aimed to minimise the difference between temperatures computed in a representative setup (see Fig. 3.13) – modelled by a finite elements model – and the average experimental temperature of the uncovered setup. The simulations were performed considering as target temperature $T_h = 23.9$ °C, relative humidity $RH = 40\%$, ambient temperature $T_{amb} = 17.5$ °C and solar irradiance $I_{rr} = 426$ W m^{-2} , which were obtained averaging the respective experimental values in the first 100 mins of experiment. The resulting equivalent convection coefficient representative of the tested outdoor conditions was evaluated as $h_{out} = 22.2$ $\text{W m}^{-2} \text{K}^{-1}$.

3.2 Analytical prediction of the textile performance

3.2.1 Numerical evaluation of the surface free energy of cylindrical fibers

First, starting from the analysis of the free energy of a symmetric droplet deposited on a fiber, this paragraph presents a theoretical model relating the surface

free energies of the materials considered and the geometrical characteristics of the system to the expected theoretical contact angle. Then, reasoning inversely, starting from the measurements of θ shown in section 3.1.2, the equivalent surface energy of the fibers is evaluated, thus estimating the effect of oxidation occurred during their extrusion process which has, therefore, modified their wettability. In this paragraph, the subscripts l , s and v refer to the three-phases composing the system: the liquid drop, the solid fiber and the vapor-gas mixture surrounding the others, namely air, respectively. On ideal, planar surfaces, the equilibrium condition at the three-phases contact line can be described by the Young's equation [156, 157]:

$$\gamma_{sv} - \Pi_e = \gamma_{sl} + \gamma_{lv} \cos \theta_e \quad (3.7)$$

where γ_{lv} and γ_{sv} are the surface tension of the liquid and of the solid phase immersed in saturated vapour of the liquid, γ_{sl} is the fiber-liquid surface tension and Π_e is the equilibrium pressure of adsorbed vapor of the liquid on the surface, which can usually be neglected for polymers with low surface free energy [156]. The surface tension is composed by two components: $\gamma = \gamma^d + \gamma^p$, where γ^d is the dispersive component (due to the London forces) and γ^p the polar component (due to the hydrogen bonding and dipole-dipole interaction). According to the method proposed by Owens, the surface tension of the solid substrate can be computed from the adhesion energy as [156, 158]:

$$\gamma_{sl} = \gamma_{lv} + \gamma_{sv} - 2 \left(\sqrt{\gamma_{sv}^d \gamma_{lv}^d} + \sqrt{\gamma_{sv}^p \gamma_{lv}^p} \right), \quad (3.8)$$

which, combined with Eq. 3.7, allows to compute the equilibrium contact angle on a planar surface as a function of their surface tensions:

$$\theta_e = \arccos \left(2 \frac{\sqrt{\gamma_{sv}^d \gamma_{lv}^d} + \sqrt{\gamma_{sv}^p \gamma_{lv}^p}}{\gamma_{lv}} - 1 \right). \quad (3.9)$$

Considering pure water in air, with $\gamma_{lv} = 72.8 \text{ mN m}^{-1}$ and $\gamma^p = 51.0 \text{ mN m}^{-1}$ [159], only surfaces with predominantly polar surface tension are strongly hydrophilic. Eq. 3.9 can be used to compute θ_e of a water droplet on an ideal, planar surface. As an example, nylon 6.6, a common material in textile industry, presents [159] $\gamma_{sl}^d = 33.7 \text{ mN m}^{-1}$ and $\gamma_{sl}^p = 7.8 \text{ mN m}^{-1}$, which results in a weak hydrophilicity with $\theta_e = 71.3^\circ$. On the other hand, PE has a similar dispersive component, while lower polar surface tension [159] $\gamma_{sl}^p = 1.1 \text{ mN m}^{-1}$, resulting in a weak hydrophobicity with $\theta_e = 94.4^\circ$.

To evaluate the effect of the fiber shape on its surface energy and the resulting contact angle, we consider a nylon fiber in the following discussion. Since the flat surface of nylon is already hydrophilic, we calculate the expected change in the contact angle caused by the fiber surface deviation from the planar surface. We

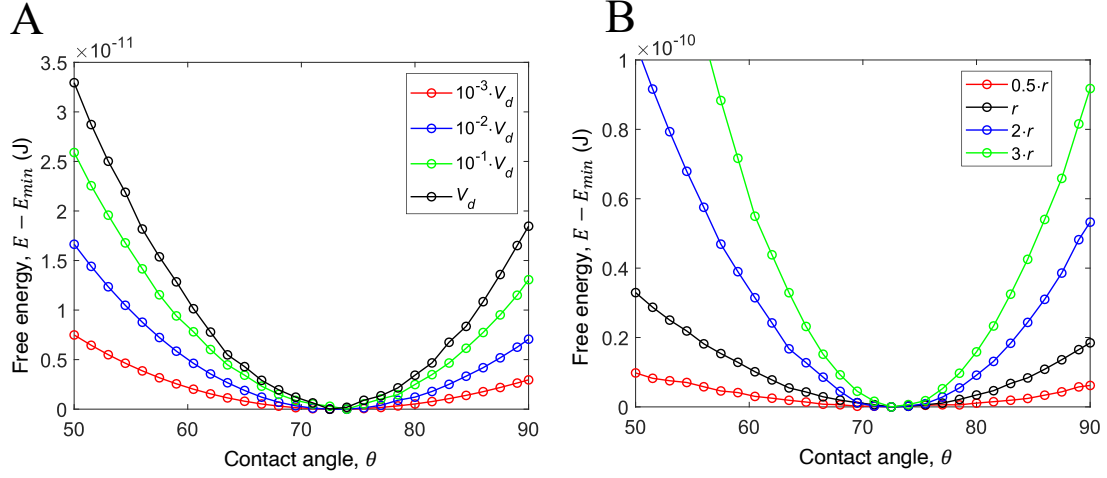


Figure 3.14: **Surface free energy landscape of a droplet on a circular fiber.** (A-B) Free energy of a water droplet on a nylon fiber. The black dashed curves are obtained for $\gamma_{lv} = 72.8 \text{ mN m}^{-1}$, $\gamma_{sv} = 41.4 \text{ mN m}^{-1}$, $r = 13.5 \text{ }\mu\text{m}$ and $V_d = 1.29 \cdot 10^{-11} \text{ m}^3$. The droplet volume (A) and fiber radius (D) on the surface do not affect the value of the equilibrium contact angle, which is only determined by the surface tensions at the contact line, but change the free energy landscape, making it steeper for larger droplets on larger fibers.

consider a liquid drop on a cylindrical fiber, whose free energy E can be evaluated as:

$$E = 2\pi r (L' - L_d) \gamma_{sv} + A_d \gamma_{lv} + 2\pi r L \gamma_{sl}, \quad (3.10)$$

where r and L' are the radius and total length of the fiber, A_d and L_d are the surface area and length of the liquid droplet. The three terms in the right-hand side of Eq. 3.10 account for the contributions of the dry fiber, the shape of the drop and the solid-liquid interface to the total F of the dry fiber, respectively. Eq. 3.10 can be re-arranged to neglect the initial F of the dry fiber, constant for any configuration of the drop [160]:

$$E = A_d \gamma_{lv} + A_{df} (\gamma_{sl} - \gamma_{sv}) \quad (3.11)$$

where $A_{df} = 2\pi r L$ is the cylindrical liquid-solid contact surface. Thus, considering a drop with a fixed volume V_d and surface tension γ_{lv} , its equilibrium contact angle θ_e on a fiber with a given γ_{sl} is determined by the minimization of Eq. 3.11, according to the second principle of thermodynamics.

The influence of the fiber radius r , droplet volume V_d and surface tension on the equilibrium contact angle θ_e was numerically investigated. A MATLAB routine has been implemented to compute E_i for each θ_i in the range between 0° and 90° . For

each θ_i in that range, the routine computes the shape parameters L_i and T_i from Eqs. 2.7 to 2.9, with the constraint of observing the conservation of the droplet volume, namely $V_{d_i} = V_d$, where the droplet volume V_{d_i} can be computed from Eq. 2.11. The volume conservation implies that lower values of θ_i result in flattened drops and higher solid-liquid contact area, while higher values of θ_i lead to sphere-like drops and lower solid-liquid contact area. Once the shape parameters L_i and T_i are determined for a given θ_i , the surface area of the droplet A_{d_i} can be computed from Eq. 2.10 and the solid-liquid contact area as $A_{df_i} = 2\pi r L_i$. These values can be substituted into Eq. 3.11 to compute E_i . As previously described, θ_e is unique and identified as the θ_i minimizing E .

The described procedure requires to select a fiber radius r and a droplet volume V_d , besides the surface tensions of the materials involved, to compute θ_e . To be pertinent with the fibers proposed in this work, we evaluated r and V_d from the image of the water drop shown in Fig. 3.2. Note that any other pair of parameters r and V_d within the validity range of the hypothesis of negligible effect of gravity can be used. Thus, multiples and sub-multiples of r and V_d were used to evaluate their effect on θ_e . Given the shape parameters $r = 13.5 \mu\text{m}$, $L_d = 310 \mu\text{m}$ and $T_d = 289 \mu\text{m}$ measured from the microscope image, its contact angle $\theta_e = 69.4^\circ$ was computed from Eqs. 2.7 to 2.9, while its volume $V_d = 1.29 \cdot 10^{-11} \text{ m}^3$ was evaluated from Eq. 2.11. The capillary length for water [114] $l_c = \sqrt{\gamma_{lv}(\rho g)^{-1}} = 2.7 \text{ mm}$ is larger than L_d and T_d , thus the hypothesis of negligible effect of gravity is valid.

Figs. 3.14C-D explore the effect of the droplet volume and fiber radius, respectively, on the FE of a system composed by a water drop with $\gamma_{lv} = 72.8 \text{ mN m}^{-1}$ on a nylon 6.6 fiber with $\gamma_{sv} = 41.4 \text{ mN m}^{-1}$. To simplify the representation, the curves were shifted downwards by their minimum value. The black lines are obtained for $V_d = 1.29 \cdot 10^{-11} \text{ m}^3$ and $r = 13.5 \mu\text{m}$. It can be observed that the minimum of the FE is localized at $\theta_e = 73.3^\circ$, approximately the same value obtained from Eq. 3.9 for a water drop on an ideal planar surface of nylon. This result is consistent with the hypothesis of Carrol[122] and the results reported by Extrand *et al.* [161]. Furthermore, different values of V_d and r do not modify the equilibrium contact angle θ_e but only affect the free energy landscape, making it steeper for larger droplets and fibers, thus hindering deviations from the equilibrium configuration. On the contrary, on a more hydrophilic fiber, such as glass, characterized by [162] $\gamma_{sv} = 70.5 \text{ mN m}^{-1}$, $\gamma_{sv}^p = 47.5 \text{ mN m}^{-1}$ and an equilibrium contact angle with water of approximately 15° and under the assumption of $\Pi_e = 0$, smaller droplet size results in a steeper free energy landscape, coherently with the results of McHale and co-workers [163].

Thus, the analysis performed proved that the water-fiber equilibrium contact angle is not influenced by the fiber radius r or drop volume V_d but is uniquely determined by the surface tensions of the materials involved. Furthermore, its value is the same as the one evaluated on an ideal planar surface, calculable via Eq. 3.9.

According to the results presented above, pristine PE is weakly hydrophobic, presenting a theoretical equilibrium contact angle with water of $\theta_e = 94.4^\circ$ when cast as either a planar or a cylindrical surface. However, the experimental evaluation of the water-fiber contact angle was $\theta = (71.3 \pm 3.3)^\circ$, lower than the theoretical value, and inhomogeneous along the same fiber (see Fig. 3.3). Furthermore, the chemical characterization of the fibers surface through FTIR-ATR spectroscopy, presented in section 3.1.3, highlighted only the absorption peaks of pure PE, proving the purity of the bulk material used to cast the fibers. Thus, we concluded that the surface of the fibers was weakly functionalized during the fabrication process by a low degree of oxidation and the presence of surface charges [164]. The results presented in Figs. 3.14C-D demonstrated that, given the surface free energy of a liquid drop on a solid substrate immersed in air, the equilibrium contact angle for planar or cylindrical surfaces is only determined by the surface tension of the materials. Thus, Eq. 3.9 can be iteratively solved by increasing the polar component of the surface tension (γ_{sv}^p), which is responsible for the hydrophilic interactions, until the predicted equilibrium contact angle (94.4°) is equal to the experimental one (71.3°). According to this procedure, γ_{sv}^p increases from 1.1 mN m^{-1} to 9.4 mN m^{-1} , for a total surface tension of $\gamma_{sv} = 40.7 \text{ mN m}^{-1}$, approximately 25% larger than the theoretical value of pristine PE and similar to the surface tension of nylon.

However, the functionalization of the PE fibers is not permanent, as demonstrated by repeating multiple times the 10-minutes vertical wicking test described in section 3.2.1 on the same woven PE sample. As it can be observed in Fig. 3.4, the height reached by the water front H_{10} decreases each repetition, proving progressive decrease of the fibers surface tension, in agreement with other observations of charged insulators exposed to water [165]. However, the hydrophilicity of the woven PE can be restored by repeat oxidation in the presence of oxygen even at ambient temperatures [149, 153] e.g., due to exposure to UV light in the solar spectrum. Furthermore, it was also observed experimentally that mechanical friction – a process that naturally occurs in the process of fabrics wearing, washing, and tumble-drying easily restores the PE fabrics hydrophilicity. As a perspective, charged particles might be encapsulated in the PE fibers during the fabrication, increasing the hydrophilicity by their electric field without being washed away by the flowing water.

3.2.2 Theoretical wicking performance

The model described in section 2.2 was used to explore the influence of the parameters on the dynamic wicking of an ideal yarn when $\phi_{cr} < \phi < \phi_m$, under the assumption that the maximum capillary height is larger than the height of the meniscus, approximated as the fiber radius, namely $H_m \gg r$.

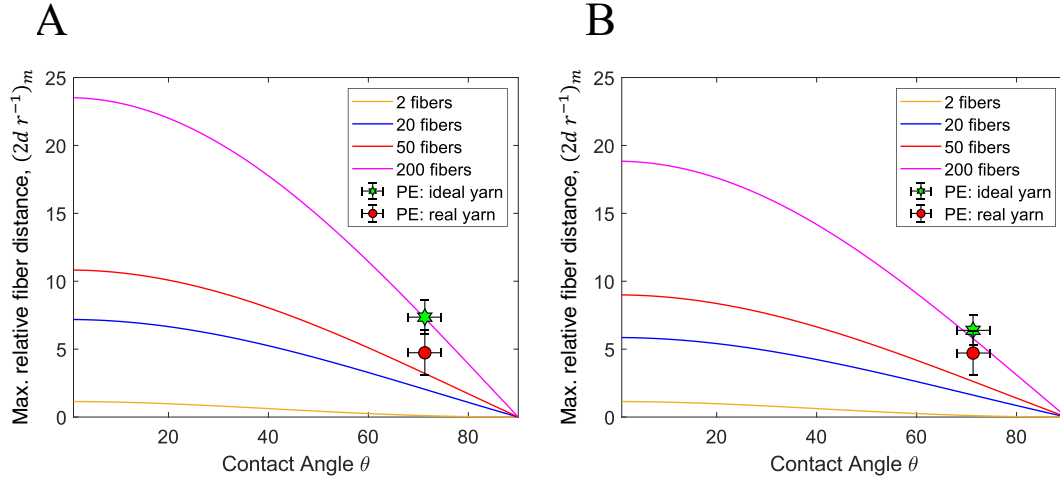


Figure 3.15: **Maximum fiber distance in a finite-size yarn.** The maximum porosity ϕ_m for hexagonal (A) and square (B) fiber arrangement was expressed in terms of the maximum relative fiber distance $(2d/r)_m$, computed with Eq. 2.29. This parameter can be used to retrieve ϕ_m through Eq. 2.16. The lines show the model predictions for ideal yarns with different number of hexagonal- or square-arranged fibers. Intuitively, lower values of θ allow wicking with lower fiber packing density, while increasing the number of fibers yields capillary suction with less hydrophilic fibers. The green star shows the model predictions for the ideal yarn, computed with the growth model proposed, considering $n_f = 247$ and $\theta = 71.3^\circ$. The reported error bars were evaluated considering the effect of the uncertainty of the measured contact angle on the resulting value of $(2d/r)_m$. The red circle shows the maximum relative fiber distance for a real yarn, considering the same θ , while n_{fB} and n_{fD} were obtained from micro-CT scans.

Growth model to assess the maximum porosity

Fig. 3.15 shows the dependence of the maximum relative fiber distance $(2d/r)_m$ on n_f and θ according to the model described in section 2.2.3. The parameter $(2d/r)_m$ is computed from Eq. 2.29 and is used to evaluate ϕ_{max} through Eq. 2.16 for the hexagonal and square fibers arrangement, respectively. The green hexagram shows $(2d/r)_m$ when the proposed growth model is used, considering $n_f = 247$ and $\theta = 71.3^\circ$. This ideal result is compared with the actual yarn structure (red circle), evaluated for the same value of θ , while n_{fB} and n_{fD} were counted from 11 yarn

cross-sections images obtained via micro-CT, where

$$\begin{aligned} \sum_i^{n_{fB}} \delta_i &= 2/3\pi (n_{fB}/2) + 4/3\pi (n_{fB}/2) , \\ \sum_i^{n_{fB}} \delta_i &= 2\pi + \pi/2 (n_{fB} - 4) , \end{aligned} \quad (3.12)$$

hold for the hexagonal and square structures, respectively. The uncertainty on the experimental value of the contact angle was used to compute a maximum and minimum value of ϕ_m for each configuration. Finally, the results were averaged, and the error bars evaluated considering the dispersion of the data and the effect of the uncertainty of the contact angle.

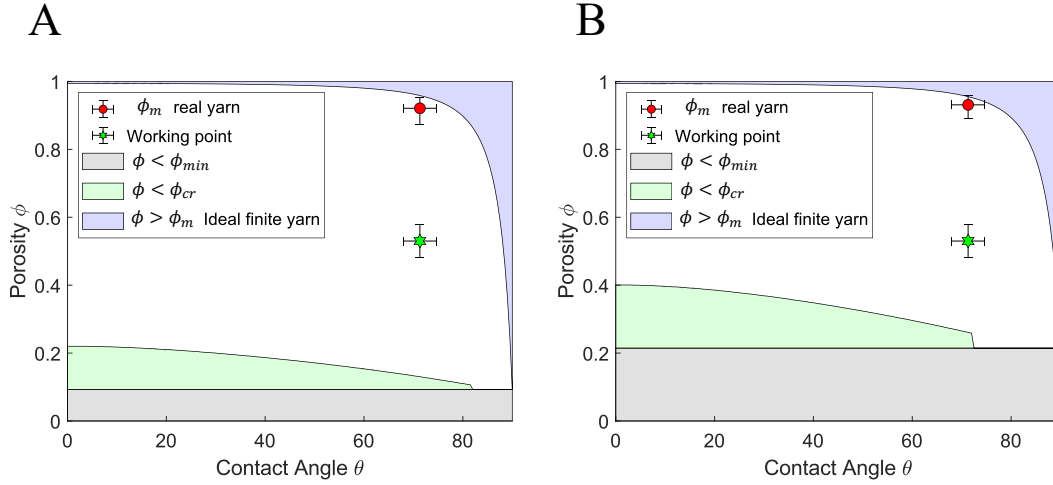


Figure 3.16: **Limits of the model for simulating the yarn composed of 247 fibers with the values of fiber radii extracted from the experimental data.** Domain of validity of the theoretical model used to predict the wicking properties of the woven PE textile for (A) hexagonal and (B) square fibers arrangements. The working point and its error bars are evaluated considering the experimental data obtained from the characterization of the PE fibers, namely $\theta = (71.3 \pm 3.3)^\circ$ and $\phi = (53.0 \pm 4.8)\%$. ϕ_m of the real yarn (red dot) is computed according to the methodology described in section 2.2.3.

Fig. 3.16 shows the domain of the model validity (white area) for a yarn composed of 247 fibers, with the fibers diameter obtained from the experimental measurements of the woven PE yarns. The red circle shows the maximum yarn porosity ϕ_m (within experimental uncertainty) computed from Eq. 2.29 for $\theta = (71.3 \pm 3.3)^\circ$, while n_{fB} and n_{fD} were evaluated from the yarn cross-sections

images, as previously described. The green hexagram corresponds to the combination of parameters of the real PE yarn used in this work: $\theta = (71.3 \pm 3.3)^\circ$ and $\phi = (53.0 \pm 4.8)\%$. Since both the hexagonal and square fiber arrangements fall within the white area, it is possible to approximate the maximum capillary height H_m with Eq. 2.27.

Model predictions of the wicking performances of an infinite and sparse ideal yarn

The model described in detail in section 2.2 has been used to explain the results of the wicking experiments for the woven PE textile and to predict the optimum yarn configuration to maximize the fabric wicking performance. Figs. 3.17A-B show the effects of the water-fiber contact angle θ and of the yarn porosity ϕ on the maximum height of the water front H_m , computed with Eq. 2.27 for different values of the fiber radii. The results shown in Fig. 3.17A-B are produced for the square arrangement of fibers, but similar conclusions can be drawn for the hexagonal structure. The data show that the capillary pressure increases when the yarn is composed by small, hydrophilic and densely packed fibers, yielding larger values of H_m . However, this combination of parameters may not yield the optimized wicking properties of the system, which can be expressed by the highest point reached by the water front after a given imbibition time H_t .

Fig. 3.17C-D illustrate the effect of the yarn porosity and the fiber radius on the height reached by the water front after 10 minutes of imbibition (i.e. H_{10}), for a hexagonal (panel C) or square (panel D) arrangements of fibers with a contact angle of $\theta = 71.3^\circ$, as experimentally characterized (see section 2.5 for the details on the time-dependent model). The color shaded areas are used to represent the domain of applicability of the model. The plots show the predicted performances of the woven PE textile, computed considering the measured average fiber diameter $2r = 18.5 \mu\text{m}$ and a yarn porosity of $\phi = 53\%$, in the limit of infinite-size periodic-lattice yarn. As it can be seen, the performance of the ideal textile depends non-linearly on r and ϕ .

The data in Fig. 3.17C-D show that depending on the yarn symmetry and the average fiber diameter, the optimal wicking properties of the yarn are achieved at different porosity values. The value of H_{10} for each yarn configuration is determined by two competing phenomena: the capillary pressure, which is a function of the maximum capillary height ($P_c = \rho g H_m$), and the viscous friction between water and the fibers, which is a function of the microscopic permeability K along the fibers axis. H_{10} increases with the increase of either P_c and K . As shown in Fig. 3.17A-B, the capillary pressure increases when the yarn is composed of small, hydrophilic and densely packed fibers. On the other hand, K increases in yarns composed of large and widely-separated fibers, as the resistance to the water motion decreases [134]. As a result, yarns composed of small fibers present better overall wicking

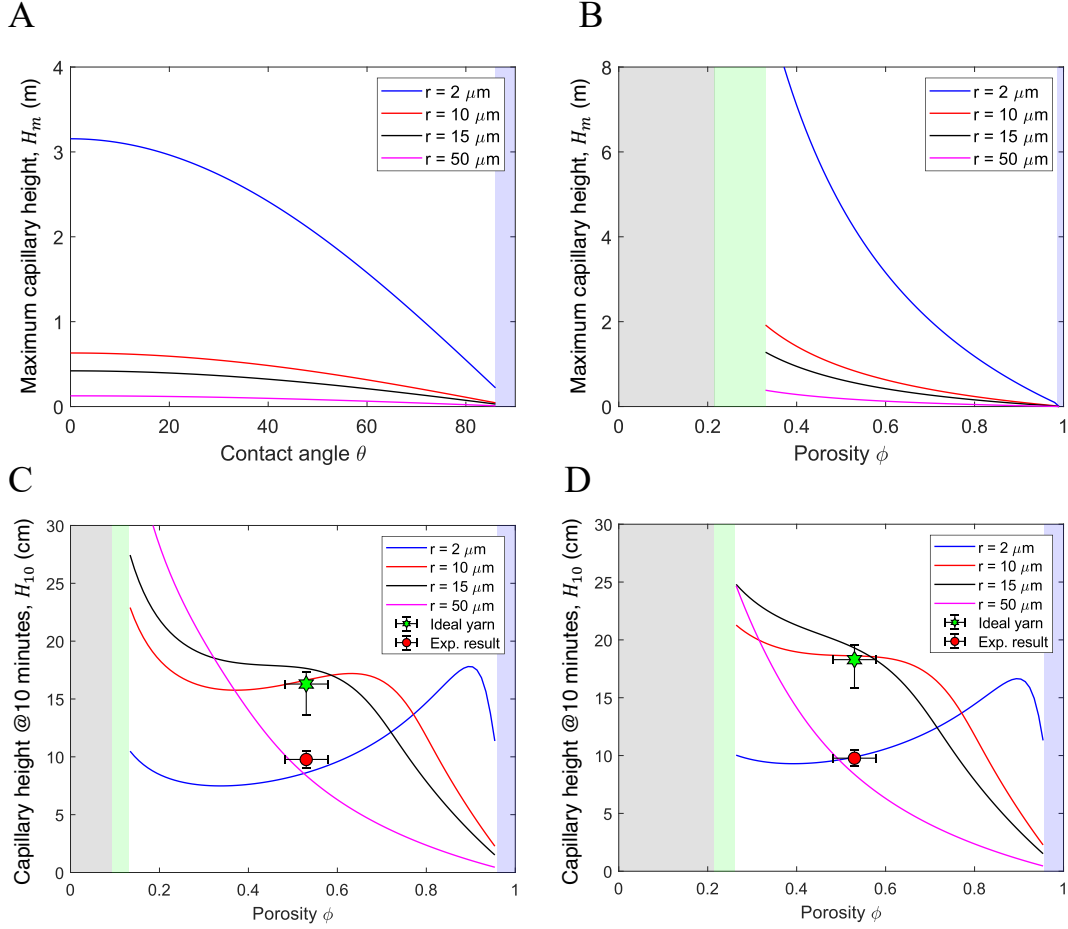


Figure 3.17: **Theoretical predictions of the woven PE textile wicking performance.** (A-B) Maximum capillary height H_m in a square-symmetry yarn as a function of the contact angle (A) and the yarn porosity (B) for different fiber radii computed with Eq. 2.27. The two plots are obtained considering $\phi = 0.5$ (A) and $\theta = 50^\circ$ (B), respectively. The color-shaded areas highlight the upper and lower bounds of validity of the proposed model: $\phi < \phi_{min}$ (gray), $\phi < \phi_{cr}$ (green) and $\phi > \phi_m$ (blue). (C-D) Theoretical prediction of the water column height after 10 minutes of vertical imbibition (H_{10}) for $\theta = 71.3^\circ$ considering a hexagonal (C) or square (D) fiber arrangement and different fiber radii. The green hexagon reports H_{10} for an infinite ideal yarn composed of fibers with diameters of $(18.5 \pm 6.2) \mu\text{m}$, contact angle of $(71.3 \pm 3.3)^\circ$, with porosity of $(53.0 \pm 4.8) \%$. The red circles correspond to the experimentally measured H_{10} value for the woven PE textile.

properties for large values of ϕ , while low-porosity yarns are favored when larger fibers are used.

3.2.3 Model fitting and structure optimization

The theoretical model introduced in section 2.2 was used to investigate the influence of different structural parameters of a yarn on the final capillary performance of a textile (see section 3.2.2), while still remaining under assumptions of ideality (i.e., infinite array of straight and parallel fibers). In this section, the predictions obtained through pure theoretical modeling are compared with the experimental capillary rises shown in section 3.1.4. For this purpose, the absolute permeability of the textile K is also evaluated through Eqs. 2.60 and 2.61 (see section 2.4.4). The values of the model parameters used for the comparison were obtained through experimental characterization (see sections 3.1.1 and 3.1.2) and are equal to $2r = (18.5 \pm 6.2) \mu\text{m}$, $\phi = (53.0 \pm 4.8)\%$, and $\theta = (71.3 \pm 3.3)^\circ$.

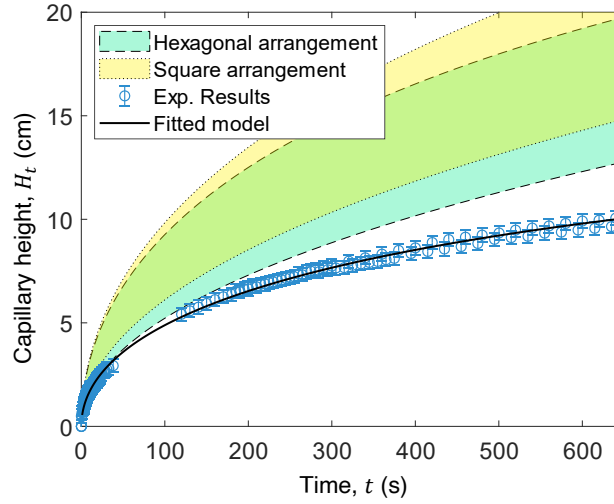


Figure 3.18: **Comparison between theoretical predictions and experimental results.** Comparison of the vertical wicking model predictions to the experimental results. The ideal model predictions (shaded areas) are calculated for yarns with the fiber diameters of $(18.5 \pm 6.2) \mu\text{m}$, contact angle of $(71.3 \pm 3.3)^\circ$, and porosity of $(53.0 \pm 4.8)\%$. A single parameter comprising all the real yarn non-idealities was fitted on the experimental data set.

Figure 3.18 compares the model predictions of wicking action in the ideal hexagonal-lattice and square-lattice yarns with the experimental results of the vertical dynamic imbibition of the woven PE. The intervals of the model predictions for each ideal periodic-lattice yarn were computed within the experimental uncertainty of the fiber diameter, the contact angle and the yarn porosity. Since the real textile structure (see Figs. 3.1D-F) is more complex than the simple linear model geometry, the ideal-yarn model overestimates the experimental performance of the woven PE textile.

To account for the non-parallelism of the fibers in the yarn, the deviation from the ideal periodic pattern, yarn bending, a finite number of fibers in the yarn, and water evaporation occurring during the test, the model was modified by including a reduction coefficient, fitted on the experimental data. The non-ideality of the real yarn was accounted for via a single coefficient c_7 , included to reduce the capillary pressure: $P_c = \rho g (c_7 H_m)$. For both fiber arrangements, the reduction coefficient A was scanned through 30 equidistant points in the range $0.3 \leq c_7 \leq 0.5$, and the other model parameters (namely, ϕ , r , and θ) were consequently fitted on 171 experimental data points obtained from five different vertical wicking tests. The fitting was performed by minimizing the root mean squared error (RMSE) between the modeling prediction and the experimental data set. The best fit for the hexagonal fiber arrangement was obtained with $\phi_H = 0.554$, $2r_H = 21.6 \mu\text{m}$, $\theta_H = 73^\circ$ and $c_{7,H} = 0.46$, while the coefficients fitting the data with a square yarn symmetry are $\phi_S = 0.554$, $2r_S = 20.1 \mu\text{m}$, $\theta_S = 71^\circ$ and $c_{7,S} = 0.36$ (black line, Fig. 3.18). For both arrangements of fibers, the fitted values of porosity and contact angle are within 5% with respect to the average experimental value, while the fitted value of the fibers diameter are 13% and 17% larger, for the square and hexagonal arrangements, respectively. The result is consistent with the large uncertainty related to the experimentally-measured fiber radii. The fitted model prediction for the square-symmetry ideal yarn with 60% performance reduction exhibited the best agreement with the experimental data obtained, as well as with the measured value of the maximum wicking height $H_m = (13.8 \pm 0.8)$ cm measured in the woven PE fabric.

Finally, Figs. 3.19A-B show the 3D plots illustrating the dependence of H_{10} on both the yarn porosity and the individual fiber diameter for the fiber contact angle of 71.3° for the square fiber arrangement (panel A) and the hexagonal fiber arrangement (panel B). The model was then used to predict the optimum fiber size and yarn configuration to achieve efficient moisture wicking action. As it can be observed, the optimal fibers radius and porosity in a square-lattice yarn composed of fibers with the contact angle of 71.3° are predicted to be approximately $15 \mu\text{m}$ and 45%, respectively, while the optimum hexagonal-lattice yarn was predicted to have fibers of $20 \mu\text{m}$ in diameter and the porosity of 45%. Although the wicking performance can be further improved by reducing the yarn porosity below 45%, the porosity range chosen in Fig. 3.19 represents typical values for wearable woven textiles and provides a compromise between efficient capillary moisture transport and the fabric mechanical flexibility. The parameters of the PE multi-filament yarn proposed in this chapter (marked with a star on Fig. 3.19) are not far from the optimum model predictions.

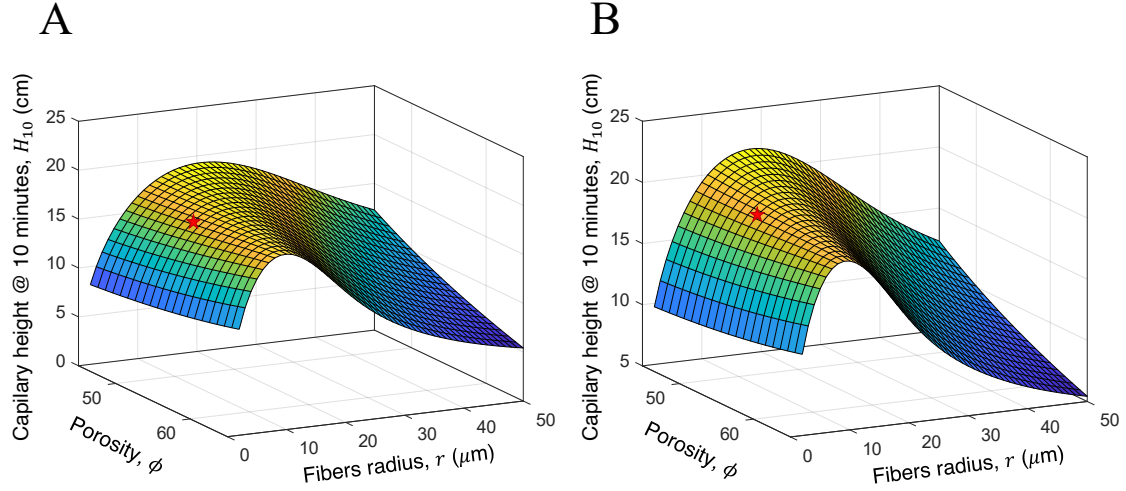


Figure 3.19: **Fabric structure optimization to achieve efficient wicking.** (A-B) The height of the wet area in the ideal square-lattice PE yarn 10 minutes after exposure as a function of the fiber radius and the yarn porosity for a fixed contact angle of 71.3° . The red stars represents the predicted performance of a yarn with the same combination of fiber radius and porosity as those experimentally evaluated for the PE woven fabric. The height of the wet area in the ideal hexagonal-lattice PE yarn 10 minutes after exposure as a function of the fiber radius and the yarn porosity for a fixed contact angle of 71.3° .

3.3 Finite elements analysis of the textile performance

The proposed analytical model was used to analyze in a simple and effective way the impact of various structural parameters on the performance of a fabric under some simplifying assumptions. The fitting procedure on the experiments performed in section 3.2 showed that, as expected, the ideality assumptions lead to an overestimation of the wicking performance compared to the real fabric, which are instead affected by the weaving process. Moreover, the proposed model only allows to study simple woven structures: complex knitting patterns or non-woven fabrics, where structural parameters can be better described by probability distributions, might lead to even larger deviations. Consequently, the formulation proposed in section 2.5, based on the representative element volume approach, can be a viable alternative to study capillary transfer in both structured and unstructured fabrics. Moreover, considering the problem of thermoregulation by means of fabrics, mass transfer constitutes only a part of the whole problem, which necessarily has to include heat transfer as well. In fact, a numerical implementation of the problem allows to combine capillary transport with other heat transfer mechanisms, such as

evaporative and radiative.

In this section, the experimental characterization of wicking performance reported in section 3.1 is used to fit the van Genuchten model parameters (see section 3.3.1); then, evaporative and radiative heat transport are formulated theoretically and compared with the experimental evidence (see sections 3.3.2 and 3.3.3, respectively). Finally, the different components of the model, formulated and tested separately, are combined and used to determine the performance of the proposed fabric in a case study (see section 3.3.4).

3.3.1 Wicking

The data obtained from the vertical wicking tests (blue circles) were used to estimate the material dependent parameters L , β and n of Eq. 2.91 for the woven PE fabric (solid black line). The best-fit parameters evaluated by comparing the experimental and the numerical results are $L = 0.324$, $\beta = 6.7192 \text{ m}^{-1}$ and $n = 7.79$. The resulting curve (see Fig. 3.20A, solid black line) fits the experimental data with a R-Squared value of 0.997. The speed of water within the textile during wicking was approximated with the time derivative of the water front speed (see Fig. 3.20A, solid red line), as commonly done under the sharp-front approximation [131]. The water speed tends to decrease during the transient, as the capillary pressure is balanced by increased losses due to viscous friction. The maximum value of water speed is observed at the beginning of the wicking transient, with a peak of approximately $2 \cdot 10^{-3} \text{ m/s}$. This result allows to neglect the advective contribution to heat transfer.

The obtained values of L , β and n enable to extend the analysis from 1-D to more complex 2-D or 3-D systems, which could not be investigated relying on purely analytical models. As an example, Fig. 3.20B shows a 2-D circular textile sample which wicks water from its center (see also Supplementary Video 2 or the [online material](#) labelled as MMC-S2). The non-hydrophilic areas (e.g. holes) within the domain alter the water transport, but can be easily implemented with a finite elements model with the same mathematical formulation used for its 1-dimensional counterpart.

3.3.2 Evaporation

The evaporation of the wetting fluid from the porous medium was modelled according to the Hertz-Knudsen equation [166, 167]:

$$\dot{m}_{ev} = E\phi\sqrt{\frac{M_w}{2\pi R_g}}\left(\frac{P_{sat}(T_w)}{\sqrt{T_w}} - RH\frac{P_{sat}(T_v)}{\sqrt{T_v}}\right), \quad (3.13)$$

where T_w is the temperature of the evaporating liquid, T_v is the vapour temperature, R_g is the universal gas constant, M_w is the molecular weight of water, P_{sat} is

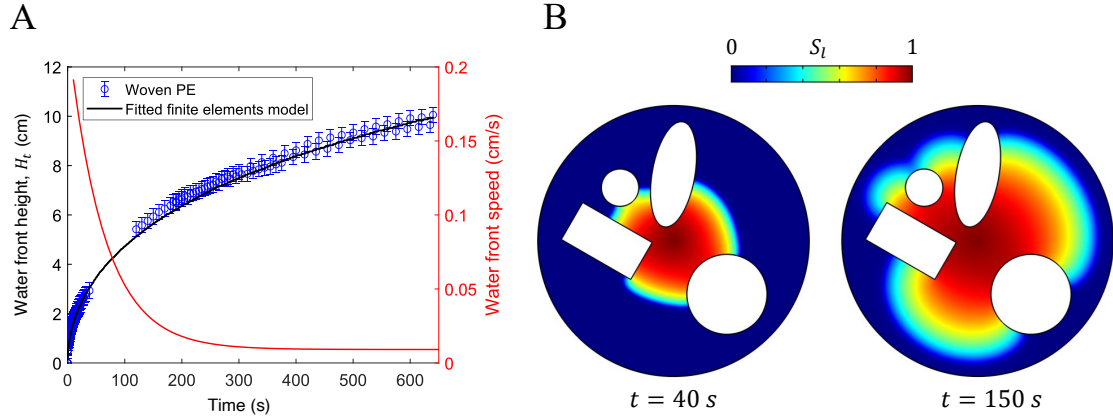


Figure 3.20: **Finite element implementation of 1-D and 2-D wicking.** (A) Fitting of the van Genuchten’s parameters on the obtained experimental data. The average speed of water (solid red line) was approximated as the numerical derivative of the water front height with respect to time. The low water speed within the fabric allows to neglect convection in the transient heat-transfer simulation. (B) The model parameters calibrated from the wicking experiments can be used to study the wicking transient in 2-D geometries, where – for example – hydrophobic zones can be implemented as impermeable holes. Notice that the circular sample shown is supposed to wick water from the center.

the saturation pressure at a given temperature, E is dimensionless evaporation rate, which depends on environmental conditions (*i.e.* the vapour stratification above the evaporating liquid) [166], and ϕ is the porosity of the porous surface. Notice that the Hertz-Knudsen equation here includes ϕ to take into account the reduced evaporating surface with respect to a corresponding free liquid surface. In the present work, the evaporating liquid and its vapour were assumed at thermal equilibrium [167], thus $T_w = T_v$. The saturation pressure was evaluated according to the Antoine’s equation (see Eq. 2.96).

The evaporation rate from a surface at temperature T is related to the ambient conditions through Eq. 3.13, which however requires to evaluate the evaporation rate constant E , a function of setup-specific conditions and reported to span several order of magnitudes [168]. Thus, the value of E corresponding to the experimental setup and test conditions reported in section 3.1.5 was calibrated by a finite element model built in the COMSOL Multiphysics software. The model, which implicitly couples heat and mass transfer, was employed to iteratively change the value of E until the obtained numerical temperature trends matched those reported in Fig. 3.10C. With respect to experiments, the 2-D simulation domain and its boundary conditions (see Fig. 3.21A) were modelled to mimic the experimental setup described in section 3.1.5. Coherently with the estimation of the van Genuchten’s

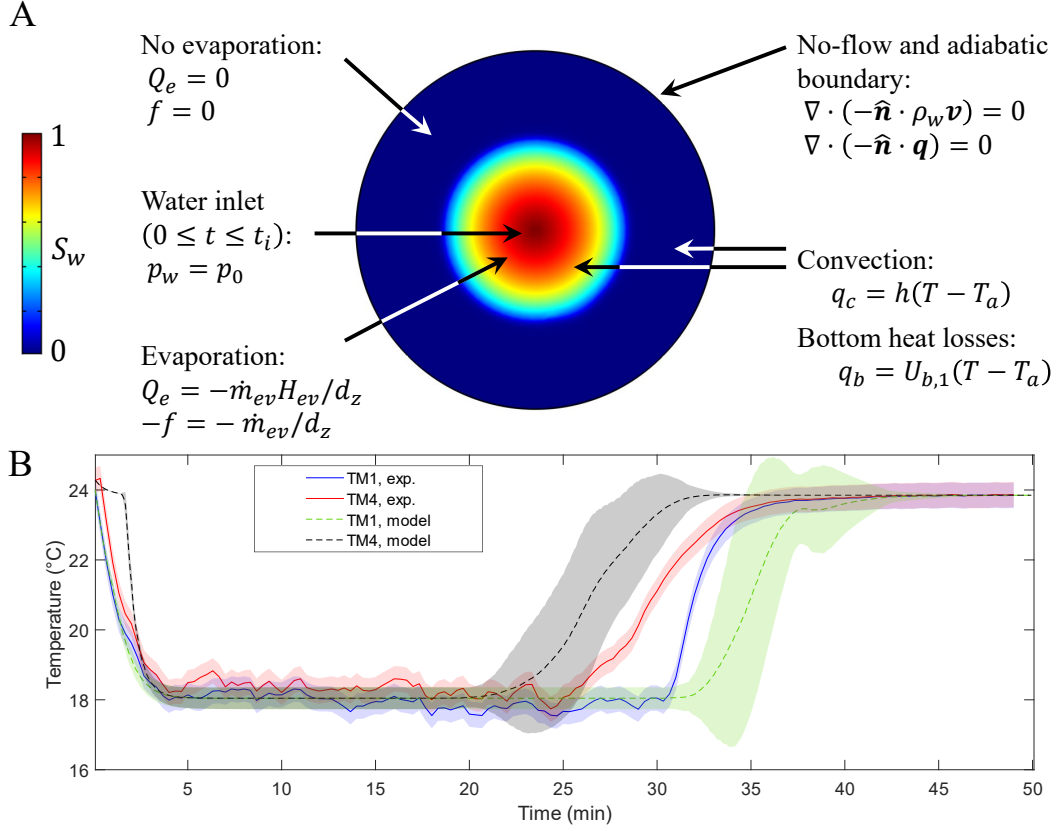


Figure 3.21: **Modelling of water evaporation from the porous fabric.** (A) Schematic of the 2-dimensional simulation setup and its boundary conditions for the evaporation process. The sink term $-f$ and the volumetric heat flux Q_e were only applied where $S_w > S_0$, while the boundary convective heat flux q_c and thermal losses q_b were considered over the entire domain. (B) Comparison between the experimental (blue and red solid lines) and modelled (green and black solid lines) temperature transients used to validate the evaporation model and fit the evaporation coefficient E in Eq. 3.13. The solid and dashed lines represent the average values and their shaded contour their uncertainty.

parameters (see section 3.3.1) and given the narrow range of temperatures experimentally observed (see Fig. 3.10C-D), the thermophysical properties of water used to model the mass transfer were considered as constant, while the polynomials used to compute the temperature dependent properties of air and water are reported in Appendix A. At this stage, the effect of radiative heat transfer was neglected.

As described in section 2.5, wicking dynamics was modelled by Eq. 2.88 with similar assumptions: the outermost circular boundary was considered as impermeable; a point-wise injection well condition was imposed at the center of the circular domain (with $P_w = P_0$) to simulate the wetting by a water droplet; the horizontal

orientation of the setup allowed to neglect the effect of gravity. Furthermore, the sink term was evaluated from Eq. 3.13 and suppressed if the water saturation was lower than S_0 , namely:

$$-f = \begin{cases} 0 & \text{if } S_w \leq S_0 \\ -\dot{m}_{ev}/d_z & \text{if } S_w > S_0, \end{cases} \quad (3.14)$$

where $d_z = 346 \mu\text{m}$ is the thickness of the textile, evaluated as described in section 3.1.1. The initial values of the pressure field were taken according to the step function:

$$P_w(x, y) = \begin{cases} P_0 & \text{if } x^2 + y^2 \leq R_0 \\ P_0 - P_c(S_0) & \text{if } x^2 + y^2 > R_0, \end{cases} \quad (3.15)$$

where x and y are the two horizontal spatial coordinates, $R_0 = 1 \text{ mm}$ is the size of the injection well (namely the size of the zone considered wet at the beginning of the simulation) and $S_0 = 0.01$ is the assumed initial saturation in the domain. The energy balance equation was used to model heat transfer in the computational domain:

$$(\rho c_p)_{eff} \frac{\partial T}{\partial t} + \nabla \cdot \mathbf{q} = Q, \quad (3.16)$$

considering:

$$\begin{aligned} (\rho c_p)_{eff} &= \phi \rho_m c_{p,m} + (1 - \phi) \rho_F c_{p,F}, \\ \mathbf{q} &= -k_{eff} \nabla T, \\ k_{eff} &= \phi k_m + (1 - \phi) k_F, \end{aligned} \quad (3.17)$$

where the subscripts m and F respectively refer to the porous matrix and the fluid domain, T is the moist fabric temperature, c_p is the specific heat at constant pressure, \mathbf{q} is a generic boundary heat flux (expressed in W m^{-2}), Q is the generic source/sink term (expressed in W m^{-3}), k_m and k_F are the thermal conductivities of the porous matrix and of the fluid domain, respectively. Given the low velocity of the water in the domain, the velocity field v was set to 0 (see section 3.3.1 for further details). The thermophysical properties of the fluid within the porous medium domain ρ_F , $c_{p,F}$ and k_F were obtained by averaging those of water and air based on the local saturation of the pores (e.g. the density of fluid domain was computed as $\rho_F = S_w \rho_w + S_{nw} \rho_{nw}$), while the thermal properties of the porous matrix were experimentally characterised and considered as constant.

The volumetric heat flux due to evaporation $Q = Q_e$ (see Fig. 3.21A) was evaluated as:

$$Q_e = \begin{cases} 0 & \text{if } S_w \leq S_0 \\ -\dot{m}_{ev} H/d_z & \text{if } S_w > S_0, \end{cases} \quad (3.18)$$

where $H = 2276 \text{ kJ/kg}$ is the enthalpy of vaporisation of water considered as constant. In perspective, the enthalpy of vaporization can be considered as a function

of the wet textile temperature according to the following polynomial expression [169]:

$$H = M_w^{-1} \left(44.458 X^{3/8} + 14.636 X^{(1+3/8)} - 27.946 X^{(2+3/8)} + 13.985 X^{(3+3/8)} \right), \quad (3.19)$$

being X defined as $X = (T_c - T) / (T_c - T_t)$, where T is the temperature of the wet textile (expressed in K), $T_c = 647.126$ K and $T_t = 273.16$ K are the critical and triple point of water, respectively. However, the enthalpy of water at 18 °C evaluated through Eq. 3.19 – which is the same temperature measured experimentally during the evaporation tests – deviates only 8% from the value used and does not have a significant effect on the results of the fit performed.

The boundary heat losses due to convection (see Fig. 3.21A) were evaluated as $\hat{\mathbf{n}} \cdot \mathbf{q} = q_c = h(T - T_{amb})$, where $T_{amb} = 23.9$ °C is the average ambient temperature during the tests, and the convection coefficient h for natural convection over an horizontal plate was evaluated as [170]:

$$h = \frac{k_{air}}{\delta_l} \cdot C_h \cdot Ra^{1/4}, \quad (3.20)$$

where δ_l is the characteristic length (ratio between the area and the perimeter of the circular domain), k_{air} is the thermal conductivity of air computed at the average temperature $T_{av} = (T_{amb} + T)/2$, Ra is the Rayleigh number and C_h is a multiplying constant so that [170]:

$$C_h = \begin{cases} 0.54 & \text{if } T_{amb} < T \text{ and } 10^4 \leq Ra \leq 10^7 \\ 0.27 & \text{if } T_{amb} > T \text{ and } 10^5 \leq Ra \leq 10^{10}. \end{cases} \quad (3.21)$$

The Rayleigh number was evaluated as:

$$Ra = \frac{g\beta(T - T_{amb})L^3Pr}{(\mu_a/\rho_a)^2}, \quad (3.22)$$

where $\beta \approx 1/T_{av}$ is the approximated expansion coefficient of air [171] and $Pr = 0.7$ is the Prandtl number of air. The boundary heat losses through the bottom side of the setup $\hat{\mathbf{n}} \cdot \mathbf{q} = q_b$, where $\hat{\mathbf{n}}$ is the versor perpendicular to a boundary surface (see Fig. 3.21A) were evaluated as reported in section 3.1.7.

To mimic the experimental imbibition and subsequent drying of the textile, the simulation was performed as a combination of three consecutive, time-dependent computational steps. First, the pressure field in the domain represented in Fig. 3.21A was equilibrated by simulating the water transport model only for 0.5 seconds, neglecting the evaporation of the fluid to grant numerical stability. Then, the simulation was carried out while coupling the heat and mass transfer physics

until $t = t_i$, where t_i is the time at which the overall volume of water wicked by the textile V_w matched the volume of the droplet deposited during the experiment, namely $V_w = (0.25 \pm 0.02)$ mL. The volume of water wicked by the textile at a given time-step was evaluated as:

$$V_w = \int_A (\delta S_w d_z \phi) dA, \quad (3.23)$$

being

$$\delta = \begin{cases} 0 & \text{if } S_w \leq S_0 \\ 1 & \text{if } S_w > S_0, \end{cases} \quad (3.24)$$

and A the upper surface of the circular sample. Third, the drying process was simulated until $t = 2000$ s while removing the pressure constraint at the center of the textile, namely after stopping the water uptake.

The experimental data presented in Fig. 3.10C were used to evaluate the evaporation constant E in Eq. 3.13, which is a characteristic of the experimental testing conditions. First, the wicking model was used to estimate the time of the wicking transient t_i , namely the time required to a 2-dimensional circular textile sample to be wicked by a volume of water equal to the droplet used in the experiments. Note that the experimental procedure prescribed to lay the water droplet on a textile previously deposited on the substrate surface was described in section 3.1.5 (see Figs. 3.9C). As a result, the absorption and spread of water was not only due to pure wicking, as assumed in the model, since the pressure field was influenced by the weight of the textile itself. Thus, the modelled imbibition time t_i is a simplified numerical counterpart of the absorption phenomenon observed in the experiment. The imbibition transient was simulated using the values of the retention parameters L , β and n previously evaluated and, as discussed in section 3.3.1, the effect of water evaporation during the wicking transient was neglected. With a simulated imbibition time $t_i = 58.7$ s, the volume of water wicked by the textile was $V_w = 0.243$ mL, coherent with the volume of the water droplet used for the experiment (0.25 ± 0.02) mL. It is worth to point out that the width of the transition $\omega = 0.8$ of the ramp function r used in Eq. 2.91 affects the profile of S_w during the wicking transient and, thus, t_i . However, as discussed in Ref. [102], its effect on the estimated imbibition time t_i is negligible.

To evaluate the evaporation constant E , the experimental temperature curves of the thermistors TM1 and TM4 were compared with the results of simulation. The low temperature difference between the drying textile and the ambient resulted in an average Rayleigh number $Ra < 10^5$, thus below the range of validity reported in Eq. 3.21 to evaluate the convection coefficient h . As a consequence, h was estimated as $h = (6.0 \pm 0.2)$ W m⁻² K⁻¹, which considered the effect of the forced ventilation in the laboratory environment and is coherent with the minimum

convection coefficient reported for still air conditions, approximately $5 \text{ W m}^{-2} \text{ K}^{-1}$ [171]. The best fitting curves were obtained for $E = 0.079$, the results are shown in Figs. 3.21B. The computed temperature at the center of the sample (see Fig. 3.21B, dashed green line) recovers accurately the experimental one (solid blue line), while the discrepancy between TM4 (solid red line) and the respective computed value (dashed black line) could be ascribed to both experimental and theoretical inaccuracies, for instance: the manual deposition of both the water droplet and the textile sample on the support; the constraint imposed to the evaporation rate by Eq. 3.14 and 3.18, which limits the evaporation to the regions with $S_w > S_0$. An important parameter to determine the efficiency of the moisture transport of textiles is the wet-to-dry time: in the considered testing conditions, this was experimentally estimated as $(29.4 \pm 0.5) \text{ min}$, which is in good agreement with the results of the simulation, namely $(34 \pm 2) \text{ min}$.

In conclusion, it is worth to point out that evaporation is a particularly complex phenomenon, as it strongly depends on several properties of the boundary layer above the evaporating surface: concentration of water vapour, interfacial temperature, air-flow velocity, pressure and size of the evaporating surface. However, the proposed heat and mass transfer model was able to recover the experimental behaviour of the tested material by employing a single, condition-specific scaling coefficient E .

3.3.3 Radiative heat transfer

For the semi-transparent fabric, it holds [171]:

$$\alpha_f(\lambda) + \tau_f(\lambda) + r_f(\lambda) = 1, \quad (3.25)$$

where α_f , τ_f , r_f are respectively the absorption, transmission and reflection coefficients for a given wavelength λ and the subscript f refers to the fabric. The surface of the heater is modelled as an opaque medium, thus:

$$\alpha_h(\lambda) + r_h(\lambda) = 1, \quad (3.26)$$

where the subscript h refers to the surface of the heater. According to the Kirchhoff's law, the wavelength-dependent absorption and emissivity were assumed equal for both the fabric and the heater [171], namely: $\epsilon_{f/h}(\lambda) = \alpha_{f/h}(\lambda)$. As reported in section 3.1.6, the experimental evaluation of the optical properties of the semi-transparent fabric was done in the wavelength range from $\lambda_i = 0.25 \mu\text{m}$ to $\lambda_e = 2.5 \mu\text{m}$, and from $\lambda_i = 2.5 \mu\text{m}$ to $\lambda_e = 20 \mu\text{m}$. In these ranges, the average optical properties can be computed as [172]:

$$\bar{\alpha}_f = \frac{\int_{\lambda_i}^{\lambda_e} \alpha_f(\lambda) I_{rr}(\lambda) d\lambda}{\int_{\lambda_i}^{\lambda_e} I_{rr}(\lambda) d\lambda}, \quad (3.27)$$

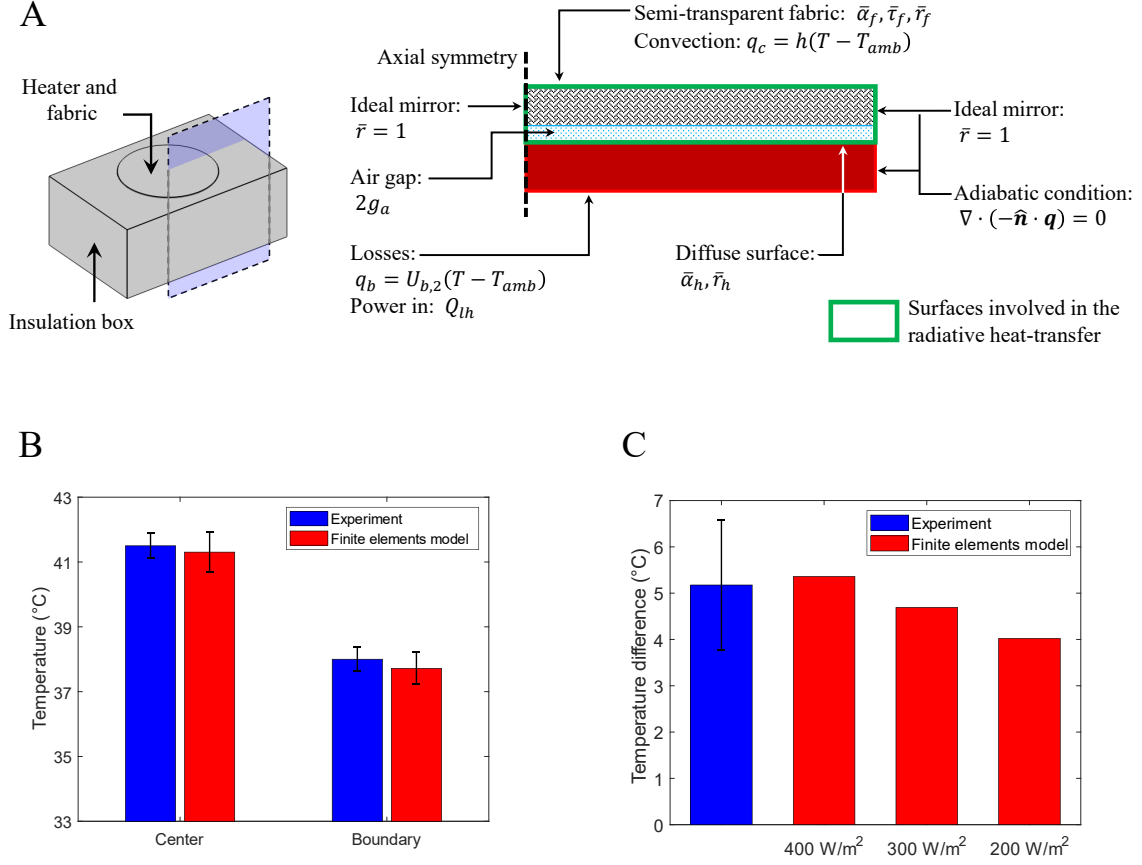


Figure 3.22: **Modelling of the radiative heat transfer properties.** (A) Schematics of the 2-dimensional simulation setup, highlighting the surfaces involved in the radiative heat transfer (solid green lines). The contribution of the air gap to heat transfer was assimilated to a conductive resistance, since both convective and radiative contributions can be neglected for such a layer of air with micrometer thickness. (B) Comparison between the measured and computed temperatures at the center and boundary of the specimen at the steady state of indoor test, considering the covered configuration. (C) Comparison between the measured and computed temperature difference between the covered and uncovered setups in the outdoor configuration. The experimental temperature difference, evaluated from the temperature trends in Fig 3.11C, was obtained as the time-average of the last 150 min recorded. To evaluate the effect of the varying solar irradiance, the results were computed for three different values of I_{rr} , showing a general good agreement with the measurement.

where $I_{rr}(\lambda)$ is the wavelength dependent incident radiation on the surface. The average transmission $\bar{\tau}_f$ and reflection \bar{r}_f coefficients were evaluated similarly to Eq. 3.27.

The radiative heat transfer process in the considered experiment includes the interaction between three bodies: the opaque heater, the semi-transparent textile and the ambient, where the latter is considered as a black-body. Considering an external incident radiative heat flux $I_{rr}(\lambda)$ and assuming the air gap between the heater and the fabric as a non-participating medium, the heat absorbed by the fabric $-\hat{\mathbf{n}} \cdot \mathbf{q} = q_{r,f}^{ext}$, expressed in W m^{-2} , can be computed as:

$$q_{r,f}^{ext} = \left(\bar{\alpha}_f + \sum_{n=1}^{\infty} \bar{\tau}_f \bar{\alpha}_f \bar{r}_f^{n-1} \bar{r}_h^n \right) \int_{\lambda_i}^{\lambda_e} I_{rr}(\lambda) d\lambda, \quad (3.28)$$

where I_{rr} was evaluated by hemispheric integration of the Plank's black body radiation $E_r(T, \lambda)$ (expressed in $\text{W}/(\text{m}^3\text{sr})$) on the solid angle θ in the case of indoor conditions (namely $I_{rr}(\lambda) = \int_0^\pi E_r(T_{amb}, \lambda) d\theta$), and $I_{rr}(\lambda) = \int_0^\pi E_r(T_{sky}, \lambda) d\theta$ in the case of outdoor conditions, $I_{rr}(\lambda) = \text{AM0}$ for solar radiation. The summation in Eq. 3.28 considers the share of incoming radiation transmitted by the fabric, reflected by the substrate, and absorbed by the fabric. As this contribution progressively decreases, it was evaluated only for $n < 6$, as the contribution becomes numerically negligible for $n \geq 6$. Similarly, the specific heat flux absorbed by the heater from an incident external source can be evaluated as:

$$q_{r,h}^{ext} = \left(\bar{\tau}_f \bar{\alpha}_h + \sum_{n=1}^{\infty} \bar{\tau}_f \bar{\alpha}_h \bar{r}_f^n \bar{r}_h^n \right) \int_{\lambda_i}^{\lambda_e} I_{rr}(\lambda) d\lambda. \quad (3.29)$$

The specific heat fluxes absorbed by the fabric $q_{r,f}^{int}$ and by the heater $q_{r,h}^{int}$ due to the mutual infrared heat transfer, considering the two surfaces as parallel plates with unitary view factor, was evaluated as:

$$\begin{aligned} q_{r,f}^{int} = & \bar{\alpha}_f \left(\sum_{n=0}^{\infty} \bar{\alpha}_h \bar{r}_f^n \bar{r}_h^n \right) \int_0^\pi \int_{\lambda_i}^{\lambda_e} E_r(T_h) d\lambda d\theta + \\ & \bar{\alpha}_f \bar{r}_h \left(\sum_{n=0}^{\infty} \bar{\alpha}_f \bar{r}_f^n \bar{r}_h^n \right) \int_0^\pi \int_{\lambda_i}^{\lambda_e} E_r(T_f) d\lambda d\theta, \end{aligned} \quad (3.30)$$

and

$$\begin{aligned} q_{r,h}^{int} = & \bar{\alpha}_h \left(\sum_{n=0}^{\infty} \bar{\alpha}_f \bar{r}_h^n \bar{r}_f^n \right) \int_0^\pi \int_{\lambda_i}^{\lambda_e} E_r(T_f) d\lambda d\theta + \\ & \bar{\alpha}_h \bar{r}_f \left(\sum_{n=0}^{\infty} \bar{\alpha}_h \bar{r}_h^n \bar{r}_f^n \right) \int_0^\pi \int_{\lambda_i}^{\lambda_e} E_r(T_h) d\lambda d\theta. \end{aligned} \quad (3.31)$$

The software COMSOL Multiphysics was used to validate the radiative heat transfer model and to fit the thermal properties of the heater used for the experiments. A schematic of the simulation setup is reported in Fig. 3.22A. Eq. 3.16 was solved in the computational domain to determine the surface temperature of the heater.

The incident radiation $I_{rr}(\lambda)$ was studied into two wavelength ranges: the solar radiation in the ultra-violet (UV), visible (VIS) and near-infrared (NIR) range; the thermal emission in the infrared radiation (IR). In the former case, $I_{rr}(\lambda)$ was evaluated from the AM0 spectrum, appropriately scaled to match a target value of specific input power; in the latter case, it was evaluated from the temperature-dependent Planck's law:

$$E_r(T, \lambda) = \frac{2h_P c_l^2}{\lambda^5} \frac{1}{\exp\left(\frac{h_P s_l}{k_B \lambda T}\right) - 1}, \quad (3.32)$$

where $E_r(T, \lambda)$ is expressed in $\text{W}/(\text{m}^3\text{sr})$, h_P the Planck's constant, s_l the speed of light and k_B the Boltzmann's constant. In the indoor test, the environment is considered as a black-body at the ambient temperature $T = T_{amb}$, while in case of outdoor conditions the environment is considered at $T = T_{sky}$, which was evaluated as a function of the ambient temperature and relative humidity [171]:

$$T_{sky} = T_{amb} \left(0.711 + (5.6 \cdot 10^{-2}) T_{dp} + (7.3 \cdot 10^{-5}) T_{dp}^2 \right)^{1/4}, \quad (3.33)$$

where T_{amb} and T_{sky} are expressed in K, T_{dp} is the dew-point temperature expressed in degrees Celsius, which was computed according to the Magnus-Tetens approximation:

$$T_{dp} = c_4 \gamma (c_3 - \gamma)^{-1}, \quad (3.34)$$

where $\gamma = (c_3 T_{amb} (c_4 + T_{amb})^{-1} + \ln(RH))$, T_{amb} and T_{dp} are expressed in degrees Celsius, $c_3 = 17.27$ and $c_4 = 237.7$ °C. Note that Eq. 3.34 is valid in the temperature range $0^\circ\text{C} \leq T_{amb} \leq 60^\circ\text{C}$. To reduce the computational cost of simulation, the insulation box was replaced by the boundary heat flux $q_b = U_{b,2}(T - T_{amb})$ (see Fig. 3.22A and section 3.1.7).

The four surfaces participating to the radiative heat transfer are the top surface of the heater, the top surface of the fabric and the lateral surfaces of the fabric and the air gap (see Fig. 3.22A, solid green line). To maintain the adiabatic conditions on the lateral surfaces, the lateral sides were supposed to be ideal mirrors facing an environment at their same temperature. Notice that the optical properties of the fabric evaluated experimentally (see section 3.1.6) were concentrated on its top surface, thus the volume enclosed between these four surfaces was considered as transparent. Instead, the heater was supposed to be opaque and its top surface to be optically diffuse. The radiative thermal energy transfer between the fabric and heater can be included in Eq. 3.16 as boundary heat fluxes $q_{r,i}$, where the subscript i refers to the i -th heat source due to radiative heat transfer computed from Eqs. 3.28, 3.29, 3.30 and 3.31. In particular, when simulating outdoor conditions, the effect of solar radiation was evaluated by Eqs. 3.28 and 3.29 with $I_{rr}(\lambda) = \text{AM0}$.

The optical properties of the fabric in the infrared spectrum were averaged using Eq. 3.27, where $I_{rr}(\lambda)$ was obtained from Eq. 3.32 considering $\lambda_i = 2.5 \mu\text{m}$, $\lambda_e = 20 \mu\text{m}$ and $T = 50^\circ\text{C}$; whereas, the UV-VIS-NIR properties were obtained considering $\lambda_i = 0.25 \mu\text{m}$, $\lambda_e = 2.5 \mu\text{m}$ and the AM0 spectrum. The average optical properties of the heater in the IR wavelength range were fitted from the temperatures obtained by the uncovered setup. The resulting optical properties employed in the simulation of the fabric and heater are reported in Tab. 3.1.

	$\bar{\alpha}$	$\bar{\tau}$	\bar{r}
Fabric, IR	0.42	0.25	0.33
Fabric, UV-VIS-NIR	0.17	0.35	0.48
Heater, IR	0.87	0	0.13
Heater, UV-VIS-NIR	0.26	0	0.74

Table 3.1: Optical properties of the dry PE textile and opaque heater from the experimental characterisation.

The optical properties in the IR range for the wet textile were obtained averaging those of water, considered as black-body in the IR spectrum, and those of the dry textile reported in Tab. 3.1, that is:

$$\begin{aligned}
 \bar{\alpha}_{f,wet} &= S_{nw}\bar{\alpha}_f + S_w, \\
 \bar{\tau}_{f,wet} &= S_{nw}\bar{\tau}_f, \\
 \bar{r}_{f,wet} &= S_{nw}\bar{r}_f.
 \end{aligned}
 \tag{3.35}$$

Given the high transparency of water to the solar spectrum and the low thickness of the textile, the optical properties of the wet fabric in the UV-VIS-NIR range were considered as equal to those of the dry textile.

The comparison between the measured and computed temperatures at the steady state for the indoor experiment is reported in Fig. 3.22B. The experimental results and the theoretical predictions are in good agreement and comparable within their uncertainty. The simulation results show the effect of the air gap between the heaters surface and the fabric on the substrate temperature: the local surface temperature varies of approximately 1.3°C and 1°C , respectively, at the center and boundary of the setup, varying the air gap thickness in the range $71 \mu\text{m} \leq g_a \leq 212 \mu\text{m}$. Therefore, an accurate evaluation of the thermal contact between the fabric and its substrate is crucial to obtain reliable numerical results. Figure 3.22C compares the theoretical and experimental results in outdoor conditions. The temperature difference between the covered and uncovered setups was evaluated by averaging the experimental results between minutes 160 and 300, where the solar irradiance varied between 370 W m^{-2} and 100 W m^{-2}

(blue bar). Since the temperature difference was more scattered with respect to the indoor test, simulations were performed considering three different values of solar irradiance $I_{rr} = [200, 300, 400] \text{ W m}^{-2}$, while the ambient temperature and external convection coefficient were fixed at $T_{amb} = 17.5^\circ\text{C}$ and $h = 22.2 \text{ W m}^{-2} \text{ K}^{-1}$, respectively, and the sky temperature was evaluated considering $RH = 40\%$. The numerical result obtained are in good agreement with the experimental one, with a maximum deviation of 22% (with $I = 200 \text{ W m}^{-2}$), coherently with the experimental uncertainty.

The radiative cooling properties of the woven PE fabric tested are indeed mild (25% transparency in the IR spectrum, 45% reflectance in the UV-VIS spectrum, see Tab. 3.1): this is mainly due to the fiber size (approximately $20 \mu\text{m}$), which favors capillary transport over radiative heat transfer. The radiative performance of PE fabrics could be improved by reducing the fibers size to the order of 100 nm: further laboratory and in-field tests performed on commercial non-woven textiles made of PE nanofibers (Tyvek[®]) showed excellent radiative cooling properties, despite being hydrophobic and, therefore, not suitable for apparel. Although it is difficult to predict the optical properties of multidimensional materials (e.g., a mixture of micro- and nanofibers) or composites (e.g., nanoparticles dispersed in a polymeric matrix) without considerable modeling efforts, the thermal performance of fabrics could be enhanced by improving their design. For example, materials favoring different transport mechanisms (i.e., capillarity or radiative heat transfer) could be layered. Note that favoring one transport mechanism could hinder the other: for example, wet fibers would exhibit high IR absorbance and thus poorer radiative cooling properties. Following this concept, a thin layer with excellent UV-VIS reflection, although it may be hydrophobic (e.g., Tyvek[®]), could be placed on top of a hydrophilic layer optimized for capillary transport. Being thin with high porosity, the top layer could provide minimal resistance to water vapor diffusion, while reducing the thermal load due to solar radiation. Since both materials could be entirely made of PE, this multi-layer design would remain easily recyclable. In this direction, the characterization and simulation procedure proposed in this thesis would be particularly advantageous in shifting a materials science issue into a design optimization problem, thus being able to achieve high performance through rational design.

3.3.4 Performance assessment

By means of simple experimental procedures (see section 3.1) and numerical modelling (see sections 3.3.1, 3.3.2 and 3.3.3), the material-dependent properties (the average porosity, thickness, absolute permeability, wicking parameters and optical properties) and condition-specific parameters (the evaporation rate E) of a novel woven PE material were evaluated and used to calibrate a comprehensive model for the mass transfer in porous media. However, the procedure required a few

accessory simulations to provide setup-specific parameters essential to recover the experimental results: the heat transfer coefficients of the polystyrene insulations, the outdoor convection coefficient and the non-homogeneous heating characteristic of the silicone heaters (see section 3.1.7). For the sake of clarity, the workflow of the proposed characterisation procedure was summarised in the block diagrams shown in Figs. 3.23 and 3.24, where the setup-specific parameters are highlighted with dash-dotted contours. Evidently, if any of the condition-specific or setup-specific parameters were known *a priori* or simplifying assumptions employed (e.g. adiabatic conditions replacing the heat transfer coefficients $U_{b,1/2}$), the accessory simulations would be avoided, easing the procedure.

The data obtained can be used to estimate the thermal performance of a known material exposed to different working conditions. This section presents an application-specific sensitivity analysis aimed to assess how different ambient conditions affect the thermal performance of the woven PE textile characterised in this work, which was specifically designed for passive personal thermal management. Approaching this optimisation problem with modelling is beneficial, given the large number of variables and the strong non-linearity of the system response to the input parameters.

The simulations were performed employing the setup used to validate the radiative heat transfer model in Fig. 3.22A. Similarly, the solutions were computed using a steady state solver, hence the wicking transient was neglected and the textile, if wet, was assumed as completely saturated by water, namely $S_w = 0.99$. A few numerical assumptions were made: the supplied specific heat flux q_{in} (expressed in W m^{-2}) was supposed to be homogeneously supplied by the silicone heater; both indoor and outdoor conditions were simulated considering natural convection, thus the convection coefficient h was evaluated from Eqs. 3.20, 3.21 and 3.21; if the lower limits of the Ra number expressed in Eq. 3.21 were not satisfied, the convection coefficient was assumed equal to $h = 6 \text{ W m}^{-2} \text{ K}^{-1}$; the fitted evaporation rate $E = 0.079$, the enthalpy of vaporisation $H = 2276 \text{ kJ kg}^{-1}$ and the absolute permeability $K = 1.7 \cdot 10^{-12} \text{ m}^2$ (see section 3.1.4) were assumed as constants.

Fig. 3.25A shows the ratio between the radiative (IR) $q_r^{f \rightarrow a}$ and the evaporative heat fluxes emitted by the top surface of the wet woven PE fabric for indoor conditions. The textile surface temperature T is a fundamental parameter to evaluate the evaporative and radiative heat fluxes, thus it was represented on the left horizontal axis of Fig. 3.25A, although it is an output from the simulations. Model predictions show that evaporation is the principal cooling mechanism for most of the configurations tested, while $q_r^{f \rightarrow a}$ is limited (or even made negative for $q_{in} = 0$) by the increased optical temperature of the surrounding environment $T_{sky} = T_{amb}$, which determines the radiative heat transfer with the environment. However, the combination of high values of RH and surface temperature (caused by higher values of q_{in}) might invert the trend. The results obtained for outdoor conditions (see Fig. 3.25B) outline an opposite situation. The curves displayed were obtained varying

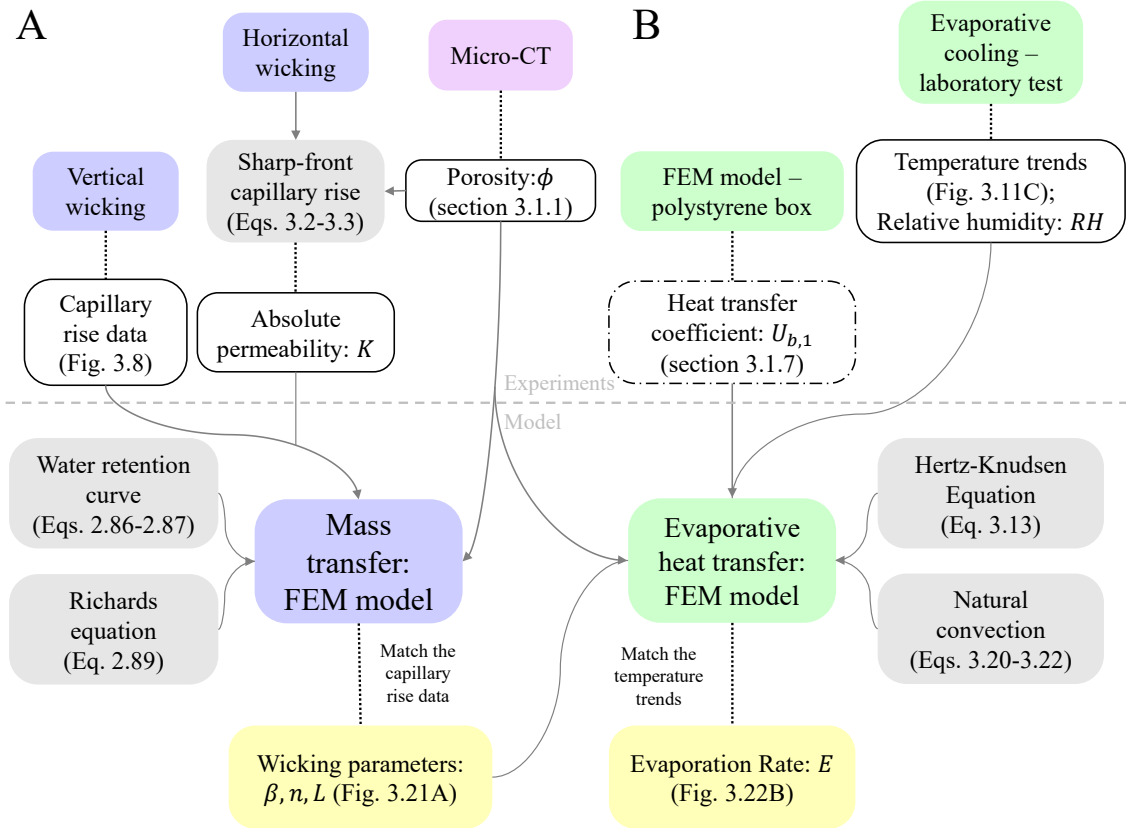


Figure 3.23: **Detailed procedure to investigate wicking and evaporative heat transfer.** Graphical flow-charts of the procedure used to characterise (A) the wicking properties, (B) the evaporation rate in the tested conditions and validate the models. Blue and green boxes report experimental or modelling activity referred to wicking (see sections 2.5, 3.1.4 and 3.3.1) and evaporative heat transfer (see sections 3.1.5 and 3.3.2), respectively. White boxes indicate the result of each experimental or modelling step; white point-dashed boxes reports the complementary results needed to characterise the experimental setup; the yellow boxes reports the main outcome of the characterisation procedure.

the supplied specific heat flux in the range $0 \text{ W m}^{-2} \leq q_{in} \leq 200 \text{ W m}^{-2}$ and the incident solar radiation in the range $0 \text{ W m}^{-2} \leq I_{rr} \leq 1000 \text{ W m}^{-2}$. The radiative heat transfer in outdoor conditions is considerably favoured by a reduced value of T_{sky} , which is a function of humidity and ambient temperature. As a consequence, high values of RH and low values of T_{amb} results in low evaporation rates and high IR emissions, favouring radiative over evaporative heat transfer. A direct evaluation of the user comfort level is provided by the fabric substrate temperature, namely the temperature of the fabric bottom layer directly in contact with the simulated skin.

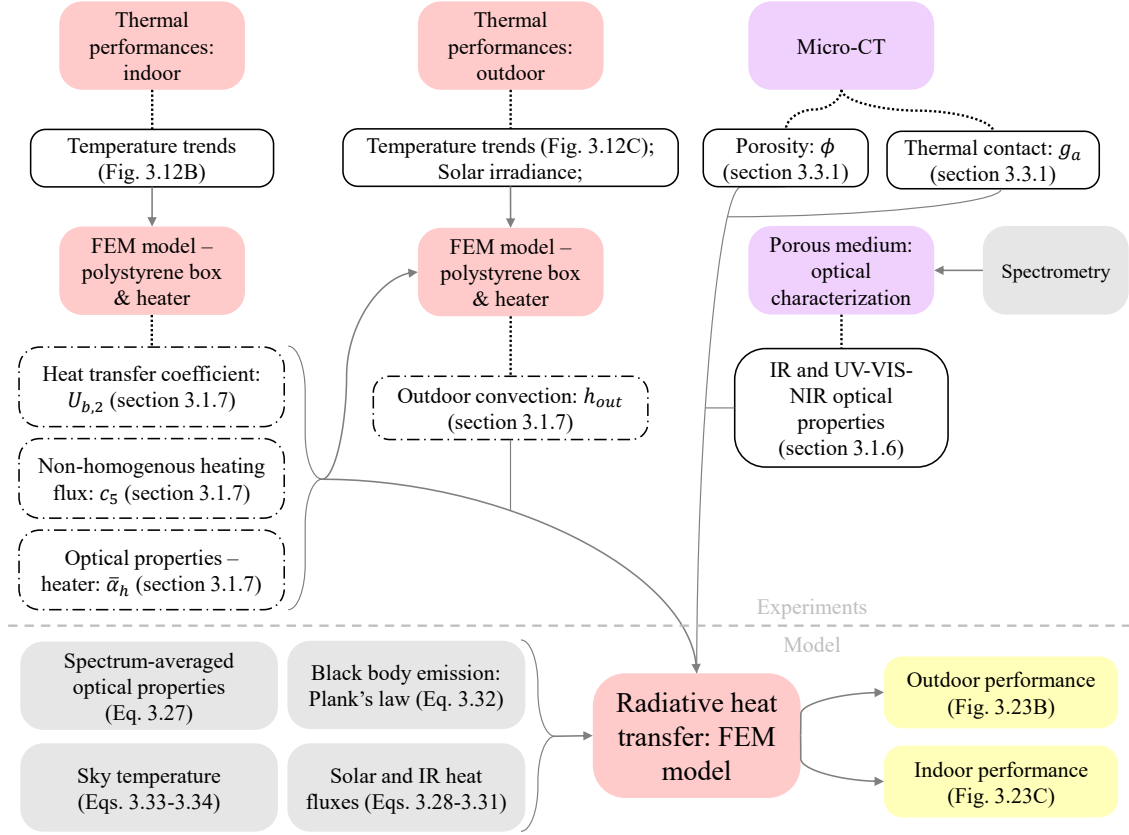


Figure 3.24: **Detailed procedure to investigate radiative heat transfer.** Graphical flow-charts of the procedure to calibrate and validate the radiative heat transfer model. Red boxes refer to experimental or modelling activity described in sections 3.1.6 and 3.3.3, respectively. White boxes indicate the result of each experimental or modelling step; white point-dashed boxes report the complementary results needed to characterise the experimental setup; the yellow boxes report the main outcome of the validation procedure.

The effect of different cooling capacities on the substrate temperature – which mimics the skin in personal thermal management applications – is represented in Figs. 3.26A-B, where the relative temperature difference between the dry and wet substrate (namely, $(T_{dry} - T_{wet})/T_{dry}$) in outdoor conditions was represented as a function of the ambient humidity and solar irradiance. In particular, Fig. 3.26A was obtained considering the optical properties of the proposed woven PE fabric (see Tab. 3.1), while Fig. 3.26A with the ideal optical properties in the IR spectrum which maximise its radiative cooling performances, $\bar{\tau}_f = 1$. Note that both the analysis were performed considering the optical properties of the fabric in the UV-VIS-NIR spectrum in Tab. 3.1. To simplify the visualisation of the obtained data, they are divided into three ranges of ambient temperature and input heat flux.

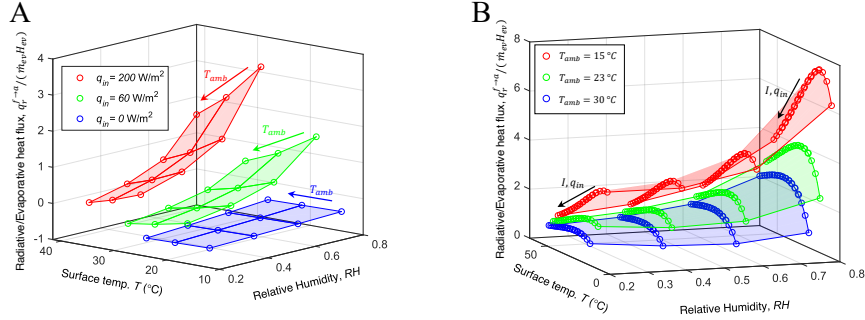


Figure 3.25: **Cooling performance of a PE fabric for personal passive thermal management at different ambient conditions.** (A) Analysis of the ratio between the radiative (IR) and evaporative heat fluxes from the fabric top surface in indoor conditions. For most of the configurations simulated, evaporation was found to be the principal cooling mechanism. (B) Analysis of the ratio between the radiative (IR) and evaporative heat fluxes from the fabric top surface in outdoor conditions for different environmental parameters. Differently from the indoor configuration, the radiative heat flux prevailed over evaporative one for low values of T_{amb} and high values of RH , q_{in} and I_{rr} .

As expected, the average temperature of the substrate surface is always lower if covered by a wet fabric (see Fig. 3.26A) despite presenting worse optical properties. The relative temperature difference remains within 20% for the lowest evaporation rates (namely, $RH = 80\%$), regardless the other ambient conditions, and progressively increases for lower values of RH . The largest relative differences, with a peak value of approximately 67%, are obtained for low values of ambient temperature, relative humidity, specific input heat flux and solar irradiance, coherently with the previous analysis of the cooling fluxes. Note that, in this condition, the surface temperature of the substrate is lower than 10 °C (see Fig. 3.26A), therefore large relative differences correspond to low absolute deviations. However, it is worth noting that the optimal configuration for maximizing the relative temperature difference between the two case studies (namely, favoring radiative heat transfer over evaporative cooling) corresponds to an ambient condition where, generally, cooling is not required for personal thermal management, namely at low temperatures. Nevertheless, even considering an ideally transparent porous textile (namely $\bar{\tau}_f = 1$), evaporation plays a crucial role (see Fig. 3.26B): when exposed to a solar irradiance of 1000 W m^{-2} , the wet textile was on average 11% and 27% colder with respect to the dry ideal fabric at $RH = 80\%$ (lower evaporation rate) and $RH = 20\%$ (higher evaporation rate), respectively.

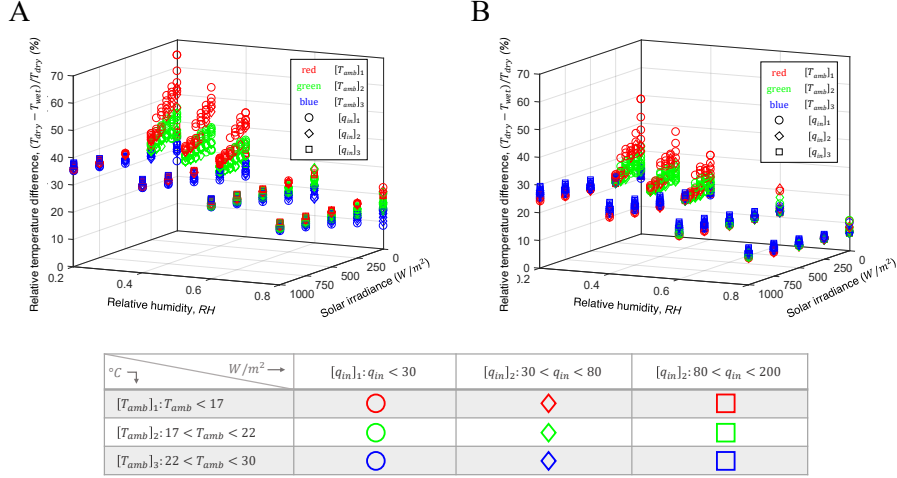


Figure 3.26: **Comparison between real and ideal fabrics for personal thermal management.** (A) Ratio between the surface temperature of dry and wet conditions in outdoor for the considered woven PE fabric and (B) for an ideal fabric with $\bar{\tau}_f = 1$. As expected, the average temperature of the simulated skin is lower if covered by a wet fabric, and this effect is more pronounced for high values of both I_{rr} and RH . The ranges of temperature and supplied heat flux reported in the legends of panels (A)-(B) are explained in the embedded table.

3.4 Conclusions

This Chapter investigated the feasibility of using polyethylene to realize engineered fabrics with enhanced radiative and evaporative cooling capabilities. Furthermore, it presented a comprehensive theoretical and experimental procedure to characterise and simulate water wicking and evaporation in capillary porous media in a systematic and self-consistent way.

The first part of the chapter was focused on the fabrication and experimental characterization of a plain woven PE fabric (see section 3.1). Polyethylene fibers were extruded by the project partners via melt spinning. To overcome the hydrophobic nature of polyethylene, which limits the use of PE for apparel manufacturing, the final step of the extrusion process was performed under a jet of air, which promoted a weak oxidation of their surface. As a result, the average water-fiber contact angle decreased by about 25% with respect to the theoretical value for pristine PE. Further exposure to oxygen plasma, performed in separate tests, demonstrated the possibility of additionally reducing the contact angle up to 45% compared to pristine PE (achieved after 10 minutes of exposure). Being hydrophilic, the fibers were woven into a fabric that exhibited exceptional capillary and drying performances, which were compared with those of other commercial fabrics: the PE sample dried 17% and 59% faster than polyester and cotton fabrics,

respectively, and exhibited capillary properties comparable to cotton and 35% better than polyester. The excellent performance achieved is due to the ability of PE fibers to drag water on their surface while remaining impermeable, thus preventing the fluid from penetrating inside the fibers themselves – which normally happens with natural fibers – and evaporate more quickly at low temperatures. Fast drying times are also important to ensure the hygiene of the material: low residence times of water in the fabric prevent the development of bacterial colonies or molds. Considering contexts where frequent washing of large quantities of fabrics is required, such as hospitals, this can translate into considerable energy savings. Finally, the proposed PE fabric presented a 25% transparency in the IR spectrum, considerably higher than the measured 5% of conventional cotton fabrics, allowing body heat to be dissipated more effectively via radiation. At the same time, PE fabric was sufficiently opaque to be worn (36% in the visible spectrum) and, similarly to cotton, was highly reflective in the solar spectrum (48% and 58% for the PE fabric and cotton, respectively), therefore shielding the user by incoming radiation.

The capillary properties observed experimentally was interpreted by the analytical model presented in section 2.2, relating micro-structural parameters such as fiber size, hydrophilicity, and arrangement to the resulting capillary properties and permeability. Although simplifying assumptions of ideality were used, it was shown that it is possible to optimize the fabric design to maximize its capillary performance, which, as shown by the evaporation tests, is crucial to achieve rapid diffusion and drying of the absorbed water or sweat.

Finally, experimental and modelling techniques were employed to evaluate the thermal performance of the woven PE textile. The objective was to determine which heat transfer mechanism prevails in a given working condition, outlining some guidelines for the rational design of novel materials for personal thermal management. The simulation results presented show the importance of optimizing the optical properties of textiles for personal thermal management purposes. When used indoors, evaporative cooling predominates in the case low metabolic rates apply (e.g., 60 W m^{-2} , typical of a resting adult), whereas radiative cooling only becomes relevant when considering moderate to intense physical activity (e.g., about 200 W m^{-2}) and humid environments (e.g., $RH > 50\%$). In contrast, radiative heat transfer is invariably relevant outdoors, making a contribution equal to or up to 7 times that of evaporative, especially in humid and cold environments.

As mentioned above, PE was never proposed before for garment production due to the poor breathability and wettability of the fibers, but it would reduce the environmental impact of the textile industry. In fact, as explained in Chapter 1, only a small percentage of the total amount of PE produced is recycled, despite several viable processes already exist on an industrial scale. This is due to the lack of economic viability of the single-use products most commonly fabricated: new types of high-value products made from PE can make its recycling profitable and help close the material life cycle. In contrast, commercially available fabrics with evaporative

cooling performance are typically composed of two or three layers of different materials, which complicates or prevents their recycling. Finally, accessories such as buttons, hooks, zippers and labels can be made from PE, enabling a single-material platform ideal for efficient automated recycling. A clear recycling pathway for PE fabrics and garments is expected to reduce the probability of them ending up in landfills. It can also offer an opportunity to recycle previously accumulated large amounts of PE waste, whose recycling is currently not economically viable due to the absence of added-value products.

Chapter 4

Multistage and passive cooling process driven by salinity difference¹

Chapter 3 proposed a new all-polyethylene fabric with enhanced cooling performance, while also offering the possibility of recycling low-value waste into single-material garments. Their proven radiative and evaporative cooling capabilities promise to contribute reducing the energy demand of cooling system during warm seasons; however, it remains unrealistic to imagine the complete replacement of traditional solutions such as HVAC systems in favor of personal thermal management technologies. Therefore, inspired by the works of Chiavazzo and co-workers [96] and Woods et al. [173], this Chapter proposes the design, realization and experimental characterization of a novel passive cooling device which aims to reduce the energy cost of buildings thermal management. Contrary to traditional refrigeration cycles, the proposed process is solely based on the evaporation and condensation of water from salt solutions operating within the device. By proposing a passive design, the cooling device can operate without relying on external high-quality energy input and in off-grid installations. This characteristic is made possible by capillarity, which allows to operate the working fluids without relying on mechanical moving parts or auxiliaries, and by concentration-driven evaporation processes. It's worth to point out that pumps will be typically needed only to extract the generated cooling load and, similarly, a fan for heat removal would be beneficial for improving performance, although not necessary when relying upon natural convection.

First, the Chapter focuses on the functioning principle, fabrication and characterization procedure of the cooling device. The core unit of the passive cooler –

¹Part of the work included in this chapter was also previously published by Alberghini et al. in Ref. [54].

based on commonly available materials – develops a net cooling capacity at nearly ambient pressure. This property is due to the spontaneous evaporation and condensation of water vapour, imposed by the different activities of two solutions separated by hydrophobic membranes, and to the capillary action naturally occurring within hydrophilic layers. On the one hand, the enthalpy of evaporation associated to the vapour flux generates temperature differences and a net heat flux across the device. On the other hand, the use of hydrophilic materials allows a passive supply of the liquid phase, without the need of active pumps. In a multi-core (or multi-stage) design, the proposed lab-scale prototype provided nearly 100 W m^{-2} maximum cooling capacity when it operates with a sodium chloride solution at 3.1 molal, while approximately 170 W m^{-2} with a calcium chloride solution at the same concentration.

Subsequently, a lumped parameter model was used to interpret the experimental results and to estimate the performance of the passive cooler under a wider range of operating parameters (e.g. different ambient temperature, number of stages or presence of an air gap above the membrane), thus allowing the optimization of the device layout. Straightforward applications of the suggested cooler can be found in hot or tropical regions where salt is naturally available (e.g. solar saltworks or salt mines) [174]. Alternatively, if combined with passive and low-cost solar distillation, the proposed device can pave the way to completely passive solar distillation/cooling cycles, where solar radiation is exploited for establishing salinity differences between solutions to be subsequently used for cooling purposes.

4.1 Functioning principle

The proposed device provides a cooling capacity Q by exploiting the salinity difference between two solutions (see a schematic in Fig. 4.1A). This salinity and thus vapour pressure difference between the solutions induces a net vapour flow from the evaporating to the condensing layer, thus generating the cooling capacity of a single-stage device. Multi-stage configurations are possible by employing the enthalpy of condensation of one stage to trigger the solvent evaporation in the subsequent one. These evaporation-condensation processes allow to remove heat from the lower-temperature chamber at temperature T_f and to transfer it into the higher-temperature external ambient ($T_{amb} > T_f$). The device is able to operate without any moving mechanical parts or auxiliary, and it can be therefore classified as a passive cooling technology. The tested lab-scale prototype of the passive cooler consists of four identical stages where, in each stage, a hydrophobic microporous membrane keeps two liquid phases separated by a submillimetre distance (see Fig. 4.1B). One liquid phase with high salinity is contained in a thin cavity at the top part of each stage and consists of a salt (e.g. sodium chloride) solution at fixed salinity; whereas, a second liquid phase with low salinity is embedded in a

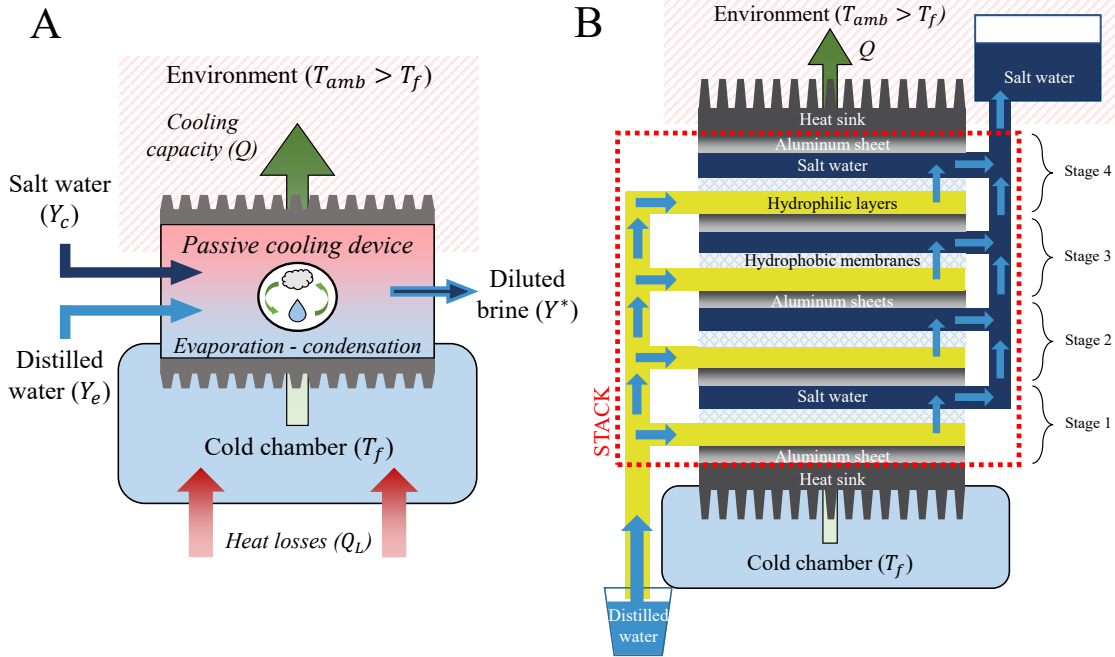


Figure 4.1: **Layout and schematics of the passive cooling device.** (A) Schematic of the working principle of the passive cooler: the salinity difference between two solutions generates a net vapour flux from the evaporating to the condensing layers. These evaporation-condensation processes in multiple stages allow to remove heat from the lower-temperature chamber and to transfer it into the higher-temperature external environment. (B) Schematic layout of the 4-stage modular passive cooler. The actual experimental setup adopted in the present work is reported in Fig. 4.3.

thin hydrophilic layer at the bottom part of the stage. In our setup, the latter liquid phase consists of distilled water. Each stage is sandwiched by two thin aluminum plates, which separate successive stages while easing conductive heat transfer through the device. A thin hydrophilic strip is connected to the hydrophilic layer located at the bottom of each stage and ensures a continuous supply of distilled water from a storage basin by capillary forces alone, without the need of a pump or any other circulation means. The salt water basin, instead, is positioned to induce a small hydraulic head (≈ 15 cm) in the condensers, thus ensuring their complete filling during operations. In general, heat sinks should be attached to the top and bottom sides of the cooler, to enhance heat transfer with the external environment and the refrigerated chamber, respectively.

A single stage of the cooler is detailed in Fig. 4.2A along with the characteristic driving forces of the process. The difference in salinity and thus water activity causes a vapour pressure disparity between the two liquid phases, which is in turn

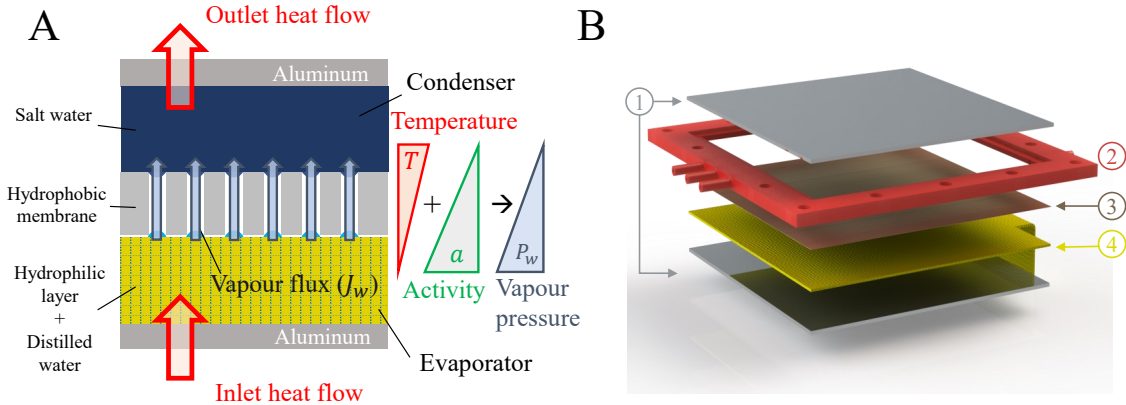


Figure 4.2: **Working principle of the passive cooling device.** (A) Working principle of one stage of the passive cooler: two solutions with different salinity are separated from each other by a hydrophobic membrane. Such salt concentration difference creates an activity gradient (green triangle), which leads to a net vapour flux. The transfer of enthalpy of evaporation establishes a temperature gradient between the two solutions (red triangle), which is opposed to the previous activity one. (B) Graphical representation of the assembly of one stage of the cooling device. A 3D-printed plastic frame (2, red) hosts the cavity forming the condenser, which is sealed by an aluminum plate (1, grey) and a hydrophobic membrane (3, brown), respectively. The hydrophilic layer (4, yellow), that is the evaporator, is placed between the membrane and another aluminum plate.

responsible for a net water vapour flux from distilled water (i.e. evaporator) to salt solution (i.e. condenser). A transfer of enthalpy of evaporation occurs in this process, and this establishes a temperature difference across the membrane: salt water in the cavity is heated up, while distilled water in the hydrophilic layer is cooled down. Such temperature gradient across the membrane is opposed to the activity gradient, therefore reducing the net vapour flux. As a result, the actual working condition of each stage of the cooler comes from a balance between the contrasting temperature and activity effects on the overall vapour pressure across the membrane (see section 4.4).

The main components of our specific realization of one cooling stage are shown in Fig. 4.2B. Each stage is implemented in a 3-D printed plastic frame, which is made of acrylonitrile butadiene styrene (Dimension Elite, Stratasys) treated with a polymeric sealer (Nano-Seal 180W, Jeln). The hydrophobic membrane is made of polytetrafluoroethylene (1.0 μm pores, ANOW Microfiltration, see section 4.3 for a detailed characterisation), and it is glued to the bottom side of the plastic frame. The top side of the plastic frame, instead, hosts a 2 mm cavity containing salt water, which is enclosed by an upper aluminum plate (1 mm thickness). The hydrophilic layer impregnated by distilled water and positioned below the membrane is made

of microfibre, and it is supported by a bottom aluminum plate (1 mm thickness). The cooling prototype has an effective thermal area of $A_{net} = 1.69 \cdot 10^{-2} \text{ m}^2$. It is worth to point out that our cooling device is highly modular and flexible: depending on the target cooling capacity, a variable amount of stages could be easily assembled, and different salt solutions adopted (below the saturation limit, at operating temperature).

4.2 Device characterization

4.2.1 Experimental setup

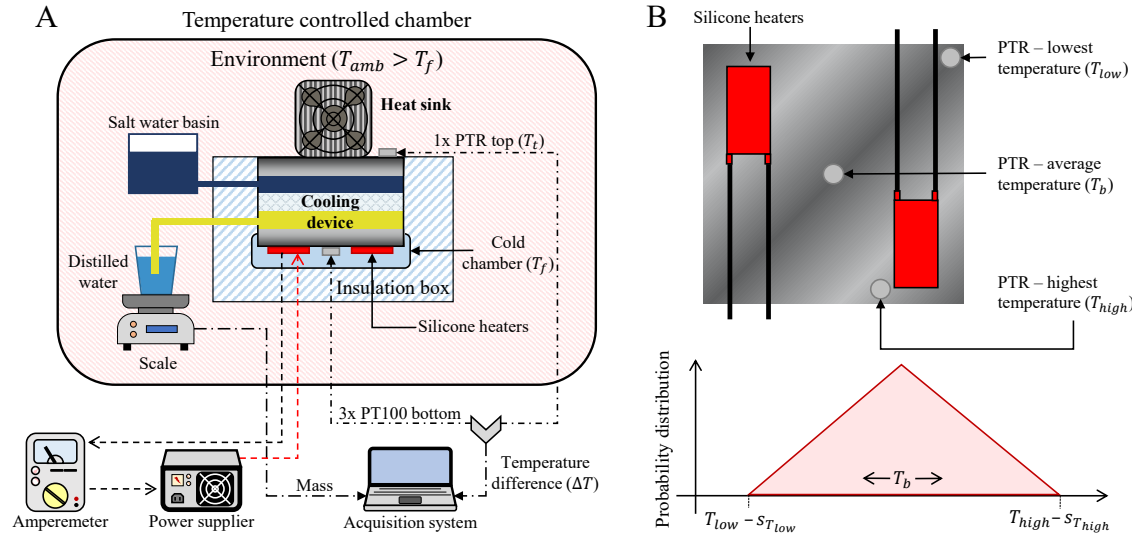


Figure 4.3: **Experimental setup to measure cooling capacity.** (A) Schematic of the experimental setup adopted to assess the cooling capacity of the passive cooler. For the sake of simplicity, only a single stage of the cooling device has been represented here. The acquisition system was employed to measure the temperature difference across the device (ΔT) and the weight (m) of distilled water in the basin. (B) Schematic of the positioning of the silicone heaters and the three thermoresistances on the first-stage evaporator of the device. The highest and lowest temperatures measured on the plate, namely T_{low} and T_{high} , and their uncertainties were used to evaluate the uncertainty of the average plate temperature (T_b) as explained in Appendix B.

To assess the performances of the cooling device, the test rig represented in Fig. 4.3 was implemented. The experimental setup includes a temperature-controlled test chamber, the prototype of passive cooler and two flat silicone heaters with their power supplier. Four 100- Ω thin film platinum resistance thermometers (PRTs), a

DC amperemeter, a precision balance and a digital refractometer were employed for measuring temperatures, heat flux, distillate mass and salinity of aqueous solutions, respectively. The passive cooler was tested in a chamber with controlled temperature (M120-VF oven, MPM instruments), which mimics the external environment at fixed T_{amb} . The cooler prototype (pictured in Fig. 4.4) was enclosed in a polystyrene box to minimise the thermal losses towards the chamber: the last-stage condenser (i.e. the aluminum sheet on the top surface of cooler) was the only side of cooler in direct contact with the surrounding ambient during tests. This side was glued (heat sink compound with $0.65 \text{ W m}^{-1} \text{ K}^{-1}$ thermal conductivity, RS Pro) to a forced convection heat sink (convective heat transfer coefficient equal to $728 \text{ W m}^{-2} \text{ K}^{-1}$), to improve heat transfer with the controlled temperature chamber. Two flat silicone heaters (57.6Ω , Franco Corradi) powered by an electric power supplier (PS 3003, HQ Power) were glued to the bottom aluminum plate of cooler (i.e. first-stage evaporator), to provide an adjustable heat flux [95]. The hydrophilic strips connecting evaporators with the distilled water basin were covered by a polyethylene film to minimize water evaporation in the environment. The cooler assembly was kept together by four M5 bolts through the corners of the plastic frames. The temperature of the first-stage evaporator and last-stage condenser were measured to estimate the temperature drop across the cooler prototype. To this purpose, four $100\text{-}\Omega$ PRTs (IEC 60751 tolerance class AA, TC Direct) were employed, and their signal was acquired by a dedicated data acquisition system - DAQ (PicoLog PT104, Pico). The $100\text{-}\Omega$ PRTs were glued to the aluminum sheets in contact with the first-stage evaporator and last-stage condenser, respectively. A DC amperemeter (34401A, Agilent) was adopted to measure the electric current flowing through the heaters and, thus, the thermal power supplied to the first-stage evaporator. The distilled water consumed by evaporators was assessed through a precision balance (PS1000 R2, Radwag). A digital refractometer (HI 96801, Hanna Instruments) was used to monitor the salinity of salt water and distillate basins and to check the possible contamination of evaporators at the end of each test.

4.2.2 Experimental protocol

Different thermal loads were applied to the cooler prototype through the silicone heaters, to explore its characteristic operating curve $q\text{-}\Delta T$. Since the polystyrene envelope does not guarantee a perfect insulation from the external environment, heat losses were estimated to correctly evaluate the specific heat flux removed by the cooler q . The thermal conductance G of the polystyrene envelope was computed as $G = Q/\Delta T$, after providing a constant heat flux from the silicone heaters and then measuring the resulting temperature difference by means of the PRTs. Four independent tests were performed, and the obtained average value was equal to $G = (8.5 \pm 0.6) \cdot 10^{-2} \text{ W K}^{-1}$ (see Appendix B for details). Therefore, the actual

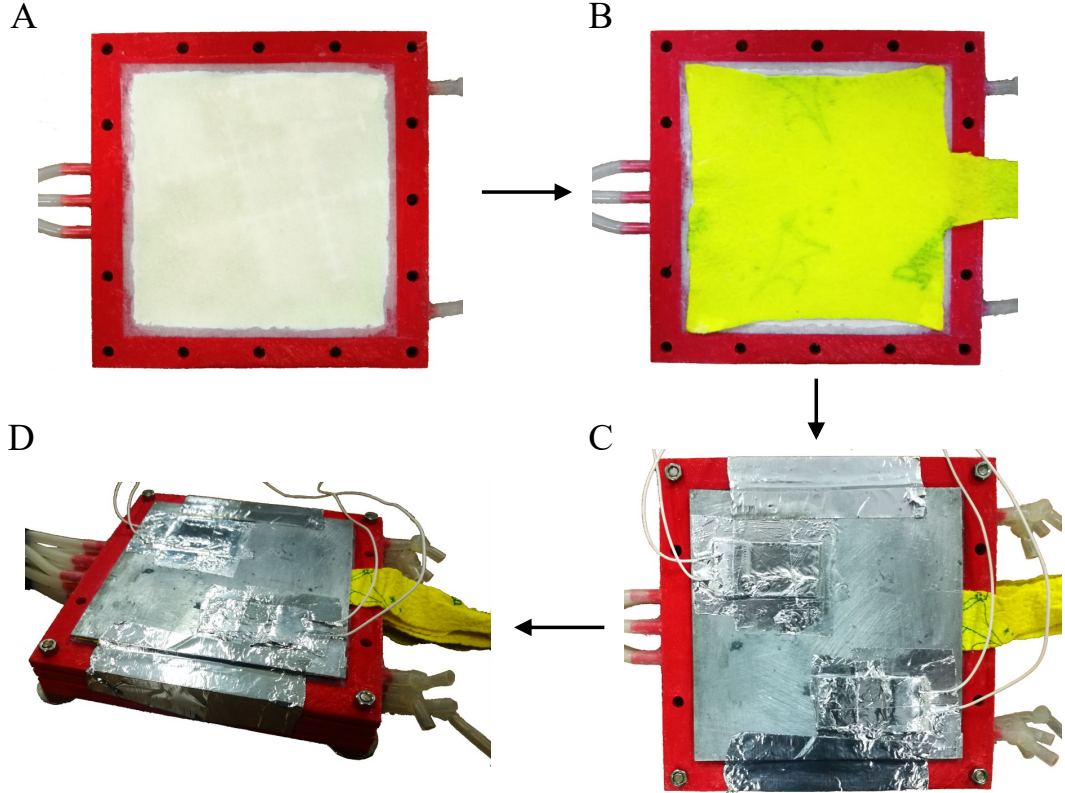


Figure 4.4: **Assembly of the passive cooling device.** The main components of the tested prototype of cooler and the assembly process are pictured. **(A)** Assembly of the first stage of cooler, which is in contact with the silicone heaters. The plastic frame (red, acrylonitrile butadiene styrene) supports the membrane (white, PTFE with pore size $1.0 \mu\text{m}$ and thickness approximately $0.1 \mu\text{m}$). On the top side of the membrane (i.e. first-stage condenser), salt water is supplied through three plastic tubes, which can be seen on the left-hand side of the plastic frame; on the bottom side of the membrane (i.e. first-stage evaporator), distilled water is supplied through **(B)** a hydrophilic layer (yellow, microfibre). **(C)** A rigid plate (grey, aluminum) separates the first-stage evaporator from the two silicone heaters. **(D)** Assembled cooling device with 4-stage, where the first stage is still visible at the top.

specific thermal power removed by the cooler in each test was calculated as:

$$q = \frac{Q + Q_L}{A_{net}}, \quad (4.1)$$

where $Q = VI$, I and V are the electric current and voltage supplied to the heaters, $Q_L = G(T_A - T_B)$ are the thermal losses, T_{amb} is the temperature of environment where the cooler operates, T_b is the average temperature of first-stage evaporator

and A_{net} is the effective thermal area of the passive cooling device. During tests, the temperature difference across the cooler prototype ΔT was measured by four PRTs to allow an estimation of temperature uniformity and the associated temperature uncertainty of the tests: one was placed in the centre of the last-stage condenser, whereas other three were attached in different positions of the first-stage evaporator (centre of aluminum sheet, closest and farthest point from the heaters, see Fig. 4.3B). The specific flow rate of distilled water (J , $\text{m}^3 \text{s}^{-1} \text{m}^{-2}$) consumed by evaporators was evaluated as:

$$J = \frac{\Delta m}{\rho A_{net} \Delta t} - J_{ev}, \quad (4.2)$$

where Δm is the weight difference of distillate basin between the beginning and the end of each test (with Δt duration), ρ is the density of distilled water and J_{ev} is the specific flow rate of distilled water evaporated in the environment from the basin and the hydrophilic strips before entering the evaporators, therefore not providing any useful effect. The latter has been measured as $J_{ev} = 0.22 \text{ L m}^{-2} \text{ h}^{-1}$ by monitoring the distillate basin weight with time when the evaporation-condensation processes in the cooler were inhibited by the application of impermeable polyethylene films above the membranes, in each cooling stage.

4.3 Measurement of the membrane resistance coefficient

The hydrophobic membrane resistance coefficient B (see section 2.6) is a crucial parameter to determine the performance of the proposed cooling device. First, the value of B was experimentally measured for the membranes used in the device; second, the experimental results were compared with their theoretical counterpart. Once validated, the transport model reported in section 2.6 was used to evaluate the effect of different membrane parameters, typical of commercialized models, on the achievable cooling capacity.

The hydrophobic microporous membrane employed in the passive cooling device was made of polytetrafluoroethylene (PTFE) and characterised by pores with nominal diameter of $1.0 \mu\text{m}$ (ANOW Microfiltration). The resistance coefficient B of the membrane is experimentally measured by means of a diffusion cell (PermeGear 15 mm Side Bi Side Cell, 7 mL volume). Such experimental setup is composed by two cavities filled respectively with distilled and salt water separated from each other by the hydrophobic membrane, which is in direct contact with the two solutions. Each chamber communicates with the environment through a graduated capillary tube, which allows to visualize the free surface of liquid. If the two cavities are kept at the same temperature during experiments, water vapour flows through the membrane following the activity gradient, namely from distilled to salt water side,

and this causes a variation in the liquid levels in both capillary tubes. The water level at the salt water side is measured every hour with a high-resolution camera, in order to evaluate the specific mass flow rate J_w of water vapour through the membrane. The average air temperature T_{amb} of the room is monitored by an ambient thermometer. Two magnetic stirrers are used to avoid both ion polarization and temperature boundary layer at each side of the membrane. The membrane resistance coefficient was then computed as:

$$B = \frac{J_w}{A \Delta P_w}, \quad (4.3)$$

where A is the active surface of the membrane and ΔP_w is the vapour pressure difference across the membrane, which depends on the temperature and activity coefficients of water in the two solutions. Notice that J_w was computed by linearly fitting (least square method) the salt water level measured in the graduated capillary tube with time, over more than 9 hours of test. Five independent measurements of B were performed, obtaining: $(6.4 \pm 1.0) \cdot 10^{-7} \text{ kg m}^{-2} \text{ Pa}^{-1} \text{ s}^{-1}$; $(5.9 \pm 0.9) \cdot 10^{-7} \text{ kg m}^{-2} \text{ Pa}^{-1} \text{ s}^{-2}$; $(8.7 \pm 1.2) \cdot 10^{-7} \text{ kg m}^{-2} \text{ Pa}^{-2} \text{ s}^{-2}$; $(6.7 \pm 1.0) \cdot 10^{-7} \text{ kg m}^{-2} \text{ Pa}^{-1} \text{ s}^{-1}$; $(6.2 \pm 1.0) \cdot 10^{-7} \text{ kg m}^{-2} \text{ Pa}^{-1} \text{ s}^{-1}$. Finally, the results were averaged and the expanded uncertainty estimated considering a coverage factor $k = 2$, which for a normally distributed probability is equivalent to a confidence interval of 95%. Concluding, the value of membrane resistance coefficient estimated by the model is equal to $B = (6.8 \pm 1.5) \cdot 10^{-7} \text{ kg m}^{-2} \text{ Pa}^{-1} \text{ s}^{-1}$, in good agreement with the experimental one, that is $B = (6.8 \pm 1.1) \cdot 10^{-7} \text{ kg m}^{-2} \text{ Pa}^{-1} \text{ s}^{-1}$ (see Fig. 4.5).

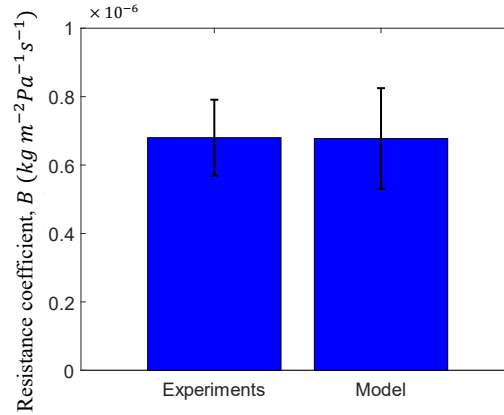


Figure 4.5: **Experimental results and modelling predictions of membrane resistance coefficient.** The upper and lower bounds of the parameters employed for the modelling computations are shown in Tab. S2: the modelled value of the membrane resistance coefficient was evaluated by averaging the values obtained combining the three parameters listed, while the related error bar estimated considering their standard deviation.

4.4 Lumped-parameters heat transfer model

The experimental performance of the prototype was interpreted by a theoretical model comprising the mass transfer through hydrophobic membranes and a lumped-parameter representation of the device layout. By relying on the electrical network analogy, the temperature distribution within the cooling device was evaluated by defining some nodes within its stratigraphy and, analogously to the Kirchhoff's law, imposing energy conservation in each node, namely: $\sum_i q_i^j = 0$, where q_i^j represents the i -th specific heat flux entering or exiting the j -th node. Here, two possible heat fluxes were considered: latent heat fluxes due to the evaporation/condensation of water, and conductive heat fluxes through adjacent nodes; thermal losses towards the distilled and salt water reservoirs were neglected motivated by the low thermal conductivity of water and synthetic fibers.

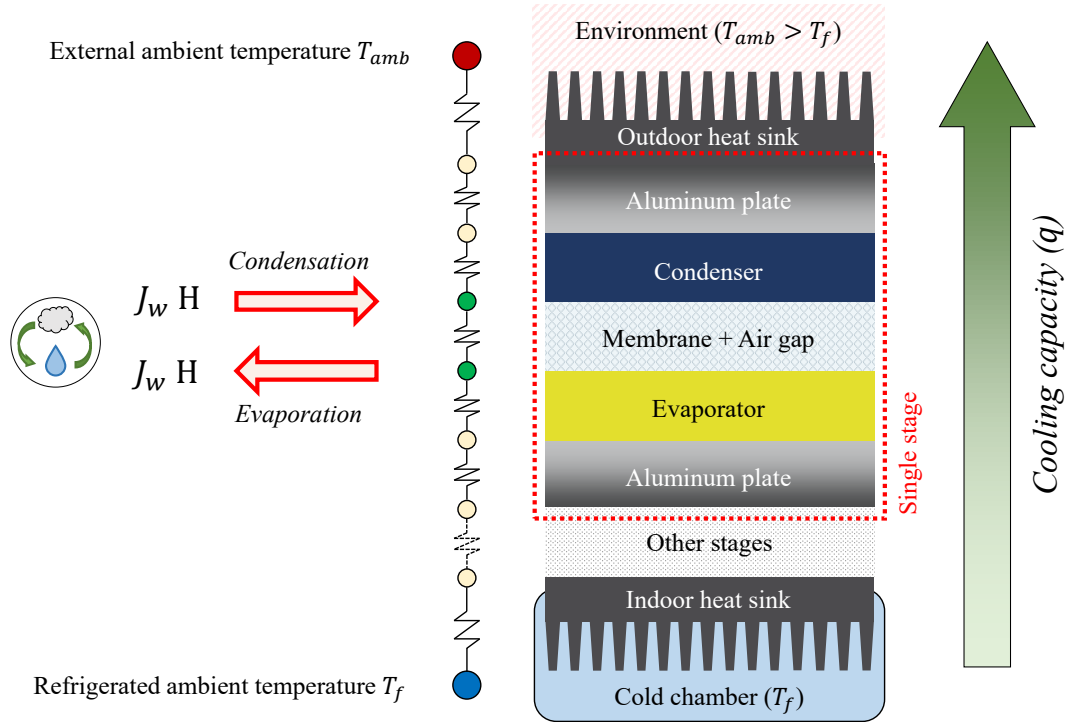


Figure 4.6: **Lumped model for the heat transfer in the passive cooler.** Association between the lumped thermal resistances represented in the picture and the different parts of the multi-stage passive cooler. The evaporation and condensation of water in the evaporators and condensers generate the additional transfer of enthalpy of evaporation through the stages (see the red arrows), which is responsible of the cooling capacity of the device.

A schematic of the equivalent thermal network for a single stage is shown in Fig.

4.6. The net vapor fluxes through the membranes determine the cooling capacity generated in each stage (see red arrows in Fig. 4.6) and was evaluated according to the mass transfer model described in section 2.6. Consistently with the procedure used to derive the net mass flux through the membrane, the nodes of the network were placed below each membrane and above each air gap (green nodes in Fig. 4.6), while the other nodes were unified by considering their resistances as in series (yellow nodes). Thus, considering an n -stages device, $2n+2$ nodes can be identified, including two nodes for the top and bottom layers with temperatures T_t and T_b , respectively. These two additional nodes were used to estimate the temperature difference across the device $\Delta T = T_t - T_b$. The energy conservation of the top and bottom layers, namely the last and first nodes of the thermal network, respectively, were expressed as:

$$\begin{aligned} 0 &= \frac{T_c^n - T_t}{R_t} - \frac{T_t - T_{amb}}{R_{hs}} \\ 0 &= q - \frac{T_b - T_e^1}{R_b}, \end{aligned} \quad (4.4)$$

where the superscripts of the condensers and evaporators temperatures refer to their position in the thermal network; q is the specific thermal load applied to the cooler (therefore, extracted from the conditioned environment); $R_{hs} = 1/h_{hs}$ is the thermal resistance of the top heat sink, characterized by a convection coefficient h_{hs} which, for the sake of simplicity was assumed as $h_{hs} \rightarrow \infty$, implying $T_t \rightarrow T_{amb}$; $R_t = (d_c/\lambda_c + d_{al}/\lambda_{al})$ is the thermal resistance between the last-stage condenser and the top layer of the device, composed of $d_c = 2$ mm of water and an aluminum plate with thickness $d_{al} = 1$ mm; $R_b = (d_{ev}/\lambda_{ev} + d_{al}/\lambda_{al})$ is the thermal resistance between the first-stage evaporator and the bottom layer of the device. Note that, while $\lambda_{al} = 290 \text{ W m}^{-1} \text{ K}^{-1}$ and $\lambda_c = 0.6 \text{ W m}^{-1} \text{ K}^{-1}$ were evaluated from the respective material properties, the thermal conductivity of the evaporators was evaluated as the porosity-weighted average of the thermal properties of water and synthetic fabric, namely: $\lambda_{ev} = \phi_{ev}\lambda_f + (1 - \phi_{ev})\lambda_m$, with $\phi_{ev} \sim 0.9$ (see its characterization in Chapter 5), $\lambda_f = 0.6 \text{ W m}^{-1} \text{ K}^{-1}$ and $\lambda_m = 0.25 \text{ W m}^{-1} \text{ K}^{-1}$. Note that, as T_f is solely determined by the performance of the bottom heat sink and by other factors not related with the investigated device, this study assumed $T_f \rightarrow T_b$. Similarly, the nodes equations for the last-stage condenser and the first-stage evaporator were respectively expressed as:

$$\begin{aligned} 0 &= -\frac{T_c^n - T_e^n}{R_{me}} - \frac{T_c^n - T_t}{R_t} + J_w^n H \\ 0 &= \frac{T_b - T_e^1}{R_b} + \frac{T_c^1 - T_e^1}{R_{me}} - J_w^1 H, \end{aligned} \quad (4.5)$$

where $J_w^j H$ is the thermal flux due to the evaporation/condensation process of the vapour flux J_w^j (expressed in $\text{kg m}^{-2} \text{ s}^{-1}$ and referred to the j -th stage); $R_{me} =$

$(d_{me}/\lambda_{me} + d_a/\lambda_a)$ is the combined thermal resistance of the membrane and air gap layer, where their equivalent thermal conductivity was evaluated as the porosity-weighted average between air and a polymer thermal conductivity. Similarly, the nodes equation of any other evaporator and condenser of the j -th stage in the network were respectively be expressed as:

$$\begin{aligned} 0 &= \frac{T_c^j - T_e^j}{R_{me}} + \frac{T_c^{j-1} - T_e^j}{R_c} - J_w^j H \\ 0 &= -\frac{T_c^j - T_e^j}{R_{me}} - \frac{T_c^j - T_e^{j+1}}{R_c} + J_w^j H, \end{aligned} \quad (4.6)$$

where $R_c = (d_c/\lambda_c + d_{al}/\lambda_{al} + d_{ev}/\lambda_{ev})$ is the equivalent thermal resistance between the condenser node of stage j -th and evaporator node of stage j -th+1, comprising a water cavity, aluminum plate and hydrophilic porous layer.

The evaluation of the latent contribution $J_w H$ requires some considerations about the heat transfer across the membrane and air gap layer. Considering an elementary layer element dz , Eqs. 4.4 and 4.5 was combined to evaluate the specific heat flux flowing from an evaporator (hydrophilic layer) to a condenser (salt water cavity):

$$q = J_w H(Y, T) - \lambda_{me} \frac{dT}{dz}, \quad (4.7)$$

where λ_{me} is the effective thermal conductivity of the considered layer, which can be assumed as a constant being $\lambda_{me} \sim \lambda_a$, and H is the enthalpy of vaporization of water, which depends on the salinity Y and temperature T of the solution.

As it can be observed, both J_w and H depend on the feed salinity and temperature (see Eq. 2.106 for the expression used to evaluate J_w across a membrane and an air gap). Note that the temperature is not constant within the layer and changes progressively passing from evaporator to condenser. To determine the relationship between these quantities and evaluate the temperature profile across the layer, the contribution of H can be broken down into its latent and sensible contributions considering the following hypothetical process: on the evaporator side, liquid water is heated from temperature T to a generic reference temperature T_r , evaporates at reference salinity Y_r , and, subsequently, the water vapour is cooled down from T_r to T [144]. This process was formalized as:

$$\begin{aligned} H(Y, T) &= c_{p,l} (T_r - T) + H(Y_r, T_r) - c_{p,w} (T_r - T) = \\ &= H(Y_r, T_r) - \Delta c_p (T - T_r), \end{aligned} \quad (4.8)$$

where $c_{p,l}$ and $c_{p,w}$ are the isobaric specific heat capacities of the liquid and vapour phases of water, respectively, and $\Delta c_p = c_{p,l} - c_{p,w}$. Note that, for the sake of simplicity, the effect of salinity on $c_{p,l}$ was neglected. Eq. 4.8 was substituted into Eq. 4.7, obtaining:

$$q = J_w [H(Y_r, T_r) - \Delta c_p (T - T_r)] - \lambda_{me} \frac{dT}{dz}. \quad (4.9)$$

Eq. 4.9 was re-arranged to evaluate the following differential equation:

$$\frac{dT}{dz} + \frac{J_w \Delta c_p}{\lambda_{me}} T = \frac{J_w (H(Y_r, T_r) + \Delta c_p) - q}{\lambda_{me}}, \quad (4.10)$$

which, for the sake of simplicity, can be rewritten in the form $T' + AT = B$, where A and B are constant parameters. The solution of Eq. 4.10 has the form $T = c_1 \exp(-Az) + B/A$, where the constant c_1 can be evaluated considering as boundary initial condition $T|_{z=0} = T_e$, leading to the following expression of the temperature profile:

$$T(z) = \frac{B}{A} + \left(T_e - \frac{B}{A}\right) e^{-Az}. \quad (4.11)$$

Considering that both the membrane and air gap thicknesses are in the order of 10^{-4} m, Eq. 4.11 was rewritten considering its first-order Taylor expansion around 0, leading to:

$$T(z) = T(0) + T'(0)z = T_e - A \left(T_e - \frac{B}{A}\right) z, \quad (4.12)$$

which, considering that $T|_{z=d_{me}+d_a} = T_c$, leads to $B = (T_c - T_e)/(d_{me} + d_a) + T_e A$. Recalling the definitions of A and B , and considering that $R_{bm} = (d_{me} + d_a)/\lambda_{me}$, the former equation was rearranged as:

$$q = J_w H(Y_r, T_r) - \frac{T_c - T_e}{R_{me}}. \quad (4.13)$$

Therefore, by posing the evaporator temperature and salinity as reference conditions, Eq. 4.13 shows how to evaluate the enthalpy of vaporization as a function of the temperature profile within the device and can be used to analyse the contributions of the different parameters to the achievable specific cooling capacity. Since the heat and mass transfer phenomena are intrinsically coupled, the model was solved iteratively for a given working condition (namely, given a target value of q).

The lumped-parameters heat and mass transfer model is a useful tool to evaluate the impact of different configurations and working conditions on the performance of the cooling device. As an example, Fig. 4.7A reports the temperature distribution within a 4-stage device for increasing values of extracted specific heat flux q . As it can be observed, higher values of q increase the temperature difference between each stage (e.g., see the temperature drop between the nodes 1-C and 2-E), thus reducing the achievable ΔT across the device. The characteristic zigzag pattern of the temperature distribution is due to evaporation (in nodes marked E) and condensation (in nodes marked C) processes, thus dictated by the membrane transport properties. Fig. 4.7B investigates the effect of different numbers of stacked stages on the achievable ΔT at fixed $q = 50 \text{ W m}^{-2}$ and $T_{amb} = 30^\circ\text{C}$, suggesting a proportionality between these two factors. As demonstrated, the proposed model is crucial to optimize the performance of this technology. Therefore, the model

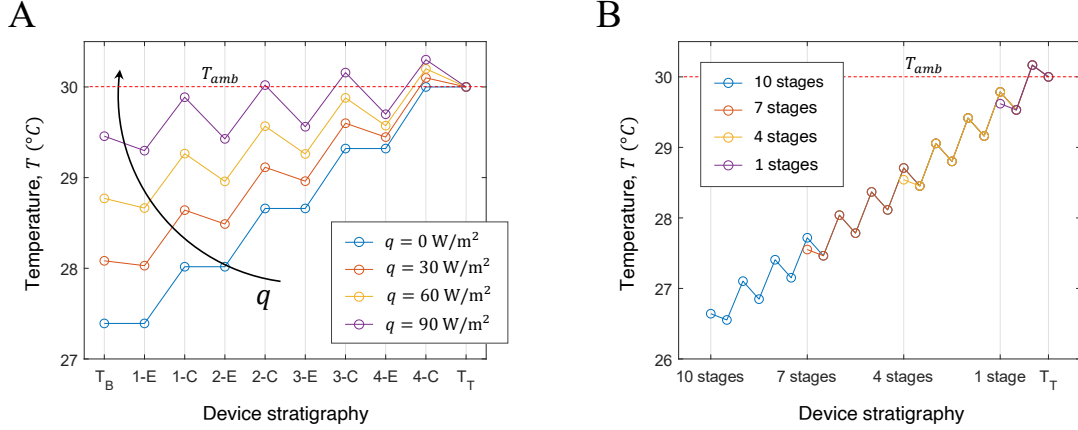


Figure 4.7: **Temperature profile within the cooling device.** (A) Temperature profile within a 4-stage device when operating with a salty feed at $Y = 170 \text{ g/L}$ for increasing extracted thermal load q . (B) Temperature profile obtainable stacking 1, 4, 7 and 10 stages when extracting $q = 50 \text{ W m}^{-2}$.

was first validated against experimental results (see section 4.5) and then used to extrapolate the performance of different configurations of the passive cooling device when subjected to different operating conditions (see section 4.6).

4.5 Cooling performance: experimental investigation

The cooling performance of a 4-stage prototype was assessed employing the test rig shown in Fig. 4.3A, considering constant ambient temperature $T_{amb} = (30.0 \pm 0.5) \text{ °C}$ and salinity of NaCl-water solution $Y_c = (170 \pm 2) \text{ g L}^{-1}$. Thirteen independent tests have been carried out to obtain the characteristic $q - \Delta T$ curve of the cooler, being q the specific cooling capacity (i.e., the extracted heat flux normalized by A_{net}) and $\Delta T = T_t - T_b$ the temperature difference between the first-stage evaporator and last-stage condenser (see Fig. 4.7). During the experiments, a heat sink was placed between the last-stage condenser and the external ambient; whereas, all the other sides of the prototype were covered by insulating material to reduce thermal losses. In each test, the prototype was subject to a specific thermal load q supplied by two silicon heaters positioned below the first-stage evaporator (see Fig. 4.3B and Fig. 4.4), therefore leading to a steady state value of ΔT . The minimum cooling capacity was achieved when the electrical heaters were switched off: in this conditions, the thermal power removed by the cooler only accounted for the thermal losses, thus the maximum ΔT could be observed. When heaters were switched on, the cooling capacity increased and thus ΔT reduced. Fig. 4.8A

presents the typical time evolution of the temperature of external environment (green line), first-stage evaporator (blue line) and last-stage condenser (red line) of the prototype, during a test with an applied thermal load of $q = 25 \text{ W m}^{-2}$. When the cooler started to operate ($t = 0 \text{ s}$), the condenser temperature rapidly increases above T_{amb} , therefore allowing a net heat flux from the condenser to the surrounding environment. At the same time, the evaporator temperature decreases below T_{amb} , therefore providing a cooling effect. The device was considered to have reached steady state conditions when each measured temperature presented variations lower than $3 \cdot 10^{-4} \text{ K s}^{-1}$ over 150 samples. The operating ΔT achieved for a specific q was then evaluated by computing the temperature difference between the first-stage evaporator and last-stage condenser, obtained by averaging a 1500 s time interval at the steady state. Since experiments were performed in batch, namely with a fixed amount of distilled and salt water in the respective feeding basins, the vapour flux from the evaporators progressively dilutes the salt solution in the condensers, therefore gradually reducing the difference in chemical potential across the membrane. As noticeable in Fig. 4.8A, this leads to a progressive reduction in the cooling performances of the device. As a matter of fact, a stable functionality for longer times could be eventually achieved by continuously regenerating the salinity gradient through the membrane.

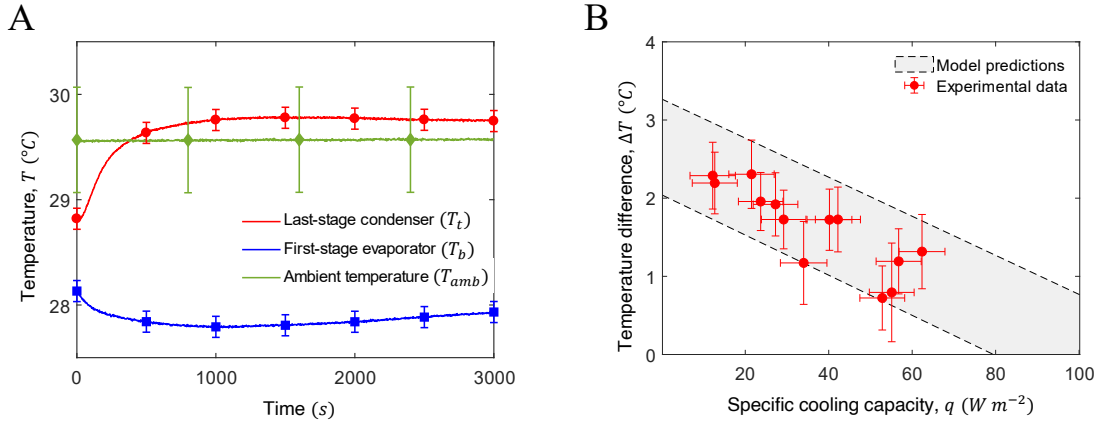


Figure 4.8: **Experimental cooling performance.** (A) Time evolution of the last-stage condenser (red), first-stage evaporator (blue) and ambient (green) temperatures during a typical laboratory test with the 3.1 molal NaCl solution applying a thermal load of 25 W m^{-2} . (B) Experimental results (red dots) and modelling predictions (grey band) of the specific cooling capacity of the passive cooler with respect to the considered temperature difference across the device with the 3.1 molal NaCl solution. The reported band is enclosed between the minimum and maximum values obtained by varying the main input parameters of the model according to the bounds reported in Tab. S2.

The obtained $q - \Delta T$ characteristic curve of the prototype is reported with red

circles in Fig. 4.8B. The maximum cooling capacity achieved by the prototype – corresponding to a vanishing temperature difference across it – was extrapolated by a first order polynomial interpolation of the experimental results, and was approximately equal to 100 W m^{-2} . From this condition, a progressive increase in ΔT causes a reduction of the specific cooling capacity, as a greater part of the enthalpy of vaporization is devoted to contrast the sensible heat flux across the device. At the limit, when the thermal power removed by the cooler is null, the evaporation-condensation process is entirely addressed to maintain the maximum achievable ΔT , which is found to be approximately 3 K. Clearly, the average consumption of distilled water by the evaporators increases with q , with values in the range $2.3\text{-}3.0 \text{ L m}^{-2} \text{ h}^{-1}$ (see Fig. 4.9A). Notice that – for the whole duration of tests (2 months) – no fouling or scaling was observed on the hydrophobic membranes or hydrophilic layers and, therefore, no significant degradation of cooling performances was noticed for the tested prototype over time.

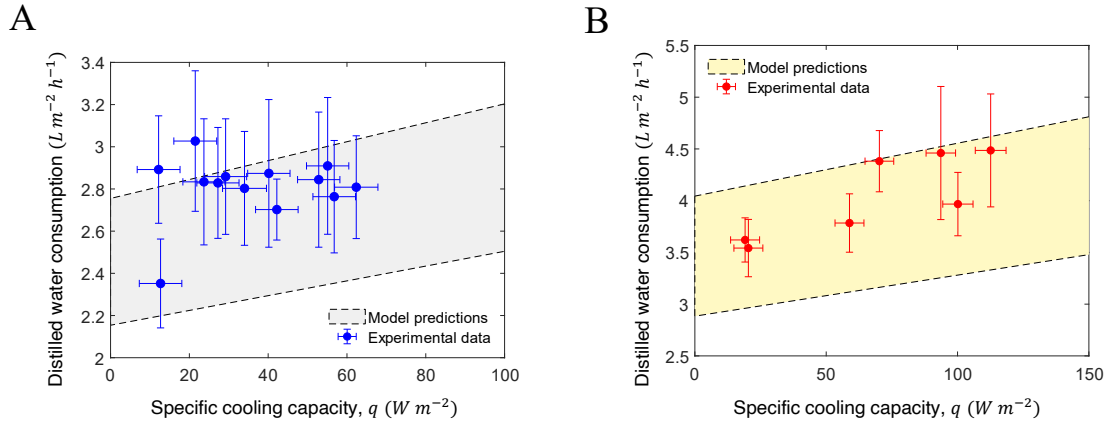


Figure 4.9: **Distillate consumption by the passive cooler.** Experimental results and modelling predictions of the distilled water consumption by the passive cooling device during laboratory tests, considering 3.1 molal (A) NaCl and (B) CaCl_2 solutions at the condenser side.

The obtained experimental results were then compared with the predictions obtained by the lumped-parameters model described in section 4.4 and reported as a grey band in Fig. 4.8B. Modelling predictions display a reasonably good agreement with the experimental measurements, at least within the model’s interval of uncertainty. The reported band of uncertainty was estimated considering the highest and lowest predictions obtained within the explored interval of model parameters: boundary values of the model parameters were identified according to their uncertainty, and all their combinations were explored.

Despite being based on evaporation, the working principle of the proposed device is substantially different from adiabatic evaporative cooling, which is one of the

simplest non-cyclical passive cooling approaches. It is well-known, though, that the maximum temperature difference and the maximum achievable cooling load are both strongly dependent on the intermittent value of the atmospheric relative humidity, with vanishing performance at nearly saturation conditions. It follows that evaporative cooling may be not effective in regions with very high humidity levels (e.g. tropical and sub-tropical regions). On the contrary, a system exploiting salinity differences is not affected at all by the atmospheric humidity value. As an example, consider the average summer conditions in Dubai, where temperatures can be in the order of 40 °C and the relative humidity about $RH = 90\%$ during the summer season [175]. Under these conditions, the maximum temperature difference achievable by evaporative cooling (therefore neglecting the effect of convection) can be estimated by the psychrometric plot, which reports a ΔT of 1.7 °C and 3.5 °C for $RH = 90\%$ and $RH = 80\%$, respectively. On the other hand, the water evaporation rate through a surface S can be estimated by the Hertz-Knudsen equation (Eq. 3.13, see section 3.3.2). Under the assumption of thermal equilibrium at the liquid-vapour interface [167], Eq. 3.13 can be rewritten as:

$$\dot{m}_{ev} = h_m \frac{M_w}{R_g T} (1 - RH) P_{sat}(T) \quad (4.14)$$

with h_m being the convective mass transfer coefficient of water vapour in air and T the temperature of the liquid-vapour interface. The mass transfer coefficient h_m can be estimated from the Sherwood number, defined as $Sh = h_m L D_w^{-1}$, being L the characteristic length of the system under investigation and D_w the molecular diffusion of water vapour in air (evaluated through Eq. 2.100). Considering water undergoing natural convection-driven evaporation, it holds [176]:

$$Sh = 0.23 Sc^{1/3} Ra^{0.321}, \quad (4.15)$$

where $Sc = \mu (\rho D_w)^{-1}$ the Schmidt number and Ra the Rayleigh number, being the latter defined in Eq. 3.22. Thus, considering a unitary evaporating surface ($1 \text{ m} \times 1 \text{ m}$), an ambient temperature of $T = 40 \text{ °C}$ and a conservative relative humidity $RH = 80\%$, the mass transfer coefficient can be estimated as $Sh \approx 105$, consistently with previous experimental investigations [177]. Therefore, employing Eq. 4.14, the related cooling load can be evaluated as $\dot{m}_{ev} H \approx 58.6 \text{ W m}^{-2}$ for $RH = 80\%$, being H the enthalpy of evaporation of water evaluated through Eq. 3.19. Furthermore, note that the above estimates do not include “parasitic” convective heat transfer towards the environment due to the unavoidable coupling of convective mass and heat transfer phenomena, where the higher the Sherwood the higher the Nusselt number: considering natural convection, the related heat losses can be evaluated considering a heat transfer coefficient in the range of 5-10 $\text{W m}^{-2} \text{ K}^{-1}$ [178]. The analysis performed has shown that a passive approach only comprising the adiabatic evaporation of a fluid, either from a free or porous

surface, has similar limitations to radiative cooling, namely modest cooling loads and excessive dependence on environmental conditions and can be used to develop cooling capacities considerably lower than the proposed device.

4.6 Different operating conditions

The cooling performance of the passive device depends on the considered operating conditions and design parameters, for instance on the adopted salt solution, number of assembled stages, external ambient temperature and stratigraphy of each stage. This section investigates the effect of several parameters on the overall device performance.

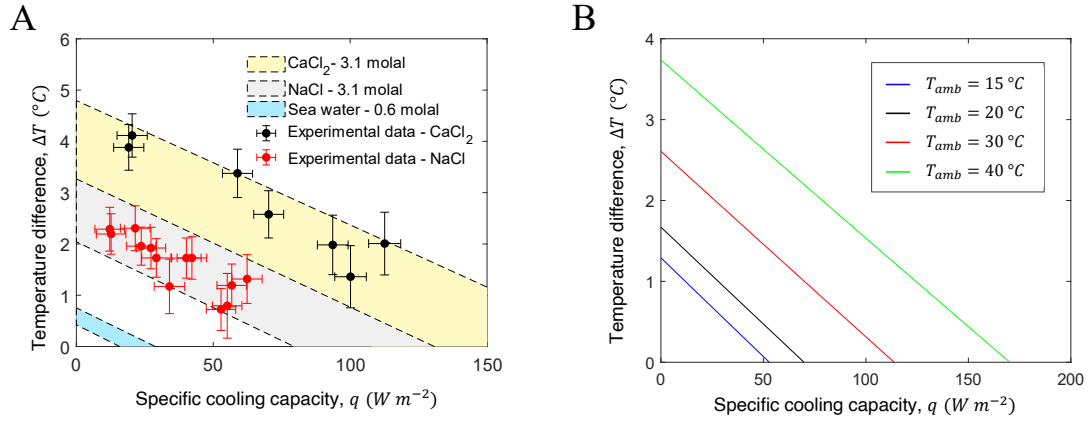


Figure 4.10: **Cooling performance with different configurations.** (A) Cooling performance of the 4-stage passive cooler as predicted by the lumped parameter model for different aqueous solutions. While the evaporators contain distilled water in all cases, the condensers were supposed to contain seawater (0.6 molal, blue band: theoretical prediction), a 3.1 molal dilution of NaCl (red dots: experimental data; grey band: theoretical model) or a 3.1 molal dilution of CaCl₂ (black dots: experimental data; yellow band: theoretical model). (B) Modelling predictions for the characteristic curves of a 4-stage assembly at different ambient temperature T_{amb} and fixed 3.1 molal NaCl solution. According to Antoine equation (see Eq. 2.96), higher T_{amb} implies greater vapour fluxes through the membrane, hence better cooling performances than the case experimentally assessed (solid red line, $T_{amb} = 30$ °C).

4.6.1 Influence of salt type and concentration

The water activity in the salt solution in the condensers is one of the main parameters affecting the transfer of enthalpy of vaporization across the membrane

and, hence, the cooling capacity. The water activity depends on the type and molality of dissolved salt ions. First, the performances of the 4-stage prototype were experimentally assessed when operating with an aqueous CaCl_2 solution at the same molal concentration (3.1 molal) and ambient temperature $T_{amb} = 30^\circ\text{C}$ of the NaCl solution previously tested. The experiments were performed applying the same experimental protocol described previously. Coherently with the reduction in the activity, the $q - \Delta T$ characteristic curve shows a significant increase in the maximum temperature difference and specific cooling capacity obtainable from the passive cooler (see Fig. 4.10A), which were increased up to approximately 4.5 K and 170 W m^{-2} , respectively. The flux of enthalpy of vaporization was increased by the lower water activity in the calcium chloride solution, thus consuming a greater quantity of distilled water ($3.5 - 4.5 \text{ L m}^{-2} \text{ h}^{-1}$ depending on the cooling power (see Fig. 4.9B) with respect to the tested sodium chloride solution. The experimental results (black dots) are compared with the modelling predictions (yellow band) in Fig. 4.10A, showing substantial agreement. Second, the lumped-parameters model – validated against the experimental results in Fig. 4.8B and in Fig. 4.10A – was employed to explore also the effect of molality on the characteristic $q - \Delta T$ curve of the passive cooler. For example, the molality of NaCl solution was varied, while still considering a 4-stage cooler at $T_{amb} = 30^\circ\text{C}$. Starting from the value considered in the experiments (3.1 molal), model predictions showed a large decrease in the cooling performances with a lower molality: considering a NaCl solution with a typical seawater salinity (0.6 molal), the maximum temperature difference and specific cooling capacity dropped to 0.6 K and 20 W m^{-2} , respectively. The effect of the ambient temperature on the cooling capacity of the proposed device was also investigated by the model. In detail, Fig. 4.10B shows the cooling performances as a function of T_{amb} ranging from 15°C to 40°C . The results show better cooling performances at higher ambient temperatures due to the enhanced evaporation process, as evident from the temperature dependence of the Antoine equation (see Eq. 2.96). Considering typical summer conditions (e.g. $T_{amb} = 40^\circ\text{C}$), the cooling capacity can reach values up to 165 W m^{-2} at vanishing temperature difference.

4.6.2 Influence of device stratigraphy

The validated lumped-parameters model was employed to estimate how the number of stacked modular stages n affects the cooling performances of the resulting multi-stage device (see Fig. 4.11A). On the one hand, the maximum cooling capacity is not affected by n ; on the other hand, the maximum obtainable temperature difference increases accordingly with n : the achievable value of ΔT_m with a 10-stages configuration (solid green line) is twice the one obtained with the setup experimentally tested (4 stages, solid black line). Notice that the evaporation rate is not uniform across the multi-stage device due to the different working temperatures of each stage: those working at lower temperatures develop lower cooling

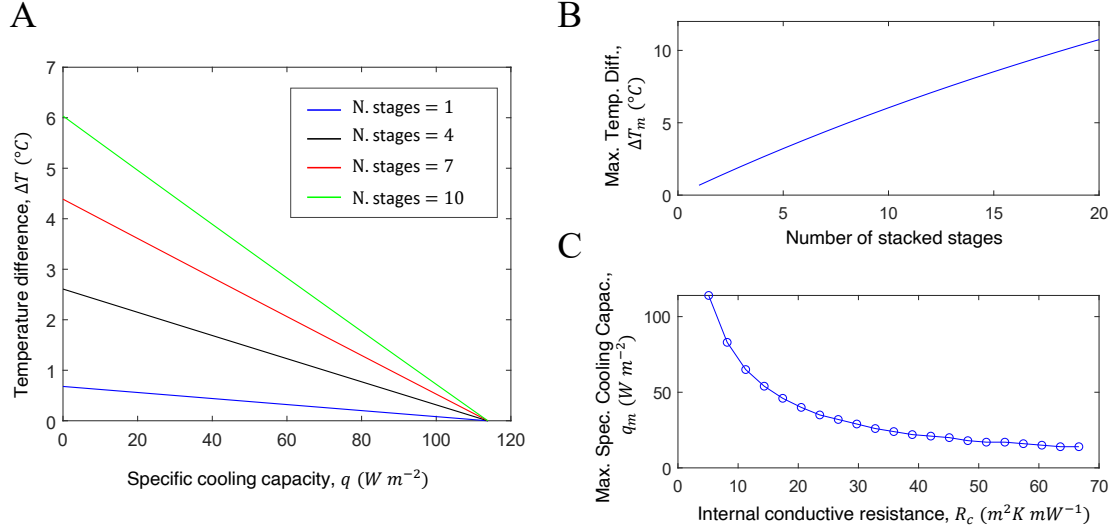


Figure 4.11: **Impact of the number of stacked stages: modelling predictions.** (A) Modelling predictions for the passive cooler performance with different number of stages but fixed molality (3.1 molal NaCl solution) and $T_{amb} = 30^{\circ}\text{C}$. Increasing the number of stages significantly enhances the maximum temperature difference achievable across the device ΔT_m , while it does not affect the achievable maximum cooling capacity q_m . (B) Non-linear dependence between ΔT_m and the number of stacked stages due to the temperature-dependent mass flux across the membrane: stages working at lower temperature develop lower cooling capacity. (C) Impact of the internal conductive resistance R_c on q_m . Internal heat losses rapidly increase the temperature drop between each stage, leading to $\Delta T = 0$ for lower values of q . This behaviour was also suggested by the temperature distribution reported in Fig. 4.7A.

capacity, accordingly with Antoine equation (see Eq. 2.96). As a consequence, ΔT_m does not increase linearly with n (see Fig. 4.11B). Note that the maximum number of stackable stages, here limited to 20, is strongly influenced by other engineering considerations: since each stage is fed by capillary action (in this case, the evaporators), the maximum height and extension of the device are also determined by the capillary properties of the porous material used. In particular, the capillary pressure must ensure sufficient hydraulic head for the distilled water to reach the highest stage and spread over its entire surface, which, moreover, is subject to evaporation. The investigation of the relationship between properties of the porous material used and the actual maximum size and performance of the device is beyond the scope of this section, but is explored in greater detail in Chapter 5.

Finally, the model was used to evaluate the effect on the maximum achievable cooling capacity of the conductive resistance between condensers and next-stage evaporators R_c (i.e., between nodes 2-C and 3-E in Fig. 4.7A). Note that R_c does

not affect ΔT_m as, the temperature drop between two adjacent stages is negligible for $q = 0$ (see blue curve in Fig. 4.7A). As it can be observed in Fig. 4.11C, increasing R_c reduces the attainable q_m , which highlights the need of designing thin and conductive stages. Therefore, to maximise the device performance is crucial to minimize the thermal resistance of the saltwater cavity (without compromising the device operating principle) and of the hydrophilic layer, envisioning a highly conductive capillary material replacing the used synthetic non-woven textile.

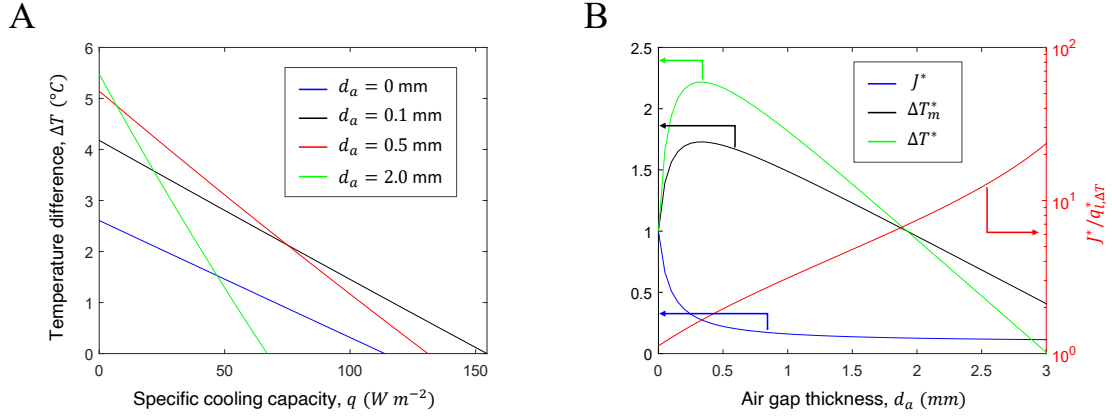


Figure 4.12: **Impact of the air gap thickness: modelling predictions.** (A) Modelling predictions for the 4-stage passive cooler considering an additional air gap in series to the membrane, as predicted by the lumped parameter model. In detail, the performance of the cooling device was estimated varying the thickness of the additional air gap d_a from 0 to 2 mm, with a 3.1 molal NaCl solution and $T_{amb} = 30^\circ C$. (B) Impact of the air gap thickness on the normalized vapour flux (J^* , blue curve), the normalized temperature differences across the membrane (ΔT_m^* , black curve) and the device (ΔT^* , green curve), and the ratio between J^* and the normalized conductive heat flux across the membrane ($J^*/q_{l,\Delta T}^*$, red curve). Each curve was normalized with respect to the value obtained for $d_a = 0$ mm. The curves reported were obtained considering a 1-stage device operating with a 3.1 molal NaCl solution at fixed $q = 50 W m^{-2}$ and $T_{amb} = 30^\circ C$.

Successively, the effect of including an air gap in series to the tested membrane was investigated (see Fig. 4.12A). The thickness of the additional air gap d_a was varied from 0 to 2 mm, obtaining an initial enhancement of the device performance, comprising both q_m and ΔT_m : model predictions showed that an air gap of thickness equal to $100 \mu m$ leads to a maximum temperature difference increase of 60% and to an enhancement of q_m of 30%. However, higher values of d_a have beneficial effects up to a threshold value of d_a : beyond this value, the performance starts to deteriorate because of the reduced values of the membrane coefficient B , leading to lower evaporation rates. To understand this behaviour, Fig. 4.12B analyses the effect of d_a on the latent and conductive heat fluxes involved in the membrane

transport (see the right-hand side of Eq. 4.13) and on the temperature difference across the layer. For the sake of simplicity, the reported curves were obtained considering a single stage device at fixed $q = 50 \text{ W m}^{-2}$, and were normalized with respect to the value obtained for $d_a = 0 \text{ mm}$ (e.g., $J^*(d_a) = J_w(d_a)/J_w(0)$). As it can be observed, higher values of d_a lead to a progressive reduction of the normalized vapour flux J^* (see blue curve). However, the increased air gap thickness enhances the thermal resistance of that layer R_{me} : even though the temperature difference across the membrane initially increases (see black curve), the enhanced thermal resistance decreases the conductive losses through the membrane ($q_{l,\Delta T}^*$, defined as the second member of the right-hand side of Eq. 4.13). As a consequence, despite J^* progressively decreases, the ratio between $J^*/q_{l,\Delta T}^*$ always increases for higher values for d_a (see red curve). These opposing effects lead to an initial increase of the temperature difference across the membrane ΔT_m^* and across the device ΔT^* (see red and green curves, respectively) even with a reduced consumption of distilled water. This led to the upward shifting of the black characteristic curve in Fig. 4.12A with respect to the reference condition, namely $d_a = 0$ (blue curve). Further increase of d_a , however, keeps hindering the vapour flux J^* , leading to a progressive decrease of the cooling capacity (the first member of the right-hand side of Eq. 4.13 leads the process) and, therefore, of the available temperature difference. On the other hand, ΔT_m remains considerable even for large values of d_a , as the high thermal resistance of the membrane layer R_{me} allows to maintain sustained temperature differences even with minimal vapour fluxes, if no cooling capacity is required. Note that the analysis above considers the cooling device as ideally sealed, thus neglecting potential vapor losses.

Note that increasing the air gap thickness always decreases the consumption of distilled water: as a consequence, d_a constitutes another degree of freedom for the optimization to optimize the device stratigraphy. As an example, a 4-stage device operating with 3.1 molal NaCl solution presents a reduction of approximately 60% of the consumed distilled water when operating with a $100 \mu\text{m}$ air gap (see Fig. 4.13A). Higher values of d_a would hinder the device performance, but further reduction of distilled water consumption could be useful when distilled water could not be easily supplied or regenerated. As a consequence, the device configuration can be optimized by maximising q_m , ΔT_m or by minimization of the distiller rate consumption; other the optimal trade-off between these objective function might be dictated by the requirements of a target application. As an example, the tested configuration would maximise its cooling performances by employing an air gap with thickness in the range between $100 \mu\text{m}$ and $120 \mu\text{m}$ (see Fig. 4.13B).

4.6.3 Maximum cooling capacity

Assessing the maximum performance achievable by the cooling device is a key aspect for judging its scalability and future application on real scale systems. As

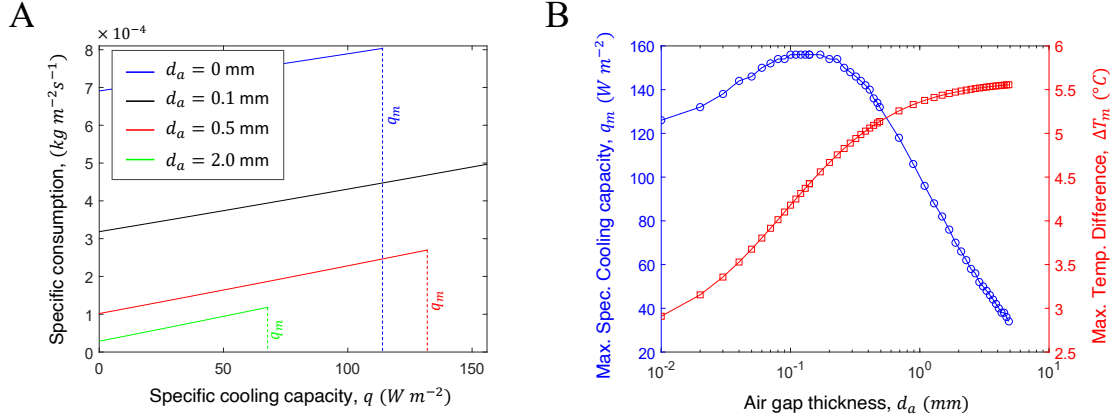


Figure 4.13: **Impact of the air gap thickness: optimization.** (A) Distilled water consumption of the configurations simulated in Fig. 4.12A. Increasing the air gap thickness always reduces the consumption of distilled water. (B) Model-based optimization of the air gap thickness for a 4-stage configuration operating with 3.1 molal NaCl solution at $T_{amb} = 30$ °C. While ΔT_m increases for higher values of d_a , the maximum achievable q_m is obtained using an air gap in the range 100 μm - 120 μm .

demonstrated in Fig. 4.11A, the number of stacked stages does not affect the maximum cooling capacity q_m ; instead, q_m is strongly influenced by the difference between the activity coefficients of the solutions in the evaporators and condensers. Therefore, q_m can be estimated by considering the condensers filled by salt solutions near their saturation limit and the evaporates filled by distilled water. The simulations were performed in the limit of ideal solutions, thus estimating the water activity coefficients a_w via Raoult's law. However, solutions near saturation may exhibit large deviations from ideality: therefore, the values of a_w for NaCl and CaCl₂ solutions were also estimated by interpolating the experimental results reported by Guendouzi and coworkers at 25 °C [179]. For the sake of simplicity, the temperature dependence of a_w , ignored by Raoult's law, was neglected anyway. Since the solubility limits of aqueous solutions of NaCl and CaCl₂ at 25 °C are 6.15 mol kg⁻¹ and 6.71 mol kg⁻¹, respectively, the model predictions were obtained considering a concentration of 6 molal. Consistently, an ambient temperature of 25 °C was considered, although higher values would lead to greater values of q_m (see Fig. 4.10B). A 4-stage device with the same stratigraphy described in section 4.2 was considered, except for an additional air gap of 0.15 mm placed in series to the hydrophobic membrane, which, as demonstrated in Fig. 4.13B, increases its performance. With this configuration, the achievable values of q_m in the limit ideal mixtures are 231 W m⁻² and 324 W m⁻² for NaCl and CaCl₂ solutions, respectively. Otherwise, considering non-ideal mixtures, the activity coefficients are 7% and 48% lower for NaCl and CaCl₂, respectively, enhancing the previous predictions to 314

W m^{-2} and 884 W m^{-2} .

However, a few remarks about the engineering feasibility of such configurations must be considered. First, high salt concentration would probably lead to membrane scaling, causing damage and rapidly degrading the device performance. Second, high cooling capacities imply high evaporation rates. Therefore, as pointed out in Chapter 5, when designing capillarity-based devices it is crucial to consider the limitations to the achievable device size posed by the transport properties of the porous materials used. For this reason, the model derived in section 2.4.5 was employed to estimate the maximum length of the evaporators before dry-out occurs. In order to apply the derived analytical model, the geometry of the evaporators (squares with a thin vertical strip for connection with the distilled water reservoir placed below, see Figs. 4.3B and 4.4) was assumed to be slightly different, i.e., considering the connection strip as wide as the side of the device. The connection strip was assumed to be vertical and isolated from the environment (i.e., null evaporation rate), while the portion of the fabric within the device was assumed to be horizontal. Thus, the model predicts the maximum length of the evaporator, net of the length of the connection strip. The predictions were performed considering an elevation of the device of 5 cm with respect to the water basin and, as a conservative condition, considering the evaporative flux predicted by the lumped-parameters on the last-stage evaporator (highest evaporation rate). The capillary properties of the non-woven textile used in the device (see green data in Figs. 5.14B and 5.16A). Considering ideal solutions of NaCl and CaCl_2 , the maximum obtainable length of the evaporators is 11 cm and 8 cm, respectively. In contrast, considering non-ideal solutions, the increased evaporative flux further reduces the achievable lengths to 8.8 cm and 3.8 cm, respectively. The results show the convenience of installing several smaller devices rather than a single, larger one to avoid dry-out and operate with solutions close to saturation.

4.6.4 Preliminary considerations on three-components mixtures

The possibility of operating the passive cooling device with different salts and solvents, pure or in mixtures, opens interesting possibilities for improving the performance achievable. This section provides some preliminary insights into the effects of adding ethanol, an extremely volatile solvent in air, to the water-salt mixtures already investigated in this Chapter. Obviously, different salts can exhibit extremely opposite behaviors in a given solvent: for example, NaCl is poorly soluble in pure ethanol (less than 10^{-4} molal), while LiCl achieves a solubility of 5.8 molal at 25 °C [180]. Consequently, solute-solvent combinations must be chosen with the aim of reducing the activity of volatile elements on the condenser side as much as possible. In this regard, it is interesting to analyze the impact on the cooling device performance of different mixtures of water-ethanol and NaCl, varying the ethanol

mass fraction $Y = m'_e / (m'_e + m'_w)$, where m'_e and m'_w are the masses of ethanol and water in the mixture expressed in kg, respectively. Note that different values of Y would lead to different solubilities of NaCl within the mixture, which can be evaluated from the various experimental results reported in the literature, such as those provided by Li and co-workers [180].

It is difficult to provide an accurate theoretical estimation of device performance operating under this configuration, since the transport model developed in section 2.6 is not suitable for describing ternary gas mixtures (i.e., air, water vapor, and ethanol). However, a first estimate of device performance can be obtained by considering some simplifying assumptions. First, the mass fluxes of water vapor and ethanol (J_w and J_e , respectively) can each be estimated by Eq. 2.106, thus neglecting their interaction within the membrane. Consequently, the latent heat flux can be calculated as $q = J_w(1 - Y)H_w + J_eYH_e$, where, for simplicity, the temperature dependence of the various terms was not indicated, and where H_w and H_e are the enthalpies of vaporization of water and ethanol, respectively. It is worth noting that H_e is about 35% of that of water, therefore a limited thermal contribution from the evaporation of ethanol can be expected. Second, since few data are available on the activity coefficients of solvents in three-components mixtures, these were estimated in the limit of ideal solutions. With this regard, data on the activity of water in the water-ethanol mixtures exhibits near-ideal behavior up to $Y = 0.3$ (see the data reported in Ref. [181]). Therefore, to provide more reliable results, the predictions were performed limiting the mass fraction of ethanol to the range $0 \leq Y \leq 0.3$, considered the same in evaporators and condensers (namely, $Y_e = Y_c = Y$). While the molal concentration of NaCl in the evaporators (m_e) was set equal to 0, that in the condensers (m_c) was set close to the solubility limit, which varies from 6.1 to 3.4 mol kg⁻¹ in the considered range of Y [180]; however, despite the relatively high concentrations, the activity coefficients of water and ethanol (a_w and a_e , respectively) were evaluated following Raoult's law as:

$$\begin{aligned} a_w &= \left(1 + \left(\frac{Y}{1 - Y}\right) \frac{M_w}{M_e} + \frac{m M_w N_i}{1 - Y}\right)^{-1} \\ a_e &= \left(1 + (1 - Y) \frac{M_e}{M_w} + \frac{m M_e N_i}{Y}\right)^{-1}, \end{aligned} \quad (4.16)$$

where M_w and M_e are the molecular weights of water and ethanol, respectively, m is the solute molality, and N_i is the number of ions dissolved in the mixture assuming total dissociation of the solute. Furthermore, the molecular diffusivity of ethanol in water was assumed as constant in the temperature range investigated and equal to $11 \cdot 10^{-6}$ m² s⁻¹ [182], while the vapor pressure of ethanol was evaluated by Antoine's equation as [183]:

$$P_e = 10^{(5.37229 - 1670.409(-40.191 + T)^{-1}) + 5} \quad (4.17)$$

where P_e is expressed in Pa and T is the reference temperature, expressed in K. Finally, the temperature dependent vaporization enthalpy of ethanol H_e was expressed as [184]:

$$H_e = \frac{50.43 \cdot 10^3}{M_e} \exp\left(0.4475 \frac{T}{513.9}\right) \left(1 - \frac{T}{513.9}\right)^{0.4989}, \quad (4.18)$$

where H_e is expressed in J kg^{-1} and T in K.

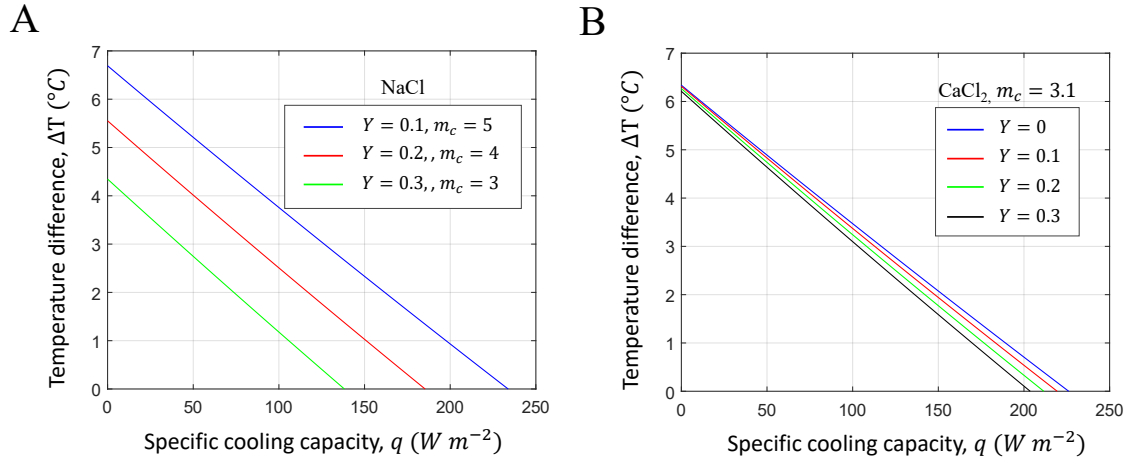


Figure 4.14: **Performance of the passive cooling device operating with water-ethanol-salts solutions.** (A) Characteristic curves evaluated considering NaCl solutions and different ethanol concentrations Y . Increasing Y reduces the solubility of NaCl, thus decreasing the maximum achievable performance. (B) Characteristic curves evaluated considering CaCl_2 solutions at 3.1 mol kg^{-1} and different ethanol concentrations Y .

The modelling results (see Fig. 4.14A) were obtained considering a 4-stages device with the same stratigraphy discussed in section 4.2, except for the addition of a 0.15 mm air gap in series with the membrane, which was demonstrated to enhance the performance (see Fig. 4.13B). As discussed above, higher values of Y result in lower solubility of NaCl, and thus in reducing the maximum salt concentration that can be used in the condenser. Consequently, the addition of ethanol to the water-NaCl electrolyte solution would not be beneficial to the performance of the device because of the low solubility of NaCl in ethanol. Note that the difference between m_c and the corresponding solubility limit was less than 0.5 mol kg^{-1} .

To further investigate the effect of ethanol, CaCl_2 was also considered as solute, which exhibits higher solubility in ethanol than NaCl. Therefore, remaining in the limit of ideal solutions, the molal concentration of calcium chloride was set at 3.1 molal (as experimentally tested and reported in section 4.5), while the ethanol concentration was varied in the range $0 \leq Y \leq 0.3$ (see Fig. 4.14B). Model results were

obtained under the same operating conditions and stratigraphy as those considered for the water-ethanol and NaCl mixture. As it can be observed, higher values of Y lead to slightly worse performance of the device. In fact, although ethanol has a steeper vapor pressure curve than water, the lower enthalpy of vaporization nullifies its positive effects. Note that the results presented should be considered only as a preliminary estimate of the device performance with three-components mixtures, as high concentrations of ethanol or solutes would lead to deviations with respect to the assumptions made.

Although the ethanol configurations considered showed worse performance than the water-salt binary mixtures tested in this Chapter, the concept certainly deserves further investigation, both through experiments and a more accurate theoretical framework to overcome the simplifications assumed in this brief analysis. In particular, the optimal solvent mixtures for this application should exhibit high solubility to multi-charged salts, a steep vapor pressure curve, and a high enthalpy of vaporization.

4.6.5 Performance comparison with radiative cooling technologies

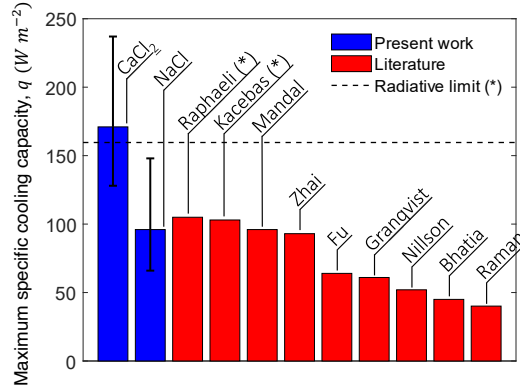


Figure 4.15: **Comparison with other passive cooling technologies.** Comparison between the performances of the proposed device and different daytime radiative cooling technologies reported in the literature. The results reported refer to the works of Raphaeli [185], Kacebas [186], Mandal [79], Zhai [78], Fu [187], Granqvist [82], Nilsson [188], Bhatia [84] and Raman [77]. The references labelled with (*) refer to modelling results. The maximum specific cooling capacity at vanishing temperature difference for the proposed device was extrapolated from the experimental results by linear fitting (least square method). The thermodynamic limit of daytime radiative cooling was computed at $T_{amb} = 30^{\circ}C$ [80].

Finally, the experimental results obtained for the proposed passive cooler were

compared with the performances of different passive cooling technologies found in the literature. In particular, Fig. 4.15 highlights that the extrapolated maximum cooling capacity of the passive device observed in our experiments (4 stages, CaCl_2 solution, 3.1 molal, $T_{amb} = 30^\circ\text{C}$) is 50% higher with respect to the best-performing daytime radiative cooler from the literature, and it eventually exceeds the theoretical limit of radiative cooling without depending on favourable atmospheric conditions [80]. It is worth pointing out that the present device is based on completely different physical phenomena as compared to passive radiative systems, and these were reported only for providing the reader with a reference of another competing passive technology. For the sake of fairness, we should also notice that the comparison is meaningful if the concentration difference between the salt solutions in the cooler is initially available. On the contrary, more care should be used when the concentration difference should be sustained by solar distillation, as low activity water solutions are associated to the highest cooling performance but also to the lowest distillation productivities.

4.7 Passive solar cooling

Without loss of generality, the experiments were operated in batch conditions. Therefore, after a sufficiently long time interval, the salt solution in the condensers was progressively diluted by the water vapour, thus leading to a progressive reduction in the cooling driving force. Clearly, technological applications of the present passive cooler alone can be envisioned mostly in hot regions with natural availability of high salinity solutions (e.g. nearby solar saltworks or salt mines). However, alternative applications could be also imagined if a continuous regeneration of the salinity difference between evaporators and condensers could be ensured: the passive cooler should be then coupled with a second device capable to restore the salinity difference between the two feeds.

To this end, coupling the passive cooler with the passive solar distiller (e.g., see Refs. [96, 121, 189, 190]) would keep the resulting solar-driven cooling system as completely passive and off-grid. In fact, the considered passive distiller exploits the solar energy collected by a highly absorptive material to drive multiple evaporation-condensation processes, which separate fresh water from a feeding salt solution. As a result, the salinity of solution in the inlet basin increases; whereas, the produced distillate is discharged into the outlet basin, therefore counterbalancing the opposite action of the cooler. No pumps are required to operate the passive solar distiller, since the inlet solution is absorbed by capillarity and the outlet one is discharged by gravity. A possible scheme of the coupled system and the related thermodynamic cycle are depicted in Fig. 4.16A, where – for the sake of simplicity – both cooling and distillation devices are depicted as composed by a single stage. Note that the distiller device was intentionally schematized above the cooling device to favour a

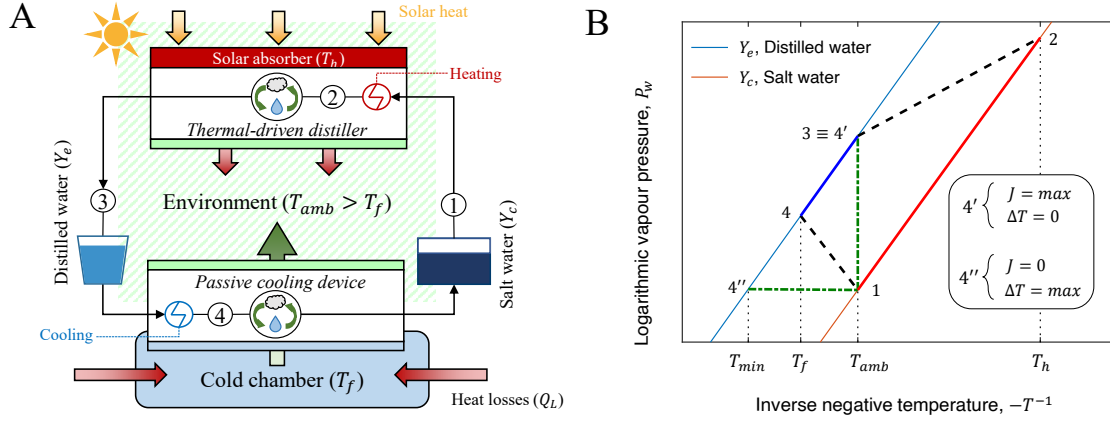


Figure 4.16: **Stable operating cycle of the passive cooler.** (A) Schematic of a possible coupling between the passive cooler and a thermal-driven device for salt water distillation. (B) Qualitative thermodynamic cycle of a single-stage cooling and distillation devices. The temperature of cooler evaporator and distiller condenser were assumed to be equal to T_f and T_{amb} , respectively. Point (4) identifies a generic working temperature of the cooler (namely, T_f) below T_{amb} .

good salt stratification into the salt water basin. In the representation, the working temperatures of first- or last-stages condensers and evaporators of both devices were supposed to be equal to those of the environment they were in contact with, namely T_{amb} and T_f .

Assuming a constant solar irradiance driving the distillation process and equilibrium conditions, a steady salinity difference between the distilled (Y_e) and salt (Y_c) water basins should be eventually achieved in the coupled system. In particular, the outlet solution from the cooling device (point 1 in Fig. 4.16B, with Y_c concentration and T_{amb} temperature) is heated up by the solar absorber (point 2, with Y_c concentration and T_h temperature). Then, the temperature difference through the distiller triggers the evaporation-condensation process and thus generates distilled water (point 3, with Y_e concentration and T_{amb} temperature), which can readily feed the cooler and provide the cooling effect to the refrigerated chamber (point 4, with Y_e concentration and T_f temperature) by means of the salinity-driven evaporation process. Moving this operating point along the isosteric curve of distilled water Y_e , points (4') and (4'') identify the extreme working conditions of the proposed device. Point (4') identifies the highest temperature of heat extraction (namely, $T_f = T_{amb}$), where $\Delta T = 0$ and both water vapour flux and extracted heat are maximum. On the other hand, point (4'') identifies the lowest temperature of cooler operations, namely $T_f = T_{min}$, where the temperature difference across the device is maximum while the net water vapour flux is null. Guidelines for obtaining a stable operating cycle for the passive cooler are reported in Fig. 4.17.

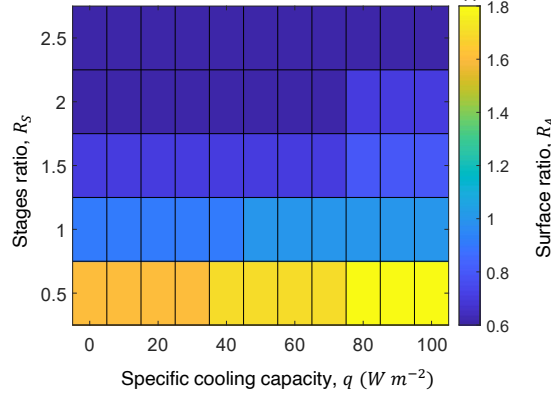


Figure 4.17: Coupling between the cooling device and the passive solar distiller proposed in Ref [96]. R_S is the ratio between the number of stages of the distiller and the ones of the cooler; R_A is the ratio between the solar collecting area of the distiller and the active area of the cooler. Potential regeneration capabilities of the salinity gradient in the cooler are evaluated considering that the condensers are fed by salt water with NaCl concentration equal to 170 g L^{-1} .

Achieving continuous regeneration of the salinity difference is theoretically possible by properly tuning the number of stages and the solar absorbing area of the passive solar distiller as a function of the required specific cooling power. In the plot, $R_S = N_{Distiller}/N_{Cooler}$ is defined as the ratio between the number of stages of the distiller and the ones of the cooler, whilst $R_A = A_{Distiller}/A_{Cooler}$ is defined as the ratio between the solar collecting area of the distiller and the active area of the cooler. In this chapter, the desalination technology envisioned for coupling with the proposed cooling device is that reported in Ref. [96], which working principle and layout is extensively described in Chapter 5 (see section 5.5). However, in order to easily imagine their coupling, the desalinator can be imagined as a multistage device whose operating principle is inverse with respect to the cooler: an external thermal flux drives a net vapor transport from a high salinity solution to a low concentration solution, which are divided by a hydrophobic membrane. Further details on the implementation of the theoretical model used to the data presented, its working principle and performance is reported in Appendix C.

According to the user needs, the two design parameters (R_S and R_A) can be varied to achieve a fully coupled distillation/cooling cycle while keeping the geometrical requirements of the specific application. For the sake of simplicity, N_{Cooler} is fixed to 4 to represent the experimentally tested configuration. The considered performances of the solar passive distiller were referred to an optimal stratigraphy of the device. In detail, the interface between evaporation and condensation layers includes both a 0.5 mm air gap and a hydrophobic membrane with $3.0 \text{ }\mu\text{m}$ pore

size, which were estimated according the optimization procedure reported above. Then, modelling estimates were evaluated considering an equivalent solar irradiance of 1 kW m^{-2} and ambient temperature equal to $30 \text{ }^\circ\text{C}$. Note that the greater the required cooling capacity of the device, the better is the desalination performance required to allow their stable coupled operation. This can be achieved either by a larger area of the device (color map in Fig. 4.17) or a higher number of stacked stages (y-axis in Fig. 4.17). This requirement is due to the enhanced consumption of distilled water, which increases concordant with the cooling capacity (see Fig. 4.9). Furthermore, in contrast to the cooling device, the efficiency of the distiller decreases when operating with solutions at higher salinity.

Coupling with high-salinity brines

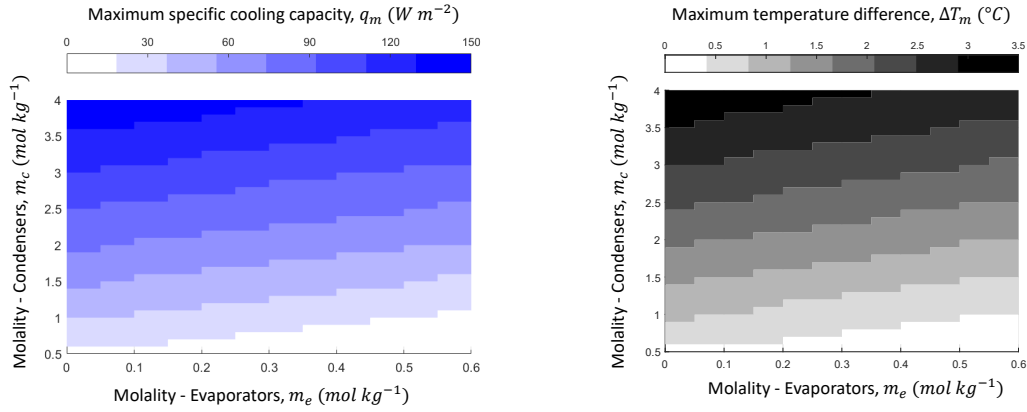


Figure 4.18: **Cooler performance operating with high-salinity brines.** (A-B) Maximum cooling capacity (A) and maximum temperature difference achievable with a 4-stage devices when operating with solutions at different salinity in the evaporators (with molality m_e) and condensers (with molality m_c). The evaporators were considered to work with NaCl solutions ranging from distilled water (0 g L^{-1} , 0 molal) to seawater (35 g L^{-1} , 0.6 molal); the condensers were supposed to work with solutions ranging from seawater to high-salinity brines (220 g L^{-1} , 4.1 molal). The results were obtained considering a 4-stage configuration with $d_a = 0 \text{ mm}$, operating at $T_{amb} = 30 \text{ }^\circ\text{C}$.

The presented cooling system can be operated either as a component of a cyclic machine, or with a net consumption of fresh and salty water. Some of the areas with cooling needs can also present water scarcity issues, where it only makes sense to operate the system in a cyclic mode. However, there are important exceptions where both cooling needs and abundant salinity differences are either naturally available (e.g. nearby salt mines or salt-works) or coming from brines produced in large desalination plants. In the latter cases, the condensers could be fed by high-salinity

solutions (i.e. brines), whereas seawater (with lower salinity) could be used in the evaporators. Following this approach, no freshwater would be needed whatsoever. Furthermore, the direct discharge of hypersaline concentrate water (e.g. brines from desalination plants) into the sea is a serious environmental and economic problem that is drawing an increasing attention in the scientific community. In order to fix ideas on the relevance of this scenario, a total production of 142 million m³ per day of brine is estimated [191], with Saudi Arabia, UAE, Kuwait and Qatar accounting for 55% of the total share and are also known to have impressive cooling needs. According to Ref. [192], over 70% of electricity consumption in Saudi Arabia is used for air conditioning and cooling. Considering an illustrative case where the condensers of our cooler could be fed by the brine produced from a desalination plant, the typical concentration range of total dissolved solids (TDS) of brines produced by reverse osmosis is 70 to 80 g L⁻¹ [193]. Currently, several concentration technologies, ranging from solar ponds to electro dialysis, are employed to increase the recovery rate of desalination plants, in order to reduce the environmental impact of high-salinity brines and ease their disposal. In particular: mechanical vapour compression can be used to reach a TDS concentration of 250 g L⁻¹ [194]; forward osmosis allows to reach concentrations ranging from 180 g L⁻¹ [195] up to 220 g L⁻¹ [196]; vacuum membrane distillation has been recently proved to achieve TDS concentrations in the range 150-300 g L⁻¹ [190, 196, 197].

The cooling potential of the proposed 4-stage device was investigated by means of the validated lumped parameters model, exploring the maximum cooling capacity q_m and achievable temperature difference ΔT_m with when operating with NaCl solutions at different concentrations. In particular, the concentration in the evaporators were supposed to range from distilled water to seawater (35 g L⁻¹, 0.6 molal), while the condensers were supposed to operate with solutions ranging from seawater to high-salinity brines (220 g L⁻¹, 4.1 molal). Coherently with the analysis performed so far, the best performing configurations are those maximising the concentration difference between evaporators and condensers.

4.8 Considerations on the environmental and life-cycle issues

The passive cooler presented in the article was made of the following materials: stainless steel (bolts and nuts); aluminum (separation plates, heat sink); acrylonitrile butadiene styrene (ABS, structural frame of each cooling stage); polytetrafluoroethylene (PTFE, membranes); microfiber (hydrophilic layers). Steel and aluminum parts are fully recyclable and, to this purpose, efficient recycling processes and facilities are well established worldwide (e.g. 34.3% of all metal wastes have been recycled in the US in 2015 [198]). Both ABS and PTFE are thermoplastics and can be recycled, even though their purity would tend to degrade with each

reuse cycle [199–201]. The employed microfiber, instead, is made of 70% viscose (regenerated cellulose fibre), 18% polypropylene and 12% polyester that, despite being partially recyclable, could be a source of microplastic accumulation in marine habitats [202]. The passive cooler could be envisioned as a device synergistic with desalination plants for mitigating their brine discharge issues. In fact, discharging the produced brine in a cost-effective and eco-friendly way still remains a serious challenge in desalination plants [203]. The most common brine disposal methods are surface water discharge or injection into saline aquifers, both presenting serious environmental risks if intensively exploited. In fact, the discharge of high-salinity solutions into the sea is a major threat to marine ecosystems, particularly to seagrasses such as the *Posidonia Oceanica* [204, 205]; whereas, the injection into confined salt water aquifers, despite being largely used for brackish water desalination, may cause contamination of the overlying potable aquifers due to underground connections or leakages [206, 207]. To mitigate the previous issues, brine should be diluted before being discharged into the receiving water body [208]. However, the brine dilution can be particularly challenging in large desalination plants, where the mass flow rate of brine is substantial and localized in a limited coastal area (e.g. Gulf nations) [191]. In this context, our cooling device would have no additional brine production, in case of both cyclic and non-cyclic operations. On the one hand, the cyclic distiller-cooler assembly (see Figs. 4.17 and 4.18) would not involve any brine disposal into the environment. On the other hand, if the passive cooler operates with a net consumption of low-salinity (e.g. seawater) and high-salinity (e.g. brine) water solutions, the final result would be the dilution of the brine from desalination plants before their final discharge into the environment.

4.9 Cost analysis of the lab-scale prototype

The prototype cost has not been optimized and, due to its small size, it does not exploit any economy of scales. The optimization of the cost in a possible industrial scenario is beyond the scope of this chapter, which is focused on the characterization of a proof of concept prototype. The table below lists the unitary cost of the materials employed, the quantity needed for one cooling stage and the considered supplier. Whenever possible, the wholesale cost of the material was considered. The overall cost of one cooling stage is approximately € 1.9, which, normalized considering the device surface of 12 cm × 12 cm, leads to a specific cost of 132 € m⁻². The following pie chart shows the percent cost splitting for a single stage.

Finally, four nuts and bolts and one additional aluminum plate should be used to assemble the 4-stage prototype, with an additional cost of 0.9 €. The forced convection heat sink used during the experiments has an approximate cost of 15 €,

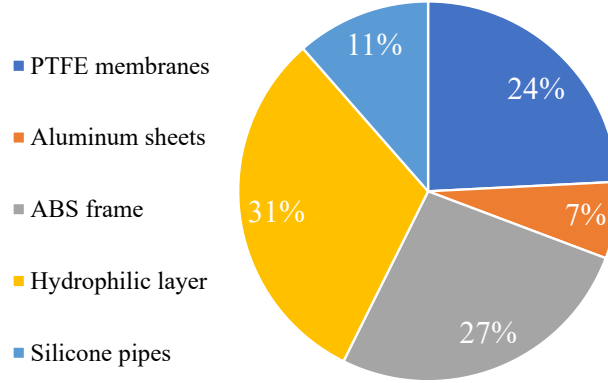


Figure 4.19: Cost analysis of the passive cooler prototype.

Material	Supplier	Unitary cost	Quantity	Total price (€)
PTFE membranes	ANOW	26.8 (€/m ²)	1.7 · 10 ⁻² m ²	0.45
Aluminum sheets	Wholesale	2.2 (€/kg)	5.5 · 10 ⁻² kg	0.12
ABS frame	Wholesale	10.1 (€/kg)	4.9 · 10 ⁻² kg	0.5
Hydrophilic layer	Henkel	9.0 (€/m ²)	6.5 · 10 ⁻² m ²	0.58
Silicone pipes	Wholesale	0.4 (€/m)	0.6 m	0.27

Table 4.1: Cost estimation of the scaled-up cooling device.

but this may change according to each specific application (i.e. it might be replaced by a natural convection heat sink).

4.10 Conclusions

This Chapter presented the experimental characterization of a novel modular and passive cooling process driven by the salinity difference between two aqueous solutions. Note that the main innovation proposed was the use of an activity-driven membrane process to generate a net cooling capacity, whereas the prototype presented, with its clearly limited functionality, was only intended to demonstrate its potential. The experiments performed with an aqueous solution of NaCl at 3.1 mol kg⁻¹ provided a maximum cooling capacity of approximately 60 W m⁻² and an extrapolated value of nearly 100 W m⁻² at a vanishing temperature difference. Instead, using a CaCl₂ solution at 3.1 mol kg⁻¹ substantially enhanced the device performance, with a maximum tested cooling capacity of approximately 110 W m⁻² and an extrapolated maximum value of nearly 170 W m⁻². The performance gap observed is due to their different activity coefficient (see Eq. 2.98): with the same molal concentration, calcium chloride results in a lower activity coefficient due to

the dissociation of its molecules into three ions, as opposed to the only two ions provided by NaCl molecules. The cooling capacity obtained with CaCl₂ is notably above the reported experimental performance of daytime radiative coolers, the most promising alternative for passive cooling, including their intrinsic thermodynamic limit. The validated model was finally used to predict the performance of the passive cooler under a wider range of operating conditions.

A peculiarity of the proposed device is its modularity, which allows to adapt the generated cooling capacity and its consumption the needs of use. The experimental and theoretical analysis performed helped to highlight general design guidelines for the proposed concept: increasing the number of stacked stages raises the achievable temperature difference across the device; the maximum cooling capacity is strongly influenced by the salinity difference between the two solutions used and by the thermal resistance between the stages; an air gap can be added in series to the hydrophobic membrane to optimize the device performance and reducing its consumption. In particular, the cooling performance of the tested device would be optimized adding an air gap with thickness in the range of 100 μm - 120 μm , which would lead to an increase of 60% and 30% of the achievable maximum temperature difference and cooling capacity, respectively, while decreasing the distilled water consumption by 50%.

Note that, although the achievable temperature differences in passive cooling systems are in the order of a few kelvin, these technologies can be used for energy-saving purposes, potentially leading to important benefits, as discussed in Chapter 1. Alternatively, following the approach of Goldstein et al. [81], substantial energy saving can be accomplished by combining passive cooling technologies with traditional vapor compression refrigeration systems, as the coupling would allow the refrigerant to cool at sub-ambient temperatures. In this sense, the proposed passive cooler may help in implementing energy-saving strategies in future sustainable air conditioning systems. Finally, it is worth noting that if the actual boundary conditions impose a temperature difference across the device larger than the maximum ΔT evaluated by the characteristic curves, the device would cease to provide cooling capacity, since the temperature gradient across the membrane exceeds the activity gradient, thus reversing the direction of the net vapour flux. Such a condition could occur when there is intense solar radiation on the top surface of the device. This situation could be counteracted by placing a solar reflector (or a material with sub-ambient radiative cooling properties) over the device, avoiding direct radiation while allowing natural or forced convection.

Chapter 5

Textured and rigid capillary materials for passive energy-conversion devices¹

Chapter 4 illustrated a new concept for a sustainable cooling device that uses capillary transport to provide evaporators with one of the fluids necessary for its operation. However, the mechanical properties of the hydrophilic layer used, a commercial non-woven fabric, pose several limitations to the scalability of the technology: for example, soft capillary materials could lose their functionality if excessively compressed; their capillary pressure limits the maximum height of the device, which places limits on the number of stackable stages and thus on final performance. In addition, their low stiffness implicate the use of polymeric membranes or spacers to avoid contamination between the solutions operating within the device. These components, besides being an additional cost (see the cost analysis in section 4.9), reduce the performance compared to a simple air gap by providing additional resistance to vapor transport and reducing the effective evaporating surface area.

This Chapter proposes a different approach to the design of passive components by replacing conventional non-structured materials with rigid and micro-structured capillary supports. For this purpose, inspired by the work of Singh and co-workers [89], V-shaped grooves were crafted by femtosecond laser etching on high-grade aluminum sheets, however other metals could be used as well [210]. In our work, the obtained micro-structure and surface chemistry were analyzed by SEM imaging and EDS spectroscopy, showing regular and well-defined geometric features (see section 5.1). The joint effects of the altered surface chemistry and geometry of

¹Part of the work included in this chapter was also previously published by Alberghini et al. in Ref. [209]. The Supplementary Videos mentioned in this chapter are included among the multimedia resources attached to the thesis.

the etched cavities provided the treated metal layer with efficient capillary properties. However, prolonged exposure to water depleted the acquired hydrophilicity, coherently with previous evidences widely reported in the [211–214]. Therefore, both textured and non-textured samples were coated by a nanometers-thick layer of SiO₂ or functionalized by oxygen plasma, and their long-term durability was tested. Notably, the capillary performance of the silica-coated grooved sample remained exceptionally stable for the whole duration of the aging tests in distilled water (approximately 250 hours). Similarly, all the functionalized samples, flat or textured, remained hydrophilic when aged in salt water at 35 g L⁻¹ (approximately 230 hours of continuous immersion were tested), suggesting the applicability of the proposed concept in passive energy-conversion devices (e.g., the passive cooler proposed in Chapter 4). Finally, the capillary properties of the samples were evaluated by vertical wicking tests and compared with those of three other materials used in different passive applications relevant for the water-energy nexus [17, 54, 96, 119, 215], including the woven polyethylene textile presented in Chapter 3. The experimental data obtained were used to calibrate the analytical theoretical model introduced in section 2.4.2, which relates the average geometry and hydrophilicity of the grooves to their capillary properties, easing the comparison with other structured or non-structured materials. Moreover, the capillary model was used to predict the geometrical parameters maximising the capillary properties of the V-shaped channels.

In view of the characterization and analysis performed, the rigid capillary material was envisaged for use in a passive device for solar desalination (see section 5.5). A lumped-parameters model for the heat and mass transfer within the device analogous to the one presented in Chapter 4 was coupled with the wicking model to investigate the optimal shape of the device in a real-scale application, thus evaluating the actual size and productivity of the engineered assembly. The model was used to extrapolate the performance of a multistage device operating with commercial hydrophobic membranes, following a device layout inspired by membrane distillation and originally proposed by Refs. [17, 96]. However, the proposed rigid capillary material allows to replace the membranes with air gaps while still avoiding contamination between the saltwater feed and the produced distilled water.

5.1 Crafting and characterization of the rigid capillary material

The rigid novel capillary material was crafted from ultra-pure aluminum plates (Al ≥ 99%), which was selected as reference material given its large abundance, low cost and off-the-shelf availability. The surface of the aluminum sheets was analysed as-received by SEM imaging and EDS spectroscopy. The preparations of the

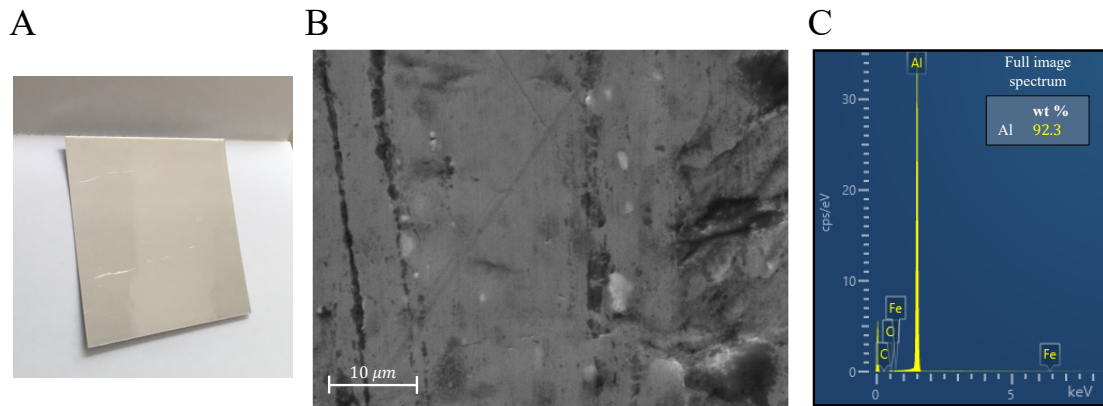


Figure 5.1: **Characterization of the as-received aluminum sheet.** (A) Photograph and (B) SEM image of the high-purity aluminum sheet (5 cm × 5 cm). (C) EDS spectroscopy of the as-received material. The tests show a high presence of aluminum on the surface. However, the aluminum content on the sample is lower than the declared 99% and might be responsible of the high measured value of the contact angle with water. Elements not shown in the legend were present in a non-significant amount.

samples for the SEM imaging comprised a preliminary cleaning treatment by ultrasonic sonication in dichloromethane (CH_2Cl_2) for 4 minutes and ultrasonication in methylbenzene for 4 minutes; the samples were rinsed with ethanol and dried for 15 minutes. The cleansing was followed by a 15 minutes oxygen-plasma treatment (100 W) and metallization with platinum by radio frequency sputtering. The cross-sectional images were obtained by cutting a 5 mm portion from the cleaned sample, which was mounted on a spring, cemented in epoxy resin and polished with abrasive paper (4000 grit). The cross-sectional images were obtained with a InLens detector with a 30 μm opening at an accelerating voltage of 4 kV, 5 kV e 7.5 kV, while the surface morphology was observed applying a 50° tilt angle and an accelerating voltage of 8.5 kV. The EDS analysis was performed on uncleaned samples directly after the engraving process. The analysis revealed minor surface defects and confirmed the high purity of the material with more than 92% Al by weight fraction (wt%) (see Fig. 5.1). The analysis also revealed negligible traces of oxygen, thus small amounts of oxides were already present on the surface.

A femtosecond laser processing procedure was used to craft homogeneous V-shaped grooves across the entire upper surface of an aluminum plate (see Fig. 5.2A). This crafting technique was selected due to its high accuracy and flexibility. Selective ablation treatment was carried out using a femtosecond laser with a wavelength of 515 nm and pulse length of 214 fs. The samples were attached to a bi-axial motorized air-bearing handling system by means of a special laboratory adhesive tape. The laser radiation exiting the femtosecond source was guided,

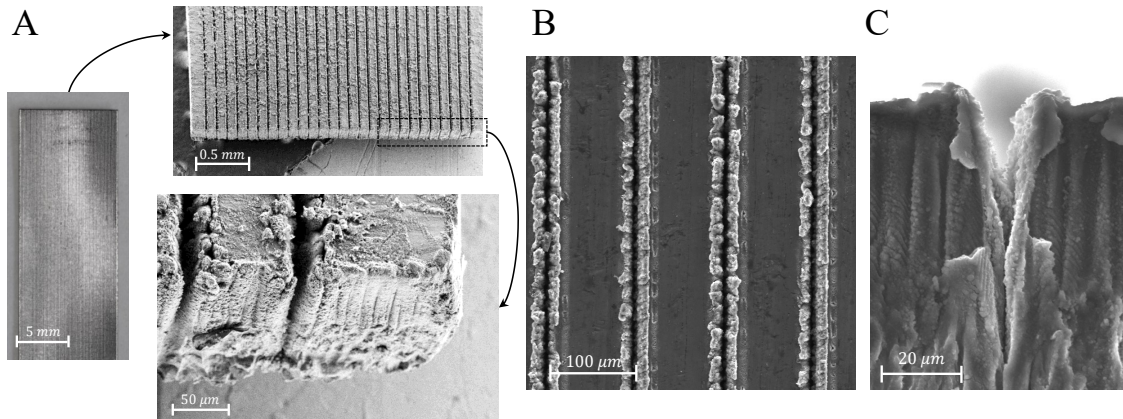


Figure 5.2: **Crafting of the laser-etched sample.** (A) A photograph and tilted SEM images of the crafted material. (B-C) Close-up SEM images of the laser-etched grooves from the (B) top and (C) section view, highlighting the realized geometrical features.

by means of dielectric mirrors, towards a plane-convex focusing lens with a focal length of 150 mm. Thus, a Gaussian laser spot with a diameter of about $50\ \mu\text{m}$ was generated and kept in a fixed position. The linear grooves were generated by the unidirectional translation of the sample below the laser spot, which was focused at a depth of $100\ \mu\text{m}$ from the top surface of the sample. The movement speed of the linear axis was between $0.25\ \text{mm s}^{-1}$ and $0.35\ \text{mm s}^{-1}$. The laser was operated at a frequency of 3 kHz, with pulse energy equal to $100\ \mu\text{J}$. The machining was performed with a constant flow of compressed air coaxial with the laser.

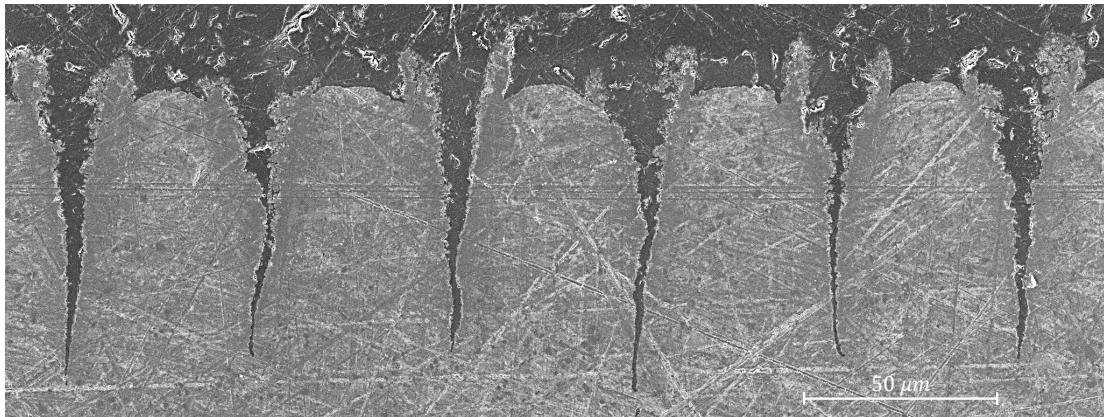


Figure 5.3: **Cross-sectional images of the grooved aluminum sample.** Full-scale SEM images of the laser-etched material.

The etched surface and the geometry of the resulting grooves were inspected by SEM imaging in top-view (see Fig. 5.2B) and section view (see Fig. 5.2C). The analysis revealed an exceptional finish and regular geometry of the obtained features: the grooves spacing is regular, while the material in between was not notably affected by the procedure. The analysis revealed an average grooves width of $w = (13 \pm 3) \mu\text{m}$, height of $h_g = (75 \pm 5) \mu\text{m}$ and a tilt angle of $\alpha = (85.8 \pm 2.6)^\circ$ (see Fig. 5.3). Moreover, the observation at high magnifications of the processed sample ($10^8\times$) showed the presence of a nanostructure on the cavity walls (see Fig. 5.4). This nanostructure is in the form of a fine porosity with dimensions less than a hundred nanometers, which results in an increase in the roughness of the solid-liquid contact area once the grooves are invaded by a fluid.

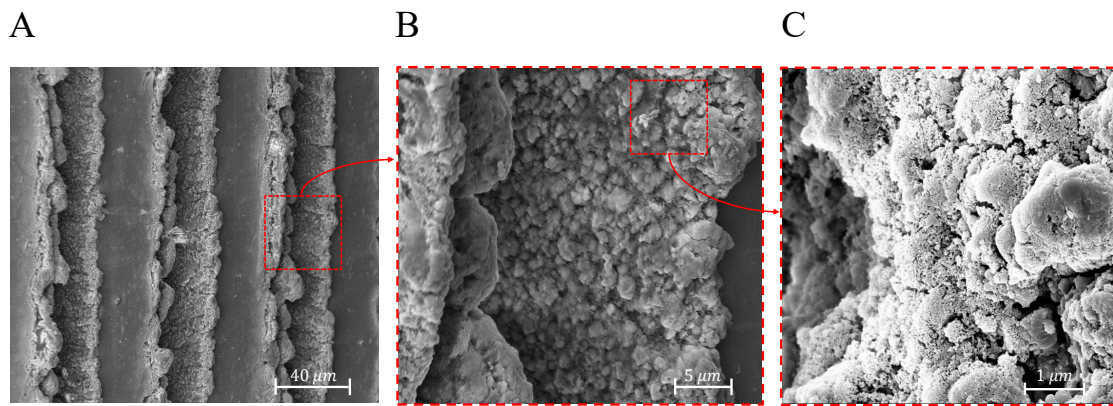


Figure 5.4: **Multi-scale features on the sample surface.** High magnification image of the nanotexture created on the grooves surface.

The chemical composition of the treated surface was analysed by EDS spectroscopy. The laser-etched grooves presented approximately 20-30 wt% of oxygen in the melted zone in proximity of the grooves (see Fig. 5.5B, right panel): the presence of oxides is mainly due to the high-temperature interaction between the treated surface and the surrounding atmosphere. No significant amounts of other elements were detected. Similarly, the lateral areas, slightly altered by the process, showed an increase in oxygen content of 9 wt%, while the untreated zone between the grooves has an oxygen content of only 2 wt% (see Fig. 5.5B, left panel), demonstrating its marginal oxidation and, therefore, the outstanding accuracy of the processing technique used.

5.2 Wetting and wicking performance

The effect of the surface oxidation produced by the laser treatment was assessed by the analysis of the water-aluminum contact angle and vertical wicking tests. The

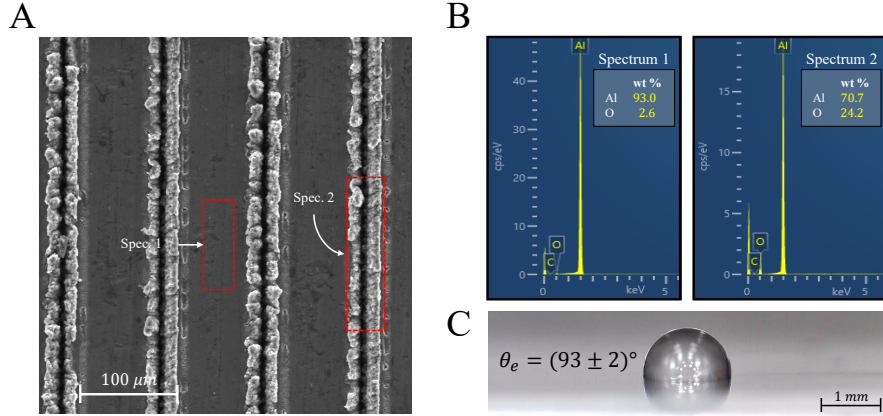


Figure 5.5: **Characterisation of the laser-etched material.** (A-B) EDS spectra of untreated (left) and treated (right) portions of the sample. Elements not shown in the legend were present in a non-significant amount. (C) Measurement of the contact angle θ_e on the untreated aluminum plate by the static sessile droplet method.

contact angle between distilled water and a pristine aluminum sheet was measured by the sessile drop method. Both surfaces of the pristine aluminum sheet were tested after being cleaned with isopropyl alcohol, dried, and then washed with deionised water and dried in open air. The drops were placed on the sample surface with a micro syringe and photographed by an optical microscope (RS PRO, 5M pixel of resolution). A ruler (RS PRO, 0.5 mm of resolution) was used to calibrate the images. The contact angle was evaluated by measuring the height h_d and half-width L_d of the droplets, under the assumption of negligible effect of gravity, namely $L_d \ll \sqrt{\gamma/(\rho g)}$ [114], which was experimentally verified for each droplet. See section 2.1.2 for further details on the numerical procedure adopted.

The experimental setup used to perform the vertical wicking measurements (see Fig. 5.6A) included a 1 cm \times 5 cm sample of the laser-etched aluminum sheet, a mechanical vertical stage, a metal bar fixed on an adjustable support, an optical microscope (RS PRO, 5M pixel of resolution), a ruler (RS PRO, 0.5 mm of resolution), and a basin filled with distilled water. The sample was suspended from the metal bar by a clip, while the water basin was placed on the adjustable vertical stage beneath the hanged sample. Before the beginning of the wicking test, the video resolution was calibrated by taking a snapshot of the metal ruler placed next to the hanged sample. The vertical stage was moved to dip approximately 2 mm of the sample, while the position of the advancing water front was recorded by the optical microscope. The images acquired were post-processed via a MATLAB[®] script to measure the time-dependent position of the water front H_t (see Fig. 5.6B-C). At the end of the test, the sample was removed from the clip and dried in open air for more than 3 hours before the test was repeated.

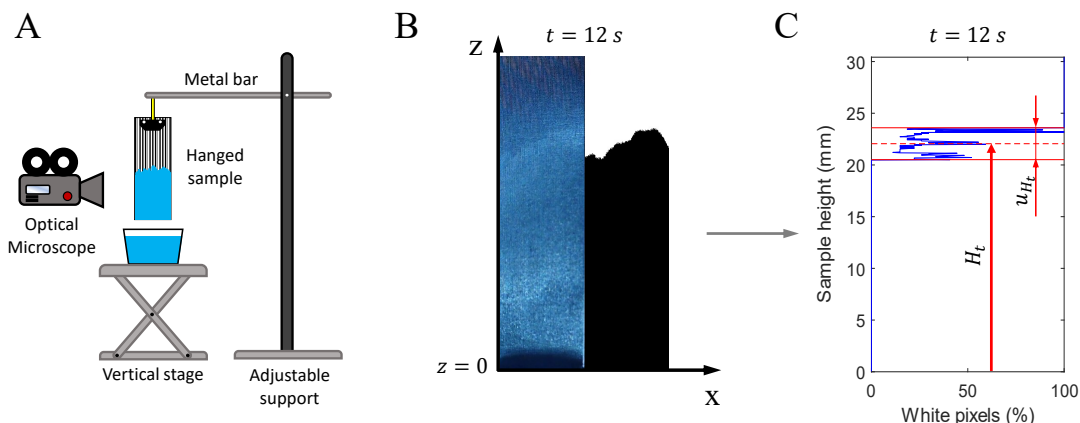


Figure 5.6: **Experimental investigation of the wicking performance.** (A) Schematics of the experimental setup and procedure used to perform the vertical wicking experiments. An optical microscope was used to record the vertical wicking experiment of a laser-etched sample hung from an adjustable support. (B-C) The images extracted from the video were post-processed and converted to black/white images via the *imbinarize* routine (B) and were used to estimate the position of the water front (C) by evaluating the percentage of white pixels in the x-axis direction.

Despite its high-energy structure, the aluminum samples presented an average contact angle with distilled water of $\theta_e = (93 \pm 2)^\circ$, characteristic of a slightly hydrophobic surface, coherently with previous observations on non-pure metal surfaces [211] (see Fig. 5.5C). However, the laser-etched specimen was able to promptly wick water as soon as it was dipped into the distilled water reservoir (see Fig. 5.7A and [Supplementary Video 3](#)). The advancing water front is not flat because the geometry and state of oxidation of the grooves vary slightly from each other: the varying surface roughness, height and angle of inclination determine the different capillary properties of each groove. However, the short-tails of their distribution allow to identify the moving water front in a range of few millimeters. The acquired images were translated into quantitative data by an image-processing tool and were used to evaluate the wicking performance of the crafted sample (see Fig. 5.7B). The sample showed stable capillary properties (tests 1-6 in Fig. 5.7B).

The observed capillary action was promoted by the combined effects of the reduced contact angle within the grooves and their geometric features. In particular, the presence of oxides made the grooves surface partially hydrophilic (namely, $0^\circ < \theta_e < 90^\circ$) which, thanks to the V-shape of the grooves, promotes the formation of concave menisci. The synergistic combination of these two factors, according to the Laplace's equation, generates an under-pressure at the air-liquid interface responsible of the observed capillarity. Note that both effects described are essential to observe wicking: a droplet on a flat and partially hydrophilic surface would simply retain a spherical cap shape, while a V-shaped groove made of a hydrophobic

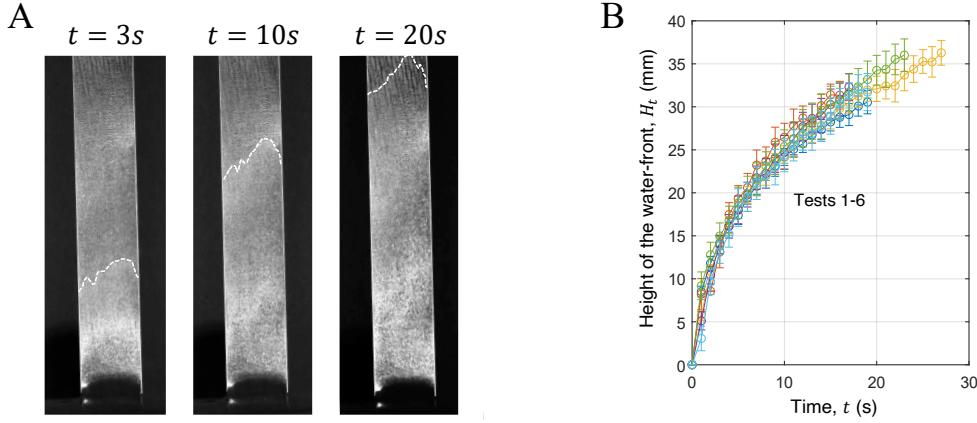


Figure 5.7: **Assessment of the obtained wicking performance.** (A) Progressive images showing the wicking transient in the laser-etched aluminum plate (see also [Supplementary Video 3](#)). (B) The capillary performance of the proposed material was evaluated by means of vertical wicking tests. Note that, between each test, the sample was simply dried in the open air.

material (namely, $\theta_e \geq 90^\circ$) would not wick water. See section 2.3 for a complete analysis of the conditions required to observe wicking in an ideal V-shaped groove.

5.3 Durability and surface functionalization

The vertical wicking performance was extremely stable for several cycles of exposure to water (see Fig. 5.7B). Thus, the durability of the component was investigated by means of an evaporation test: the grooved aluminum sheet was used to wick water from a reservoir under controlled temperature and humidity conditions (see Fig. 5.8). The water reservoir was made from a polypropylene box (10 cm \times 5 cm, 5 cm high) closed on the upper side by a specifically thermoformed plastic cover and sealed with silicone to reduce the evaporation losses. A thin slit (12 mm \times 3 mm) was hand-cut on the lid to dip the sample. The reservoir was placed on a high precision balance (Radwag, PS1000 R2), which was used with a sampling frequency of 1 sample/s to assess the evaporation rate. To ensure correct measurement of the evaporation rate, the tested sample and the remaining equipment was placed on an external adjustable support, avoiding any contact with the reservoir or the balance. The external support was composed by a vertical stage, insulating polystyrene foam, a thin copper sheet, three electrical heaters, three 100-ohm PRTs and the tested sample. The polystyrene foam was appropriately shaped and attached to the adjustable vertical stage, forming an insulating support for the sample, the heaters and the PRTs. A thin copper sheet was opportunely cut and connected to the polystyrene foam by double-sided tape. The three electrical heating

elements (Franco Corradi, $(32 \pm 1) \Omega$), connected in series, and two 100-ohm PRTs (RS PRO, tolerance class A) were attached to the copper plate facing the insulating foam. The electrical heaters were connected to a power supplier (HQ power, PS 3003) and to a high-precision amperemeter (Agilent, 34401 A). The tested sample was glued on the other side of the copper sheet, facing the environment, by a thin layer of thermal grease (RS PRO, $3.4 \text{ W m}^{-1} \text{ K}^{-1}$) and was then dipped in the reservoir for approximately 5 mm. An extra 100-ohm PRT was used to measure the ambient temperature. The PRTs signals were acquired by a dedicated DAQ device (Pico Instruments, PicoLog PT104).

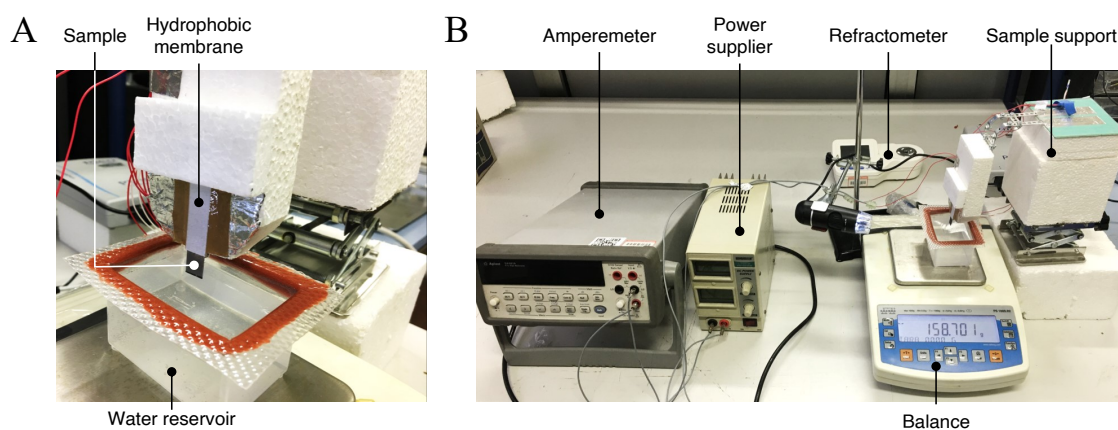


Figure 5.8: **Experimental setup used for the evaporation-based durability tests.** (A) Close-up photograph of the sample, placed on the insulation polystyrene support and covered by the hydrophobic membrane. Three electrical heating elements and two 100-ohms PRTs were placed between the sample and the insulating support to adjust and measure its temperature. (B) Experimental setup and measurement instruments used for the evaporation tests.

The measured evaporation rate \dot{m}_e was used to evaluate the stability of the wicking performance: consistent values of \dot{m}_e over time are related to a constant evaporating surface. The test results, performed with micro-filtered water, show a decreasing evaporation rate until, after 13 hours, evaporation from the specimen had ceased (see Fig. 5.9). This result can be related to a change of surface chemistry rather than to a modification of topology. During the initial wicking transient, the grooves are permeated by the aqueous solution and tend to be drained by the evaporative rate. However, due to capillary force, water is constantly supplied from the underlying basin and the phenomenon continues as long as the capillary pressure remains unvaried. As the aqueous solution flows, the dissolved ions and contaminants tend to rapidly saturate the reactive sites of the surface activated by the laser treatment, which are responsible for the observed hydrophilicity, thus inhibiting the capillary properties. To corroborate this hypothesis, SEM analysis of the sample used (see the inset of Fig. 5.9A) revealed that crystal formations

progressively covered the grooves surface without clogging the grooves completely (see Fig. 5.10). Furthermore, subsequent imbibition tests performed with the same sample revealed that the observed capillary properties were greatly reduced despite the fact that the grooves were not visibly clogged (see [Supplementary Video 4](#)). This evidence is in line with previous results reported in the literature of laser-treated aluminum [211–214]. Therefore, it is essential to increase the materials durability, for example by using nanoscale coatings or surface functionalizations to ensure the long-term durability of the component in harsh and reactive operating conditions.

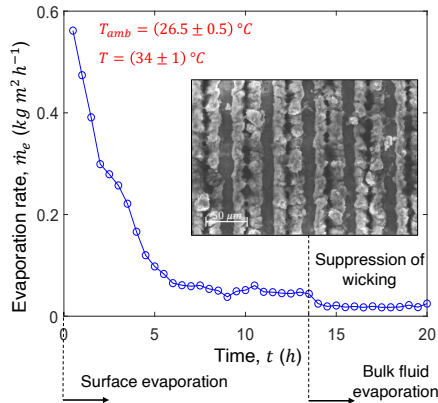


Figure 5.9: **Durability test.** The test was performed supplying the sample with approximately 1000 W m^{-2} . The decrease in evaporation rate was due to progressive saturation of the active sites on the grooves surface, thus inhibiting hydrophilicity and capillarity.

Consequently, two surface treatments were tested to improve the long-term durability of the sample, here intended as the ability of the material to maintain its functional properties when facing normal operating conditions (that is, remaining hydrophilic when exposed to aqueous solutions): a coating by radio frequency (RF) sputtering of SiO_2 and a functionalization by oxygen plasma. For the latter, first, the samples were sonicated in ethanol (3 minutes) and MilliQ water (3 minutes) and dried with N_2 flux. Subsequently a plasma treatment was performed in a Reactive Ion Etching system (RIE, SAMCO 10-NR) for 10 min at a pressure of 50 Pa, applying a power of 50 W and O_2 flux of 50 standard cubic centimeters per minute. Finally, the obtained samples were stored in a vacuum bag after insufflating nitrogen for about 1 min. For the SiO_2 coating, first the oxygen plasma treatment was performed following the same procedure described above. Successively, a conformal layer of approximately 50 nm of silica was deposited by radio frequency (RF) sputtering (Moorfield) at a pressure of 3 Pa and applying a power of 75 W for 3300 s.

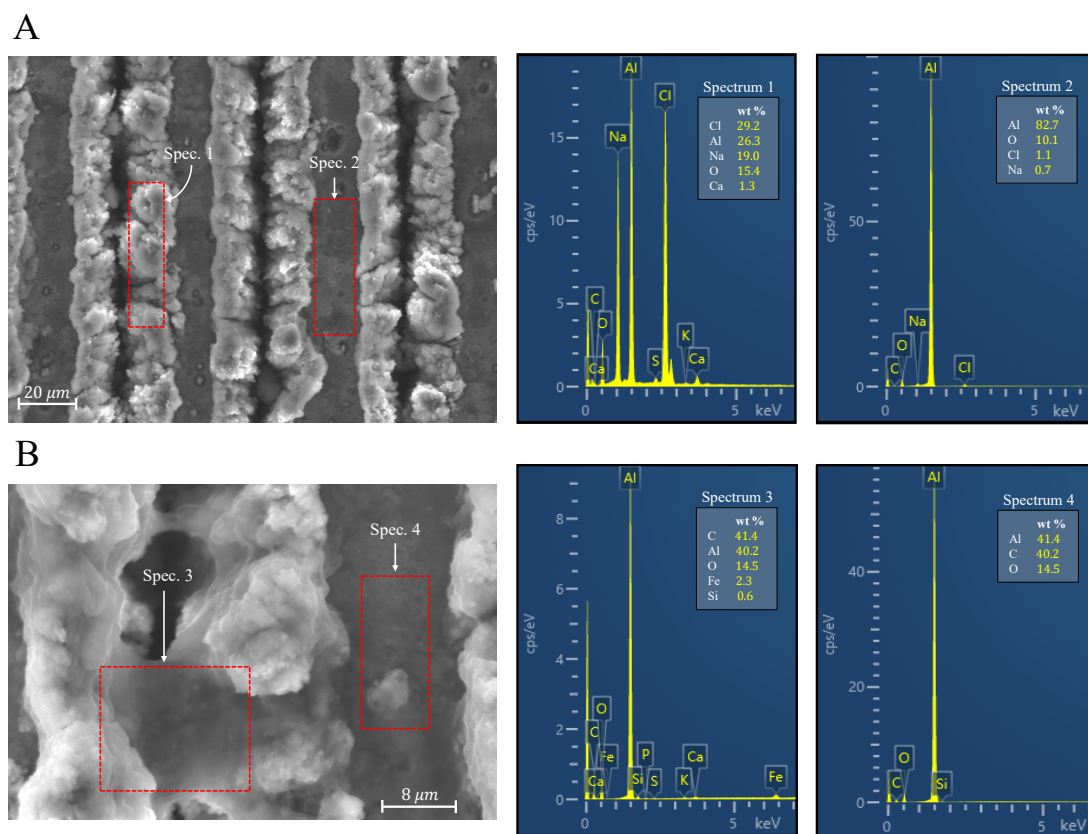


Figure 5.10: **EDS spectroscopy of the laser-etched aluminum after the evaporation test.** (A-B) SEM and EDS spectroscopy images of the proposed capillary material after long-term exposure to micro-filtered water and 1000 W/m^2 . The analyses show a high percentage of contaminants accumulated on the groove walls during the test. Note that the untreated areas (spectra 2 and 4) have low concentrations of contaminants. Elements not shown in the legend were present in a non-significant amount.

The RF sputtering technique was opted for its effectiveness in generating nanometer-thick layers of a wide range of materials, thus avoiding altering the original shape of the grooves, while SiO_2 was selected for its chemical stability, intrinsic hydrophilicity, and its ability to protect the substrate from reactive components possibly dissolved in the solution (i.e., Cl^- ions [216]). On the other hand, plasma treatment is an inexpensive and widely used cleaning procedure, but is commonly known to lose effectiveness after a few cycles of use. Thus, immediately after being treated with oxygen plasma, the sample was exposed to water vapor to saturate its active sites with hydrophilic $-\text{OH}$ groups. Both techniques (coating with SiO_2 and O_2 plasma) are easily scalable and applicable to large-scale production [217, 218].

First, the effect of the SiO_2 coating was tested on a grooved sample and on two

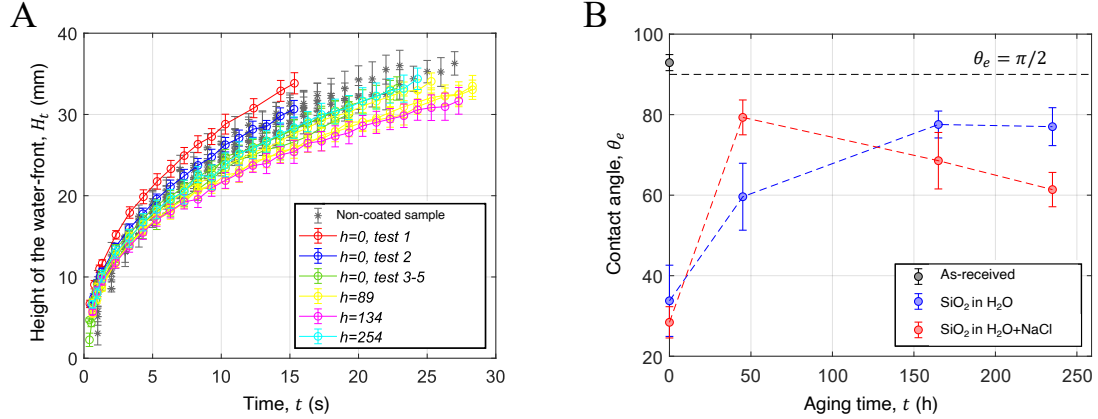


Figure 5.11: **Durability of the proposed material.** (A) Long-term durability test of the grooved aluminum sample coated with SiO_2 by radio frequency sputtering. The capillary properties remained stable for more than 250 hours of continuous immersion in distilled water (cyan data) and the performance was comparable with that of the as-machined sample (black data). Note that, without providing surface functionalization or coating, the as-processed grooved specimen lost its capillary properties after approximately 15 hours of exposure to water (see [Supplementary Video 4](#)). (B) Contact angle measurements on flat aluminum plated coated with SiO_2 and aged in distilled water (blue data) and saltwater (red data). Both samples remained hydrophilic after approximately 250 hours of aging.

untreated aluminum sheets. The former was aged in distilled water and its performance was tested by capillary rise experiments, while the flat sheets were aged in both distilled and saltwater (35 g L^{-1}) and the effectiveness of the treatment was evaluated by contact angle measurements. The laser-etched sample maintained excellent capillary properties (see Fig. 5.11A): the best performance was observed during the first test performed after being coated, which then slightly decreased until the third exposure (see Fig. 5.11A, red data). All subsequent tests showed stable and comparable performance within their uncertainty, even after more than 250 hours of continuous exposure to water (see Fig. 5.11A, cyan data), corresponding to approximately 1 month of continuous use for 8 hours per day. Note that the obtained capillary performance is comparable to that of the as-machined sample (see Fig. 5.11A, black data), thus achieving long-term durability without compromising the capillary properties initially observed. Similarly, the two flat plates coated with SiO_2 exhibited excellent wetting properties after the treatment (see Fig. 5.11B), reporting an average contact angle of $\theta_e = (31 \pm 5)^\circ$, which increased significantly after an initial exposure to the two solutions of approximately 50 hours. All the samples examined at the various aging stages exhibited values of contact angles lower than the as-received aluminum plates (see Fig. 5.11B, black data), and well below the threshold value of 90° .

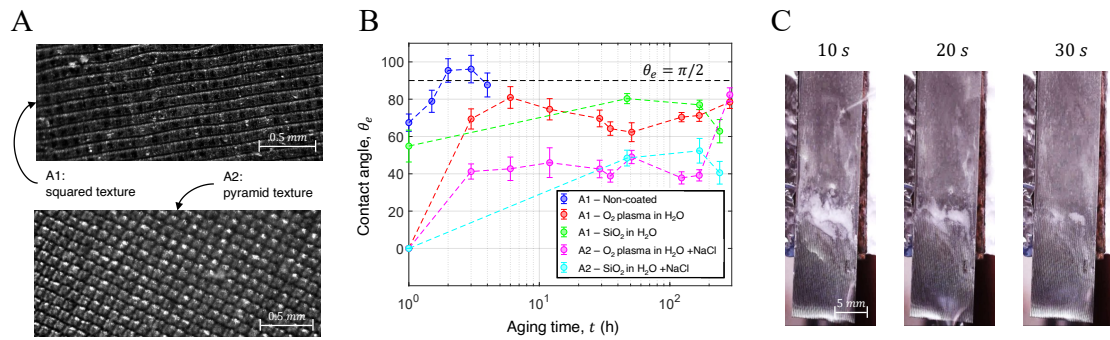


Figure 5.12: **Aging tests of different laser-etched patterns** (A) Square (A1) and pyramid (A2) textures obtained on two aluminum sheets by fs-laser etching. The samples were used to investigate the effect of the texture on the durability of the obtained hydrophilicity and to compare the efficacy of the oxygen plasma treatment and SiO_2 coating. (B) The as-machined A1 and A2 samples presented good hydrophilic properties, which however wore-out after a few immersion cycles (blue data). When functionalized with oxygen plasma (red and magenta data) or coated with SiO_2 (green and cyan data) the hydrophilicity remained stable and below 90° for more than 200 hours of immersion both in distilled (sample A1) and saltwater (sample A2). (C) Removal of salt crystals by gentle rinsing. Most crystals were removed within 40 seconds.

Subsequently, two different patterns, one with squares (A1) and one with pyramids (A2, see Fig. 5.12A), were crafted to verify whether the observed hydrophilicity and its short duration was due to the high aspect ratio of the topology obtained by laser-machining and to compare the effectiveness of the oxygen plasma treatment to that of the SiO_2 coating. Obviously, since the two textures are different, the two samples are expected to exhibit different θ_e regardless of the surface treatment applied. As anticipated, the combined effect of altered surface chemistry and texturing reduced the contact angles to $\theta_e = (67 \pm 5)^\circ$ and $\theta_e = (25 \pm 3)^\circ$ for A1 and A2, respectively (see [Supplementary Video 5](#)). However, as previously observed, the obtained hydrophilicity was depleted after a few immersion cycles in distilled water (see blue data in Fig. 5.12B and [Supplementary Video 6](#)), making it unusable for the intended application. Then, SiO_2 coating and oxygen plasma treatment were applied to both specimens and their performance was evaluated by contact angle measurements. While A1 was aged in distilled water, the effect of saltwater (35 g L^{-1}) on the two functionalizations was investigated on A2. Both surface treatments strongly improved the hydrophilicity of the samples, which also showed capillary spreading after about 100 min of immersion in both solutions (see red, magenta, and cyan data in Fig. 5.12B, and [Supplementary Video 7](#) for plasma-treated samples). Successively, θ_e increased for all tested configurations but remained stably below 90° for more than 200 hours of aging in both distilled and saltwater. The

presented results proved that simple surface functionalizations or coatings can dramatically increase the stability of performance of the proposed concept, even when operating with high salinity feeds.

The effect of precipitation or crystallization of contaminants on the sharp and rough surface of the grooves might lead to clogging and reduced performance. This condition might occur when operating with feeds at high salt concentrations and high evaporation rates and is one of the main challenges in applications like solar desalination [219–222]. Nevertheless, the salt crystals can be easily removed by gently rinsing the sample surface, even with salt or micro-filtered water, for approximately 40 seconds (see Fig. 5.12C and [Supplementary Video 8](#)).

5.4 Modelling and experimental evaluation of the capillary properties

Then, in order to compare the capillary properties obtained with those of other novel or commercial materials, both structured (i.e., with tailored and homogeneous pores) and unstructured (e.g., non-woven fabrics), it is essential to relate the microstructure of the proposed material to its capillary properties. In particular, the wicking performance can be described mainly in terms of capillary pressure p_c and absolute permeability K , which are functions of the surface chemistry (via θ_e) and geometry (via the height h_g and angle of inclination α) of the laser-etched grooves. Derivation of their analytical expression would allow the optimisation of the groove design parameters for a target application and provide guidelines for the chosen machining technique, which may not be limited to femtosecond laser.

The crafted laser-etched pattern made the aluminum sheet a fully-fledged porous medium which, consequently, can be described using a suitable theoretical framework. However, the different geometry, surface roughness and state of oxidation related to each groove make it convenient to model the pattern as a simplified homogeneous array of smooth V-shaped cavities, each with the average geometric parameters assessed by SEM image analysis (see Fig. 5.13). As accurately described in section 2.4, the time-dependent position of the water front H_t during wicking can be provided by solving the force balance between the capillary, viscous and gravitational forces, namely $F_c = F_\mu + F_g$. The capillary force F_c was derived from the solution of the Laplace's equation (see Eq. 2.1) and the surface free energy per unit length, which is a function of the solid-liquid and liquid-gas contact areas. Neglecting the effect of gravity and considering the groove entirely filled by water in the y-direction (see proofs in sections 2.3.1 and 2.3.2), the Laplace's pressure can be expressed as a function of a single, constant radius of curvature R (see Fig. 5.13). Thus, the Laplace's equation was integrated to obtain $R = h_g / [\tan(\alpha) \sin(\alpha - \theta_e)]$ (see section 2.3.2), which relates the meniscus shape, thus the capillary pressure, solely to the grooves geometry and surface chemistry. In this simplified approach,

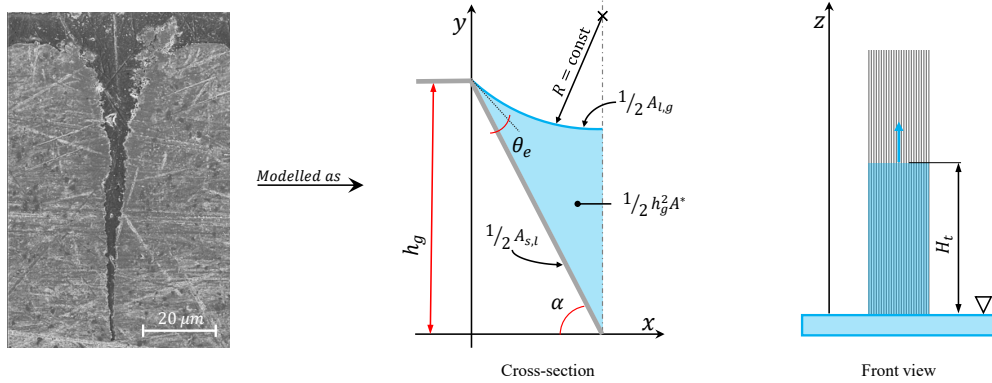


Figure 5.13: **Modelling the capillary performance of the proposed material**

The crafted grooves were represented as an ideal array of identical and smooth V-shaped cavities and their capillary properties were modelled as a function of their height h_g , tilt angle α and contact angle θ_e . The dynamic position of the water front H_t was modelled under the sharp-front approximation.

the capillary force F_c can be evaluated from the one-dimensional space derivative of the free energy per unit length, namely $F_c = -dE/dz$. In particular, the free energy per unit length E can be evaluated considering the solid-liquid and liquid-gas contact areas per unit length, $A_{s,l}$ and $A_{l,g}$ respectively (see Fig. 5.13), which can be easily evaluated with the analytical expression for R derived above; thus, $F_c = h_g \gamma P^*$, where P^* is a function of α and θ_e (see section 2.4.2). The gravitational force was evaluated as $F_g = \rho g z h_g^2 A^*$, where ρ and g are the water density and gravitational acceleration respectively, $h_g^2 A^*$ is the cross section of the groove occupied by water (see Fig. 5.13) and A^* is a function of α and θ_e . The viscous force F_μ was expressed considering a Poiseuille flow, assuming that the viscous losses are determined by the cross section $h_g^2 A^*$ rather than by the meniscus shape (see section 2.4.2). Thus, the one-dimensional force balance can be rewritten as a non-linear first order differential equation, which can be solved to obtain an analytical expression for the water front position:

$$H_t = C_2^{-1} C_1 \left[1 + W_0 \left(-\exp \left(-1 - C_2^2 t (8\pi\mu C_1)^{-1} \right) \right) \right], \quad (5.1)$$

where $C_1 = h_g P^* \gamma$, $C_2 = h_g^2 A^* \rho g$ and W_0 is the main branch of the Lambert function (see section 2.4.2 for a detailed proof).

The model described allows to evaluate the wicking performance of the rigid capillary material by relying on three parameters only, which are related to the average geometry of the grooves (i.e., their height h_g and tilt angle α) and their surface chemistry (through the equilibrium contact angle θ_e). However, the oxidation of the cavities surface and their irregular roughness changed the value of θ_e with respect to the one measured on the untreated aluminum surface. Thus, the

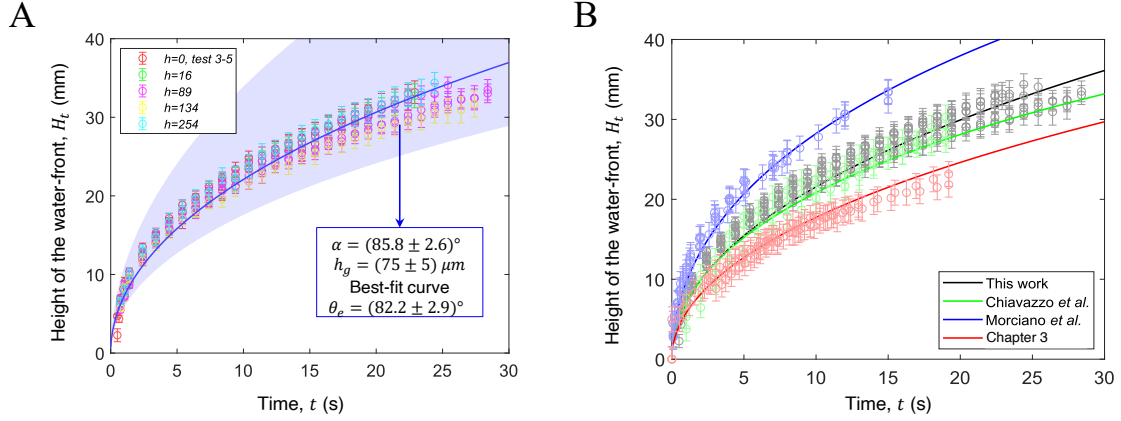


Figure 5.14: **Model fitting and comparison of the capillary performance** (A) The obtained data were used to fit the value of θ_e from the theoretical model by the least-squares method. (B) The wicking performance were compared with those of other hydrophilic textiles used in passive applications (green and blue data) [17, 96], including the woven PE textile presented in Chapter 3 (see red data).

apparent contact angle θ_e was evaluated by least squares fitting of the theoretical position of the water front H_t on the experimental data obtained, resulting in $\theta_e = (82 \pm 3)^\circ$. Note that the model fitting was performed on the data obtained from the aged sample coated by SiO_2 (green, yellow, magenta and cyan data in Fig. 5.14A). The reported uncertainty on θ_e was estimated through the fitting procedure by considering the experimental uncertainties of h_g and α , which led to the shaded blue area in Fig. 5.14A.

To assess the applicability of the proposed material, capillary properties of the aged sample (see Fig. 5.14B, black data) were compared with those of three other materials used for passive applications by means of vertical wicking tests: a polyethylene-based woven textile engineered for evaporative cooling proposed in Chapter 3 (see Fig. 5.14B, red data) and two non-woven fabrics employed in passive solar desalination devices [17, 96] (see Fig. 5.14B, green and blue data). The silica-coated aged material presents the second-best capillary performance with respect to the reference materials tested. The micro-porous structure of these materials is extremely different from that of the proposed material: the woven textile is composed of arrays of cylindrical fibers and its capillary properties can be ascribed to the size and arrangement of the fibers, while the non-woven textiles can be considered as a network of connected pores whose sizes can be expressed in terms of a probability distribution. The transport of a single-phase fluid in such different geometries can be modelled by Darcy's law, where the porous matrix is described in terms of its volume-averaged properties: the capillary pressure p_c , absolute permeability K and effective porosity ϕ , similarly to the procedure followed in Chapter 3. Darcy's law

and the continuity equation were combined and solved under the sharp-front approximation to derive another analytical expression of H_t (see section 2.4.3), which was then compared with the one derived for an ideal V-shaped groove, obtaining $p_c = \gamma P^* (h_g A)^{-1}$, $\phi = h_g (\delta \tan(\alpha))^{-1}$ and $K = \phi h_g^2 A^* (8\pi)^{-1}$. The wicking performance is enhanced by the increase of either the capillary pressure and the absolute permeability. However, the geometrical parameters of the grooves have competing effects on p_c and K : the capillary pressure is promoted by sharp and short grooves, while the opposite holds for the absolute permeability, as wide and tall grooves reduce the viscous losses (see Fig. 5.15). Note that the contact angle θ_e does not have an important effect on K , as it only affects the shape of the water meniscus modifying $A_{l,g}$ (see Fig. 5.13), while it changes the values of p_c by different orders of magnitude. Thus, lower values of θ_e are expected to have a major effect on the wicking performance.

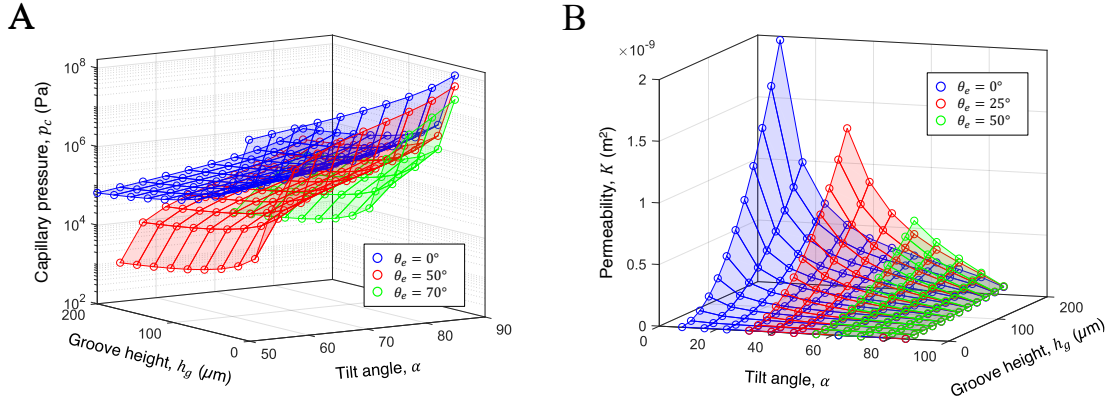


Figure 5.15: **Theoretical modelling of the capillary properties.** Theoretical predictions of (A) the capillary pressure and (B) the absolute permeability for different values of groove height h_g , tilt angle α and contact angle θ_e . The modelling predictions were performed considering an ideally smooth V-shaped groove.

The effective porosity ϕ and capillary pressure p_c of the materials used as reference in Fig. 5.14B were evaluated experimentally. To measure the effective porosity of the non-woven textiles (green and blue data in Fig. 5.14B), a large textile sample was entirely submerged in a laboratory-grade graduated cylinder. The volume of the porous matrix V_m was considered as equal to the volume of fluid displaced by the immersion of the sample. An optical microscope (RS PRO) and an image post-processing tool were used to increase the accuracy of the measurement. The total volume of each textile sample V_{tot} was evaluated by measuring its thickness, length and width with a high-resolution caliper. Thus, ϕ was defined as $\phi = 1 - V_m V_{tot}^{-1}$. Differently, the porosity of the woven textile (red data in Fig. 5.14B) was measured by a high-resolution micro-computed tomography scanner (Zeiss Xradia 620 Versa). The non-woven textile used by Chiavazzo *et al.* [96] (green data) presents

$\phi = (0.90 \pm 0.01)$, the one used by Morciano *et al.* [17] (blue data) presents a similar porosity $\phi = (0.87 \pm 0.05)$. Differently, the porosity of the ordered woven fabric described in Chapter 3 (red data) is significantly lower, namely $\phi = (0.53 \pm 0.05)$. The capillary pressure of the reference textiles was evaluated by means of capillary rise experiments. At the equilibrium, the capillary pressure is balanced by the gravitational force, namely $p_c = \rho g H_{t,m}$. For this purpose, the setup used for the wicking experiments was employed. An optical microscope, a ruler and an image post-processing tool were used to evaluate the height reached by the water front. The steady state was considered reached when the measured $H_{t,m}$ remained constant within a discrepancy of 5%.

As the effective porosity and the capillary pressure of the reference textiles were evaluated experimentally, the model was used to fit their absolute permeability from the vertical wicking data. The values of p_c and K obtained for the different materials are compared in Fig. 5.16A. As it can be observed, while the suction pressure due to the grooves geometry exceeds the others, the permeability of the two ordered geometries (namely, the woven textile and the V-shaped grooves, red and black bars respectively) is approximately one order of magnitude lower. Therefore, being able to define an optimal geometry of the porous structure (i.e., the grooves) while maximising the resulting capillary properties is crucial to increase their range of applicability and perform a correct design of the passive devices where they are put into use.

Most applications concerning capillary media in passive devices require evaporating the wicked liquid as it flows through the porous matrix. Consequently, evaporation affects the imbibition transient and, along with gravity, determines the maximum height reached by the water front $H_{t,m}$. This has a direct effect on the maximum size attainable for components relying on wicking and evaporation. Hence, the wicking model introduced in section 2.4.5, which includes an average evaporation rate, was employed to correctly model the performances of the component, as the explicit time discretization scheme used is particularly suited to investigate configurations at the dry-out limit, making it adequate to explore the limits of passive components for water transport. The model was used to evaluate $H_{t,m}$ for the reference textiles (green, blue and red bars in Fig. 5.16B) when subject to evaporation in laboratory conditions. The results were compared with the theoretical predictions for the proposed material (black bar in Fig. 5.16B) and for other rigid supports with optimal V-shaped grooves with $\theta_e = 71.3^\circ$, typical of nylon [159] (pink bar), and $\theta_e = 0^\circ$, characteristic of a super-hydrophilic surface such as clean glass [223] (yellow bar). Note that different contact angles might be achieved by surface treatment, different types of coating or by choosing as rigid support a material which is inherently hydrophilic. The performance of the proposed material is comparable to the reference ones. However, when considering a lower contact angle, the performance of the laser-etched support exceeds that of traditional materials, which, due to their non-ordered structure, have fewer degrees

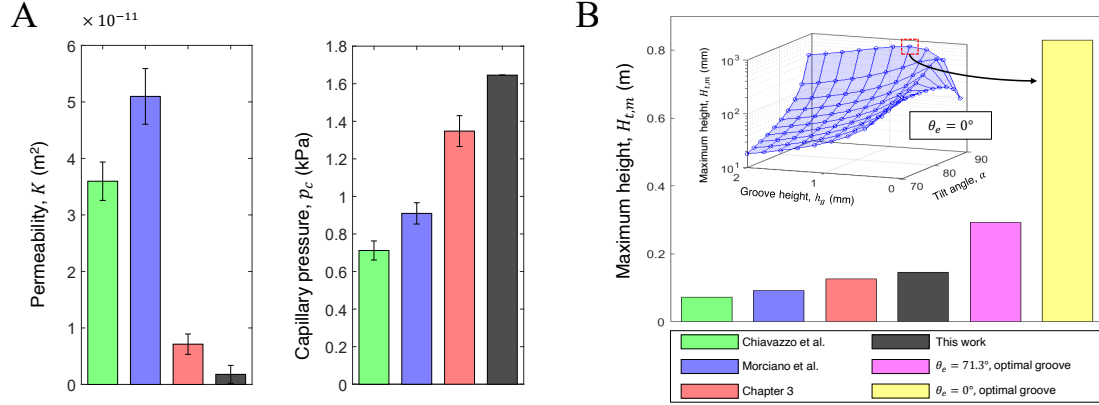


Figure 5.16: **Model fitting and comparison of the capillary performance** (A) The capillary pressure p_c and absolute permeability K of the crafted material were compared with those of other hydrophilic textiles used in passive applications (green, blue and red data) [17, 96]. (B) A novel dynamic model including the effect of evaporation in the wicking transient was used to predict and compare the performance of the proposed material (black bar), the reference textiles (green blue and red bars) and ideal V-shaped grooves with different hydrophilicity (pink and yellow bars). The theoretical predictions were performed considering a constant evaporation rate $\dot{m}_e = 0.25 \text{ kg m}^{-2} \text{ h}^{-1}$ on the sample surface exposed to the environment.

of freedom for further optimisation.

Note that the specific working condition should be considered in the optimization procedure (see the inset in Fig. 5.16B for $\theta_e = 0^\circ$): different evaporation rates affect the optimal value of h_g (see Fig. 5.17). The optimisation algorithm favors extremely sharp angles, ideally up to 89° , which might entail processing and operability issues: while a large variety of applications rely on pure liquids (e.g., electronic cooling), others might be subject to crystallisation or build-up of contaminants dispersed in the working fluid (e.g., water treatment and desalination). Therefore, the design and optimisation of the grooves geometry should include not only the fluid transport, but also the constraints due to specific applications, the device working conditions and the chemical-physical interactions at the solid-liquid interface.

5.5 Application in solar desalination

An emerging and interesting engineering application of porous materials is represented by passive solar or thermal desalination, a viable and large-scale option

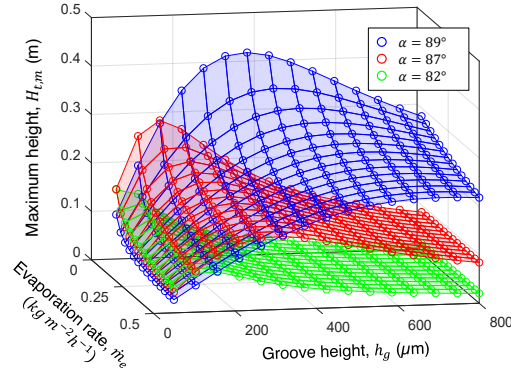


Figure 5.17: **Theoretical Prediction of the wicking performance with different evaporation rates.** Maximum height reached by the water front in vertical wicking test $H_{t,m}$ evaluated for different evaporation rates \dot{m}_e and geometrical grooves parameters, namely height h_g and tilt angle α . The predictions were performed by a novel model employing an explicit time discretization scheme to include the effect of evaporation rate in the wicking transient (see section 2.4.5). The results show how the working conditions should be included in the optimization of the geometry, as different \dot{m}_e result in different optimal values of h_g . Furthermore, the predictions show how small variation of α may result in a dramatic decrease of the resulting capillary properties.

to address water shortage. Several works proposed different novel materials allowing passive operations such as graphene-based materials [224–227], carbonized bio-materials [27, 228], carbon-based materials [106, 229–232], polymers or hydrogels [233, 234], nanofluids and/or nanoparticles [235–239] and metal oxides [28]. However, most of the designs proposed often include a single-stage evaporator and are constrained by the thermodynamic theoretical limit of $1.5 \text{ L m}^{-2} \text{ h}^{-1}$ [96], which is far below the output of active systems. Multistage passive devices offer a solution to the issue: their design allows to recover the enthalpy of condensation of one stage to drive the evaporation in the next one, thus triggering a cascade process able to go beyond the single-stage limit. Recently, various multistage prototypes utilizing solar energy and non-structured capillary materials were proposed and experimentally characterized [17, 96, 119–121, 215, 240]. Here we investigate the feasibility of replacing the traditional porous layer by embedding the developed laser-etched component in the device layout proposed in Refs. [17, 96] and successfully used as a reference in several following works [120, 121, 241, 242]. This substitution allows to improve the compactness of multistage devices, thus increasing the number of stackable stages, and to simplify their assembly on an industrial scale. At the same time, it allows to increase the stability and repeatability of their performance and general quality.

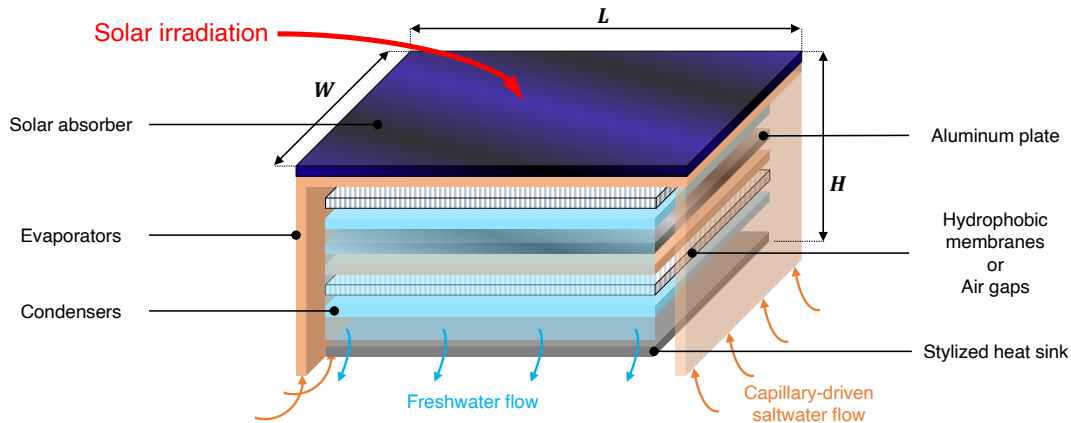


Figure 5.18: **Layout of a device for passive multistage desalination.** Stratigraphy of the proposed passive device for solar desalination. The modular design allows to stack several stages to improve the overall productivity. For the sake of simplicity, only two stages were represented.

A schematic of the device is reported in Fig. 5.18 and its layout and working principle can be briefly summarised as follows. The considered device shows a multistage configuration to recover the latent heat of condensation, thus enhancing the water productivity. Without losing generality, the schematic reported in Fig. 5.18 is referred to a two-stages configuration device. Each stage is composed by an evaporator, an hydrophobic membrane or an air gap, and a condenser (see Fig. 5.18). The latter is placed in thermal contact with the evaporator of the subsequent stage by means of an aluminum plate, enabling latent heat recovery. Evaporators supply seawater to the device, while condensers collect and channel the freshwater out of the device into an external basin. As already anticipated, evaporators and condensers are usually made of capillary porous media, thus being able to overcome small hydraulic heads (indicated with H in Fig. 5.18) and deliver the working fluids throughout the system without the need of mechanical or electrical active components. The hydrophobic membrane avoids contamination between the evaporator and the condenser, as it can not be crossed by water unless a given pressure is applied, which usually is orders of magnitude higher than the normal working pressure and depends on the membrane surface chemistry and average pores size. However, the proposed rigid porous structure allows to replace the hydrophobic membranes with simple and cost-effective air gaps [17], ensuring the planarity of the stack and, therefore, avoiding contamination between the two feeds. Since hydrophobic membranes are responsible for most of the cost of passive thermal desalination devices (see the cost analysis of the passive cooler in section 4.9), this concept appears to be an effective solution to significantly improve economic viability of passive thermal desalination devices. The first-stage evaporator is heated by an external heat source, usually solar irradiation, which is harvested

by means of a selective highly-efficient absorber, while the last-stage condenser is in thermal contact with a larger heat reservoir – usually the saltwater reservoir itself – by means of a heat sink. In this way, a temperature gradient is imposed across the device and, thus, across the membranes of each stage. The counter-posing interplay of the temperature and salinity gradients across the hydrophobic membrane imposes a net vapour pressure difference, thus generating a net vapour flux from the evaporator towards the condenser [17, 96]. The condensation of water vapour leads to the release of enthalpy, therefore heating by conduction the evaporator of the adjacent stage driving further evaporation of saltwater.

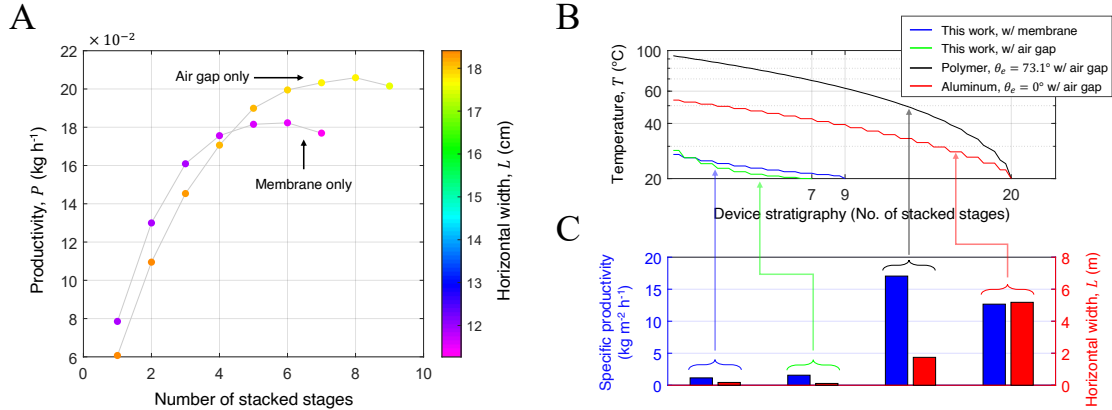


Figure 5.19: **Layout of a devices for passive multistage desalination.** (A) Modelling predictions of the device productivity P , expressed in kg h⁻¹, achievable by employing the proposed grooved aluminum layer in both evaporators and condensers, using either a hydrophobic membrane or an air gap. By varying the number of stacked stages, it is possible to identify the optimal configuration to maximize the device performance. The color bar reports the maximum horizontal width achievable L , highlighting how alternative layouts imply different operating evaporating surfaces. (B) Temperature distribution through the representation of the device by thermal network, where the number of simulated stages was highlighted on the horizontal axis. The simulations were performed considering different properties of the substrates constituting the evaporators and condensers: a conductive aluminum sheet (blue, green and red curves); a thermally insulating polymer (black curve); different levels of hydrophilicity (blue and green curves $\theta_e = 84^\circ$, black curve $\theta_e = 73.1^\circ$, red curve $\theta_e = 0^\circ$). (C) Specific productivity (blue bars) and maximum achievable horizontal width (red bars) of the configurations tested in panel B. The configuration reporting the highest specific productivity, may not present the highest overall productivity P due to poor capillary performance.

A theoretical lumped-parameter model was developed to predict the achievable performance and size of the described desalination device, considering various materials, layouts, and operating conditions (see Appendix C for a detailed derivation

and description). The Maxwell-Stefan and dusty-gas models described in section 2.6 were implemented and coupled with the time-discretized wicking model described in section 2.4.5. The resulting comprehensive theoretical framework allows estimating the maximum size achievable by the desalination device while avoiding dry-out, while simultaneously accounting for incident solar irradiation, ambient temperature, and number of phases. The performance predictions were performed considering seawater with NaCl concentration equal to 35 g L^{-1} and incident solar irradiation of 1000 W m^{-2} . The considered selective solar absorber has a solar absorbance equal to 0.95 and a limited infrared emissivity equal to 0.04. A transparent insulator reducing the natural convection (3 layers, each consisting of an ABS frame used to maintain two films of polypropylene 2 mm apart.) was considered as placed on top of the selective absorber and was included in the model with an heat transfer coefficient of $5 \text{ W m}^{-2} \text{ K}^{-1}$. On the other hand, the aluminum heat sink placed at the bottom of the full stack leads to an enhanced heat transfer coefficient equal to $150 \text{ W m}^{-2} \text{ K}^{-1}$, improving the heat dissipation and thus the temperature gradient across the device. Salt and distilled water were considered as separated by an hydrophobic membrane ($150 \mu\text{m}$ thick, porosity of 0.8 and average pore size of $1 \mu\text{m}$) or by an air gap 0.5 mm thick and with unitary porosity. The total size of the device, and thus the related evaporating area, is equal to $W \times L$ (see the schematics reported in Fig. 5.18), where W was kept constant for all the considered case studies and equal to 1 m, whilst L was the design parameter evaluated by the coupled model. Note that W does not affect the modelling predictions. Then, based on the thermal properties of the materials, the micro-structure of the porous layers, and the solar irradiation, the model estimates the maximum horizontal size (namely, $L_{hz,m}$) that the multistage device could not exceed in order to avoid dry-out phenomena. Note that the conservative criterion $L \leq 0.9 \times L_{hz,m}$ was applied. The modelling predictions were obtained considering several configurations of the capillary substrates constituting the evaporators and condensers: the proposed laser-etch material, namely a grooved aluminum sheet with the same capillary properties shown in Fig. 5.16A; a polymer substrate with $\theta_e=73.1^\circ$ and optimized grooves (resulting in $K = 8.23 \cdot 10^{-11} \text{ m}^2$ and $p_c = 4.26 \text{ kPa}$); an ideally wettable aluminum sheet with $\theta_e=0^\circ$ and optimized grooves (resulting in $K = 1.59 \cdot 10^{-10} \text{ m}^2$ and $p_c = 12.16 \text{ kPa}$).

First, the coupled model was used to evaluate the optimal configuration and overall productivity P of the desalination device when the proposed grooved material is employed in both condensers and evaporators (see Fig. 5.19A). The achievable values of the maximum horizontal width L were indicated using the color bar. Considering a traditional layout, which requires the use of a hydrophobic membrane, the maximum predicted performance was obtained by combining 6 stages with a horizontal width of about 12 cm. Note that fewer stacked stages allow for larger evaporating surfaces (see the color bar in Fig. 5.19A), as capillarity should overcome smaller hydraulic heads. However, the proposed rigid porous structure

allows to replace the hydrophobic membranes with simple and cost-effective air gaps [17], ensuring the planarity of the stack and, therefore, avoiding contamination between the two feeds. Since hydrophobic membranes are responsible for most of the cost of passive thermal desalination devices [54], this concept appears to be an effective solution to significantly improve economic viability of passive thermal desalination devices. Therefore, the modelling predictions were repeated by substituting the membrane with a 0.5 mm air gap, allowing the most expensive and fragile component of the device to be replaced with an inexpensive and robust plastic frame. This configuration resulted in an approximately 30% wider device, more stackable stages, and an approximately 10% higher values of P . The increase in performance is caused by the counterintuitive reduction in specific evaporative flux due to the air gap. As it can be seen in Fig. 5.19B, the air gap configuration (green curve) results in a lower temperature profile than the membrane layout (blue curve), and, consequently, in a lower specific productivity (see the respective blue bars in Fig. 5.19C). However, the reduced evaporation rate enables higher values of L before dry-out occurs, resulting in higher productivity. This analysis highlights how P is non-linearly determined by these competing effects, making the proposed model a necessary tool to predict the optimal device configuration.

As mentioned above, the achievable specific productivity is determined by the temperature distribution within the device, which varies according to the environmental conditions (e.g., ambient temperature and solar irradiance), the heat transfer and mass properties of the materials used in the device (e.g., membrane permeability, thermal resistance between the stages, heat losses), and the number of stacked stages. Since higher temperature profiles are related to increased specific productivity, minimizing the heat losses towards the water reservoirs is crucial to maximize the device performance. Accordingly, the model was used to evaluate the effect of the properties of the capillary substrate in two additional configurations: an insulating polymer (i.e., nylon, $\theta_e = 73.1^\circ$) and an ideally wettable aluminum layer (namely, $\theta_e = 0^\circ$), both provided with optimal grooves (which shape was evaluated via the presented capillary model). Clearly, for equal number of stacked stages, the lower thermal conductivity of the configuration comprising the polymeric substrate (see Fig. 5.19B, black line) reports a higher temperature profile than the one with aluminum (see Fig. 5.19B, red line), and also results in higher specific productivity (see the respective blue columns in Fig. 5.19C). However, P is determined by both the specific productivity (see blue bars in Fig. 5.19C) and the maximum achievable horizontal width L (see blue bars in Fig. 5.19C). Thus, the mediocre capillary performance of the polymer substrate limits L (see red bars in Fig. 5.19C), and thus also the achievable P (see Fig. 5.20), emphasizing the reduced impact of thermal losses if better capillary properties provide a larger evaporating surface.

To enhance the device performance, the horizontal section of the evaporators, must present high thermal conductivity to minimize the thermal losses within the

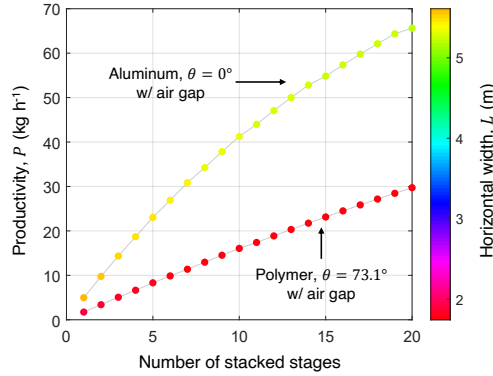


Figure 5.20: **Extrapolation of the performance of the desalination device.** Modeling predictions of the device productivity P achievable by employing two different materials as substrates in both evaporators and condensers: nylon, with $\theta_e = 73.1^\circ$; an ideally wettable aluminum sheet. Both materials were supposed as provided with optimal grooves, which shape was evaluated via the presented capillary model. The simulations were performed considering a membrane-less configuration. The color bar reports the maximum horizontal width achievable.

stack. Simultaneously, it is also necessary to reduce conductive losses towards the reservoir, which, as analysed above, would hinder the device productivity. Consequently, the vertical section of the evaporators must have low thermal conductivity. Disengaging from the engineering problem, the grooved layers were envisaged as multi-materials consisting of a vertical section of glass (hydrophilic and a good thermal insulator) and a horizontal section of aluminum, both with the same capillary properties. It is worth noting that this assumption is introduced solely on a theoretical level to show the impact of an ideal and thermally-anisotropic capillary layer, able to maximise the device performance in this particular application. The multi-material envisaged were supposed to be composed by glass (with thermal conductivity $0.8 \text{ W m}^{-1} \text{ K}^{-1}$) and aluminum (with thermal conductivity $290 \text{ W m}^{-1} \text{ K}^{-1}$) on the vertical and horizontal sections, respectively. The materials were assumed to have homogeneous capillary properties, equal to those of the two aluminum substrates (namely, the one tested and the ideally wettable one) reported above, and were used to obtain the modelling predictions shown in Fig. 5.21. Therefore, the thermal conductivity of the saturated vertical section was determined by averaging the thermophysical properties of water and glass, while that of the horizontal section was evaluated as the average of the thermophysical properties of water and aluminum. Both averages were weighted by the porosity of the considered substrate ϕ .

In this scenario, a laser-etched multi-material with similar capillary properties

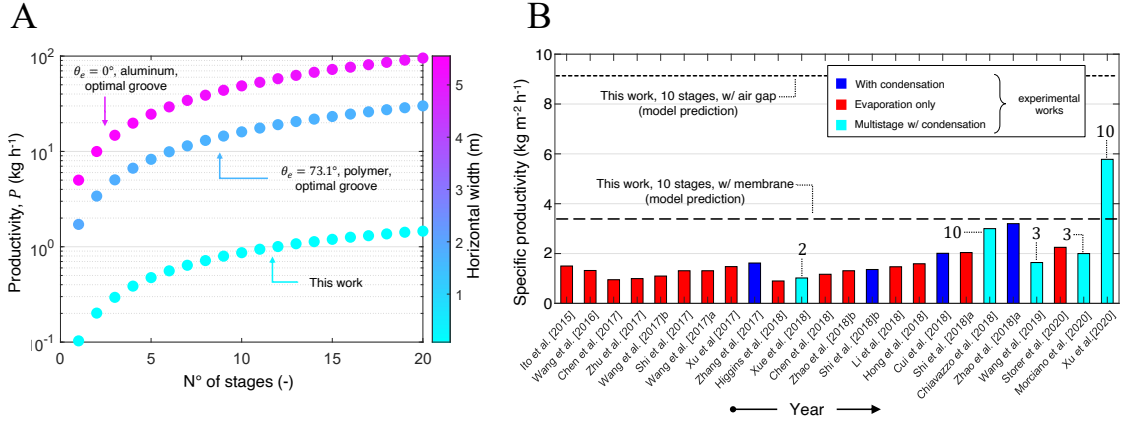


Figure 5.21: **Performance extrapolation employing perspective multi-material substrates.** (A) Modelling predictions of productivity, maximum horizontal width L and optimal number of stages for the passive desalination device. The dynamic capillary rise model and a lumped-parameters thermal model were coupled and used to evaluate the maximum length L achievable with a wicking material of known capillary properties, while avoiding dry-out. The predictions are referred to the air gap configuration. (B) Comparison between the experimental performance of different passive solar desalination devices reported in the literature (colored bars) with those predicted by the proposed model (black dashed line), including or excluding the contribution of a commercial hydrophobic membrane. The values reported above the multistage references refer to the number of modular stages tested.

as those achieved in this work allows to feed a 20-stages configuration device guaranteeing a productivity equal to 1.5 kg h^{-1} and width L equal to 8 cm (see Fig. 5.21A). The predictions were also extended to the other two configurations tested, namely the nylon substrate and the ideally wettable aluminum sheet, both engraved with optimized grooves and the latter envisaged as a multi-material (i.e., with its vertical section made of glass). In a 20s-stages configuration, the polymer-based material resulted in a productivity $P = 30.0 \text{ kg h}^{-1}$ and horizontal extension $L = 1.7 \text{ m}$; similarly, a 20-stages configuration employing the ideal multi-material allowed to achieve $P = 95.4 \text{ kg h}^{-1}$ and $L = 5.1 \text{ m}$ (see Fig. 5.21A). It is worth noting that the productivity obtained optimizing the grooves geometry on an ideally hydrophilic material is approximately 2 orders of magnitude higher than the case study reported. Therefore, maximising the capillary properties of the porous materials employed is crucial to maximise the overall performance of the device.

Finally, for the sake of completeness, a comparison between the performance of state-of-the-art devices and that of the proposed multistage device operating with the envisaged laser-etched multi-material component with the same capillary properties achieved in this work, evaluated via model extrapolation, is reported in

Fig. 5.21B. In detail, light blue and blue bars are referred to multistage and single-stage devices, respectively, able to perform a complete distillation cycle (namely, including both the evaporation and condensation processes). Instead, red bars are referred to devices able to perform a partial distillation cycle, where only evaporation takes place. The black dashed lines report the produced modelling predictions, which, for a fair comparison, were limited to 10-stage configurations. Interestingly, the use of the air gap alone allows the device to achieve a 165% increase in specific productivity with respect to the hydrophobic membrane configuration, and a 58% increase over the higher performing device [121] (see Fig. 5.21B). Note that all the state-of-the-art devices considered were manufactured on a laboratory scale, with a maximum size of the order of centimetres, whereas the device envisaged here might be easily scaled to the order of metres. This highlights how disregarding the capillary properties of the materials selected when designing a passive device involving wicking and evaporation might significantly limit its performance and the scalability of the proposed technology. Furthermore, the rigid structure of the grooves allows easier and more precise assembly of the multistage device, compared to soft materials such as fabrics or hydrogels.

5.6 Conclusions

V-shaped grooves were engraved on rigid aluminum sheets by femtosecond laser processing. As process-activated surfaces progressively lose their acquired hydrophilicity during operation due to the change of their surface chemistry, our samples were coated by SiO_2 or functionalized with oxygen plasma (RIE). Both treatments, commonly employed on industrial scale applications, significantly increased the chemical stability of the samples, either pristine or laser treated. In fact, the tests performed showed improved wettability and outstanding durability with respect to the untreated samples. The samples were aged by continuous exposure to distilled or saltwater and presented stable hydrophilicity and capillary properties for the whole duration of the test (more than 250 hours). The achieved long-term stability is a considerable improvement, as several references presenting new materials for steam generation tested their performance for a continuous time of approximately 1 hour [27, 224, 226, 228–231, 233–235], only rarely exceeding this time [106, 225, 232].

Afterwards, the wicking performance of the silica-coated grooved sample was compared with that of three other capillary materials (the woven PE fabric discussed in Chapter 3 and two other non-woven textiles, see Refs. [17, 96]), showing the second best performance in short-term vertical imbibition tests. The experimental results were then interpreted by the proposed time-discretized analytical model coupling the effect of the grooves geometry, hydrophilicity and evaporation rate. The model was then used to predict the optimal values of the geometrical

parameters of the grooves maximising their transport properties.

Finally, the capillary model was coupled with the lumped-parameter model of heat and mass transfer in multistage membrane-based devices (see Appendix C), succeeding in relating several microstructural and physical design parameters of the components (hydrophilicity, groove shape, thickness, and thermal conductivity) to the final productivity of a desalination device. The coupling of the two models requires their iterative resolution to combine thermal transfer (absorption of solar radiation, convective and conductive losses) with the mass transport phenomena (capillary wicking and membrane transport). The combined models were essential to estimate the overall productivity of the assembly by estimating the maximum achievable length to avoid dry-out when operating under average mid-day conditions.

The rigid capillary substrate allows to replace the hydrophobic membranes with inexpensive air gaps: the proposed laser-etched aluminum could be used to assemble a 8-stages membrane-less device with a predicted specific productivity of $1.6 \text{ kg h}^{-1} \text{ m}^{-2}$. Then, envisaging the fabrication of a multi-material substrate with the same capillary properties obtained in this work, a 10-stages device could achieve a 58% higher specific productivity than the best-performing passive thermal device reported in the literature [121], for the same number of stages used and without relying on membranes. The obtained predictions highlight the potential of employing a composite material with anisotropic thermal conductivity: a vertical glass section (hydrophilic and good thermal insulator) and a horizontal metallic section with the same capillary properties would minimize the thermal losses towards the water reservoirs and within the device itself. Note that the model extrapolations should be considered solely as a discussion of a relevant case study and guide the reader toward a more rational design of passive devices.

Concluding, the proposed modelling framework proved to be essential in the perspective scale-up of passive components, as it relates the capillary properties of a specific material – whether structured or not – and the target working conditions to the maximum evaporating surface exploitable. Thus, a combination of the adopted design approach and the structured rigid capillary materials paves the way for the transition from laboratory-scale prototypes, as the one proposed in Chapter 4, to real-scale devices.

Chapter 6

Conclusions and perspectives

This dissertation aimed to develop a comprehensive framework for modeling and characterizing the heat and mass transfer in porous media for passive energy applications, namely not powered by high-grade energy sources or equipped with mechanical moving parts, in the broader context of the water-energy nexus. In particular, the focus was set on capillary transport and evaporative heat transfer, which is a ubiquitous phenomenon in all the investigated applications: a polyethylene fabric for personal thermal management, a passive salinity-driven cooling device, and a multipurpose rigid, ultra-thin capillary layer (here envisioned for use in multistage passive devices). Each application combined theoretical modeling and experimental validation to demonstrate the potential of the proposed concepts. In this way, this thesis sought to create a bridge between fundamental research on heat and mass transfer phenomena and applied engineering challenges.

To this end, the theoretical basis of mass transport in capillary systems was outlined. First, the problem was approached analytically, deriving the equations necessary to describe the wettability and dynamic wicking in the considered systems, starting from a simplified representation of their geometry. In particular, a methodology to evaluate the contact angle on flat or cylindrical surfaces from images of micro-droplets was developed; two models to evaluate the porosity, capillary pressure and permeability in woven textiles and in V-shaped micro-channels were derived; a model describing imbibition in porous media subject to evaporation was formulated. Afterwards, water retention curves were used to obtain a differential formulation of the imbibition process, to be solved numerically, with the aim of extending the study to complex 2D and 3D geometries.

The developed theoretical framework was directly applied in the evaluation and optimization of the transport properties of fabrics for personal thermal management. For the first time, polyethylene was successfully used to fabricate a comfortable and high-performance garment. First, its main micro-structural features were experimentally investigated and used to infer the optimal fabric structures by means of the formulated analytical models. Then, the thermal performance of the realized

PE fabrics was measured and directly compared with that of other commercial textiles made of traditional materials. Finally, the derived differential formulations of heat and mass transfer were coupled and implemented via a finite element software to evaluate the fabric performance under different operating conditions. Overall, the results presented demonstrate the potential of using engineered polyethylene fibers to craft high-performance apparel, increasing thermal comfort and succeeding to achieve better performance than the most commonly used materials: cotton and polyester. Furthermore, the combination of the demonstrated efficient evaporative cooling and their previously discovered passive radiative cooling functionality can help to reduce HVAC energy consumption.

On a single-user level, the use of passive heat and mass transfer mechanisms was shown to be an effective strategy by managing sweat evaporation and promoting or hindering radiative heat transfer. Pushing the concept further, similar strategies were applied to a wider range of applications (e.g., thermal management of buildings) by envisioning a novel technology that could replace or support traditional cooling systems. Specifically, this work proposed a passive, modular device capable of generating a net cooling capacity based solely on capillarity and the salinity difference between two solutions. The concept was implemented in the form of a 4-stage laboratory-scale prototype, which was tested during operation with sodium or calcium chloride. Then, the obtained data were used to validate a 0-D heat and mass transfer model, which was then used to evaluate the device performance under a wider range of operating conditions and to optimize the device stratigraphy, maximizing its performance and reducing its consumption. Interestingly, achieving a maximum cooling capacity of approximately 170 W m^{-2} , the tested device was able to overcome the main limitations and performance of daytime radiative cooling.

Commonly, porous materials such as paper, non-woven fabrics, or hydrogels present non-ordered structures. As these offer limited degrees of optimization and control of their properties, this thesis proposed a rigid substrate where capillarity was promoted by etching V-shaped channels by means of a femtosecond laser. By optimizing the shape of the channels and functionalizing their surface (e.g., by deposition), the resulting chemical and transport properties could be tuned. The concept was tested on silica-coated aluminum substrates, which exhibited stable capillary properties even after prolonged exposure to distilled and salt water. After being validated on experimental data, the developed analytical models were used to propose general design guidelines for components operating close to their dry-out limit. The material was envisioned for use in a multistage solar desalination device, but its use can be extended to any passive device with a similar layout, such as the discussed cooling device. Indeed, by being thin, rigid and exhibiting tailored chemical and transport properties, the material can simplify the assembly of multistage devices by providing compactness and eliminating eventual hydrophobic membrane, still the standard on such devices and yet the most expensive and

fragile component of the stack.

On a theoretical level, the main contribution of this work was to outline a coherent framework (with a multi-scale connotation) about capillarity, suitable to link the properties of porous media with the performance of the devices in which they are used. For this purpose, the existing formulations were occasionally extended, deriving specific equations for the systems investigated and homogenizing the different formulations to easily compare the properties of structured and unstructured media. Moreover, several studies (Refs. [132, 243–245] include only a few examples) treat capillarity by simplified approaches (e.g., assimilating the porous structure to bundles of parallel cylindrical capillaries or neglecting gravity) or limited models, adequate to study only a narrow subset of cases (i.e., one-dimensional). As a result, the framework proposed is suitable to extend the analysis to more complex components (e.g., capable of better harnessing solar radiation [28]) and transient phenomena, overcoming the limit of the traditional Lucas-Washburn approach. In this scenario, the proposed models makes a timely contribution in a fast-moving scientific field [93, 246].

However, it is worth noting that the theoretical framework and simulation protocols developed in this work could be extended to other physical phenomena to provide a more detailed description on the functioning principles of the discussed applications. For example, computational fluid dynamics simulations could be used to evaluate the capillary properties of non-ideal arrays of fibers, thus going beyond the simplifying assumptions adopted, following an approach similar to that reported in Refs. [134, 135, 247]. Similarly, the optical properties of fabrics were evaluated exclusively on an experimental basis, whereas these could be inferred by simulating light scattering in fiber arrays. At the same time, as seen in Chapter 5, applications involving evaporation of salt solutions often encounter the problem of crystallization, leading to pores clogging and limiting the device performance. Future research efforts should be aimed at investigating and maximizing salt rejection through the appropriate design of microporous structures, supported by multiphysics modeling of the interested transport phenomena: diffusion, advection and other mechanisms such as Marangoni flow [17].

On an experimental level, two main research avenues could be identified to advance the proposed concepts: pursue their scale-up; explore different materials and processing techniques to overcome their current limitations.

Regarding textiles, one of the main goals was to envision a closed life cycle, namely creating single-material products (including zippers, buttons, and labels) from PE waste. As the project is in its preliminary stages, the tested fabric samples were created from virgin PE chips, while the possibility of creating high-quality fabrics from recycled raw material remains to be demonstrated. However, some of the available recycling processes can generate recycled PE of equal quality to

its virgin counterpart, which suggests that this next step could be implemented without expecting notable differences compared to the product tested in this work. More challenging, however, is the coupling between the cooling device and the solar distiller proposed in section 4.7, which is essential to ensure its continuous operation and to achieve closed-loop operation. The coupling of the two devices would keep the salinity of the supplied solution stable and, at the same time, provide the fresh water necessary for its operation. Instead, as intended when it was designed, the current prototype can only operate in batch, being able to load a limited amount of salt water that is progressively diluted during operation. The development and testing of the coupled system should be a priority direction of future research and would be a significant step forward in the scale-up of the system towards a stand-alone version. Clearly, for this application both the cooler and the distiller involve the use of high salinity fluids, and, as mentioned earlier, their scale-up could also be facilitated by the use of the capillary material proposed in Chapter 5. For this reason, it is worth re-emphasizing the importance of studying the mechanisms of salt removal: several recent studies have proposed non-structured porous materials designed to drive salt crystallization to specific confined areas [222, 248, 249]. Compared to these solutions, whose disordered micro-pores inhibits advective transport mechanisms, the material proposed has the potential to achieve even better rejection capabilities due to its open and less tortuous structure.

Besides, the perspective evaluation of materials other than aluminum would allow the exploration of alternative substrates and processing techniques, such as molding or forming, especially if high aspect ratios or surface nanotexture are not strictly required by the target application or if large surfaces are needed. Accordingly, one can envision recreating the grooved geometry on hydrophobic polymers (e.g., PTFE) that can be used for oil-water separation through selective wicking, thus broadening the spectrum of use of this concept. On the other hand, the study of the durability of laser-treated aluminum has emphasized the importance of functionalizing the surface of material to maximize their properties of interest. On the same line, inspired by the work of Dai and co-workers [250], a Janus textile could be obtained by weaving yarns with different surface functionalizations (hydrophobic and hydrophilic). This novel design strategy would allow to tailor breathability and evaporative cooling performance, therefore enhancing its comfort. Furthermore, pursuing textiles sustainability, it is crucial to investigate and address the release of micro-plastics during washing cycles, namely broken fibers separated from the yarn and conveyed into the waste water of the washing unit. This problem could be addressed by changing the composition of the PE blend used to craft the fibers: the addition of ultra-high molecular weight PE (UHMWPE) or high density PE (HDPE) to the blend would increase the mechanical properties of the resulting yarn. Obviously, the increase in strength would be achieved at the expense of other comfort parameters, such as bending, twisting and compression strength, and softness: further research in this direction would aim to define an

optimum between these properties.

Concluding, passive transport mechanisms in porous capillary media have a great potential to reduce the environmental impact of several applications in the energy field. As shown, this field is characterized by a strong multidisciplinary, ranging from applied sciences to the more engineering aspects concerning the manufacturing process and device layout. Passive devices are part of a still under-explored field of study that has the potential to revolutionize other applications, both in the energy field and not, such as sensor technology, micro-fluidics and soft-robotics. Although their operating principle is based on nano- and micro-scale phenomena, this thesis has shown that they can have a major impact on real-scale technologies with which we manage heat, water and, in a broader sense, energy.

Appendix A

Temperature-dependent physical properties of water and air

The temperature dependent thermophysical properties of water are implemented in the model by means of polynomials in the form:

$$f(T) = AT^3 + BT^2 + CT + D, \quad (\text{A.1})$$

where $f(T)$ represents the generic thermophysical property at a specific temperature T , expressed in K. The coefficients of the polynomials are retrieved from the open source software OpenFOAM [251] and are summarised in Tab. S1. Note that, as stated in section 2.5, the finite elements implementation of the time-dependent wicking used in this work assumed as constants the density and dynamic viscosity of water. The temperature dependent thermophysical properties of air were evaluated as:

$$\rho_a (\text{kg/m}^3) = \frac{101 \cdot 10^3}{287.058 \cdot T},$$

$$\begin{aligned} k_a (\text{W}/(\text{m} \cdot \text{K})) = & T^5 \cdot 1.5797 \cdot 10^{-17} + T^4 \cdot 9.46 \cdot 10^{-14} + \\ & T^3 \cdot 2.2012 \cdot 10^{-10} - T^2 \cdot 2.3758 \cdot 10^{-7} + \\ & T \cdot 1.7082 \cdot 10^{-4} - 7.488 \cdot 10^{-3}, \end{aligned} \quad (\text{A.2})$$

$$\mu_a (\text{Pa} \cdot \text{s}) = T^{1.5} \cdot 1.512 \cdot 10^{-6} (T + 120)^{-1},$$

$$\begin{aligned} c_{p,a} (\text{J}/(\text{kg} \cdot \text{K})) = & T^4 \cdot 1.9327 \cdot 10^{-10} + T^3 \cdot 8 \cdot 10^{-7} + \\ & T^2 \cdot 1.1403 \cdot 10^{-3} - T \cdot 4.489 \cdot 10^{-1} + \\ & 1.0575 \cdot 10^3, \end{aligned}$$

with T expressed in K.

	<i>A</i>	<i>B</i>	<i>C</i>	<i>D</i>
Density, ρ_w (kg/m ³)	0	$-3.65471 \cdot 10^{-3}$	1.93017	$7.64025 \cdot 10^2$
Thermal conductivity, k_w (W/(m·K))	0	$-9.29827 \cdot 10^{-6}$	$7.1857 \cdot 10^{-3}$	$-7.10696 \cdot 10^{-1}$
Dynamic viscosity, μ_w (Pa·s)	$-2.80572 \cdot 10^{-9}$	$2.90283 \cdot 10^{-6}$	$-1.00523 \cdot 10^{-3}$	$1.16947 \cdot 10^{-1}$
Specific heat, $c_{p,w}$ (J/(kg·K))	$-1.27063 \cdot 10^{-4}$	$1.3736 \cdot 10^{-1}$	$-4.86714 \cdot 10^1$	$9.85069 \cdot 10^3$

Table S1: Coefficients of the polynomials used to model the temperature-dependent properties of water.

Appendix B

Evaluation of the uncertainty of measurements

The uncertainties of experimental measurements can be divided into two categories: uncertainty components estimated from the statistical analysis of the measured values (type A evaluation); uncertainty components estimated by other means, from a priori information such as calibration, resolution and accuracy of each measuring instrument employed (type B evaluation). Both contributions could be then used to estimate the combined uncertainty as [148]:

$$U = k\sqrt{u_A^2 + u_B^2}, \quad (\text{B.1})$$

where u_A and u_B are contributions from, respectively, the type A and type B uncertainty evaluation, and k is the coverage factor. In this work, all the expanded uncertainties are estimated assuming a coverage factor $k = 2$, and all the error bars reported in the figures show a $\pm U$ interval. In the followings, a detailed description of the uncertainty estimation per each relevant quantity is presented.

B.1 Yarn porosity

The expanded uncertainty of the yarn porosity measured in Chapter 3 was evaluated as:

$$U_\phi = k\sqrt{(S_0 \cdot u_{a_1})^2 + u_{a_0}^2 + \left(a_1 \cdot \frac{u_{S_0}}{2\sqrt{3}}\right)^2 + u_{fit}^2}, \quad (\text{B.2})$$

where $S_0 = 0.5$ is the sensitivity level chosen to evaluate the yarn porosity from the microCT images, u_{a_1} and u_{a_0} are the uncertainty of the fitting parameters evaluated via the least squares method, $u_{S_0} = 0.1$ is the uncertainty of the sensitivity S_0 ,

considered as uniformly distributed. u_{fit} is the contribution to the uncertainty of the linear fit computed as the root mean squared error:

$$u_{fit} = \sqrt{\frac{\sum_{i=1}^{n_{tot}} \left((a_1 S_i - a_0) - \phi|_{S_i} \right)^2}{n_{tot} - 2}}, \quad (\text{B.3})$$

where $n_{tot} = 200$ is the total number of sensitivities computed in the range from 0.4 to 0.6, and $\phi|_{S_i}$ is the porosity computed by the “imbinarize” MATLAB function for the given sensitivity level S_i .

B.2 Position of the water front

Chapters 3 and 5 reported several measurements of the height reached by the water front. The standard uncertainty on the i -th measurement of $H_{t,i}$, with $i = (1; \dots; 6)$ was evaluated as:

$$u_{H_{t,i}} = \sqrt{\left(\frac{u_s}{2\sqrt{3}} \right)^2 + \left(\frac{u_{f_i}}{2\sqrt{6}} \right)^2}, \quad (\text{B.4})$$

where $u_s = 2$ mm is the contribution to the uncertainty of the dipping length, considered as uniformly distributed, and u_f is the thickness of the water front, whose probability distribution is considered as triangular. The uncertainty contribution of the resolution of the caliber is negligible. The expanded uncertainty on the averaged value of the final height was evaluated as:

$$U_H = k \sqrt{\frac{\sum_i^N u_{ht,i}^2}{N^2} + \frac{R^2}{N}}, \quad (\text{B.5})$$

where

$$R = \frac{\max(h_{t,i}) - \min(h_{t,i})}{2} \quad (\text{B.6})$$

is the estimation of the statistical uncertainty of the $N = 3$ measurements performed on each material.

B.3 Contact angle

The method adopted in Chapter 3 to compute the contact angle is based on the experimental evaluation of the reduced length and height of the droplets on fibers from optical images of a droplet on a fiber, respectively, expressed as:

$$\begin{aligned} l &= \frac{L_d}{r_0}, \\ t &= \frac{T_d}{2r_0}, \end{aligned} \quad (\text{B.7})$$

where L_d is the maximum length of the droplet, r_0 is the fiber radius, and T_d is the droplet thickness (see Fig. 3.2), each measured in pixels from the images acquired. The uncertainty estimated for all the three measures is $u_{px} = 8$ px, considered as uniformly distributed. The model employed to compute the contact angle from the observation of each droplet is non-linear, thus these uncertainties cannot be easily propagated. Therefore, the method was applied 4000 times for each image acquired, where, at each iteration j , the values of $r_{0,j}$, $L_{d,j}$ and T_j used are randomly generated from a normal distribution with respective mean values r_0 , L_d and T , and standard deviation $u_{px}/2\sqrt{3}$. The average contact angle $\bar{\theta}_i$ was estimated as:

$$\bar{\theta}_i = \frac{\sum_{j=1}^N \theta_j}{N}, \quad (\text{B.8})$$

with $N = 4000$, and the uncertainty $u_{\bar{\theta}_i}$ as the standard deviation of the sample. The size of N was chosen so that $\bar{\theta}_i$ and $u_{\bar{\theta}_i}$ have a variation lower than 10^{-2} if the procedure is repeated for the same combination of r , L and T . The method was applied to every evaluation of the contact angle, which was then averaged for every type of fiber analyzed, so that:

$$\begin{aligned} \theta &= \frac{\sum_{i=1}^N \bar{\theta}_i}{N}, \\ U_\theta &= k \sqrt{\frac{\sum_{i=1}^N u_{\bar{\theta}_i}^2}{N^2} + \frac{R^2}{N}}, \end{aligned} \quad (\text{B.9})$$

where $N \geq 16$ for the all the fibers tested, and R is the standard deviation of the sample.

B.4 Evaporation tests

The evaporation tests described in Chapter 3 were performed measuring the mass of the setup with a sampling frequency of 1 sample every 2 minutes. The percentage of drying mass $L(t)$ was computed as:

$$L(t) = 100 \cdot \frac{M(t) - M_0 + m_D}{m_D}, \quad (\text{B.10})$$

where $M(t)$ is the time-dependent mass of the setup, M_0 is the weight of the setup at the beginning of the test, and m_D is the mass of the water droplet. m_D was evaluated as the difference between the weight of the setup before and after the application of the water droplet, averaging the values of 5 reads with a sampling frequency of 1 sample/s. Therefore, the uncertainty on L can be estimated as:

$$u_{L(t)} = \sqrt{\left(\frac{u_{M(t)}}{m_D \sqrt{3}}\right)^2 + \left(\frac{u_{M_0}}{m_D \sqrt{3}}\right)^2 + \left(u_{m_D} \frac{M_0 - M(t)}{m_D^2}\right)^2}, \quad (\text{B.11})$$

where $u_{M(t)} = u_{M_0} = 2$ mg, considered as uniformly distributed, and $u_{m_D} = 5$ mg, considered as uniformly distributed.

B.5 Absolute permeability

The experimental data obtained from the horizontal wicking tests described in Chapter 3 (see the inset of Fig. 3.7) were fitted according to the least squares method relying on an equation in the form $h_t = C\sqrt{t}$. The obtained fitting constant C was used to evaluate the absolute permeability in Eq. 3.3, thus its expanded uncertainty was evaluated as:

$$U_K = k_u \sqrt{\left(\frac{\partial K}{\partial C} u_C\right)^2 + \left(\frac{\partial K}{\partial \phi} \frac{U_\phi}{k}\right)^2 + \left(\frac{\partial K}{\partial p_c} u_{p_c}\right)^2}, \quad (\text{B.12})$$

where $u_C = 5.77 \cdot 10^{-13}$ is the contribution to the uncertainty of the least-squares fitting on the experimental data, $U_\phi = 0.048$ is the expanded uncertainty of the average yarn porosity and $u_{p_c} = \rho_w g(U_{h_m}/k)$ is the standard uncertainty of the capillary pressure. Note that the uncertainty on the value of density of the wetting fluid was considered as negligible.

B.6 Temperature

The uncertainty of the points composing the temperature curves in Fig. 3.10C-D can be evaluated as:

$$U_T = k \sqrt{\left(\frac{u_r}{\sqrt{3}}\right)^2 + \left(\frac{u_{TM}}{2}\right)^2 + \left(\frac{u_{FSR}}{2}\right)^2}, \quad (\text{B.13})$$

where $u_r = 10^{-2}$ °C is the contribution of the logger resolution, considered as uniformly distributed, $u_{TM} = 10^{-1}$ °C and $u_{FSR} = 0.38$ °C are respectively the contribution of the thermistor sensitivity and the accuracy on the full-scale range reading of the used thermistor, both considered as normally distributed with a coverage factor $k = 2$.

The expanded uncertainty of the i -th evaluation of temperature shown in Figs. 3.12B-C and Fig. 3.21B were evaluated as:

$$U_{T,i} = k_u \sqrt{\left(\frac{u_r}{\sqrt{3}}\right)^2 + \left(\frac{u_{TM}}{2}\right)^2 + \left(\frac{u_{FS}}{2}\right)^2}, \quad (\text{B.14})$$

where $u_r = 10^{-2}$ °C is the contribution of the resolution of the digital logger considered as uniformly distributed, $u_{TM} = 10^{-1}$ °C and $u_{FS} = 0.35$ °C are respectively

the contributions of the sensitivity and the accuracy on the full-scale reading of the thermistors, both considered as normally distributed with a coverage factor $k_u = 2$. The experimental data reported in Fig. 3.22B were evaluated by time-averaging the measured temperatures by the thermistors applied on the surface of the heaters, thus their expanded uncertainty was evaluated as:

$$U_T = k_u \sqrt{2 \left(\frac{U_{T_i}}{k} \right)^2 + s_{\Delta T}^2}, \quad (\text{B.15})$$

where $s_{\Delta T}$ is the standard deviation of the temperature difference between the two thermistors ΔT . The experimental temperature difference shown in Fig. 3.22C is computed by time-averaging the temperature measurements of the two thermistors placed at the center of the heaters, thus the expanded uncertainty shown was evaluated by Eq. B.15.

The uncertainty of the computed temperature trends shown in Fig. 3.21B (green and black curves) were obtained by averaging the results of 27 simulations. Each simulation was performed using a combination of three parameters, which were varied according to their standard uncertainty: the B-type uncertainty on the measurement of relative humidity, $u_{RH} = 0.025$; the estimated uncertainty on the imbibition time t_i , $u_{t_i} = 0.5$ s; the uncertainty on the convection coefficient h , $u_h = 0.1$ W/(m²K). The 27 simulations considered the possible combinations between the average value of each parameter and the values at the extremes of each interval. The temperature curves reported in Fig. 3.21B were computed by averaging the simulation results at each considered time-step, while their expanded uncertainties were evaluated by multiplying the standard deviation of the temperatures at each considered time-step for the coverage factor $k_u = 2$.

The computed temperature values reported in Fig. 3.22B were evaluated by averaging the simulation results obtained by three different values of the air gap thickness, $[g_a, 2g_a, 3g_a]$, with $g_a = 7.1 \cdot 10^{-5}$ m. Their uncertainty was evaluated as $U_T = k_u (\max(T_i) - \min(T_i)) / 2$, where T_i is the point-dependent temperature value obtained from the i -th simulation.

Differently, the temperature drop across the cooling device reported in Chapter 4 was estimated considering the average temperatures of the top and bottom surfaces of the prototype, T_t and T_b respectively, as it can be observed in the scheme reported in Fig. 4.14A. Thus, $\Delta T = T_t - T_b$. The type A evaluation of the temperature measurement uncertainty is associated with the standard deviation of the N values of T_i temperature measurements at steady state conditions as:

$$s_{A,T} = \sqrt{\frac{\sum_i^N (T_i - \bar{T})^2}{N - 1}}. \quad (\text{B.16})$$

Hence, the standard uncertainty for ΔT was estimated considering both the uncertainty contributions of the two sensors used to measure T_t and T_b at steady state

conditions, namely:

$$u_{A,\Delta T} = \sqrt{s_{A,T_T}^2 + s_{A,T_B}^2}. \quad (\text{B.17})$$

The measurement uncertainty associated with the thermometric chain (100- Ω PRTs class AA and datalogger) was estimated from the calibration uncertainty of $U_{c,PRT} = 0.2^\circ\text{C}$ (coverage factor $k = 2$), which was obtained through four calibration points in the range 20-100 $^\circ\text{C}$. The standard uncertainty associated with the calibration polynomial was evaluated as:

$$u_{fit} = \sqrt{\frac{\sum_i^m (T_i - T_{c,i})^2}{m - (p + 1)}}, \quad (\text{B.18})$$

where T_i is the i -th temperature of the calibration curve, $T_{c,i}$ is the i -th temperature computed through the calibration polynomial, $p = 1$ is the degree of the calibration polynomial and $m = 4$ is the number of calibration points. The measurement uncertainty for each PRT was thus evaluated as:

$$u_{B,T} = \sqrt{\left(\frac{U_{c,PRT}}{2}\right)^2 + u_{fit}^2}. \quad (\text{B.19})$$

The uncertainty of ΔT across the cooling device includes the non-uniform temperature distribution in the bottom plate due to the application of two silicone heaters. Thus, the maximum temperature difference across the plate, namely $T_{high} - T_{low}$, was evaluated by two additional 100- Ω PRTs suitably placed to sample the hottest and coldest parts of the evaporator, as represented in Fig. 4.1B. $T_{high} - T_{low}$ is assumed – conservatively – with a triangular distribution, where the width of the interval was increased to include the measurement uncertainty of T_{high} and T_{low} . Therefore, the type B evaluation of the uncertainty related to ΔT is:

$$u_{B,\Delta T} = \sqrt{u_{B,T_T}^2 + u_{B,T_B}^2 + \left(\frac{\left(T_{high} + \sqrt{s_{A,T_{high}}^2 + u_{B,T_{high}}^2} \right) - \left(T_{low} - \sqrt{s_{A,T_{low}}^2 + u_{B,T_{low}}^2} \right)}{2\sqrt{6}} \right)^2}. \quad (\text{B.20})$$

B.7 Distillate flow rate

The flow rate of distilled water J_w consumed by the passive cooler reported in Chapter 4 was computed according to Eq. 4.2. The associated uncertainty was ascribed to the measurement of the distillate mass variation in the basin Δm , the duration of the test Δt (whose uncertainties are evaluated from a uniform probability distribution), and the surface-specific evaporation rate (J_w , whose measurement uncertainty is assumed as normally distributed). Instead, both ρ and A_{net} in Eq.

4.2 have negligible uncertainty with respect to the other components. Thus, the combined standard uncertainty was evaluated as:

$$u_J = \sqrt{\left(\frac{\partial J}{\partial \Delta m} \frac{u_{\Delta m}}{\sqrt{3}}\right)^2 + \left(\frac{\partial J}{\partial \Delta t} \frac{u_{\Delta t}}{\sqrt{3}}\right)^2 + u_{J_{ev}}^2}, \quad (\text{B.21})$$

where the half-width contribution to the uncertainty on the distilled water variation and the elapsed time during the test were estimated as $u_{\Delta m} = 3$ g and $u_{\Delta t} = 180$ s, respectively. The surface-specific evaporation rate J_w was experimentally evaluated by real-time acquisition of the distilled water weight in the basin when the passive cooler was not operating: the progressively decreasing mass of distilled water over a 3.5 hours test was linearly interpolated, and the uncertainty u_{J_w} was evaluated via least square fitting.

B.8 Specific thermal power

The specific thermal power q extracted by the cooling device reported in Chapter 4 was computed according to equation 4.1, where both the input thermal load provided by the flat silicone heaters and the thermal losses through the polystyrene insulation were considered. The minimal fluctuations of the voltage V and current I supplied to the silicone heaters led to their negligible type A uncertainties; whereas, the resolution of the measuring instruments (i.e. voltmeter and amperemeter) led to a uniformly distributed probability distribution function. Via Ohm's law, the measured voltage and current were considered as correlated. Hence, the standard uncertainty associated with the $Q = IV$ thermal power supplied by the silicone heaters can be estimated as:

$$u_Q = \sqrt{\left(\frac{\partial q}{\partial V} \frac{u_V}{2\sqrt{3}} + \frac{\partial q}{\partial I} \frac{u_I}{2\sqrt{3}}\right)^2}, \quad (\text{B.22})$$

where $u_I = 10^{-3}$ A and $u_V = 10^{-2}$ V are the amperemeter and voltmeter resolution, respectively. The uncertainty of the thermal losses was evaluated as:

$$u_{Q_L} = \sqrt{\left(\frac{\partial q}{\partial G} u_G\right)^2 + \left(\frac{\partial q}{\partial T_{amb}} u_{T_{amb}}\right)^2 + \left(\frac{\partial q}{\partial T_b} u_{T_b}\right)^2}, \quad (\text{B.23})$$

where u_G is the standard uncertainty of the thermal conductance of the insulation box (see the following section), $u_{T_{amb}} = 0.5$ °C is the estimated standard uncertainty of the environment temperature and u_{T_b} is the standard uncertainty on the evaporator temperature, which was evaluated following the procedure described above. Finally, the combined standard uncertainty on the specific cooling capacity was estimated as $u_q = A_{net}^{-1} \sqrt{u_Q^2 + u_{Q_L}^2}$.

B.9 Thermal conductance

The thermal conductance of the insulation box where the cooling device operates was computed as:

$$G = \frac{Q}{\Delta T}, \quad (\text{B.24})$$

where $Q = IV$ is the thermal power supplied by the silicone heaters (powered by I current and V voltage), and $\Delta T = T_f - T_{amb}$ is the difference between the temperature inside the insulation box T_f and the environment ($T_{amb} < T_f$). The latter temperatures were both estimated by repeated measurements, considering a measurement interval of 2500 s at steady state conditions. The uncertainty of Q was evaluated according to Eq. B.22; whereas, the uncertainty of ΔT was estimated according to Eqs. B.16-B.20. Note that the temperature inside the insulation box was evaluated in the closest, middle and farthest point from the heaters. Thus, the uncertainty of the thermal conductance G_i of each i -th measurement was evaluated as:

$$u_{G_i} = \sqrt{\left(\frac{\partial G}{\partial Q} u_Q\right)^2 + \left(\frac{\partial G}{\partial \Delta T} u_{B,\Delta T}\right)^2}. \quad (\text{B.25})$$

Four independent measurements of G_i were performed: $(8.5 \pm 0.6) \times 10^{-2} \text{ W K}^{-1}$; $(8.2 \pm 0.8) \times 10^{-2} \text{ W K}^{-1}$; $(8.9 \pm 1.7) \times 10^{-2} \text{ W K}^{-1}$; $(8.5 \pm 0.8) \times 10^{-2} \text{ W K}^{-1}$. The mean value for the thermal conductance was obtained by their arithmetic average, while the resulting standard uncertainty was computed as:

$$u_G = \sqrt{\frac{\sum_{i=1}^4 u_{G_i}^2}{N^2} + \frac{s_G^2}{N}}, \quad (\text{B.26})$$

where $N = 4$ is the number of tests performed and s_G the related statistical error.

B.10 Membrane resistance coefficient

The type B error $u_{B,B}$ of the membrane resistance coefficient measurements reported in 4 considered both the uncertainty involved in the measured mass flow rate through the membrane u_J and the uncertainty provided by the estimated vapour pressure difference during the tests $u_{\Delta P_w}$. In detail, possible contributions to the uncertainty of the mass flow rate came from the estimation of the water mass measurement uncertainty, namely the marks on the capillary tube $u_{tube} = 0.03 \text{ mL}$ and the uncertainty on the average thickness of water meniscus u_{men} , which were both considered as uniformly distributed. For each test performed, u_{men} was evaluated by the high-resolution camera as the half-width of the water meniscus. Thus, the uncertainty on the reads of water level in the capillary tube (converted

into kg, being ρ the water density) can be evaluated as:

$$u_{level} = \frac{\rho(T_{amb})}{10^6} \sqrt{2 \left(\frac{u_{tube}}{\sqrt{3}} \right)^2 + \left(\frac{u_{men}}{\sqrt{3}} \right)^2}, \quad (\text{B.27})$$

which, in the assumption of uncorrelated noise, can be applied to all the water level points collected during each test. Therefore, equation B.27 was used to evaluate the uncertainty of the flow rate across the membrane, that is u_J , via least square fitting. Instead, the vapour pressure difference across the membrane can be computed as $a(Y_e)P_w(T_e) - a(Y_c)P_w(T_c)$ (see section 2.6), depending on the air temperature T and water activity coefficients a of the two solutions. Since vapour pressure depends on temperature according to the Antoine's law (see Eq. 2.96), and the activity coefficients depend on salt concentration Y , the uncertainty of vapour pressure difference during the tests can be estimated as:

$$u_{\Delta P_w} = \sqrt{\left(\left(\frac{\partial P_w}{\partial T_{amb}} (1 - a) - \frac{\partial a}{\partial T_{amb}} \right) u_T \right)^2 + \left(\frac{\partial a}{\partial c} P_w(T_{amb}) \frac{U_{ref}}{2} \right)^2}, \quad (\text{B.28})$$

where $a=0.8998$ is the activity coefficient of salt water at 170 g L^{-1} computed via Eq. 2.98, $u_T = 1 \text{ }^\circ\text{C}$ is the standard uncertainty on the average temperature during the membrane permeability tests, and $U_{ref} = 2 \text{ g L}^{-1}$ is the expanded uncertainty on salt concentration, obtained by the refractometer specifications. Finally, u_{K_i} of the i -th permeability measurement was estimated by combining u_J and $u_{\Delta P_w}$ via Eq. B.1. The final result was obtained averaging the measurements performed, while the related uncertainty can be estimated similarly to Eq. B.26.

B.11 Activity coefficient

The molality of a salt solution can be computed as:

$$m = \frac{Y}{\rho(Y, T) M_s \left(1 - \frac{Y}{\rho(Y, T)} \right)}, \quad (\text{B.29})$$

where $\rho(Y, T)$ is the concentration of the solution at a given salt concentration Y and temperature T , and M_s is the molar mass of the solute. The digital refractometer, whose expanded uncertainty is $U_{ref} = 2 \text{ g L}^{-1}$, was used to evaluate the concentration of both NaCl and CaCl₂ solutions, although, in the latter case, the actual concentration was computed by a conversion polynomial evaluated by the linear interpolation of seven calibration points through least square method. Thus, the concentration of a CaCl₂ sample Y , expressed in g L^{-1} , was computed as:

$$Y_{\text{CaCl}_2} = (0.700 \pm 0.007) Y_{\text{NaCl}} + (3.9 \pm 1.3). \quad (\text{B.30})$$

The combined uncertainty on the concentration u_Y included the contributions of the refractometer U_{ref} , the statistical uncertainty evaluated considering five independent measurements on each sample and, in case of CaCl_2 solutions, the contribution attributable to Eq. B.30. The activity coefficients were computed according to equation 2.98, thus their expanded uncertainty was evaluated as:

$$U_a = k \sqrt{\left(\frac{\partial a}{\partial Y} s_Y\right)^2 + \left(\frac{\partial a}{\partial T} u_T\right)^2}, \quad (\text{B.31})$$

where $u_T = 1^\circ\text{C}$ is the standard uncertainty of the room temperature.

Plot Name	Activity a		ϕ_{me}		d_{me} (μm)		T_{amb} ($^\circ\text{C}$)
	Lower Bound	Upper Bound	Lower Bound	Upper Bound	Lower Bound	Upper Bound	
NaCl solution (Fig. 4.8B, Fig. 4.10A, Fig. 4.9A)	0.8979	0.9009	0.75	0.85	105	115	30
CaCl₂ solution (Fig. 4.10A, Fig. 4.9B)	0.8473	0.8659	0.75	0.85	105	115	30
Seawater (Fig. 4.10A)	0.9771	0.9800	0.75	0.85	105	115	30
Membrane resistance coeff. (Fig. 4.5)	0.8979	0.9009	0.75	0.85	105	115	21
NaCl: Temperature sensitivity (Fig. 4.10B)	0.8998		0.8		110		–
NaCl: N. stages and air gap sensitivity (Fig. 4.11A, Fig. 4.12A, Fig. 4.13A)	0.8998		0.8		110		30

Table S2: **Parameters values used for theoretical predictions.** Upper and lower values of the lumped parameter model parameters, used to determine the uncertainty of model estimations. The membrane porosity interval was evaluated coherently with common evidence in the literature [252, 253]; the boundary values assigned to the membrane thickness are taken coherently with the data reported by the vendor. The temperature employed for the computations of the membrane permeability is approximately the average of the values experimentally assessed during the tests.

Appendix C

Lumped-parameters representation of a passive desalination device

Section 4.4 introduced a lumped-parameter model useful for analyzing the performance of the cooling device proposed in Chapter 4. Then, as a next step towards its integration into a stand-alone system, we envisioned to couple the cooler with a solar distiller, originally proposed in the seminal work of Chiavazzo et al. [96], capable of exploiting the incident solar radiation to restore the salinity gradient between the two feeds. Finally, in Chapter 5, the original hydrophilic layers, used both in Chapter 4 and by the device inventors, were envisioned to be replaced by the proposed laser-etched capillary substrates, demonstrating the possibility of significantly enhancing the performance and scalability of the device. This appendix revisits the thermal network model introduced in section 4.4 in order to predict the performance of the desalination device. The model, validated against the results presented in Refs. [17, 96], was used in Chapters 4 and 5 to obtain the results shown.

C.1 Thermal network

The stratigraphy and operating principle of the device were thoroughly described in 5.5, and, for the sake of clarity, were summarized below and schematized in Fig. C.1. Each stage of the modular device is composed as follows: an hydrophilic porous layer is used to wick saltwater from a reservoir and feed the device: (i.e., evaporators, orange layer in Fig. C.1); an hydrophobic membrane of known transport properties (namely, thickness, porosity and average pore size); an optional air gap, placed in series to the membrane; a second hydrophilic porous layer, used to collect water vapour and channel distilled water into a second reservoir (i.e.,

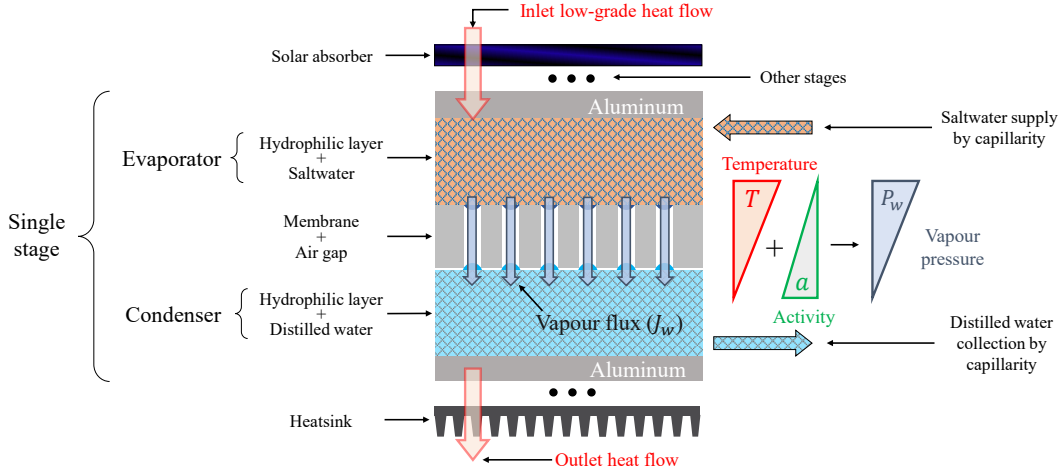


Figure C.1: **Schematics of the distillation device.** Main components, working principle and driving forces of the distillation device. The colored triangles schematize the driving forces that result in a pressure difference across the membrane and, therefore, a net vapor flux. The schematic was adapted from Ref. [96].

condensers, light-blue layer in Fig. C.1). Two adjacent stages are connected by means of a thin aluminum plates, avoiding contamination the feeds while granting low thermal resistance. In this case, in contrast to the operating principle of the cooling device, the net vapor flow is driven by the temperature gradient across the membrane and is opposed by the salinity difference. Thus, exists a minimum temperature difference required to permit the device to operate. Low-grade heat sources can be used to establish the temperature gradient across the device, noting that, to ensure proper operation conditions, the temperature inside the device should not exceed the boiling temperature of water. Here, it was assumed that solar radiation was absorbed by an optically selective surface located on the top of the device (see the black layer in Fig. C.1). Finally, the bottom device layer was coupled with a natural convection heat sink. Compared to the originally proposed device in Ref. [96], the reported thermal network formulation neglected the presence of a polypropylene convection reducer placed on top of the selective surface. Considering a stack of n identical stages, the thermal network consists of $2n + 2$ nodes, which have been arbitrarily numbered in ascending order from the top layer (the selective absorber) to the bottom layer (the last stage capacitor) of the device. The network can be formulated by imposing energy conservation on each node, thus obtaining as many equations and unknowns as there are nodes. Consequently, the energy balance of first and last nodes of the network were respectively expressed

as:

$$\begin{aligned}
 0 &= \alpha_s I_{rr} - \alpha_{ir} \sigma (T_t^4 - T_{sky}^4) - \frac{T_t - T_{amb}}{R_h} - \frac{T_t - T_e^1}{R_t} \\
 0 &= \frac{T_c^n - T_b}{R_b} - \frac{T_b - T_{res}}{R_{hs}},
 \end{aligned} \tag{C.1}$$

where σ is the Stefan-Boltzmann constant, α_{ir} and α_s respectively are the infrared and solar absorption coefficients of the selective absorber (here, according to the Kirchhoff's law, assumed equal to the respective emission coefficients), $R_h = 1/h$ is the thermal resistance due to natural convection on the top layer of the device (evaluated through Eqs. 3.20–3.22), $R_{hs} = 1/150$ is the thermal resistance of the heatsink located at the bottom of the device, T_{amb} is the ambient temperature, T_{res} is the temperature of the reservoir where the heatsink is immersed, T_{sky} is the humidity-dependent sky temperature (evaluated through Eqs. 3.33–3.34), I_{rr} is the incoming solar irradiation. Furthermore, $R_t = (d_{ev}/\lambda_{ev} + d_s/\lambda_s)$ is the thermal resistance between between the first-stage evaporator and the top of the device, being $d_s = 1$ mm and $\lambda_s = 290$ W m⁻¹ K⁻¹ the thickness and thermal conductivity of the selective surface, and $R_b = (+d_c/\lambda_c + d_{al}/\lambda_{al})$ is the thermal resistance between the last-stage condenser and the bottom of the device, comprising an aluminum sheet with thickness $d_{al} = 1$ mm, and the condensers. In this case, the evaporators and condensers were considered as made of the same material, therefore $d_{ev} = d_c = 1$ mm and $\lambda_{ev} = \lambda_c = \phi_{ev}\lambda_f + (1 - \phi)\lambda_m$ is the effective thermal conductivity of the porous matrix m saturated by the fluid f . Note that the superscripts of T_e and T_t were used to specify the stage they belong to (e.g., T_e^1 is the temperature of the first-stage evaporator).

Similarly, remembering Eq. 4.13, the node equation for the first-stage evaporator and last-stage condenser were formulated as:

$$\begin{aligned}
 0 &= \frac{T_t - T_e^1}{R_t} - \frac{T_e^1 - T_c^1}{R_{me}} - J_w^1 H(T_e^1, Y_e) - q_{ls,e}^1 - q_{lb,e}^1 \\
 0 &= \frac{T_e^n - T_c^n}{R_{me}} - \frac{T_c^n - T_b}{R_b} + J_w^n H(T_e^n, Y_e) - q_{ls,c}^n - q_{lb,c}^n,
 \end{aligned} \tag{C.2}$$

where J_w^j is the vapour flux established through the membrane of the j -th stage (see section 2.6), H is the temperature and concentration dependent heat of vaporization, R_{me} is the thermal resistance of the membrane and air gap layer (see section 4.4, q_{ls} and q_{lb} are heat fluxes related to lateral losses, which depend on the type of layer and stage considered (see section C.2 for their analytical expression). Note that, in this case, the net vapour flux is established from the saline solution towards distilled water, so the salinity of the solution comprised in the evaporators Y_e has to be considered when evaluating the enthalpy of vaporization [254], namely:

$$H(T, Y) \approx (1 - Y)H(T), \tag{C.3}$$

which is valid in the limit of ideal solutions. The temperature dependence of H was evaluated using Eq. 3.19.

Finally, the nodes equations of any other evaporator and condenser of the multistage stack were respectively expressed as:

$$\begin{aligned} 0 &= \frac{T_c^{j-1} - T_e^j}{R_c} - \frac{T_e^j - T_c^j}{R_{me}} - J_w H(T_e^j, Y_e) - q_{ls,e}^j - q_{lb,e}^j \\ 0 &= \frac{T_e^j - T_c^j}{R_{me}} - \frac{T_c^j - T_e^{j+1}}{R_c} + J_w H(T_e^j, Y_e) - q_{ls,c}^j - q_{lb,c}^j, \end{aligned} \quad (\text{C.4})$$

where $R_c = (2d_{ev}/\lambda_{ev} + d_{al}/\lambda_{al})$ is the thermal resistance between the condenser and evaporator of adjacent stages.

C.2 Lateral losses

Differently from the cooling device investigated in Chapter 4, the temperature distribution within the desalination device might reach values well beyond the ambient temperature. Therefore, to correctly estimate the device performance, its essential to include heat losses in its lumped-parameter representation.

Eqs. C.2 and C.4 introduced two heat fluxes related to thermal losses: q_{ls}^j refers to the convective losses through the lateral surface of each layer; q_{lb}^j refers to the conductive losses towards the water reservoirs via the capillary strip connecting the evaporators and condensers with the reservoirs themselves, which are essential to drive the working fluids inside and outside the device by capillarity. Note that thermal losses affect different surfaces compared to the other fluxes reported in the Eqs. C.2–C.4; therefore, to maintain consistency, it is necessary to introduce a normalization coefficient to correctly consider the weight of each flux in the thermal network.

The analytical formulations of both loss components depend on the stage considered to and whether they were referred to evaporators or condensers. The convective lateral losses of the j -th stage were expressed as:

$$q_{ls,e/c}^j = \frac{A_{ls,e/c}}{A_d} \frac{T_{e/c}^j - T_{amb}}{R_{ls}}, \quad (\text{C.5})$$

where $A_d = W \times L$ is the operating distillation surface of the device with sides W and L (see also Fig. 5.18), $A_{ls,e/c}$ is the lateral area of each condenser or evaporator, and $R_{ls} = 1/6$ is the thermal resistance due to convection with the surrounding environment, which was supposed as a constant. The lateral surfaces of the evaporators and condensers were evaluated as:

$$\begin{aligned} A_{ls,e} &= (2W + 2L - \delta)(d_{ev} + d_{al}) \\ A_{ls,c} &= (2W + 2L - \delta)(d_c + d_a), \end{aligned} \quad (\text{C.6})$$

where δ is the width of capillary strip connecting each layer to the respective water reservoir. Note that, for the sake of simplicity, the temperatures of the aluminum sheet and of the air gap in each stage were considered as equal to those of the evaporators and condensers, respectively.

The conductive losses towards the reservoirs of the j -th stage were expressed as:

$$q_{lb,e/c}^j = \frac{A_{lb} T_e^j - T_{res}}{A_d R_{lb,e/c}^j}, \quad (C.7)$$

where $A_{lb} = \delta d_{ev}$ and $R_{lb,e/c}^j$ respectively are the cross section and thermal resistance of the vertical strips connecting the evaporators and condensers to the respective basins. Having assumed $d_{ev} = d_c$, the former term is constant, while $R_{lb,e/c}^j$ clearly depends on the height of each layer with respect to the water basins:

$$\begin{aligned} R_{lb,e}^j &= \left[H_0 + \left(\frac{2n-2j}{2} + 1 \right) H_e \right] \frac{1}{\lambda_{ev}} \\ R_{lb,c}^j &= \left[H_0 + \left(\frac{2n-2j}{2} \right) H_e + H_c \right] \frac{1}{\lambda_{ev}}, \end{aligned} \quad (C.8)$$

where, $H_0 = 5$ cm is the considered height of the heatsink below the device, $H_e = d_{al} + 2d_{ev} + d_{me} + d_a$ is the vertical distance between the evaporators of adjacent stages, $H_c = d_a + d_{ev}$ is the distance between an evaporator and the condenser of the adjacent stage.

Note that the device layout considered in Chapter 4 is coherent with the original device proposed in Ref. [96], therefore $\delta = 5$ cm. On the other hand, the device layout assumed in Chapter 5 was inspired by the work of Morciano et al. [17] (coherently with the device layout shown in Fig. 5.18), therefore $\delta = 2W$ for the evaporators and $\delta = L$ for the condensers.

C.3 Performance

The described model was used throughout the dissertation to estimate the effect of different device layouts, material properties, and working conditions on its achievable performance. In this section, the impact of the main design parameters of the desalinators was investigated with the aim of clarifying some key aspects of its operation principle.

As an example, Fig. C.2 explores the effect of different number of stacked stages and salinity of the evaporating solution on the temperature profile within the device and its specific productivity. In particular, as can be seen in Fig. C.2A, both higher numbers of stages and higher salinity in evaporators tend to shift the profile within the device toward higher temperatures and, thus, due to the Antoine equation and the reduced latent heat of evaporation (see Eqs. 2.96 and C.3), to higher vapor

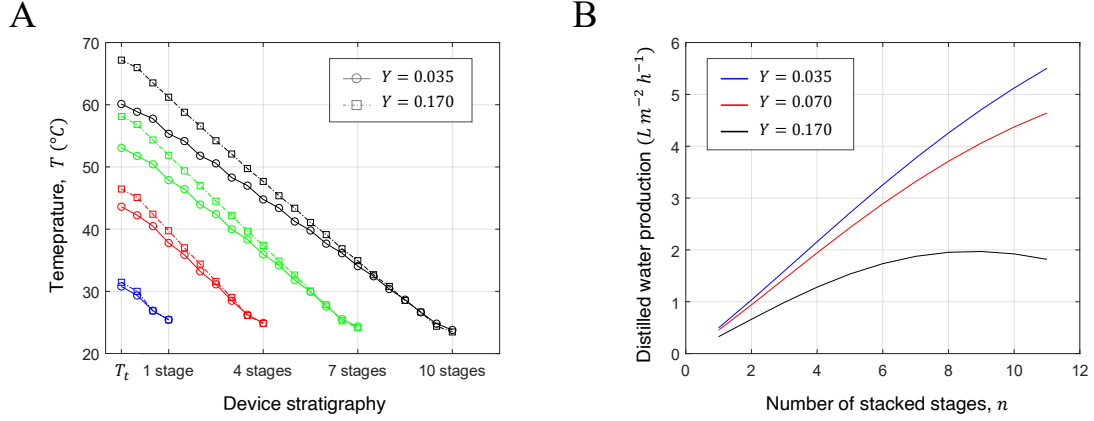


Figure C.2: **Modelling predictions: device performance.** (A) Impact of different numbers of stacked stages and salinity concentrations on the temperature profile within the device. The horizontal axis reports the nodes of the thermal network, where it was highlighted the total number of stages tested. (B) Dependency of the specific productivity of distilled water as a function of the number of stacked stages n and salinity concentration. Due to heat losses and the reduced temperature gradient across each stage, an optimum value of n maximising the device specific productivity can be identified for a each given working condition.

fluxes in each stage. In addition, it is worth noting that, in contrast to what was observed in the cooling device (see Fig. 4.7A), the different relationship between the driving forces that determine the pressure gradient straddling the membrane (see the schematics in Fig. C.1) causes the temperature profile to be more linear and no temperature inversions are present. However, counterintuitively, higher temperature profiles are not always associated with better performance: as it can be seen in Fig. C.2B, stacking a progressively higher number of stages does not necessarily increase the specific productivity of the device. In fact, more stages would reduce the temperature gradient available to each stage, thus progressively reducing their net vapor production. This phenomenon is the more pronounced the higher the salinity of the treated solution, as the activity difference opposing the temperature gradient increases. Interestingly, for each working condition, an optimal number of stages can be identified which maximizes the specific productivity of the device.

Importantly, the model can be used to optimize the thickness of the air gap in series with the membrane, which increase produces opposite effects on the device performance. In fact, thicker air gaps increase the temperature gradient across the membrane, while, at the same time, they lead to larger lateral convective heat losses and reduce the membrane coefficient B (see section 2.6), thus hindering the vapor flux J_w^j . It is therefore possible to identify an optimal thickness, which depends on several device operating parameters such as, for example, the number of stacked stages (see Fig. C.3A). Given the presented results, the simulations reported in

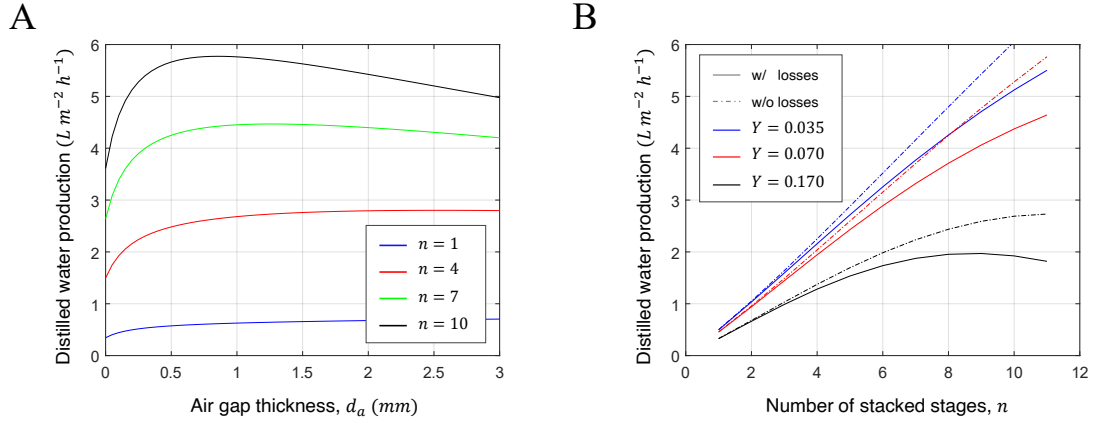


Figure C.3: **Modelling predictions: impact of the chose stratigraphy.** (A) Optimization of the thickness of an air gap placed in series to the hydrophobic membrane for different numbers of stacked stages. The results presented were obtained considering a salinity of the evaporated feed of 35 g/L. (B) Impact of considering lateral thermal losses when predicting the performance of the device. The results presented were obtained considering the device layout proposed in Ref. [96]. Including thermal losses is crucial when exploring different capillary materials for connecting evaporators and condensers to their respective reservoirs.

Chapters 4 and 5 were performed considering an air gap thickness of 0.5 mm, which, although not an optimal value for any configuration, has a positive impact on the device performance for all the considered layouts. Note that the simulations reported in Chapter 5 for the configurations comprising an air gap were performed considering either the presence of a membrane or the air gap alone.

Finally, the model was used to evaluate the effect of including lateral thermal losses in the thermal network. As it can be seen in Fig C.3B, neglecting them leads to significantly overestimate the performance of the device. The results shown in Fig C.3B were obtained considering a device configuration consistent with Ref. [96] and the device layout reported in Chapter 4; in a configuration such as the one used in Chapter 5, it is even more important to consider conductive losses towards the reservoir, as they affect a larger surface area. Consequently, the resulting performance can be significantly different by considering evaporators and condensers made of thermally insulating (i.e., the viscous used in Chapter 4) or conductive (i.e., aluminum, as hypothesized in Chapter 5) capillary materials.

Nomenclature

Greek letters

α	Grooves tilt angle; Optical absorption coefficient	$[-]$
β	Geometrical angle; Van Genuchten's parameter	$[-, m^{-1}]$
χ	Molar fraction	$[-]$
δ	Angle in the fibers-meniscus system; Wet/dry indicator function	$[-; -]$
ϵ	Optical emissivity coefficient	$[-]$
γ	Surface tension	$[m^2]$
λ	Wavelength; thermal conductivity	$[m; W m^{-1} K^{-1}]$
μ	Dynamic viscosity	$[Pa s]$
ω	Molecular vs. Knudsen diffusivity ratio	$[-]$
ϕ	Effective porosity	$[-]$
Π_e	Equilibrium pressure of adsorbed vapour	$[Pa]$
ρ	Fluid density	$[kg m^{-3}]$
σ	Stefan–Boltzmann constant	$[W m^{-2} K^{-4}]$
τ	Tortuosity; Optical transmission coefficient	$[-]$
Θ	Normalised saturation content	$[-]$
θ	Contact angle; solid angle	$[-; sr]$
ζ	Chemical potential	$[J mol^{-1}]$

Symbols

ΔP	Pressure difference	$[Pa]$
------------	---------------------	--------

Nomenclature

ΔT	Temperature difference	$[^{\circ}C]$
\dot{M}	Evaporative flux	$[kg\ s^{-1}]$
\dot{m}	Specific evaporative flux	$[kg\ s^{-1}\ m^{-2}]$
$\hat{\mathbf{n}}$	Unit vector normal to a boundary	$[-]$
\mathbf{v}	Velocity	$[m\ s^{-1}]$
A	Area	$[m^2]$
a	Activity coefficient	$[-]$
B	Membrane resistance coefficient	$[kg\ m^{-2}\ Pa^{-1}\ s^{-1}]$
C	General substitution variable	$[-]$
c	Generic integration or fitting constant	$[-]$
c_p	Specific heat at constant pressure	$[J\ kg^{-1}\ K^{-1}]$
c_t	Molar concentration	$[mol\ m^{-3}]$
D	Diffusion coefficient	$[m^2\ s^{-1}]$
d	Separation or thickness	$[m]$
E	Surface free energy; evaporation rate constant	$[J, -]$
E_r	Black-body emissivity	$[W\ m^{-3}\ sr^{-1}]$
F	Force	$[N]$
f	Mass source/sink term	$[kg\ m^{-3}\ s^{-1}]$
g	Gravitational acceleration	$[m\ s^{-2}]$
g_a	Air gap thickness	$[m]$
H	Height of the water front; Enthalpy of vaporisation	$[m; J\ kg^{-1}]$
h	Convection coefficient	$[W\ m^{-2}\ K^{-1}]$
h_g	Grooves height	$[m]$
I_{rr}	Specific incident irradiance	$[W\ m^{-2}]$
J	Specific mass flow rate	$[kg\ m^{-2}\ s^{-1}]$

Nomenclature

K	Absolute permeability	$[m^2]$
k	Thermal conductivity	$[W m^{-1} K^{-1}]$
k_r	Relative permeability	$[-]$
L	Van Genuchten's parameter	$[-]$
l_c	Capillary length	$[m]$
L_d	Droplet length	$[m]$
M	Molar mass	$[kg mol^{-1}]$
m	Molality	$[mol kg^{-1}]$
N	Molar flux	$[mol m^{-2} s^{-1}]$
n	Van Genuchten's parameter	$[-]$
P	Pressure	$[Pa]$
p	Perimeter	$[m]$
P_{in}	Input power	$[W]$
Q	Volumetric heat flux	$[W m^{-3}]$
q	Specific heat flux	$[W m^{-2}]$
R	Radius of curvature; Thermal resistance	$[m; m^2 K W^{-1}]$
r	Fiber radius; optical reflection coefficient; ramp function	$[m; -; -]$
R_g	Ideal gas constant	$[J K^{-1} mol^{-1}]$
RH	Relative humidity	$[-]$
S	Pores saturation content	$[-]$
S_r	Residual saturation content	$[-]$
T	Temperature	$[K]$
t	Time	$[s]$
T_d	Droplet thickness	$[m^3]$
U_b	Heat transfer coefficient	$[W m^{-2} K^{-1}]$

Nomenclature

V	Volume	$[m^3]$
w	Width	$[m]$
Y	Solution salinity	$[g L^{-1}]$

Bibliography

- [1] IPCC SRCCL. «Special report on climate change and land». In: *Intergovernmental Panel on Climate Change* (2019).
- [2] NASA. *Scientific Consensus: Earth's Climate Is Warming*. <https://climate.nasa.gov/scientific-consensus/>. [Online; accessed 15-February-2022].
- [3] John Cook et al. «Quantifying the consensus on anthropogenic global warming in the scientific literature». In: *Environmental research letters* 8.2 (2013), p. 024024.
- [4] Carl-Friedrich Schleussner et al. «Science and policy characteristics of the Paris Agreement temperature goal». In: *Nature Climate Change* 6.9 (2016), pp. 827–835.
- [5] Carol Finn. «AGU Updates climate change position statement». In: *Eos, Transactions American Geophysical Union* 94.34 (2013), pp. 301–301.
- [6] Ait Mimoune Hamiche, Amine Boudghene Stambouli, and Samir Flazi. «A review of the water-energy nexus». In: *Renewable and Sustainable Energy Reviews* 65 (2016), pp. 319–331.
- [7] Carey W King and Michael E Webber. *Water intensity of transportation*. 2008.
- [8] Mauro F Chavez-Rodriguez and Silvia A Nebra. *Assessing GHG emissions, ecological footprint, and water linkage for different fuels*. 2010.
- [9] Susan S Hutson. *Estimated use of water in the United States in 2000*. 1268. Geological Survey (USGS), 2004.
- [10] Joan F Kenny et al. *Estimated use of water in the United States in 2005*. Tech. rep. US Geological Survey, 2009.
- [11] Yifan Gu et al. «The feasibility and challenges of energy self-sufficient wastewater treatment plants». In: *Applied Energy* 204 (2017), pp. 1463–1475.
- [12] Ali Al-Karaghoul and Lawrence L Kazmerski. «Energy consumption and water production cost of conventional and renewable-energy-powered desalination processes». In: *Renewable and Sustainable Energy Reviews* 24 (2013), pp. 343–356.

- [13] EJ Sullivan Graham et al. «Energy for Water and Desalination». In: *Current Sustainable/Renewable Energy Reports* 4.3 (2017), pp. 109–116.
- [14] Quang T Ho et al. «Multiscale modeling in food engineering». In: *Journal of food Engineering* 114.3 (2013), pp. 279–291.
- [15] Zhi Liu et al. «Experimental and numerical studies on liquid wicking into filter papers for paper-based diagnostics». In: *Applied Thermal Engineering* 88 (2015), pp. 280–287.
- [16] Varun Kashyap and Hadi Ghasemi. «Solar heat localization: concept and emerging applications». In: *Journal of Materials Chemistry A* 8.15 (2020), pp. 7035–7065.
- [17] Matteo Morciano et al. «Solar passive distiller with high productivity and Marangoni effect-driven salt rejection». In: *Energy & Environmental Science* 13.10 (2020), pp. 3646–3655.
- [18] Swellam W Sharshir, MR Elkadeem, and An Meng. «Performance enhancement of pyramid solar distiller using nanofluid integrated with v-corrugated absorber and wick: An experimental study». In: *Applied Thermal Engineering* 168 (2020), p. 114848.
- [19] Jagannathan Mahadevan, Mukul Mani Sharma, and Yannis C Yortsos. «Capillary wicking in gas wells». In: *SPE Annual Technical Conference and Exhibition*. OnePetro. 2006.
- [20] Chao Zhang et al. «Solar-driven self-heating sponges for highly efficient crude oil spill remediation». In: *Journal of Materials Chemistry A* 6.19 (2018), pp. 8880–8885.
- [21] Xianming Dai et al. «Micromembrane-enhanced capillary evaporation». In: *International Journal of Heat and Mass Transfer* 64 (2013), pp. 1101–1108.
- [22] Hyunho Kim et al. «Water harvesting from air with metal-organic frameworks powered by natural sunlight». In: *Science* 356.6336 (2017), pp. 430–434.
- [23] Dilip Krishna Nandakumar et al. «Solar energy triggered clean water harvesting from humid air existing above sea surface enabled by a hydrogel with ultrahigh hygroscopicity». In: *Advanced Materials* 31.10 (2019), p. 1806730.
- [24] Xiaobing Zhou et al. «Harvesting electricity from water evaporation through microchannels of natural wood». In: *ACS Applied Materials & Interfaces* 12.9 (2020), pp. 11232–11239.
- [25] Guobin Xue et al. «Water-evaporation-induced electricity with nanostructured carbon materials». In: *Nature nanotechnology* 12.4 (2017), pp. 317–321.

- [26] Yun Xia et al. «Spatially isolating salt crystallisation from water evaporation for continuous solar steam generation and salt harvesting». In: *Energy & Environmental Science* 12.6 (2019), pp. 1840–1847.
- [27] Ning Xu et al. «Mushrooms as efficient solar steam-generation devices». In: *Advanced Materials* 29.28 (2017), p. 1606762.
- [28] Yusuf Shi et al. «A 3D photothermal structure toward improved energy efficiency in solar steam generation». In: *Joule* 2.6 (2018), pp. 1171–1186.
- [29] Xin Cheng, Guang Yang, and Jingyi Wu. «Recent advances in the optimization of evaporator wicks of vapor chambers: from mechanism to fabrication technologies». In: *Applied Thermal Engineering* (2021), p. 116611.
- [30] Po-Chun Hsu et al. «Radiative human body cooling by nanoporous polyethylene textile». In: *Science* 353.6303 (2016), pp. 1019–1023.
- [31] Yucan Peng et al. «Nanoporous polyethylene microfibrils for large-scale radiative cooling fabric». In: *Nature sustainability* 1.2 (2018), pp. 105–112.
- [32] Suresh B Sadineni, Srikanth Madala, and Robert F Boehm. «Passive building energy savings: A review of building envelope components». In: *Renewable and sustainable energy reviews* 15.8 (2011), pp. 3617–3631.
- [33] U.S. Department of Energy. *Residential Program Guide – Energy Data Facts*. <https://bit.ly/3BDrGSZ>. [Online; accessed 16-February-2022].
- [34] Run Hu et al. «Emerging materials and strategies for personal thermal management». In: *Advanced Energy Materials* 10.17 (2020), p. 1903921.
- [35] Hui Zhang, Edward Arens, and Yongchao Zhai. «A review of the corrective power of personal comfort systems in non-neutral ambient environments». In: *Building and Environment* 91 (2015), pp. 15–41.
- [36] Ellen MacArthur Foundation. *Fashion and the circular economy*. <https://archive.ellenmacarthurfoundation.org/explore/fashion-and-the-circular-economy>. [Online; accessed 16-February-2022].
- [37] Sandra Roos et al. «Will clothing be sustainable? Clarifying sustainable fashion». In: *Textiles and clothing sustainability*. Springer, 2017, pp. 1–45.
- [38] Gustav Sandin and Greg M Peters. «Environmental impact of textile reuse and recycling—A review». In: *Journal of cleaner production* 184 (2018), pp. 353–365.
- [39] Gustav Sandin, Greg M Peters, and Magdalena Svanström. «Using the planetary boundaries framework for setting impact-reduction targets in LCA contexts». In: *The International Journal of Life Cycle Assessment* 20.12 (2015), pp. 1684–1700.

- [40] Textile Exchange. *Preferred Fiber & Materials – Market Report 2019*. https://textileexchange.org/wp-content/uploads/2019/11/Textile-Exchange_PREFERRED-Fiber-Material-Market-Report_2019.pdf. [Online; accessed 16-February-2022].
- [41] Li Shen, Ernst Worrell, and Martin K Patel. «Environmental impact assessment of man-made cellulose fibres». In: *Resources, Conservation and Recycling* 55.2 (2010), pp. 260–274.
- [42] Motahareh Mokhtari Yazdi and Mohammad Sheikhzadeh. «Personal cooling garments: a review». In: *The Journal of The Textile Institute* 105.12 (2014), pp. 1231–1250.
- [43] Yehu Lu et al. «A novel personal cooling system (PCS) incorporated with phase change materials (PCMs) and ventilation fans: an investigation on its cooling efficiency». In: *Journal of thermal biology* 52 (2015), pp. 137–146.
- [44] Yang Guo et al. «Ultrathin, Washable, and Large-Area Graphene Papers for Personal Thermal Management». In: *Small* 13.44 (2017), p. 1702645.
- [45] Ming Fu et al. «Review on modeling heat transfer and thermoregulatory responses in human body». In: *Journal of thermal biology* 62 (2016), pp. 189–200.
- [46] Po-Chun Hsu et al. «Personal thermal management by metallic nanowire-coated textile». In: *Nano letters* 15.1 (2015), pp. 365–371.
- [47] Xu A Zhang et al. «Dynamic gating of infrared radiation in a textile». In: *Science* 363.6427 (2019), pp. 619–623.
- [48] Roland Geyer, Jenna R Jambeck, and Kara Lavender Law. «Production, use, and fate of all plastics ever made». In: *Science advances* 3.7 (2017), e1700782.
- [49] SCYL Krimm, CY Liang, and GBBM Sutherland. «Infrared spectra of high polymers. II. Polyethylene». In: *The journal of chemical physics* 25.3 (1956), pp. 549–562.
- [50] Carla Balocco et al. «Experimental transmittance of polyethylene films in the solar and infrared wavelengths». In: *Solar Energy* 165 (2018), pp. 199–205.
- [51] Jonathan K Tong et al. «Infrared-transparent visible-opaque fabrics for wearable personal thermal management». In: *ACS Photonics* 2.6 (2015), pp. 769–778.
- [52] Svetlana V Boriskina. «Nanoporous fabrics could keep you cool». In: *Science* 353.6303 (2016), pp. 986–987.
- [53] Svetlana V Boriskina et al. «Heat is the new light». In: *Optics and Photonics News* 28.11 (2017), pp. 26–33.

- [54] Matteo Alberghini et al. «Multistage and passive cooling process driven by salinity difference». In: *Science advances* 6.11 (2020), eaax5015.
- [55] Kamyar Shirvanimoghaddam et al. «Death by waste: Fashion and textile circular economy case». In: *Science of The Total Environment* 718 (2020), p. 137317.
- [56] Higgs Materials Sustainability Index. <https://msi.higg.org/>. [Online; accessed 10-November-2020].
- [57] Natascha M Van der Velden, Kristi Kuusk, and Andreas R Köhler. «Life cycle assessment and eco-design of smart textiles: The importance of material selection demonstrated through e-textile product redesign». In: *Materials & Design* 84 (2015), pp. 313–324.
- [58] Julia K Steinberger et al. «A spatially explicit life cycle inventory of the global textile chain». In: *The International Journal of Life Cycle Assessment* 14.5 (2009), pp. 443–455.
- [59] DS Achilias et al. «Chemical recycling of plastic wastes made from polyethylene (LDPE and HDPE) and polypropylene (PP)». In: *Journal of hazardous materials* 149.3 (2007), pp. 536–542.
- [60] Narinder Singh et al. «Recycling of plastic solid waste: A state of art review and future applications». In: *Composites Part B: Engineering* 115 (2017), pp. 409–422.
- [61] John Scheirs. «Polymer recycling: science, technology and applications». In: *John Wiley & Sons Ltd, Journals, Baffins Lane, Chichester, Sussex PO 19 1 UD, UK, 1998. 591* (1998).
- [62] DS Achilias and GP Karayannidis. «The chemical recycling of PET in the framework of sustainable development». In: *Water, air and soil pollution: Focus* 4.4 (2004), pp. 385–396.
- [63] James H Clark et al. *Feedstock recycling of plastic wastes*. Vol. 1. Royal society of chemistry, 1999.
- [64] Zheng Zhang et al. «Recovering waste plastics using shape-selective nano-scale reactors as catalysts». In: *Nature Sustainability* 2.1 (2019), pp. 39–42.
- [65] Subramanian Senthilkannan Muthu et al. «Recyclability Potential Index (RPI): The concept and quantification of RPI for textile fibres». In: *Ecological indicators* 18 (2012), pp. 58–62.
- [66] Farhad Memarzadeh and Weiran Xu. «Role of air changes per hour (ACH) in possible transmission of airborne infections». In: *Building Simulation*. Vol. 5. 1. Springer. 2012, pp. 15–28.

- [67] Michael J Risbeck et al. «Modeling and multiobjective optimization of indoor airborne disease transmission risk and associated energy consumption for building HVAC systems». In: *Energy and Buildings* 253 (2021), p. 111497.
- [68] Mindaugas Jakubcionis and Johan Carlsson. «Estimation of European Union residential sector space cooling potential». In: *Energy Policy* 101 (2017), pp. 225–235.
- [69] Danny HW Li, Liu Yang, and Joseph C Lam. «Impact of climate change on energy use in the built environment in different climate zones—a review». In: *Energy* 42.1 (2012), pp. 103–112.
- [70] M Mohanraj, S Jayaraj, and C Muraleedharan. «Environment friendly alternatives to halogenated refrigerants—A review». In: *International Journal of Greenhouse Gas Control* 3.1 (2009), pp. 108–119.
- [71] Yifan Yang, Gary Cui, and Christopher Q Lan. «Developments in evaporative cooling and enhanced evaporative cooling—A review». In: *Renewable and Sustainable Energy Reviews* 113 (2019), p. 109230.
- [72] Jason Woods and Eric Kozubal. «Combining liquid desiccant dehumidification with a dew-point evaporative cooler: A design analysis». In: *HVAC Research* 19.6 (2013), pp. 663–675.
- [73] Ahlem Zouaoui, Leila Zili-Ghedira, and Sassi Ben Nasrallah. «Open solid desiccant cooling air systems: A review and comparative study». In: *Renewable and Sustainable Energy Reviews* 54 (2016), pp. 889–917.
- [74] Muhammad H Mahmood et al. «Overview of the Maisotsenko cycle—A way towards dew point evaporative cooling». In: *Renewable and sustainable energy reviews* 66 (2016), pp. 537–555.
- [75] Chandrakant Wani, Satyashree Ghodke, and Chaitanya Shrivastava. «A review on potential of Maisotsenko cycle in energy saving applications using evaporative cooling». In: *Int. J. Adv. Res. Sci. Eng. Technol* 1.1 (2012), pp. 15–20.
- [76] Mehdi Zeyghami, D Yogi Goswami, and Elias Stefanakos. «A review of clear sky radiative cooling developments and applications in renewable power systems and passive building cooling». In: *Solar Energy Materials and Solar Cells* 178 (2018), pp. 115–128.
- [77] Aaswath P Raman et al. «Passive radiative cooling below ambient air temperature under direct sunlight». In: *Nature* 515.7528 (2014), pp. 540–544.
- [78] Yao Zhai et al. «Scalable-manufactured randomized glass-polymer hybrid metamaterial for daytime radiative cooling». In: *Science* 355.6329 (2017), pp. 1062–1066.

- [79] Jyotirmoy Mandal et al. «Hierarchically porous polymer coatings for highly efficient passive daytime radiative cooling». In: *Science* 362.6412 (2018), pp. 315–319.
- [80] Siddharth Buddhiraju, Parthiban Santhanam, and Shanhui Fan. «Thermodynamic limits of energy harvesting from outgoing thermal radiation». In: *Proceedings of the National Academy of Sciences* 115.16 (2018), E3609–E3615.
- [81] Eli A Goldstein, Aaswath P Raman, and Shanhui Fan. «Sub-ambient non-evaporative fluid cooling with the sky». In: *Nature Energy* 2.9 (2017), pp. 1–7.
- [82] CG Granqvist and A Hjortsberg. «Radiative cooling to low temperatures: General considerations and application to selectively emitting SiO films». In: *Journal of Applied Physics* 52.6 (1981), pp. 4205–4220.
- [83] AK Head. «Method and means for refrigeration by selective radiation». In: *Australian Patent* 239364 (1959).
- [84] Bikram Bhatia et al. «Passive directional sub-ambient daytime radiative cooling». In: *Nature communications* 9.1 (2018), pp. 1–8.
- [85] PS Liu and Guo-Feng Chen. *Porous materials: processing and applications*. Elsevier, 2014.
- [86] Bernardo Buonomo et al. «Evaluation of thermal and fluid dynamic performance parameters in aluminum foam compact heat exchangers». In: *Applied Thermal Engineering* 176 (2020), p. 115456.
- [87] Matteo Alberghini et al. «Sustainable polyethylene fabrics with engineered moisture transport for passive cooling». In: *Nature Sustainability* (2021), pp. 1–10.
- [88] Jinwoo Lee, Jaeyun Kim, and Taeghwan Hyeon. «Recent progress in the synthesis of porous carbon materials». In: *Advanced materials* 18.16 (2006), pp. 2073–2094.
- [89] Subhash C Singh et al. «Solar-trackable super-wicking black metal panel for photothermal water sanitation». In: *Nature Sustainability* 3.11 (2020), pp. 938–946.
- [90] Scott J Hollister. «Porous scaffold design for tissue engineering». In: *Nature materials* 4.7 (2005), pp. 518–524.
- [91] Mark E Davis. «Ordered porous materials for emerging applications». In: *Nature* 417.6891 (2002), pp. 813–821.
- [92] Matteo Fasano et al. «Passive heat transfer enhancement by 3D printed Pitot tube based heat sink». In: *International Communications in Heat and Mass Transfer* 74 (2016), pp. 36–39.

- [93] Nikola A Dudukovic et al. «Cellular fluidics». In: *Nature* 595.7865 (2021), pp. 58–65.
- [94] Luigi Ventola et al. «Convective heat transfer enhancement through laser-etched heat sinks: Elliptic scale-roughened and cones patterns». In: *Energies* 13.6 (2020), p. 1360.
- [95] Matteo Morciano et al. «Efficient steam generation by inexpensive narrow gap evaporation device for solar applications». In: *Scientific reports* 7.1 (2017), pp. 1–9.
- [96] Eliodoro Chiavazzo et al. «Passive solar high-yield seawater desalination by modular and low-cost distillation». In: *Nature sustainability* 1.12 (2018), pp. 763–772.
- [97] Shao-Lin Wu et al. «Solar-driven evaporators for water treatment: challenges and opportunities». In: *Environmental Science: Water Research & Technology* 7.1 (2021), pp. 24–39.
- [98] Chenlin Zhang et al. «Designing a next generation solar crystallizer for real seawater brine treatment with zero liquid discharge». In: *Nature communications* 12.1 (2021), pp. 1–10.
- [99] Lin Zhao et al. «A Passive High-Temperature High-Pressure Solar Steam Generator for Medical Sterilization». In: *Joule* 4.12 (2020), pp. 2733–2745.
- [100] Seol Ha Kim et al. «Boiling heat transfer and critical heat flux evaluation of the pool boiling on micro structured surface». In: *International Journal of Heat and Mass Transfer* 91 (2015), pp. 1140–1147.
- [101] Ayokunle Olanrewaju et al. «Capillary microfluidics in microchannels: from microfluidic networks to capillarie circuits». In: *Lab on a Chip* 18.16 (2018), pp. 2323–2347.
- [102] Matteo Alberghini et al. «Characterisation and modelling of water wicking and evaporation in capillary porous media for passive and energy-efficient applications». In: *Applied Thermal Engineering* (2022), p. 118159.
- [103] Kan Li et al. «Structured cone arrays for continuous and effective collection of micron-sized oil droplets from water». In: *Nature communications* 4.1 (2013), pp. 1–7.
- [104] H Jeremy Cho et al. «Nanoengineered materials for liquid–vapour phase-change heat transfer». In: *Nature Reviews Materials* 2.2 (2016), pp. 1–17.
- [105] George Ni et al. «A salt-rejecting floating solar still for low-cost desalination». In: *Energy & Environmental Science* 11.6 (2018), pp. 1510–1519.

- [106] Yuchao Wang, Lianbin Zhang, and Peng Wang. «Self-floating carbon nanotube membrane on macroporous silica substrate for highly efficient solar-driven interfacial water evaporation». In: *ACS Sustainable Chemistry & Engineering* 4.3 (2016), pp. 1223–1230.
- [107] George M Whitesides. «The origins and the future of microfluidics». In: *nature* 442.7101 (2006), pp. 368–373.
- [108] David Juncker et al. «Autonomous microfluidic capillary system». In: *Analytical chemistry* 74.24 (2002), pp. 6139–6144.
- [109] C Duprat et al. «Wetting of flexible fibre arrays». In: *Nature* 482.7386 (2012), pp. 510–513.
- [110] P-A Auroux et al. «Miniaturised nucleic acid analysis». In: *Lab on a Chip* 4.6 (2004), pp. 534–546.
- [111] David N Breslauer, Philip J Lee, and Luke P Lee. «Microfluidics-based systems biology». In: *Molecular Biosystems* 2.2 (2006), pp. 97–112.
- [112] Luca Bergamasco, Matteo Alberghini, and Matteo Fasano. «Nano-metering of solvated biomolecules or nanoparticles from water self-diffusivity in bio-inspired nanopores». In: *Nanoscale research letters* 14.1 (2019), pp. 1–11.
- [113] Huidong Liu et al. «A bioinspired capillary-driven pump for solar vapor generation». In: *Nano Energy* 42 (2017), pp. 115–121.
- [114] Pierre-Gilles De Gennes, Françoise Brochard-Wyart, and David Quéré. *Capillarity and wetting phenomena: drops, bubbles, pearls, waves*. Springer Science & Business Media, 2013.
- [115] Junfeng Xiao et al. «Study of imbibition in various geometries using phase field method». In: *Capillarity* 2.4 (2019), pp. 57–65.
- [116] Han Hu et al. «Multiscale modeling of the three-dimensional meniscus shape of a wetting liquid film on micro-/nanostructured surfaces». In: *Langmuir* 33.43 (2017), pp. 12028–12037.
- [117] Edward W Washburn. «The dynamics of capillary flow». In: *Physical review* 17.3 (1921), p. 273.
- [118] Yusuf Shi et al. «A 3D photothermal structure toward improved energy efficiency in solar steam generation». In: *Joule* 2.6 (2018), pp. 1171–1186.
- [119] Giovanni Antonetto et al. «Synergistic freshwater and electricity production using passive membrane distillation and waste heat recovered from camouflaged photovoltaic modules». In: *Journal of Cleaner Production* 318 (2021), p. 128464.
- [120] Wenbin Wang et al. «Simultaneous production of fresh water and electricity via multistage solar photovoltaic membrane distillation». In: *Nature communications* 10.1 (2019), pp. 1–9.

- [121] Zhenyuan Xu et al. «Ultrahigh-efficiency desalination via a thermally-localized multistage solar still». In: *Energy & Environmental Science* 13.3 (2020), pp. 830–839.
- [122] BJ Carroll. «The accurate measurement of contact angle, phase contact areas, drop volume, and Laplace excess pressure in drop-on-fiber systems». In: *Journal of colloid and interface science* 57.3 (1976), pp. 488–495.
- [123] HM Princen. «Capillary phenomena in assemblies of parallel cylinders: I. Capillary rise between two cylinders». In: *Journal of Colloid and Interface Science* 30.1 (1969), pp. 69–75.
- [124] HM Princen. «Capillary phenomena in assemblies of parallel cylinders: II. Capillary rise in systems with more than two cylinders». In: *Journal of Colloid and Interface Science* 30.3 (1969), pp. 359–371.
- [125] RR Rye, JA Mann, and FG Yost. «The flow of liquids in surface grooves». In: *Langmuir* 12.2 (1996), pp. 555–565.
- [126] Amir Faghri and Yuwen Zhang. *Transport phenomena in multiphase systems*. Elsevier, 2006.
- [127] Giuseppe Soligno, Marjolein Dijkstra, and René van Roij. «The equilibrium shape of fluid-fluid interfaces: Derivation and a new numerical method for Young’s and Young-Laplace equations». In: *The Journal of chemical physics* 141.24 (2014), p. 244702.
- [128] Alban Sauret et al. «Wetting morphologies on an array of fibers of different radii». In: *Soft Matter* 11.20 (2015), pp. 4034–4040.
- [129] George I Loeb and Malcolm E Schrader. *Modern approaches to wettability: theory and applications*. Springer Science & Business Media, 2013.
- [130] Die Yang et al. «Dynamics of capillary-driven flow in open microchannels». In: *The Journal of Physical Chemistry C* 115.38 (2011), pp. 18761–18769.
- [131] Reza Masoodi and Krishna M Pillai. *Wicking in porous materials: traditional and modern modeling approaches*. CRC Press, 2012.
- [132] Daxiang Deng et al. «Characterization of capillary rise dynamics in parallel micro V-grooves». In: *International Journal of Heat and Mass Transfer* 77 (2014), pp. 311–320.
- [133] TS Chow. «Wetting of rough surfaces». In: *Journal of Physics: Condensed Matter* 10.27 (1998), p. L445.
- [134] Mohamad Karaki et al. «A comparative analytical, numerical and experimental analysis of the microscopic permeability of fiber bundles in composite materials». In: *Int. J. Compos. Mater* 7.3 (2017), pp. 82–102.

- [135] Alexander L Berdichevsky and Zhong Cai. «Preform permeability predictions by self-consistent method and finite element simulation». In: *Polymer Composites* 14.2 (1993), pp. 132–143.
- [136] N Fries et al. «The effect of evaporation on the wicking of liquids into a metallic weave». In: *Journal of colloid and interface science* 321.1 (2008), pp. 118–129.
- [137] Myron B Allen III. «Numerical modelling of multiphase flow in porous media». In: *Advances in Water Resources* 8.4 (1985), pp. 162–187.
- [138] Yechezkel Mualem. «A new model for predicting the hydraulic conductivity of unsaturated porous media». In: *Water resources research* 12.3 (1976), pp. 513–522.
- [139] J Chen, JW Hopmans, and ME Grismer. «Parameter estimation of two-fluid capillary pressure–saturation and permeability functions». In: *Advances in Water Resources* 22.5 (1999), pp. 479–493.
- [140] M Th Van Genuchten. «A closed-form equation for predicting the hydraulic conductivity of unsaturated soils». In: *Soil science society of America journal* 44.5 (1980), pp. 892–898.
- [141] Markus Nordlund and Véronique Michaud. «Dynamic saturation curve measurement for resin flow in glass fibre reinforcement». In: *Composites Part A: Applied Science and Manufacturing* 43.3 (2012), pp. 333–343.
- [142] COMSOL Multiphysics. *Two-phase flow in Column*. https://www.comsol.it/model/download/667241/models.ssf.twophase_flow_column.pdf. [Online; accessed 04-November-2020].
- [143] R Krishna and JA Wesselingh. «The Maxwell-Stefan approach to mass transfer». In: *Chemical engineering science* 52.6 (1997), pp. 861–911.
- [144] Akshay Deshmukh and Menachem Elimelech. «Understanding the impact of membrane properties and transport phenomena on the energetic performance of membrane distillation desalination». In: *Journal of Membrane Science* 539 (2017), pp. 458–474.
- [145] CL Yaws and HC Yang. «To estimate vapor pressure easily». In: *Hydrocarbon Processing;(USA)* 68.10 (1989).
- [146] Ray E Bolz and George L Tuve. *CRC handbook of tables for applied engineering science*. CRC press, 2019.
- [147] JS Mackie and P Meares. «The diffusion of electrolytes in a cation-exchange resin membrane I. Theoretical». In: *Proceedings of the Royal Society of London. Series A. Mathematical and Physical Sciences* 232.1191 (1955), pp. 498–509.

- [148] BIPM et al. «Evaluation of measurement data – Guide to the expression of uncertainty in measurement». In: *Joint Committee for Guides in Metrology, JCGM 100:2008* ().
- [149] PA Kralchevsky et al. «Capillary meniscus interaction between colloidal particles attached to a liquid—fluid interface». In: *Journal of Colloid and Interface Science* 151.1 (1992), pp. 79–94.
- [150] Meni Shimel et al. «Enhancement of Wetting and Mechanical Properties of UHMWPE-Based Composites through Alumina Atomic Layer Deposition». In: *Advanced Materials Interfaces* 5.14 (2018), p. 1800295.
- [151] Emad Yousif and Raghad Haddad. «Photodegradation and photostabilization of polymers, especially polystyrene». In: *SpringerPlus* 2.1 (2013), pp. 1–32.
- [152] Aya E Abusrafa et al. «Modification of polyethylene by RF plasma in different/mixture gases». In: *Coatings* 9.2 (2019), p. 145.
- [153] MR Sanchis et al. «Surface modification of low density polyethylene (LDPE) film by low pressure O₂ plasma treatment». In: *European Polymer Journal* 42.7 (2006), pp. 1558–1568.
- [154] Hana Drnovská et al. «Surface properties of polyethylene after low-temperature plasma treatment». In: *Colloid and Polymer Science* 281.11 (2003), pp. 1025–1033.
- [155] FT Wallenberger. «The effect of absorbed water on the properties of cotton and fibers from hydrophilic polyester block copolymers». In: *Textile Research Journal* 48.10 (1978), pp. 577–581.
- [156] Daniel K Owens and RC Wendt. «Estimation of the surface free energy of polymers». In: *Journal of applied polymer science* 13.8 (1969), pp. 1741–1747.
- [157] Amir Faghri and Yuwen Zhang. *Transport phenomena in multiphase systems*. Elsevier, 2006.
- [158] Daniel Y Kwok and August W Neumann. «Contact angle measurement and contact angle interpretation». In: *Advances in colloid and interface science* 81.3 (1999), pp. 167–249.
- [159] Toshio Hata, Yasuaki Kitazaki, and Takanori Saito. «Estimation of the surface energy of polymer solids». In: *The Journal of Adhesion* 21.3-4 (1987), pp. 177–194.
- [160] Glen McHale and MI Newton. «Global geometry and the equilibrium shapes of liquid drops on fibers». In: *Colloids and Surfaces A: Physicochemical and Engineering Aspects* 206.1-3 (2002), pp. 79–86.

- [161] CW Extrand and Sung In Moon. «Contact angles on spherical surfaces». In: *Langmuir* 24.17 (2008), pp. 9470–9473.
- [162] Bo S Westerlind and John C Berg. «Surface energy of untreated and surface-modified cellulose fibers». In: *Journal of applied polymer science* 36.3 (1988), pp. 523–534.
- [163] Glen McHale et al. «Wetting of a high-energy fiber surface». In: *Journal of colloid and interface science* 186.2 (1997), pp. 453–461.
- [164] Luuk K Koopal. «Wetting of solid surfaces: fundamentals and charge effects». In: *Advances in colloid and interface science* 179 (2012), pp. 29–42.
- [165] VM Moreno-Villa et al. «Effect of surface charge on hydrophobicity levels of insulating materials». In: *IEE Proceedings-Generation, Transmission and Distribution* 145.6 (1998), pp. 675–681.
- [166] Frank E Jones. *Evaporation of water with emphasis on applications and measurements*. CRC Press, 1991.
- [167] Jintu Fan et al. «An improved model of heat and moisture transfer with phase change and mobile condensates in fibrous insulation and comparison with experimental results». In: *International Journal of Heat and Mass Transfer* 47.10-11 (2004), pp. 2343–2352.
- [168] Aaron H Persad and Charles A Ward. «Expressions for the evaporation and condensation coefficients in the Hertz-Knudsen relation». In: *Chemical reviews* 116.14 (2016), pp. 7727–7767.
- [169] GR Somayajulu. «New equations for enthalpy of vaporization from the triple point to the critical point». In: *International journal of thermophysics* 9.4 (1988), pp. 567–575.
- [170] Adrian Bejan. *Convection heat transfer*. John Wiley & Sons, 2013.
- [171] John A Duffie, William A Beckman, and Nathan Blair. *Solar engineering of thermal processes, photovoltaics and wind*. John Wiley & Sons, 2020.
- [172] Matteo Alberghini et al. «Coffee-based colloids for direct solar absorption». In: *Scientific reports* 9.1 (2019), pp. 1–11.
- [173] Jason Woods et al. «Modeling of a membrane-based absorption heat pump». In: *Journal of Membrane Science* 337.1-2 (2009), pp. 113–124.
- [174] Renato De Medeiros Rocha et al. «Brazilian solar saltworks-ancient uses and future possibilities». In: *Aquatic Biosystems* 8.1 (2012), pp. 1–6.
- [175] *Geography and climate in Dubai*. <https://www.dubai.com/v/geography/>. [Online; accessed 28-January-2022].
- [176] SM Bower and JR Saylor. «A study of the Sherwood–Rayleigh relation for water undergoing natural convection-driven evaporation». In: *International Journal of Heat and Mass Transfer* 52.13-14 (2009), pp. 3055–3063.

- [177] Tibor Poós and Evelin Varju. «Dimensionless evaporation rate from free water surface at tubular artificial flow». In: *Energy Procedia* 112 (2017), pp. 366–373.
- [178] Yunus A Cengel, Sanford Klein, and William Beckman. *Heat transfer: a practical approach*. Vol. 141. WBC McGraw-Hill Boston, 1998.
- [179] Mohamed El Guendouzi, Abderrahim Dinane, and Abdelfetah Mounir. «Water activities, osmotic and activity coefficients in aqueous chloride solutions at $T = 298.15$ K by the hygrometric method». In: *The Journal of Chemical Thermodynamics* 33.9 (2001), pp. 1059–1072.
- [180] Miyi Li et al. «Solubilities of NaCl, KCl, LiCl, and LiBr in methanol, ethanol, acetone, and mixed solvents and correlation using the LIQUAC model». In: *Industrial & engineering chemistry research* 49.10 (2010), pp. 4981–4988.
- [181] Matthew Allan and Lisa J Mauer. «Dataset of water activity measurements of alcohol: water solutions using a Tunable Diode Laser». In: *Data in brief* 12 (2017), pp. 364–369.
- [182] Magin Lapuerta, Juan Pablo Hernandez, and John R Agudelo. «An equation for the estimation of alcohol-air diffusion coefficients for modelling evaporation losses in fuel systems». In: *Applied thermal engineering* 73.1 (2014), pp. 539–548.
- [183] Carl B Kretschmer and Richard Wiebe. «Liquid-Vapor Equilibrium of Ethanol–Toluene Solutions». In: *Journal of the American Chemical Society* 71.5 (1949), pp. 1793–1797.
- [184] Vladimir Majer and Vaclav Svoboda. «Enthalpies of vaporization of organic compounds: a critical review and data compilation». In: (1986).
- [185] Eden Rephaeli, Aaswath Raman, and Shanhui Fan. «Ultrabroadband photonic structures to achieve high-performance daytime radiative cooling». In: *Nano letters* 13.4 (2013), pp. 1457–1461.
- [186] Muhammed Ali Kecebas et al. «Passive radiative cooling design with broadband optical thin-film filters». In: *Journal of Quantitative Spectroscopy and Radiative Transfer* 198 (2017), pp. 179–186.
- [187] Yang Fu et al. «Daytime passive radiative cooler using porous alumina». In: *Solar Energy Materials and Solar Cells* 191 (2019), pp. 50–54.
- [188] Torbjörn MJ Nilsson, Gunnar A Niklasson, and Claes G Granqvist. «A solar reflecting material for radiative cooling applications: ZnS pigmented polyethylene». In: *Solar Energy materials and Solar cells* 28.2 (1992), pp. 175–193.

- [189] Peng Wang. «Emerging investigator series: the rise of nano-enabled photothermal materials for water evaporation and clean water production by sunlight». In: *Environmental Science: Nano* 5.5 (2018), pp. 1078–1089.
- [190] Hyung Won Chung, Jaichander Swaminathan, David M Warsinger, et al. «Multistage vacuum membrane distillation (MSVMD) systems for high salinity applications». In: *Journal of Membrane Science* 497 (2016), pp. 128–141.
- [191] Edward Jones et al. «The state of desalination and brine production: A global outlook». In: *Science of the Total Environment* 657 (2019), pp. 1343–1356.
- [192] Ayhan Demirbas, Ayman A Hashem, and Ahmed A Bakhsh. «The cost analysis of electric power generation in Saudi Arabia». In: *Energy Sources, Part B: Economics, Planning, and Policy* 12.6 (2017), pp. 591–596.
- [193] Akshay Deshmukh et al. «Membrane distillation at the water-energy nexus: limits, opportunities, and challenges». In: *Energy & Environmental Science* 11.5 (2018), pp. 1177–1196.
- [194] Tiezheng Tong and Menachem Elimelech. «The global rise of zero liquid discharge for wastewater management: drivers, technologies, and future directions». In: *Environmental science & technology* 50.13 (2016), pp. 6846–6855.
- [195] Robert L McGinnis et al. «Pilot demonstration of the NH₃/CO₂ forward osmosis desalination process on high salinity brines». In: *Desalination* 312 (2013), pp. 67–74.
- [196] José Morillo et al. «Comparative study of brine management technologies for desalination plants». In: *Desalination* 336 (2014), pp. 32–49.
- [197] Mohammadali Safavi and Toraj Mohammadi. «High-salinity water desalination using VMD». In: *Chemical Engineering Journal* 149.1-3 (2009), pp. 191–195.
- [198] United States Environmental Protection Agency. *Advancing Sustainable Materials Management: Facts and Figures Report*. https://www.epa.gov/sites/default/files/2021-01/documents/2018_ff_fact_sheet_dec_2020_fnl_508.pdf. [Online; accessed 28-January-2022].
- [199] María de Gracia Trujillo García et al. «Recycling of acrylonitrile–butadiene–styrene using injection moulding machine». In: *Procedia Technology* 22 (2016), pp. 399–406.
- [200] Arunachalam Lakshmanan. *Sintering Techniques of Materials*. BoD–Books on Demand, 2015.

- [201] Changlin Cao et al. «Recycling and application of wasted polytetrafluoroethylene via high-energy ball milling technology for nitrile rubber composites preparation». In: *Polymer Engineering & Science* 56.6 (2016), pp. 643–649.
- [202] Mark Anthony Browne et al. «Accumulation of microplastic on shorelines worldwide: sources and sinks». In: *Environmental science & technology* 45.21 (2011), pp. 9175–9179.
- [203] Sabine Lattemann and Thomas Höpner. «Environmental impact and impact assessment of seawater desalination». In: *Desalination* 220.1-3 (2008), pp. 1–15.
- [204] Rachel Einav, Kobi Harussi, and Dan Perry. «The footprint of the desalination processes on the environment». In: *Desalination* 152.1-3 (2003), pp. 141–154.
- [205] Jose Luis Sanchez-Lizaso et al. «Salinity tolerance of the Mediterranean seagrass *Posidonia oceanica*: recommendations to minimize the impact of brine discharges from desalination plants». In: *Desalination* 221.1-3 (2008), pp. 602–607.
- [206] Muftah H El-Naas. «Reject brine management». In: *Desalination, trends and technologies* (2011), pp. 237–252.
- [207] AMO Mohamed, M Maraqa, and J Al Handhaly. «Impact of land disposal of reject brine from desalination plants on soil and groundwater». In: *Desalination* 182.1-3 (2005), pp. 411–433.
- [208] Ozeair Abessi. «Brine Disposal and Management—Planning, Design, and Implementation». In: *Sustainable Desalination Handbook*. Elsevier, 2018, pp. 259–303.
- [209] Matteo Alberghini et al. «Textured and Rigid Capillary Materials for Passive Energy-Conversion Devices». In: *Advanced Materials Interfaces* (2022), p. 2200057.
- [210] L Ventola et al. «Micro-structured rough surfaces by laser etching for heat transfer enhancement on flush mounted heat sinks». In: *Journal of Physics: Conference Series*. IOP Publishing, 2014, p. 012017.
- [211] Jaroslaw Drelich et al. «Hydrophilic and superhydrophilic surfaces and materials». In: *Soft Matter* 7.21 (2011), pp. 9804–9828.
- [212] Synthia Divin-Mariotti et al. «Effects of micro-knurling and femtosecond laser micro texturing on aluminum long-term surface wettability». In: *Applied Surface Science* 479 (2019), pp. 344–350.

- [213] Anne-Marie Kietzig et al. «Laser-patterned super-hydrophobic pure metallic substrates: Cassie to Wenzel wetting transitions». In: *Journal of Adhesion Science and Technology* 25.20 (2011), pp. 2789–2809.
- [214] Pavel Bizi-Bandoki et al. «Time dependency of the hydrophilicity and hydrophobicity of metallic alloys subjected to femtosecond laser irradiations». In: *Applied Surface Science* 273 (2013), pp. 399–407.
- [215] Matteo Morciano et al. «Sustainable freshwater production using passive membrane distillation and waste heat recovery from portable generator sets». In: *Applied Energy* 258 (2020), p. 114086.
- [216] DCL Vasconcelos et al. «Corrosion resistance of stainless steel coated with sol-gel silica». In: *Journal of non-crystalline solids* 273.1-3 (2000), pp. 135–139.
- [217] Kwang-Hyuk Choi et al. «Characteristics of flexible indium tin oxide electrode grown by continuous roll-to-roll sputtering process for flexible organic solar cells». In: *Solar Energy Materials and Solar Cells* 93.8 (2009), pp. 1248–1255.
- [218] Luca Bonandini et al. «Roll-to-Roll Atmospheric Plasma Treatment: A Green and Efficient Process to Improve the Hydrophilicity of a PET Surface». In: *ChemSusChem: Chemistry & Sustainability Energy & Materials* 3.5 (2010), pp. 591–596.
- [219] Peng Tao et al. «Solar-driven interfacial evaporation». In: *Nature energy* 3.12 (2018), pp. 1031–1041.
- [220] Zhangxin Wang et al. «Pathways and challenges for efficient solar-thermal desalination». In: *Science advances* 5.7 (2019), eaax0763.
- [221] Lenan Zhang et al. «Passive, high-efficiency thermally-localized solar desalination». In: *Energy & Environmental Science* 14.4 (2021), pp. 1771–1793.
- [222] Yaixin Zhang et al. «Structure Architecting for Salt-Rejecting Solar Interfacial Desalination to Achieve High-Performance Evaporation With In Situ Energy Generation». In: *Advanced Science* 7.9 (2020), p. 1903478.
- [223] David Quéré. «Non-sticking drops». In: *Reports on Progress in Physics* 68.11 (2005), p. 2495.
- [224] Yoshikazu Ito et al. «Multifunctional porous graphene for high-efficiency steam generation by heat localization». In: *Advanced Materials* 27.29 (2015), pp. 4302–4307.
- [225] Le Shi et al. «Rational design of a bi-layered reduced graphene oxide film on polystyrene foam for solar-driven interfacial water evaporation». In: *Journal of Materials Chemistry A* 5.31 (2017), pp. 16212–16219.

- [226] Panpan Zhang et al. «Vertically aligned graphene sheets membrane for highly efficient solar thermal generation of clean water». In: *ACS nano* 11.5 (2017), pp. 5087–5093.
- [227] Linfan Cui et al. «High rate production of clean water based on the combined photo-electro-thermal effect of graphene architecture». In: *Advanced Materials* 30.22 (2018), p. 1706805.
- [228] Mingwei Zhu et al. «Tree-inspired design for high-efficiency water extraction». In: *Advanced Materials* 29.44 (2017), p. 1704107.
- [229] MW Higgins et al. «Carbon fabric based solar steam generation for waste water treatment». In: *Solar Energy* 159 (2018), pp. 800–810.
- [230] Chaoji Chen et al. «Highly flexible and efficient solar steam generation device». In: *Advanced Materials* 29.30 (2017), p. 1701756.
- [231] Hadi Ghasemi et al. «Solar steam generation by heat localization». In: *Nature communications* 5.1 (2014), pp. 1–7.
- [232] Xiayun Huang et al. «Facile polypyrrole thin film coating on polypropylene membrane for efficient solar-driven interfacial water evaporation». In: *RSC advances* 7.16 (2017), pp. 9495–9499.
- [233] Qiaomei Chen et al. «A durable monolithic polymer foam for efficient solar steam generation». In: *Chemical science* 9.3 (2018), pp. 623–628.
- [234] Fei Zhao et al. «Highly efficient solar vapour generation via hierarchically nanostructured gels». In: *Nature nanotechnology* 13.6 (2018), pp. 489–495.
- [235] Juan Wang et al. «High-performance photothermal conversion of narrow-bandgap Ti₂O₃ nanoparticles». In: *Advanced Materials* 29.3 (2017), p. 1603730.
- [236] Xinzhi Wang et al. «Investigation of photothermal heating enabled by plasmonic nanofluids for direct solar steam generation». In: *Solar Energy* 157 (2017), pp. 35–46.
- [237] Jianqiu Zhao et al. «A hydrophobic surface enabled salt-blocking 2D Ti₃C₂ MXene membrane for efficient and stable solar desalination». In: *Journal of Materials Chemistry A* 6.33 (2018), pp. 16196–16204.
- [238] Seunghyun Hong et al. «Nature-inspired, 3D origami solar steam generator toward near full utilization of solar energy». In: *ACS applied materials & interfaces* 10.34 (2018), pp. 28517–28524.
- [239] Xiuqiang Li et al. «Enhancement of interfacial solar vapor generation by environmental energy». In: *Joule* 2.7 (2018), pp. 1331–1338.
- [240] Guobin Xue et al. «Highly efficient water harvesting with optimized solar thermal membrane distillation device». In: *Global Challenges* 2.5-6 (2018), p. 1800001.

- [241] Chaoji Chen, Yudi Kuang, and Liangbing Hu. «Challenges and opportunities for solar evaporation». In: *Joule* 3.3 (2019), pp. 683–718.
- [242] Wenbin Wang et al. «Solar Seawater Distillation by Flexible and Fully Passive Multistage Membrane Distillation». In: *Nano Letters* (2021).
- [243] Geoffrey Vaartstra et al. «Capillary-fed, thin film evaporation devices». In: *Journal of Applied Physics* 128.13 (2020), p. 130901.
- [244] Davoud Jafari, Wessel W Wits, and Bernard J Geurts. «Metal 3D-printed wick structures for heat pipe application: Capillary performance analysis». In: *Applied thermal engineering* 143 (2018), pp. 403–414.
- [245] Reza Masoodi and Krishna M Pillai. «Darcy’s law-based model for wicking in paper-like swelling porous media». In: *AIChE journal* 56.9 (2010), pp. 2257–2267.
- [246] Shile Feng et al. «Three-dimensional capillary ratchet-induced liquid directional steering». In: *Science* 373.6561 (2021), pp. 1344–1348.
- [247] Mi Ae Choi et al. «Permeability modeling of fibrous media in composite processing». In: *Journal of Non-Newtonian Fluid Mechanics* 79.2-3 (1998), pp. 585–598.
- [248] Yun Xia et al. «Spatially isolating salt crystallisation from water evaporation for continuous solar steam generation and salt harvesting». In: *Energy & Environmental Science* 12.6 (2019), pp. 1840–1847.
- [249] Yang Shao et al. «Designing a bioinspired synthetic tree by unidirectional freezing for simultaneous solar steam generation and salt collection». In: *EcoMat* 2.1 (2020), e12018.
- [250] Bing Dai et al. «Bioinspired Janus textile with conical micropores for human body moisture and thermal management». In: *Advanced Materials* 31.41 (2019), p. 1904113.
- [251] Hrvoje Jasak, Aleksandar Jemcov, Zeljko Tukovic, et al. «OpenFOAM: A C++ library for complex physics simulations». In: *International workshop on coupled methods in numerical dynamics*. Vol. 1000. IUC Dubrovnik Croatia. 2007, pp. 1–20.
- [252] Sharmiza Adnan et al. «Commercial PTFE membranes for membrane distillation application: Effect of microstructure and support material». In: *Desalination* 284 (2012), pp. 297–308.
- [253] Mohammad Mahdi A Shirazi, Ali Kargari, and Meisam Tabatabaei. «Evaluation of commercial PTFE membranes in desalination by direct contact membrane distillation». In: *Chemical engineering and processing: Process intensification* 76 (2014), pp. 16–25.

BIBLIOGRAPHY

- [254] Mostafa H Sharqawy, John H Lienhard, and Syed M Zubair. «Thermophysical properties of seawater: a review of existing correlations and data». In: *Desalination and water Treatment* 16.1-3 (2010), pp. 354–380.